

# Exploring the use of synchrotron X-ray scattering methods for the detection of heterogeneous nucleation

---

Thesis submitted for the degree of

Doctor of Philosophy

at the University of Leicester

by

Adam Jonathan Brown

Department of Engineering

University of Leicester

**2014**

**Abstract: *Exploring the use of synchrotron X-ray scattering methods for the detection of heterogeneous nucleation*** by Adam Brown

The process of solidification is fundamental to a wide range of engineering processes. In most practical cases, such as in grain refinement of aluminium alloys, heterogeneous nucleation is the predominant route by which the transformation of liquid to solid is initiated. The mechanism by which solid crystal grows from heterogeneous particles is widely investigated but not fully understood. This study explores a novel approach to investigating nucleation through the use of synchrotron X-ray scattering techniques. The novel approach provides unprecedented access to the interactions at the solid-liquid interface and permits *in-situ* data collection as phase transformations proceed. Liquid aluminium was used as a relevant test case, and solid  $\text{Al}_2\text{O}_3$  and  $\text{TiB}_2$  substrates are used to represent, respectively, a model case and industrially relevant scenario for grain refinement. Experimental results reveal the undercooling required for nucleation in the  $\text{Al}/\text{Al}_2\text{O}_3$  system. They also provide detail on thermal expansion in the aluminium prior to melting. Crystal Truncation Rod analysis reveals the existence of a 'transition layer' between  $\text{Al}_2\text{O}_3$  and  $\text{Al}$ , which is suggested to arise to accommodate residual strain in the solidified aluminium. For the  $\text{Al}/\text{TiB}_2$  system, an innovative sample preparation method facilitated investigation of the interface between the materials, providing an experimental model of a  $\text{TiB}_2$  particle within an aluminium melt. Results indicate the proclivity for the formation of  $\text{Al}_3\text{Ti}$  in the system, and lead to the proposal that this is likely to occur even in situations in which the assumed Ti content suggests otherwise.

## **Publications**

1. Brown, A.J., H.B. Dong, P.B. Howes, and C.L. Nicklin. "Exploring the Use of a Synchrotron X-Ray Scattering Method to Investigate Nucleation." *Materials Science Forum* 765 (July 2013): 102–6.
2. Brown, A.J., H.B. Dong, P.B. Howes, and C.L. Nicklin. "In Situ Observation of the Orientation Relationship at the Interface Plane between Substrate and Nucleus Using X-Ray Scattering Techniques." *Scripta Materialia* 77 (April 2014): 60–63.

## **Awards**

1. East Midlands Materials Society (EMMS) Young Person's Lecture Competition: East Midlands heat (University of Leicester, February 2013): **Winner**
2. Institute of Materials, Minerals and Mining (IOM<sup>3</sup>) Young Person's Lecture Competition: National Final (London, April 2013): **Winner**
3. IOM<sup>3</sup> World Lecture Competition: World Final (Hong Kong, October 2013): **Third Place**

## **Acknowledgements**

I would first like to thank my supervisor, Professor Hongbiao Dong. He has been immensely supportive of me throughout my time at university, and has been a constant source of encouragement and advice. He is a true credit to the department. Huge thanks also go to Dr. Paul Howes, a true gentleman and scholar without whom this project would have been impossible. His knowledge, support and advice have been invaluable. It has been an absolute pleasure to work closely with both Hongbiao and Paul throughout this project.

My great thanks to the beamline teams, both at Diamond and ESRF, for their unwavering support and willingness to help at any hour during my experiments. Special thanks to Chris Nicklin and Jonathan Rawle at I07, and Roberto Felici and Francesco Carla at ID03.

I would like to thank all the members of staff in the Department of Engineering who have supported me; particularly Profs. Helen Atkinson and Sarah Hainsworth, and Drs. Andrew McMullan and Dave Weston. Thanks also to all the technical and administrative staff for being so friendly and willing to help with my experiments and with the unique idiosyncrasies of postgraduate study. Thanks also to the various individuals in the chemistry and physics departments who helped enormously in experiment preparation; particularly Dr. Adrian Boatwright and Michael McNally.

Thanks to all my wonderful friends, including, but not limited to: all the Leicesterfarians, past and present, particularly my fellow engineering PhDers Tris, Mike and Scott; my University Challenge teammates; Thursday Club; the Goodrich posse; and all my great pals in Birmingham, Manchester and Bristol. All the entertainment and joy over the last 4 years has kept me going through the hard times. Special thanks to my Bredon buds; Bunj, Mr Nacci and S. Charles Mitchell, for all the tomfoolery, hi-jinks and the gentle ribbing that has kept me grounded throughout my university life!



My departed friend Jack, you gave me so much belief and confidence for my future in engineering. I miss you terribly and I'm so sorry you're not around to see the next stage. Rest easy buddy.

Thanks to my family for instilling and encouraging my passion for science and engineering. I am so grateful for their love and support throughout my university career and I hope I have made them proud. Finally, thanks to my wonderful girlfriend Marie Nugent, whose love, support, and patience has been unwavering and has kept me sane through the most challenging PhD years...now it's my turn to return the favour!

## Table of Contents

<b>1</b>	<b>Introduction and Literature Review.....</b>	<b>1</b>
1.1	Background.....	1
1.2	Nucleation: Basics and Classical Homogeneous Nucleation .....	6
1.3	Classical Heterogeneous Nucleation .....	14
1.4	Extensions to the classical approach .....	19
1.5	Nucleation by adsorption.....	22
1.6	Liquid Ordering at the Liquid/Solid interface .....	26
1.7	Practical Application: Grain Refinement.....	35
1.7.1	Grain Refinement Theory .....	35
1.7.2	Grain Refinement Practice .....	36
1.8	Synchrotron X-ray Scattering .....	49
1.8.1	Introduction.....	49
1.8.2	X-ray Crystallography .....	49
1.8.3	Scattering from atoms .....	57
1.8.4	Surface XRD and Crystal Truncation Rods .....	59
1.8.5	Relevance to current project.....	66
1.9	Remaining Challenges .....	67
1.10	Aims of this work.....	68
<b>2</b>	<b>Experiments .....</b>	<b>70</b>
2.1	General methodology.....	71
2.2	Beamlines .....	74
2.3	Materials and Sample Preparation .....	79
2.3.1	Experiment One.....	79
2.3.2	Experiment Two.....	83
2.3.3	Experiment Three .....	83

2.3.4	Experiment Four .....	87
2.4	Heater Design .....	93
2.5	Experimental Procedure.....	100
2.5.1	Experiment One.....	100
2.5.2	Experiment Two.....	103
2.5.3	Experiment Three .....	106
2.5.4	Experiment Four .....	110
2.6	Software used in Data Analysis .....	114
<b>3</b>	<b>Results: In-situ Observation of Al/Al<sub>2</sub>O<sub>3</sub> Melting and Solidification..</b>	<b>117</b>
3.1	Experiment One .....	117
3.1.1	S1 .....	117
3.1.2	S2 .....	131
3.1.3	S3.....	136
3.1.4	E1 Conclusions.....	139
3.2	Experiment Two .....	141
3.3	Experiment Three .....	142
3.3.1	Sample X.....	142
3.3.2	E3 S1: Imaging approach .....	143
3.3.3	E3 S2: CTR profile undercooling assessment .....	151
3.3.4	E3 Conclusions.....	161
3.4	Conclusions .....	163
<b>4</b>	<b>Results: Ordered structures at Al/Al<sub>2</sub>O<sub>3</sub> interface determined through Crystal Truncation Rod analysis .....</b>	<b>165</b>
4.1	Experiment One .....	167
4.2	Experiment Three .....	172
4.2.1	Sample X: Al on Al <sub>2</sub> O <sub>3</sub> .....	172
4.2.2	Sample W: Clean Al <sub>2</sub> O <sub>3</sub> .....	175

4.2.3	Comparing effects on surface structure of evaporation vs. crystallisation .....	178
4.2.4	Fitting: Introduction .....	181
4.2.5	Fitting: No Physical Constraints.....	185
4.2.6	Fitting: Physical Constraints .....	189
4.3	Conclusion of CTR work .....	197
<b>5</b>	<b>Results: Understanding the mechanism at the interface between TiB<sub>2</sub> and Al melt.....</b>	<b>200</b>
5.1	Experiment Three: Sample A .....	202
5.1.1	Characterisation .....	202
5.1.2	Heating and Cooling .....	207
5.2	Experiment Four .....	216
5.2.1	Sample V .....	216
5.2.2	Sample VIII .....	230
5.3	Evidence for formation of Al <sub>3</sub> Ti at the Al/TiB <sub>2</sub> interface .....	254
5.3.1	Experiment Three .....	255
5.3.2	Experiment Four .....	260
5.4	Conclusions on the formation of Al <sub>3</sub> Ti in the system .....	265
<b>6</b>	<b>Conclusions .....</b>	<b>268</b>
6.1	Feasibility study .....	268
6.2	Key outcomes .....	269
6.3	Future Work .....	271
<b>7</b>	<b>References .....</b>	<b>273</b>

## List of Tables

Table 1-1 - Orientation relationships in materials of interest. Note that the parallel planes are the same in both cases; there are two close-packed directions for the $\text{Al}_3\text{Ti}$ which satisfy the orientation relationship. ....	42
Table 1-2- Detail of lattice mismatch along planes of interest .....	42
Table 2-1 – Brief summary of experiments E1 – E4 .....	70
Table 2-2 - Diffractometer specification.....	75
Table 2-3 - Bill of Materials used in Heater .....	96
Table 2-4 - Peak positions and corresponding d-spacings from S1 .....	101
Table 3-1 - Peak Positions and corresponding d-spacings with X-ray energy = 15keV ( $\lambda=0.826\text{\AA}$ ). Values of 'd' and ' $\theta$ ' are related through Bragg's Law.....	119
Table 3-2 – Samples used in E3 .....	142
Table 3-3 - Peak Positions and corresponding d-spacings with X-ray energy = 20keV ( $\lambda=0.62\text{\AA}$ ).....	143
Table 4-1 – Values of parameters used to achieve fit in Figure 4-14 .....	187
Table 4-2 - Values of parameters used for 'Best Fit (physical)' in Figure 4-19. Fits '1' and '2' result in the same values apart from differences in <i>Scale</i> and <i>occupancy</i> 9. These are indicated in the table. ....	195
Table 5-1 – Diffractometer angles .....	201
Table 5-2 – Peak positions and corresponding <i>d</i> values (atomic spacing) for materials of interest in investigation of the Al/TiB <sub>2</sub> system. X-ray energy 19.9 keV ( $\lambda=0.623\text{\AA}$ ). Specific references to the individual studies from which structural data is taken are given in the first column. ....	203
Table 5-3 - Peak positions and corresponding d-spacings for materials of interest in investigation of the Al/TiB <sub>2</sub> system. X-ray energy 19.9 keV ( $\lambda=0.623\text{\AA}$ ) .....	217
Table 5-4 – Morphological transitions in Al layer.....	244
Table 5-5 - Peak positions and corresponding d-spacings for materials of interest in investigation of the Al/TiB <sub>2</sub> system. X-ray energy 19.9 keV ( $\lambda=0.623\text{\AA}$ ) .....	255

## List of Figures

Figure 1-1 – Schematic plot of total free energy change against nuclear radius	9
Figure 1-2 - Free energy change against nuclear radius at different temperatures.....	11
Figure 1-3 – Schematic illustration of contributions to nucleation rate .....	13
Figure 1-4 – The spherical cap model for heterogeneous nucleation.....	15
Figure 1-5 – Activation energy barrier comparison for homogeneous vs heterogeneous case.....	17
Figure 1-6 – Schematic of nucleation rates indicating undercooling requirement for homogeneous vs heterogeneous case .....	18
Figure 1-7 - Schematic of nucleation in free growth scenario. Examples of nucleant areas on a) a surface patch and b) a nucleant particle are shown. c) shows schematically the critical condition for free growth as the solid-liquid interfacial radius $r_{sl}$ approaches a minimum. ....	19
Figure 1-8 - HRTEM image of AlP layer on Al catalyst nucleating solidification of Si. Modified from [25]; original image from [26] .....	23
Figure 1-9 - HRTEM image of $Al_3Ti$ layer on $TiB_2$ nucleating solidification of Al. Modified from [27] .....	24
Figure 1-10 – Schematic representation of atomic-scale ordering in liquid adjacent to solid substrate .....	27
Figure 1-11 – Schematic of $Al_2O_3$ HCP unit cell showing various crystallographic planes referred to in studies under review .....	28
Figure 1-12 – HRTEM image of liquid Al in contact with solid $Al_2O_3$ (006) plane at $\sim 750^\circ C$ ( $T_m$ for Al = $660.4^\circ C$ ). White line indicates scan of average intensity across interface; minima in intensity corresponding to positions of identified liquid layers at 1 and 2. Inset shows a schematic of $Al_2O_3$ crystal and first layer of Al atoms. Reproduced from [6].....	29
Figure 1-13 - a) HRTEM image of liquid Al in contact with solid $Al_2O_3$ (112) R-plane. Inset shows a simulated image (from MD) used for comparison. b) Inset from a) enlarged and overlaid with atomic structure; atom positions based on the assumption of a transient $Al_2O$ phase. c) Enlarged view of atomic structure from b). Modified from [5] .....	30
Figure 1-14 - Schematic of binary Al-Ti phase diagram. Modified from [51].....	37

Figure 1-15 - Indicating $\text{TiB}_2$ particles in solidified Al matrix without solute Ti. a) shows a single $\text{TiB}_2$ particle while b) shows a cluster present at the grain boundaries. Reproduced from [7].....	38
Figure 1-16 - Indicating $\text{TiB}_2$ particles in solidified Al matrix with solute Ti at concentration a) 0.01%wt and b) 0.05%wt. Reproduced from [7] .....	38
Figure 1-17 – TEM images of a $\text{TiB}_2$ particle in quenched Al-based metallic glass with schematic of $\text{TiB}_2$ crystal structure. a) Bright-field image. Remaining images are dark-field, showing b) the boride particle. c) Al crystals nucleated on {001} boride faces. d) Layer on {001} boride faces suggested to be $\text{Al}_3\text{Ti}$ . Inset shows selected area diffraction pattern used to orient electron beam to run parallel to $\langle 110 \rangle \text{TiB}_2$ direction. Modified from [27].....	40
Figure 1-18 – HRTEM image of $\text{Al}_3\text{Ti}$ layer on $\text{TiB}_2$ nucleating solidification of Al. The layer between the boride surface and Al matrix has atomic spacing consistent with those of $\text{Al}_3\text{Ti}$ . Modified from [27].....	41
Figure 1-19 – TEM images of $\text{TiB}_2$ particles in quenched Al-based metallic glass with schematic of $\text{TiB}_2$ crystal structure. a) Bright field image. Remaining images are dark-field, showing b) the boride particle, c) Al crystals nucleated on (001) boride faces, and d) the thin $\text{Al}_3\text{Ti}$ layer on the boride surfaces. Inset shows selected area diffraction pattern. Beam axis is parallel to $\langle 110 \rangle \text{TiB}_2$ direction. Modified from [51] (originally presented in [14]).....	43
Figure 1-20 – Bright-field TEM image showing close-up of boride particle. Crystalline Al is observed only on faces/ledges/steps which have a (001) orientation – no crystalline Al is observed to have nucleated on any other surfaces. Reproduced from [14].....	44
Figure 1-21 - Schematic representation of Bragg's Law. $k_i$ and $k_f$ are the wavevectors of the incident and scattered beams respectively. Physically, $k_i$ and $k_f$ are planar front waves with wavelength $\lambda$ . $d$ is the interplanar spacing between planes of atoms within a single crystal. For constructive interference to occur, the path difference $2d\sin\theta$ must be equal to an integer number of wavelengths $n\lambda$ . .....	50
Figure 1-22 - Schematic indicating the formation of momentum transfer $Q$ .....	52
Figure 1-23 – Schematic showing the generation of the reciprocal lattice. Shown in 2D for ease of understanding (assume $a_3/b_3$ are 'out of page').....	53

Figure 1-24 - Ewald construction in 2D. The reciprocal lattice is set up such that the spacing between lattice points is $2\pi/d$ where $d$ is the real space interplanar distance. This reflects the periodicity in the wave and simplifies later calculation .....	54
Figure 1-25 - Schematic showing the specular and off-specular directions in scattering geometry in relation to the incident beam and sample normal. Note that $\theta$ refers to the scattering angle in both the specular ( $\theta_i$ ) and off-specular ( $\theta_i'$ ) directions. ....	55
Figure 1-26 – Schematic showing generation of diffraction patterns from a) an ‘infinite’ crystal and b) the same crystal but cleaved to produce a surface from which scattering takes place. The respective diffraction patterns for each situation are shown on the right hand side of the figure. In the case of b) streaks of scattering, called crystal truncation rods, are produced in the direction perpendicular to the surface and link the Bragg peaks. ....	60
Figure 1-27 - Schematic of intensity variation along Crystal Truncation Rod ...	61
Figure 1-28 - Schematic of intensity variation to CTR from sample with extra layer at $n = -1$ .....	62
Figure 1-29 - Schematic indicating how CTR intensity profiles are recorded. a) indicates the condition that the diffractometer geometries must create; i.e. the Ewald sphere intersects with the CTR generated from the surface. b) indicates that the intensity profile is progressively recorded as the scan proceeds up the rod. ....	64
Figure 2-1 – General overview of experimental setup .....	73
Figure 2-2 – Schematic representations of a) z-axis and b) (2+3) circle diffractometers. The geometries are fundamentally similar, the only differences being that for the (2+3), a v-circle is added for the detector azimuth, and the $\gamma$ -circle rotates the whole detector arm rather than just the detector itself. Reproduced from [106] .....	76
Figure 2-3 – Sample position for E1 at I07: a) $\delta/\omega$ rotation circle b) $\alpha/\gamma$ rotation circle c) sample normal d) X-ray beam in e) diffracted X-ray beam out (to detector, out of shot). Refer to Figure 2-2 to clarify alignment of rotation circles. ....	77
Figure 2-4 - Sample position for E3 at ID03: a) $\delta/\omega$ rotation circle b) $\alpha$ rotation circle c) detector moves along this linear track and is rotated in place to create $\gamma$	



rotation d) sample normal e) X-ray beam in f) diffracted X-ray beam out to g) detector. Refer to Figure 2-2 to clarify alignment of rotation circles. ....	78
Figure 2-5 – Basic substrate geometry. Dimensions in mm .....	80
Figure 2-6 – AFM investigation of E1 Al <sub>2</sub> O <sub>3</sub> single crystal (001) sample surface. ....	81
Figure 2-7 - EDX analysis of the E1 sample, confirming presence of Al and O and lack of impurities .....	83
Figure 2-8 - Surface Profilometry measurements on Mo substrates prepared for E3.....	85
Figure 2-9 - Samples prepared for E3. Left - sample X, Right – sample A.....	87
Figure 2-10 - Surface Profilometry measurements on Mo substrates prepared for E4 .....	88
Figure 2-11 - Molybdenum pieces prepared and fixed for deposition of Al. Polished pieces a) and b) are clamped to threaded rods which are then fixed into the heater assembly. The two smaller cylindrical pieces c) on the bottom rod at are samples prepared for the micro-furnace (see section 2.4).....	90
Figure 2-12 – Setup for deposition of TiB <sub>2</sub> on E4 samples. Samples are mounted at a); the threaded rods are rotated such that the sample surfaces directly face the TiB <sub>2</sub> sputtering target located at b). The sample and mounting assembly is heated during deposition via the potted heating element located at c).....	90
Figure 2-13 - Heater prototype testing at DLR .....	93
Figure 2-14 - Heater Design for E2. a) Exploded view of heater assembly. b) Operating principle .....	95
Figure 2-15 - Assembled heater testing .....	97
Figure 2-16 - Heat transfer simulation for heater, performed using SolidWorks. Node 1: 724°C; Node 2: 723°C.....	99
Figure 2-17 – Zoom in on Figure 2-16 to highlight node positions (i.e. intended thermocouple positions on heater). ....	99
Figure 2-18 – Pilatus 100k detector image from E1 S1 showing initial condition (false colour map applied for clarity; actual images are greyscale) .....	102
Figure 2-19 – Naming convention for E3.....	107
Figure 2-20 – Naming convention for E4. Unlike E3, the scan and image numbers are not linked. Scan and image numbers at I07 are recorded from the	

start of the original beamline operation, rather than being ‘reset’ at the start of each users beamtime.....	111
Figure 3-1 - SEM micrograph of sample surface, showing granular morphology of sputter-deposited Al film. The size of individual granules is approximately 200nm.....	118
Figure 3-2 – Initial detector image from Al/Al <sub>2</sub> O <sub>3</sub> sample at room temperature, showing the features of interest. Line ‘a-a’ indicates projection for Figure 3-4. ....	120
Figure 3-3 – 3D volume indicating how the sequential plot in Figure 3-4 relates to the images collected from the Pilatus detector as shown in Figure 3-2.....	121
Figure 3-4 – <i>In situ</i> X-ray diffraction patterns for the Al/Al <sub>2</sub> O <sub>3</sub> system. The y-axis plots diffraction patterns sequentially through the heating and cooling cycle. Heating was manually ramped to ~350°C prior to the implementation of the displayed heating and cooling cycle using isothermal holds. ....	122
Figure 3-5 - Detector image from endpoint of heating/cooling scan.....	124
Figure 3-6 – Schematic showing transformation of the Al{111} feature from a) ring to b) spot-like. Rectangle indicates the field of view of the detector.....	125
Figure 3-7 – SEM micrograph of solidified Al. The featureless dark grey areas in the middle of the image are exposed regions of the Al <sub>2</sub> O <sub>3</sub> substrate surface. All other areas are Al. Primary Al dendrites are observed in the centre of the image. ....	129
Figure 3-8 – Heating & cooling profile used for E1 S1. Dark red dashed line indicates temperature level at which Al features were observed to disappear. The blue dashed lines demarcate the scan in which the Al feature reappearance was observed. ....	130
Figure 3-9 – Temperature profile used for E1 S2. Dotted lines indicate temperature levels at which Al (111) peak disappeared (red) and reappeared (light blue – final scan showing no (111) feature; dark blue – (111) feature present).....	132
Figure 3-10 – Selected specular data from E1 S2 during heating. Large central peak at $2\theta = 20.2$ arises from Al {111}. Smaller peak at $2\theta = 22$ arises from Al <sub>2</sub> O <sub>3</sub> {0006}. Peak at $2\theta = 22.8$ is suggested to arise from oxide. Part of the detector image is included to assist the reader in identifying the correlation between these and the <i>I</i> vs $2\theta$ plot.....	133

Figure 3-11 - Selected specular data from E1 S2 during cooling. $\text{Al}_2\text{O}_3$ (006) peak at $2\theta = 22$ remains visible throughout. Central Al {111} returns on scan at $583.8^\circ\text{C}$ . ....	135
Figure 3-12 – Temperature profile used for E1 S3. Dashed lines indicating disappearance and reappearance of Al features as before. ....	136
Figure 3-13 – Selected specular data from E1S3 during heating .....	137
Figure 3-14 - Selected specular data from E1S3 during cooling .....	138
Figure 3-15 – Suggested morphological transitions in E1 sample resulting from heating and cooling cycles. Note that Al grains in the second image are shown ‘flattened’ but in reality may have a columnar or equiaxed morphology. ....	139
Figure 3-16 – Temperature profile achieved with heater device during E2 ....	141
Figure 3-17 – Images from Al/ $\text{Al}_2\text{O}_3$ sample indicating disparity of powder-like features at different sample rotations. Stated $2\theta$ position ( $15.45^\circ$ ) is centred on the red dot in the lower right quadrant. Bright ‘spot’ on both images is the $\text{Al}_2\text{O}_3$ {0001} feature. Within the image: a) feature only appearing at $\text{sax}=0$ b) feature only appearing at $\text{sax}=-2$ c) feature appearing at both $\text{sax}=0$ and $\text{sax}=-2$ therefore arising from the Al layer .....	144
Figure 3-18 – Temperature profile applied to sample X for initial imaging scans .....	145
Figure 3-19 – Detector images showing phase transition in Al layer. Ring is clearly visible to right hand side of image in a)-c), and a faint structure persists to f) as indicated. It is no longer present in g) and h). Image d) is blacked out due to an error.....	146
Figure 3-20 – Detector images showing reappearance of Al {111} feature. Feature returns in image d) and develops in intensity over e)-h). ....	149
Figure 3-21 – Initial (0,1) rods from sample X. Note some of the data points around the Bragg peaks have been deleted to keep the y-axis within a reasonable limit. The numbers 939, 940 and 941 in the legend refer to the corresponding scan numbers from the ESRF data. Callouts a-d correspond to images in Figure 3-23. ....	152
Figure 3-22 – Schematic indicating how powder features can superimpose on CTR data. a)->b)->c) shows a scan ‘up’ the (0,1, $l$ ) CTR (increasing ‘ $l$ ’). Co-ordinated diffractometer motion keeps the rod in the centre of the detector as the scan proceeds. Powder features arise from the Al layer as it is also	

illuminated by the X-ray beam. As the diffractometer moves, the rod remains stationary, but powder features move relative to it. Thus at certain values of ' $l$ ', powder features are coincident with the position of the CTR in reciprocal space, and so are superimposed on the profile, as in c).....	154
Figure 3-23 – Direct detector images from scan #939. Refer to Figure 3-21 for corresponding locations within scan. Note that the detector slits have been closed to restrict background scattering. a) General image showing the CTR itself (intersection with Ewald sphere). b) peak at $l = 4.5$ likely arising from Al. c) powder ring. d) peak at $l = 5.5$ likely arising from Al. Note the brightness of image d) has been significantly increased to highlight the shape of the feature. ....	155
Figure 3-24 – Profile applied to sample X during collection of CTRs. Callouts indicate the scan number recorded at that point with dashed lines indicating the start of the scan. The red and blue lines indicate the exact time during the corresponding scan at which the Al {111} peak is recorded. ....	156
Figure 3-25 – $(0,1,l)$ rods recorded in scan 943. ....	157
Figure 3-26 – $(0,1,l)$ rods recorded in scan 944. ....	158
Figure 3-27 – $(0,1,l)$ rods recorded in scans 943 and 944; presented as a combined figure.....	158
Figure 3-28 – $(0,1,l)$ rods recorded in scans 951 and 954; presented as a combined figure (N.B. these are consecutive scans; 952 was abandoned due to implementation of realignment scans from 953 on).....	159
Figure 3-29 – Schematic illustration of possible morphology changes in Al and $\text{Al}_2\text{O}_3$ through E1 and E3.....	162
Figure 4-1 – Schematic indicating how CTR intensity profiles are recorded. a) indicates the condition that the diffractometer geometries must create; i.e. the Ewald sphere intersects with the CTR generated from the surface. b) indicates that the intensity profile is progressively recorded as the scan proceeds up the rod. ....	165
Figure 4-2 - Temperature profile for E1 S2 .....	167
Figure 4-3 – Selected $(1,0,l)$ rods during heating, showing the expected Bragg peaks at $l = 4$ and $l = 10$ and scattering intensity variation along the rod.....	168
Figure 4-4 - Selected $(1,0,l)$ rods during cooling .....	169
Figure 4-5 - Selected $(0,1,l)$ rods during heating.....	169

Figure 4-6 - Selected (0,1, $l$ ) rods during cooling .....	170
Figure 4-7 - Profile applied to sample X during CTR collection. Callouts indicate the scan number recorded at that point with dashed lines indicating the start of the scan. Melting was detected in 944, and solidification in 954. For these, red and blue lines indicate the specific point during the scan at which the Al {111} peak is recorded.....	173
Figure 4-8 – Selected (0,1) CTRs collected from sample X during heating and cooling. Refer to legend and Figure 4-7 to observe the temperatures at which the rods were recorded. Bragg peaks at $l = 2$ and $l = 8$ with characteristic intensity in between. Sharp peaks between $l = 4$ and $l = 6$ arise from the superposition of powder-like features as described in 3.3.3.....	174
Figure 4-9 – (0,1) rods from sample W (1330 and 1351) compared with those from sample X (944 and 986), showing the effect of the presence of Al on the surface of $\text{Al}_2\text{O}_3$ .....	176
Figure 4-10 – (0,1), (1,0) and (1,1) rods collected <i>before</i> (1329-1331) and <i>after</i> (1371-1373) evaporation of Al onto sample W .....	179
Figure 4-11 – Schematic representation of .bul file used to represent the bulk $\text{Al}_2\text{O}_3$ structure. Atomic positions are given in the form of coordinates in x, y, z; the values are proportions of the unit cell lattice parameters (displayed in the first line of the text).....	183
Figure 4-12 – Schematic representation of .fit file used to represent the surface of the $\text{Al}_2\text{O}_3$ substrate. Occupancy and vertical displacement parameters refer to the individual atoms (or layers of atoms) as indicated.....	184
Figure 4-13 - Model setup for ROD. The surface layer (white) sits on a bulk crystal (black) which extends to minus infinity. Adapted from Ref [86].....	185
Figure 4-14 - Best fit to representative (0,1) CTR from Sample X.....	186
Figure 4-15 – Schematic indication of the change to the $\text{Al}_2\text{O}_3$ surface structure suggested by the data fitting. The modified structure represents an expansion of the original along z. Oxygen positions are shown with O <i>and</i> Al atoms, to reflect the possibility that Al may in fact be present instead of O, as discussed in the text. ....	188
Figure 4-16 – Crystal structures of a) $\text{Al}_2\text{O}_3$ (001) and b) Al(111). Images are scaled relative to each other such that the Al atoms are of equal size. Crystallographic axes are shown beneath the structures. Note that b) presents	

the unit cell with <i>two</i> layers of Al (111) following the ABAB stacking sequence.	
.....	190
Figure 4-17 – Schematic representation Al (111) planes, 30° rotation about [111] axis, followed by mapping onto Al <sub>2</sub> O <sub>3</sub> (001) surface. On the lower portion of the image, the first Al unit cell (small, grey circles) shows only the atoms within an individual (111) crystal plane (layer A). The second Al unit cell (larger, black circles) shows all remaining atoms in the unit cell (following the ABAB stacking sequence) .....	191
Figure 4-18 – Modified .fit file to represent Al <sub>2</sub> O <sub>3</sub> surface <i>and</i> the first interfacial Al (with an approximately (111) structure). Diagram is schematic; stated positions may not exactly correspond. Inset shows the equilibrium Al (111) crystal structure from a ‘side view’ (along [110]) for reference. ....	193
Figure 4-19 – Best fits to representative (0,1) rod from sample X. Series <i>Best Fit (no physical constraints)</i> is a repeat of the fit from Figure 4-14.....	194
Figure 4-20 – Schematic indication of the change to the Al <sub>2</sub> O <sub>3</sub> surface structure suggested by physical best fits. Arrows on atoms at position #9 indicate the displacement in x/y indicated by the parameter displacement 10. ....	196
Figure 4-21 - Summary of findings in Chapter 4. a) indicates, schematically, the ideal CTR profile obtained from a clean Al <sub>2</sub> O <sub>3</sub> (001) surface. b) indicates the addition of Al, with (111) planes parallel to the substrate surface, would not result in any modification to this profile due to the lack of registry with the substrate. c) indicates the existence of a semi-ordered region between the substrate and crystal and the modification to the CTR that results. The transitionary region is suggested to accommodate strain between the substrate and the crystal.....	198
Figure 5-1 – Diffractometer angles used for characterisation. a) shows the z-axis diffractometer of the type used at ID03 (I07 is fundamentally the same, with y rotating the whole diffractometer rather than just the detector). b) indicates the physical directions of the characterisation scans and how they relate to sample geometry. Adapted from [106].....	201
Figure 5-2 – Out-of-plane characterisation from E3 sample A. Angle of incidence varies from 5° - 15°. ....	204

Figure 5-3 – In-plane characterisation from E3 sample A. Angle of incidence 0.2° (grazing-incidence) .....	205
Figure 5-4 – Combined in-plane and out-of-plane scans from E3 sample A..	206
Figure 5-5 – Temperature profile applied to sample A. The slow cooling ramp was terminated slightly early due to limited remaining beamtime. The heater was switched off at that point generating the rapid cooling seen from ~29,000 seconds.....	208
Figure 5-6 – Selected in-plane scans indicating thermal expansion in the Al layer during heating. Arrows indicate movement of Al peaks due to thermal expansion.....	209
Figure 5-7 – Selected in-plane scans showing phase transition in Al, with accompanying temperature profile applied over each scan. ....	209
Figure 5-8 – In-plane scans showing phase transition in Al; data scaled to highlight the suggested broad TiB <sub>2</sub> (101) feature located between $2\theta = 17^\circ$ and $2\theta = 19^\circ$ .....	211
Figure 5-9 - SEM images of sample A. Insets in top right indicate approximate position of image on sample surface. a) Centre of the sample (beam focus position). b) Edge of the sample showing a number of crystallites, assumed to be Al, though this has yet to be reliably established. Smaller, needle-shaped structures visible in b) may be either crystallites or features of the TiB <sub>2</sub> surface. The small, deeper black regions are likely areas where the TiB <sub>2</sub> coating has broken away.....	213
Figure 5-10 – Mosaic of SEM images from sample A from edge (far left) to centre (far right) of surface. Scale bar in bottom right of image is 200 $\mu$ m (total distance covered by the above is approx. 4.2mm) .....	214
Figure 5-11 – Initial characterisation scans from E4 sample V. Plot shows in-plane $\delta$ scan (145013) with angle of incidence 0.3° and out-of-plane $\alpha/\gamma$ scan (145012) with angle of incidence varying from 5-10° .....	218
Figure 5-12 – In-plane scans of sample surface before and after evaporation of Al.....	220
Figure 5-13 – Schematic of morphology generated in E4 samples.....	221
Figure 5-14 – Temperature profile applied to sample V. Scan 145254 takes place at maximum temperature and is shown in Figure 5-15.....	222

Figure 5-15 – In plane scans of sample surface. Plots from Figure 5-12 (145013 and 145035) are repeated; 145254 is a scan performed during the high temperature hold at ~750°C .....	223
Figure 5-16 – In plane scans of sample V surface. Features of interest in scan 145676 have been highlighted .....	224
Figure 5-17 - Out of plane scans of sample V surface. Key features are annotated. ....	225
Figure 5-18 – Enlarged view ( $2\theta = 14^\circ$ - $16^\circ$ ) of the out-of-plane scans of sample V surface superimposed on material data.....	227
Figure 5-19 – Out-of-plane characterisation scan from E4 sample VIII with angle of incidence varying from $5^\circ$ - $15^\circ$ .....	231
Figure 5-20 – In-plane characterisation scan from E4 sample VIII with angle of incidence $0.3^\circ$ .....	232
Figure 5-21 - Combined in-plane and out-of-plane scans from E4 sample VIII .....	233
Figure 5-22 – Highlighted region of out-of-plane characterisation scan, comparing sample V (145012) with sample VIII (146501).....	234
Figure 5-23 – Detector at $2\theta = 15.3^\circ$ showing two distinct rings.....	235
Figure 5-24 - Initial condition in sample VIII as shown at ‘monitoring position’; i.e. centred at the Al {111} peak position. It is debatable whether the feature at $16.2^\circ$ is indeed Ti as the beam is not expected to penetrate to the depth of the Ti layer in this geometry. The feature therefore likely arises either from Ti on the edge of the sample, or from other materials in supporting structures around the sample. ....	236
Figure 5-25 – Full out-of-plane characterisation of sample VIII before and after heating followed by immediate quenching. Vertical bars indicate expected peak positions for some materials of interest. Figure highlights the disappearance of the Al {200} feature and strengthening of Al {111}. ....	237
Figure 5-26 – Out of plane characterisation before and after heating: enlarged region $2\theta = 10^\circ$ - $20^\circ$ .....	238
Figure 5-27 – In-plane characterisation of sample VIII before and after heating followed by immediate quenching. Vertical bars indicate expected peak positions for some materials of interest (a selection are annotated). Figure	



highlights the disappearance of the Al {111} feature and strengthening of the Al {200}.....	239
Figure 5-28 – Montages of detector images from in-plane scans before and after thermal cycling. Refer to Figure 5-27 for comparison. Figure highlights the orientation relationship between TiB <sub>2</sub> and Al which arises on cooling. ....	241
Figure 5-29 - Detector images from out-of-plane scans at Al {111} peak position ( $2\theta = 15.3^\circ$ ). Brightness and contrast settings are the same in all images. a) shows the Ti {002} ring from sample V. b) shows the same Ti {002} ring, with the Al {111} ring also present, from sample VIII prior to heating. c) shows the resulting feature at the same position after heating and subsequent quenching. ....	242
Figure 5-30 - Detector images from out-of-plane scans at a range of Al positions – a), b), c), d). Shows the transition of features before and after heating/quenching. Brightness and contrast settings are the same in all images. ....	244
Figure 5-31 – Unit cell constructions for Al.....	247
Figure 5-32 –Suggested morphology for solidified Al layer in sample VIII. ....	247
Figure 5-33 – Micrographs of sample VIII surface after quenching, from a) optical microscopy and b) SEM. Solidified Al covers the majority of the surface; coverage is broken up by 3 distinct feature types, examples of which have been identified and marked.....	248
Figure 5-34 – EDX mapping of sample VIII surface. a) SEM micrograph showing mapped area. b) indicates areas with high Al content. c) indicates areas with high Ti content. d) clarifies the different character of the “patch” and “blister” regions by overlaying the Al onto the Ti map. Black areas in b), i.e. regions with no Al counts, are made transparent; this is then overlaid on the Ti map. Therefore in d), patch regions appear the same as c) as they comprise solely Ti; blisters appear darker due to the mixed Al-Ti content in these regions. Note that the brightness and contrast of the EDX images has been artificially increased for clarity. ....	249
Figure 5-35 – Indicating the mixed Al-Ti content of the blister regions; patch and pure Al areas also shown for comparison. ....	250
Figure 5-36 – Comparison of out-of-plane scans for samples V and VIII with expected peak positions for alternative Ti-B compounds .....	252

Figure 5-37 – Schematic of binary Al-Ti phase diagram. Modified from [51]..	254
Figure 5-38 – Selected in-plane scans from sample A during cooling stages. Region of ‘shoulder formation’ highlighted. Strong Mo {110} peak at $2\theta = 16.08$ and broad $\text{TiB}_2$ {101} feature centred at $2\theta = 17.57$ . Temperatures at which scans were recorded are indicated in Figure 5-39. ....	256
Figure 5-39 – ‘Zoom in’ on previous figure to highlight shoulder formation, suggesting the existence of $\text{Al}_3\text{Ti}$ {112}. Temperatures at which scans were recorded are indicated in Figure 5-39. ....	257
Figure 5-40 - Temperature profile indicating time and temperature of selected scans.....	257
Figure 5-41 – Expected peak positions from a range of oxide phases in the $2\theta$ region $15^\circ$ - $17^\circ$ . Note the strength of the $\text{Al}_3\text{Ti}$ feature in comparison to the oxide phases .....	259
Figure 5-42 – Post-cooling scans (at room temperature) from sample V .....	260
Figure 5-43 – Post-cooling scans (at room temperature) from sample VIII. Note that the peak in the in-plane scan at $2\theta = 15.3^\circ$ arises from the edge of the sample rather than the interfacial region (see Figure 5-28 for comparison) ...	261
Figure 5-44 – Detector images indicating possible formation of $\text{Al}_3\text{Ti}$ . Ti {002} peak shift in E4 sample V is suggested to arise from strain in the Ti interlayer as discussed following Figure 5-17. Behaviour of Ti {002} and Al {111} features from sample VIII are discussed in Figure 5-29.....	262
Figure 5-45 – Scans from sample V comparing post-cooled structure with morphology at high temperature ( $\sim 750^\circ\text{C}$ ). Highlights area around the $\text{Al}_3\text{Ti}$ {112} peak. Scan (145255) shows features present in this region at high temperature.....	264
Figure 5-46 – Proposal for the formation of $\text{Al}_3\text{Ti}$ in the experimental samples, using sample VIII as a schematic case. a) shows the original, sputter-deposited Al layer transitioning to the liquid state on heating. b) $\text{Al}_3\text{Ti}$ forms while at the interface between liquid Al and $\text{TiB}_2$ substrate. c) shows the suggested structure on cooling; i.e. $\text{Al}_3\text{Ti}$ as an interfacial layer between $\text{TiB}_2$ substrate and solidified Al crystal, with orientation relationship $\text{TiB}_2$ (001) // $\text{Al}_3\text{Ti}$ {112} // Al {111}, as suggested by out-of-plane scattering data. ....	267

## Abbreviations

XRD	X-Ray Diffraction
SXRD	Surface X-Ray Diffraction
XRR	X-Ray Reflectivity
CTR	Crystal Truncation Rod
UoL	University of Leicester
DLS	Diamond Light Source
ESRF	European Synchrotron Radiation Facility
CCD	Charge-coupled device
ROI	Region of Interest
TEM	Transmission Electron Microscopy
HRTEM	High-Resolution Transmission Electron Microscopy
SEM	Scanning Electron Microscopy
EDX	Energy dispersive X-ray analysis
MD	Molecular Dynamics
ICSD	Inorganic Crystal Structure Database
T/C	Thermocouple
XTM	Crystal thickness monitor
UHV	Ultra-high vacuum
FIJI	FIJI is just ImageJ
HCP	Hexagonal close-packed
BCC	Body-centred cubic
FCC	Face-centred cubic
EAM	Embedded atom method
KDP	Potassium dihydrogen phosphate
DLR	Deutsches Zentrum für Luft- und Raumfahrt

## 1 Introduction and Literature Review

The opening section of this chapter (1.1) provides a general context for the work and gives some background information. Sections 1.2 to 1.8 introduce fundamental concepts in nucleation, grain refinement, and the X-ray scattering methodology used in the study. Finally, sections 1.9 and 1.10 briefly introduce the project itself.

### 1.1 Background

The process of solidification is fundamental to a wide range of engineering processes. Manufacture of many engineering components depends on the transition of materials from an easily manipulated and transportable liquid form to a rigid and predictable solid structure with required material properties. In most material systems, the process can be described basically as a phase transformation from liquid to solid when the temperature is lowered below the **freezing point** of the system. Most metals **crystallise** upon freezing; i.e. the constituent atoms arrange into an ordered crystal structure composed of repeated **unit cells**, forming microscopic crystallites which are referred to as **grains** in metallurgy. Individual grains are separated by **grain boundaries**, defining the borders at which crystallites of different orientations meet. The character of the grain structures has a strong correspondence to the properties of the material, and thus the ability to understand and control this is fundamental to achieving desired properties in engineering applications.

Perhaps the most important application of the above principles within engineering is the manufacturing process of casting, the basic principles of which can be outlined as follows: during casting, molten metal is introduced into a mould, and takes on the shape of the cavity within. The metal is then cooled, providing the driving force for it to transit to a solid phase. The solidified part is then removed from the mould. The process allows for the creation of complex component geometries which may not be achievable through other common manufacturing methods such as forging or milling. Careful control of casting

parameters, such as cooling rate, allows for a degree of control over the microstructure in the final part, allowing properties to be tailored to specific requirements.

Casting remains a vitally important process for global industry. According to a recent census [1], world casting production currently stands at 98.6 million metric tonnes. In the UK, around 25,000 people are employed directly in the industry across around 450 foundries (ICME<sup>1</sup> data) [2] thus it represents a vital element of British industry as well as one in which there is particular UK expertise. Casting is the primary process in the manufacture of a huge range of products, from small, high precision, highly specified components such as aero-engine turbine blades, through medium-sized parts such as aluminium engine blocks for automotive applications, to vast single-piece castings used as structural sections in oil rigs weighing many tonnes. With requirements for higher performance, better quality, and weight reduction in engineering applications; for example in automotive engine blocks, a better understanding of solidification in casting is paramount.

The first 'step' in the transformation of a system from a liquid to a solid is **nucleation**; the initial formation of solid material from the melt. Fundamentally, nucleation refers to the localised formation of a distinct thermodynamic phase. In metals, which solidify by crystallisation, nucleation describes the point at which atoms or molecules begin to arrange themselves into a characteristic **crystal structure**. Usually, nucleation occurs at specific sites; impurity particles or regions such as the edge of a container, which provide energetically favourable sites for nucleation to occur. This is known as **heterogeneous nucleation**. Nucleation can also occur **homogenously**; in this case, the event is spontaneous and random, and requires the system to be significantly **undercooled**, bringing the temperature below the equilibrium freezing point. These methods of nucleation will be further explained later in this report. The process of **growth** describes the next step of solidification. Here nuclei which have reached a **critical size** will continue to increase in volume, proceeding

---

<sup>1</sup> Institute of Cast Metals Engineers

until the entire system has solidified. In metals, regions which solidify with a particular crystal orientation will form distinct **grains**; the size and distribution of which influence material properties.

As previously stated, the control of solidification is of critical importance to the development of a reliable component. There is usually a desire for a uniform **grain structure** (giving uniform, isotropic properties). Commonly, **grain refinement** (achieving a uniform small grain size) is desired as it gives a higher strength material. This is achieved by either directly adding or allowing heterogeneous particles to form in the melt. A real-life example can be found in casting of **aluminium** and its alloys; hugely important engineering materials used for products as diverse as engine components, cookware and vehicle chassis. To refine the grain structure, **grain refiner master alloys** are added to the melt, a typical example being the alloy Al-5Ti-B. In this, the boron constituent is bound in the form of titanium diboride ( $\text{TiB}_2$ ) particles. Dispersed in a pure aluminium melt, the borides are preferential sites for nucleation of solid Al. An even distribution results in a uniform population of grains.

The importance of nucleation in processing of aluminium is reflected in the wealth of study undertaken in the field. Investigations on the micro- and atomic-scale have revealed complex phenomena which can either assist or hinder the nucleation process and alter the resulting microstructure. Because metals are opaque to visible light, and because nucleation occurs at atomic scale and over pico/nano second timescales, studying the process is challenging. In the past nucleation has been studied by examining as-cast structures or using techniques which halt the procession of nucleation before significant growth can occur, allowing post-hoc examination. More recently, *in-situ* investigation of nucleation has been permitted through use of non-contact techniques, such as X-ray scattering. *In-situ* study can be problematic as the solidification of metals occurs at high temperatures, placing great demands on equipment used in experimentation and in assessing the influence of high temperature on reliable measurement. Techniques which halt the nucleation process have shown promise and will be discussed in greater detail later in this thesis, but debate remains as to whether such techniques can really be seen as analogous to real,

industrial solidification processes. Such challenges provide the motivation to explore novel techniques to study nucleation.

This study explores the feasibility of X-ray scattering techniques to:

1. Examine interactions at the solidification interface
2. Assess nucleation **undercooling** against a specific substrate crystal plane
3. Observe resulting **orientation relationships**
4. Observe changes to material structure; i.e. **thermal expansion** and **strain**
5. Assess the modification to the surface structure of a substrate during solidification

Using X-ray scattering techniques allows structural and morphological information to be collected directly from samples as they undergo processes such as heating and cooling; particularly appropriate for studies of nucleation and solidification, which are usually difficult to study *in-situ*. There are two experimental cases, focusing on specific material systems of interest.

The first case is designed to investigate the solidification of aluminium against a single-crystal aluminium oxide ( $\text{Al}_2\text{O}_3$ ) substrate. The primary objective is to assess the feasibility of synchrotron X-ray studies of this field; Al/ $\text{Al}_2\text{O}_3$  is a highly appropriate choice for such experimentation. The material system itself is one which is found in a range of scientific applications e.g. nanowire growth [3], and often serves as a 'model system' in study of the solid-liquid interfaces which necessarily exist as a precursor to nucleation of solid material [4]–[6].

The second case is designed to investigate the solidification of aluminium against  $\text{TiB}_2$ . The latter material is commonly used in the aluminium processing industry for **grain refinement** [7]. While the associated industrial processes are well established, the exact mechanisms of solidification and resultant influence on the aluminium structure are not fully understood. The experiments herein are intended to shed light on these issues, provide a more scientific basis for the grain refinement mechanisms, and establish an experimental framework in which altered, new or improved grain refinement processes can be investigated.

Within this thesis:

**Chapter 1** details relevant theory and background for nucleation, grain refinement and X-ray scattering, and presents a review of the supporting literature.

**Chapter 2** details the experimental methods used.

**Chapter 3** details the results of experiments using the Al/Al<sub>2</sub>O<sub>3</sub> system.

**Chapter 4** details the results of Crystal Truncation Rod (CTR) analysis.

**Chapter 5** details the results of experiments using the Al/TiB<sub>2</sub> system.

**Chapter 6** concludes the study and suggests avenues for future work.



## 1.2 Nucleation: Basics and Classical Homogeneous Nucleation

Nucleation defines the localised 'budding' of a distinct phase within another due to the influence of some driving force. The most widely used example, and indeed the one that is to be explored in this work, is in the transformation of liquid to solid; however the instigation of any phase transformation (solid->liquid, liquid->gas, gas->liquid etc) is also referred to as nucleation.

As explained, nucleation occurs through two distinct routes – homogeneously and heterogeneously – the difference being the site at which nucleation events occur. These will be explored separately, but share a common basis. Note that the specific nomenclature in the following sections is based on the treatment in the textbook by Callister & Rethwisch [8] however a range of other sources have provided valuable guidance and understanding [9], [10]

A thermodynamic way to understand the nucleation process is through the concept of Gibbs free energy. The **Gibbs free energy** is a function of the **enthalpy**  $H$  of a system (i.e. its energy) and the **entropy**  $S$  (a measure of the disorder/randomness of the atoms/molecules of the system). If both the pressure and volume of a system are maintained constant, Gibbs free energy can be defined simply by the following expression, where  $T$  is the absolute temperature of the system:

$$G = H - TS \quad [1]$$

The state in which the solid and liquid phases of a one-component system are in equilibrium with one another can be determined from a consideration of the enthalpy and entropy of the system. This can be written for both solid and liquid phases:

$$G_s = H_s - TS_s \quad [1.a]$$

and

$$G_l = H_l - TS_l \quad [1.b]$$

Therefore the subtraction of equation [1.a] and [1.b] for the transformation from liquid to solid gives:

$$\Delta G_{(l \rightarrow s)} = \Delta H_{(l \rightarrow s)} - T \Delta S_{(l \rightarrow s)} \quad [1.c]$$

where  $\Delta H_{(l-s)}$  is the molar enthalpy change and  $\Delta S_{(l-s)}$  is the molar entropy change. Equilibrium between solid and liquid phases occurs when  $\Delta G_{(l-s)} = 0$ . This occurs at the equilibrium melting temperature  $T_m$  when:

$$\Delta H_{(l \rightarrow s)} = T_m \Delta S_{(l \rightarrow s)} \quad [1.d]$$

Solidification will only begin to occur once the change in free energy  $\Delta G$  is negative ( $G_{liquid} \geq G_{solid}$ ). If a system is in this state, solidification can occur spontaneously. This is the fundamental process behind **homogeneous nucleation**.

Gibbs free energy can be considered as the quantity which defines the **driving force** for nucleation. In using it to describe the nucleation process, some important assumptions are made:

1. The system in question is a **pure material**
2. Nuclei – i.e., localised ‘buds’ of the solid phase – manifest as **clusters** of atoms assembled into a structure which is the same as that found in the bulk solid. Initially these clusters are termed **embryos**, becoming nuclei once they are stable according to the conditions described in the following section.
3. The ‘shapes’ of nuclei are **spheres** with a radius ‘r’

During nucleation, there are two contributions to Gibbs free energy as shown in Figure 1-1:

1. **Volume free energy**  $\Delta G_v$  arising from the free energy difference between solid and liquid phases. If the system temperature is below that for equilibrium solidification, the quantity will be negative. It increases in magnitude (i.e. becomes more negative) with increasing volume (nuclear radius  $r$ ) as more atoms attach to the embryo. The contribution to Gibbs free energy is the product of the volume free energy with the volume of the spherical nucleus:

$$\frac{4}{3}\pi r^3 \Delta G_v \quad [2]$$

2. **Surface free energy**  $\gamma$  which describes the energy associated with the formation of an interface between the solid and liquid phases. This quantity increases with increasing nuclear radius  $r$  as a larger nucleus requires a greater area of interface. The quantity is positive and provides a total contribution based on the area of the interface, thus:

$$4\pi r^2 \gamma \quad [3]$$

The total Gibbs free energy can be thus described by the following equation, and understood more easily by plotting total free energy change against the radius of a nucleus; shown in Figure 1-1:

$$\Delta G = \frac{4}{3}\pi r^3 \Delta G_v + 4\pi r^2 \gamma \quad [4]$$

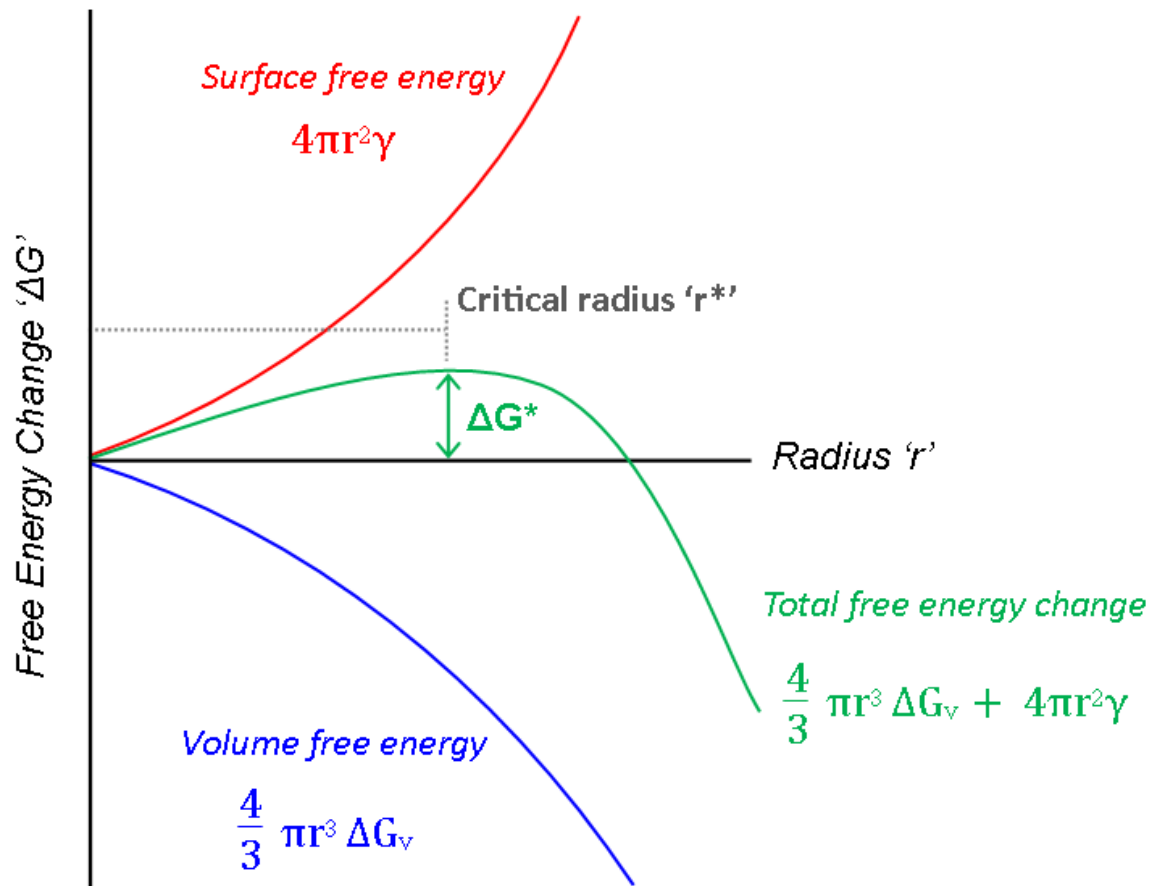


Figure 1-1 – Schematic plot of total free energy change against nuclear radius

The above figure indicates the conditions necessary for the formation of a stable nucleus. The (green) curve associated with the total free energy change first increases as the surface free energy contribution dominates. It then reaches a maximum ( $\Delta G^*$ ) before decreasing as the volume free energy contribution begins to dominate. In physical terms, this means that as atoms cluster together, forming an **embryo**, the free energy first increases due to the requirement to form an interface. If such a cluster reaches a **critical radius,  $r^*$** , continued growth as a **nucleus** becomes energetically favourable due to the stability of a larger structure. There is an associated critical free energy – known as the **activation free energy,  $\Delta G^*$** , which can be thought of as the **energy barrier** to nucleation.

A direct expression for the critical radius  $r^*$  can be obtained via differentiating equation [4] with respect to  $r$ .

$$\frac{d(\Delta G)}{dr} = \frac{4}{3}\pi\Delta G_v (3r^2) + 4\pi\gamma(2r) = 0 \quad [5]$$

Solving for  $r=r^*$ , the following is obtained:

$$r^* = -\frac{2\gamma}{\Delta G_v} \quad [6]$$

Substituting this into [4] gives an expression for  $\Delta G^*$ :

$$\Delta G^* = \frac{16\pi\gamma^3}{3(\Delta G_v)^2} \quad [7]$$

These expressions define the critical parameters required for formation of a stable nucleus.

After the green curve in Figure 1-1 has passed through the maximum at  $r^*$ , the volume free energy  $\Delta G_v$  dominates. Surface and volume free energy vary with  $r^2$  and  $r^3$  respectively so the latter term quickly becomes the greater influence. This quantity is thus the driving force for further solidification, and is a function of the system temperature.

As illustrated in Figure 1-2, as system temperature is lowered, for example from  $T_1$  to  $T_2$ ,  $\Delta G_v$  becomes more negative. This has an influence on the total free energy change  $\Delta G$  as shown:

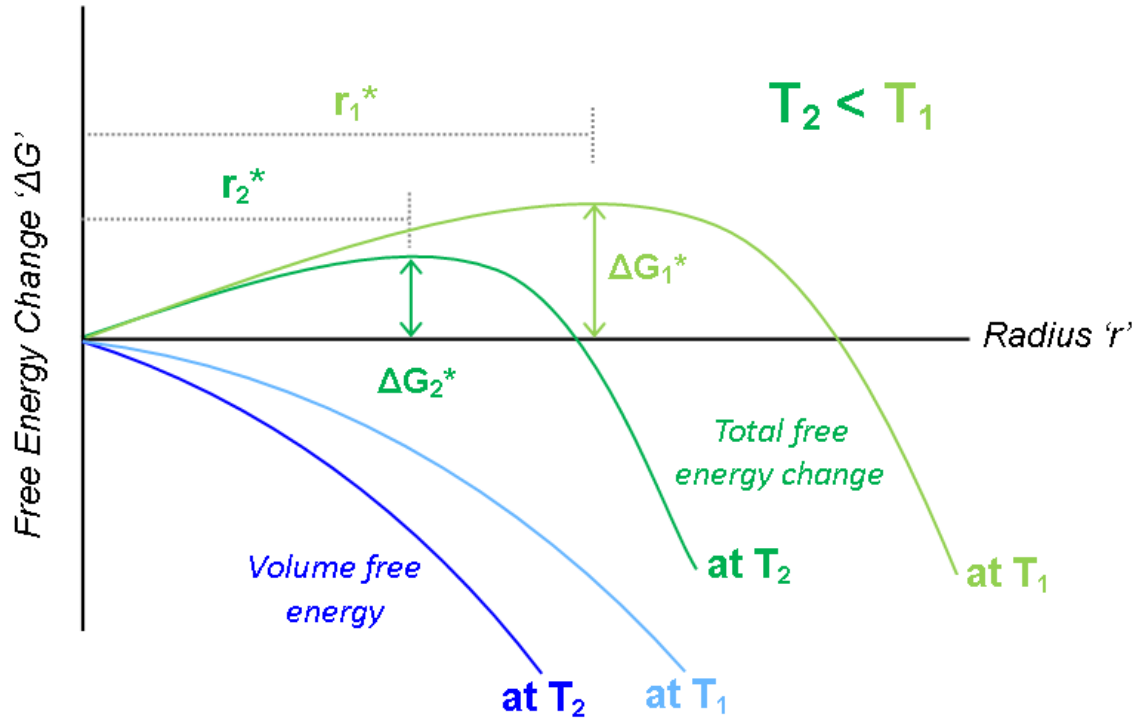


Figure 1-2 - Free energy change against nuclear radius at different temperatures

At the lower temperature  $T_2$  there is a larger (i.e. more negative) contribution of  $\Delta G_v$  resulting in a smaller energy barrier ( $\Delta G_2^*$ ) and smaller critical radius ( $r_2^*$ ) required for the formation of a stable nucleus.

$\Delta G_v$  itself is related to temperature through the following expression; in which  $\Delta H_f$  refers to the **latent heat of fusion** (i.e. the inherent heat in the material released through solidification):

$$\Delta G_v = - \frac{\Delta H_f (T_m - T)}{T_m} \quad [8]$$

If this expression for  $\Delta G_v$  is substituted into the expressions [6] and [7] for the critical parameters, expressions are obtained which describe their dependence on temperature:

$$r^* = \left( \frac{2\gamma T_m}{\Delta H_f} \right) \left( \frac{1}{T_m - T} \right) \quad [9]$$

$$\Delta G^* = - \left( \frac{16\pi\gamma^3 T_m^2}{3\Delta H_f^2} \right) \frac{1}{(T_m - T)^2} \quad [10]$$

These expressions show algebraically the decrease in  $r^*$  and  $\Delta G^*$  with decreasing temperature; the conclusion being that nucleation will occur more readily at lower temperatures. The amount the system is cooled below its equilibrium solidification temperature ( $T_m - T$ ) is referred to as **undercooling**.

Another important consideration is the **rate of nucleation**. There are a number of elements to this. First, following on from the previous analysis, is the concept that the number of stable nuclei  $n^*$  (with  $r > r^*$ ) in a system is dependent on temperature:

$$n^* = K_1 \exp \left( - \frac{\Delta G^*}{kT} \right) \quad [11]$$

Here  $K_1$  is a constant defining the number of available nucleation sites per unit volume, and  $k$  is the Boltzmann's constant. Further to this, there is a temperature dependent relationship for the clustering of atoms (to form the initial solid-phase embryos) which occurs via short range diffusion. The material dependent diffusion coefficient defines the ease by which this process takes place. The frequency at which atoms attach themselves to a forming solid-phase embryo  $v_d$  is defined:

$$v_d = K_2 \exp \left( - \frac{Q_d}{kT} \right) \quad [12]$$

The quantity  $Q_d$  is the activation energy for diffusion; a minimum critical energy required to instigate the process. The  $K_2$  term in this expression is a temperature-independent constant. In a similar fashion to that used to create the graph in Figure 1-1, the contributions of [11] and [12] are combined to visualise the total **rate of nucleation**  $\dot{N}$ :

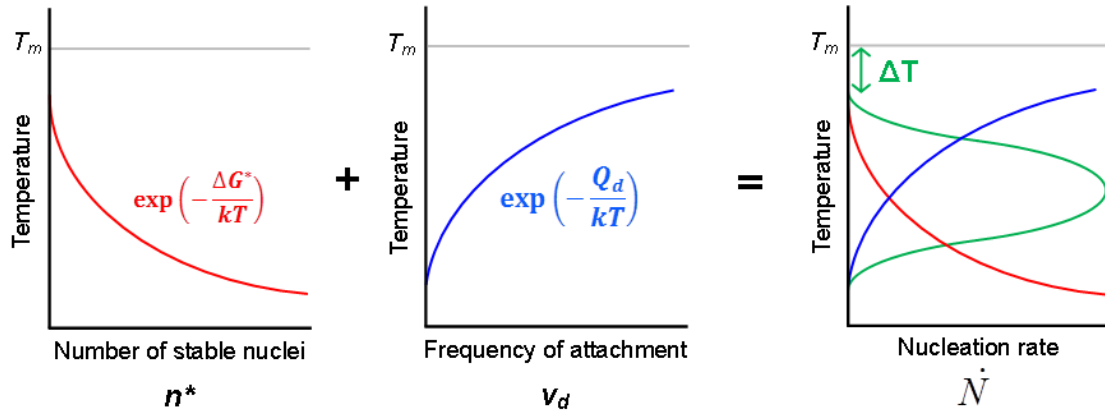


Figure 1-3 – Schematic illustration of contributions to nucleation rate

The total nucleation rate, as can be seen from the figure above, is proportional to the product of the number of stable nuclei  $n^*$  and the frequency of attachment  $v_d$ . Combining [11] and [12] the expression is derived as follows:

$$\dot{N} = K_3 n^* v_d = K_1 K_2 K_3 \left[ \exp\left(-\frac{\Delta G^*}{kT}\right) \exp\left(-\frac{Q_d}{kT}\right) \right] \quad [13]$$

The additional constant  $K_3$  in this expression defines the number of atoms on the surface of a nucleus. Using Figure 1-3, we can describe the process of nucleation. At high temperatures (i.e. close to  $T_m$ ) the rate is slow as the driving force for nucleation is small (recall Figure 1-2). As the temperature is lowered, the rate increases as this driving force becomes larger. Continuing diminishment of temperature lowers the rate of diffusion which drives the frequency of attachment  $v_d$ . The lower atomic mobility in the system means atoms cannot attach as readily to forming nuclei and the rate decreases. The combination of these effects means the curve for nucleation rate first gradually increases, passes through a maximum at the point where the increasing driving force for nucleation is balanced exactly by the decreasing atomic mobility, then decreases to a minimum level.

$\Delta T$  in Figure 1-3 indicates **undercooling**. A measurable nucleation rate will only be established at a undercooling which provides a required driving force. The temperature dependence of the nucleation rate is such that this value



represents a relatively sharp transition – before the undercooling is reached, no appreciable nucleation is observed. At or beyond the undercooling, nucleation begins almost instantaneously. For homogenous nucleation, the magnitude of this undercooling can be significant; several hundred degrees Kelvin in some systems. In most practical cases, however, solidification begins at a temperature somewhat closer to the equilibrium solidification temperature  $T_m$ . Clearly there must be an alternative mechanism at work. This leads us onto the next section, in which we discuss **heterogeneous nucleation**.

### 1.3 Classical Heterogeneous Nucleation

In real systems it is readily observed that solidification begins at undercooling values far smaller than those predicted by classical homogeneous nucleation theory. There is often some undercooling present before the process begins, but this is usually on the order of several degrees Kelvin, as opposed to several hundred. In **heterogeneous nucleation**, nuclei form on pre-existing surfaces which provide energetically favourable sites for nucleation to take place. These may be particles in the melt, either impurities or specifically chosen additions; or surfaces such as the edges of the container in which the liquid resides. The effect of these heterogeneities is to lower the energy barrier  $\Delta G^*$  required for nucleation by reducing the magnitude of the contribution of **surface free energy**  $\gamma$ . Figure 1-4 clarifies understanding of this effect through an approach known as the **spherical cap model** [11], [12]:

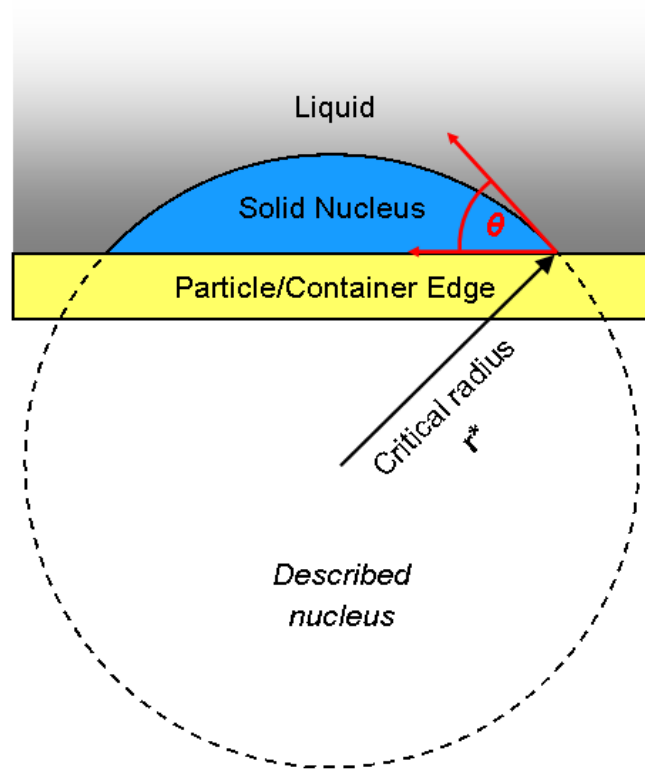


Figure 1-4 – The spherical cap model for heterogeneous nucleation

The 'spherical cap' can be understood as effectively describing a larger sphere, indicated in the figure, i.e. that which would form according to homogeneous nucleation theory. By effectively reducing the interfacial area of this sphere, the numerical quantity  $4\pi r^2$  from expression [3] is significantly lowered. The contribution of the corresponding surface free energy term is thus also lowered. The critical radius for stable nuclei in equation [9] can be rewritten as

$$r^* = -\frac{2\gamma_{sl}}{\Delta G_v} \quad [14]$$

The required volume of the spherical cap (blue area in Figure 1-4) can be calculated as

$$V_{cap} = \left( \frac{4\pi(r^*)^3}{3} \right) \times S(\theta) \quad [15]$$

Using equation [14] to replace  $r^*$  in the above equation:

$$V_{cap} = \left( \frac{4\pi \left( -\frac{2\gamma_{sl}}{\Delta G_v} \right)^3}{3} \right) \times S(\theta) \quad [16.a]$$

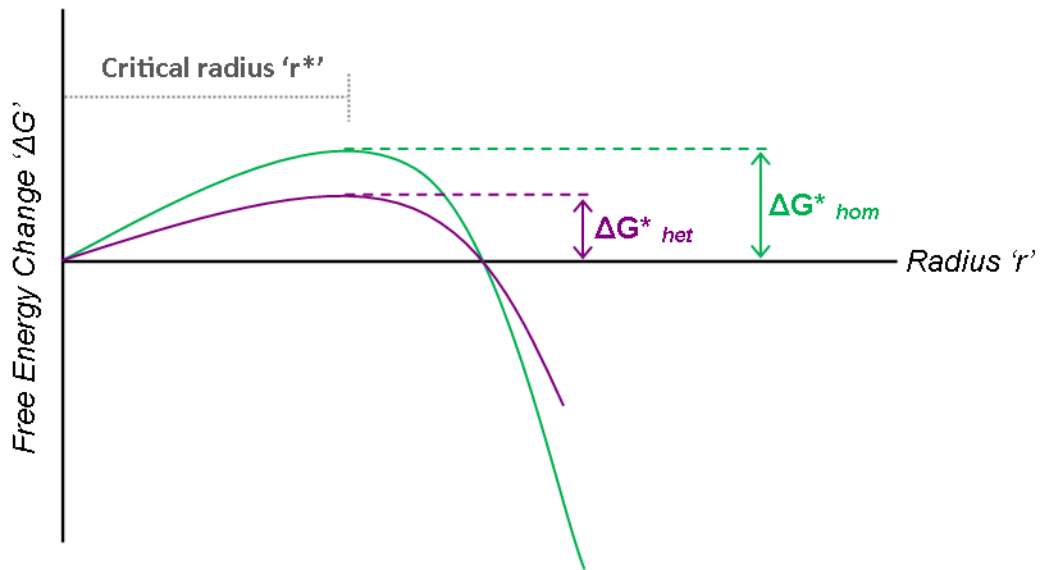
$$V_{cap} = - \left( \frac{32\pi\gamma_{sl}^3}{3(\Delta G_v)^3} \right) S(\theta) \quad [16.b]$$

Using the above equation for spherical cap volume to replace the volume in equation [4] and following the same subsequent process, equation [10] can be rewritten:

$$\Delta G^* = \left( \frac{16\pi\gamma_{sl}^3}{3(\Delta G_v)^2} \right) S(\theta) \quad [17]$$

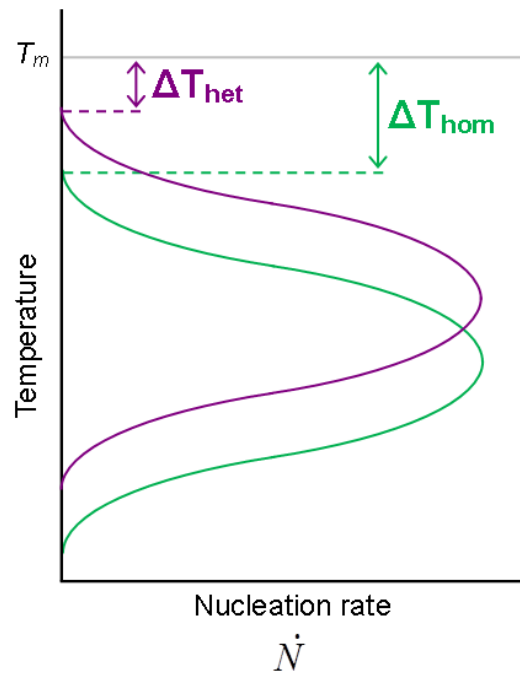
The surface free energy here is  $\gamma_{sl}$ , the  $sl$  suffix indicating this is the interfacial energy between the solid and liquid phases (as opposed to solid-particle and liquid-particle). The  $S$  term in the equations is a function of  $\theta$ , the **wetting angle** of the spherical cap. This angle can be understood as a measure of the potency of the particle or container edge as a substrate for nucleation; a lower angle indicates that a cap can form very readily; i.e. with little solid material, and a higher angle indicates the formation of a cap is more difficult as it describes a larger cap volume. In simple terms the  $S$  function can be seen as describing the shape of a spherical cap nucleus. It indicates the amount by which the **activation energy barrier**  $\Delta G^*$  for nucleation is decreased in the heterogeneous case:

$$\Delta G_{het}^* = \Delta G_{hom}^* * S(\theta) \quad [18]$$



**Figure 1-5 – Activation energy barrier comparison for homogeneous vs heterogeneous case**

Note that the critical radius  $r^*$  remains the same as for the homogeneous case, but the energy barrier  $\Delta G^*$  is decreased owing to the reduced interfacial area. The decreased activation energy barrier means that nucleation occurs much more easily and readily than in the homogeneous case. This has the effect of 'shifting' the onset of nucleation towards the equilibrium solidification temperature  $T_m$ , translating the curve of nucleation rate as shown:



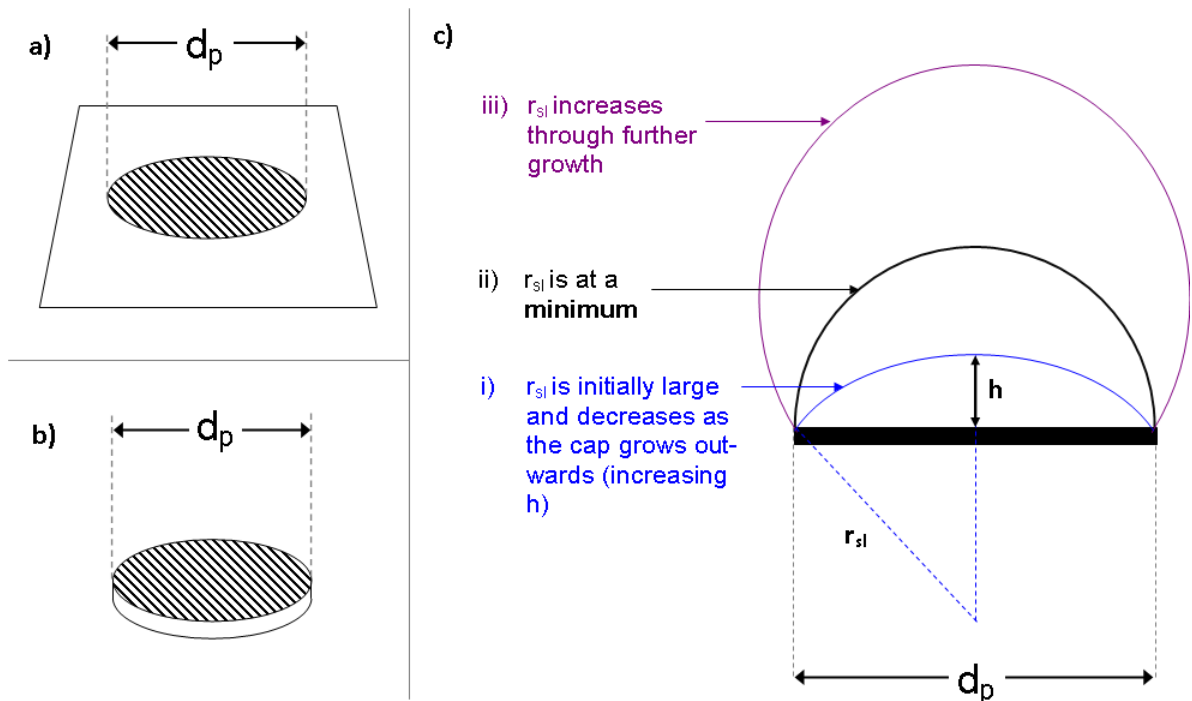
**Figure 1-6 – Schematic of nucleation rates indicating undercooling requirement for homogeneous vs heterogeneous case**

The decreased activation energy barrier allows an earlier onset of nucleation; thus the curve for nucleation rate is shifted to higher temperatures. The chart shows the significantly decreased **undercooling** for heterogeneous nucleation. This accounts for the onset of solidification observed in real systems at undercooling levels well below those predicted by homogeneous theory. Again, as the figure shows, the theory predicts a particular value for undercooling  $\Delta T$  at which nucleation will begin to occur instantaneously.

The spherical cap model is a useful means through which to understand the concept of heterogeneous nucleation. The associated contact angle effectively condenses the various factors influencing the potency of a particular substrate/melt system into one convenient measure. Such factors include the chemical properties of the materials (interactions, segregation to the interface in the case of alloys) and structural properties (crystalline orientation, lattice mismatch between the phases). Later in this section, the nucleation of Al on titanium diboride ( $\text{TiB}_2$ ) inoculant particles will be explored as a case study, and will reveal the importance of structural correlation particularly.

## 1.4 Extensions to the classical approach

Thus far, the heterogeneous nucleation model has been based on the assumption that the size of the nucleating particle is significantly larger than the critical radius for nucleation  $r^*$ . In reality the particles will either have a finite size or will only have a finite area on their surface which is suitable for promoting nucleation of the liquid. The latter theory considers so-called nucleant ‘patches’ and was first explored by Turnbull in the 1950s [13]. The equivalent in Al processing are the {001} faces of  $\text{TiB}_2$  particles, which are the only crystallographic planes observed to be active in the nucleation of crystalline Al [14]. In either case, the available area for nucleation is approximated as a circle with diameter  $d_p$  (see Figure 1-7a and b)



**Figure 1-7 - Schematic of nucleation in free growth scenario. Examples of nucleant areas on a) a surface patch and b) a nucleant particle are shown. c) shows schematically the critical condition for free growth as the solid-liquid interfacial radius  $r_{sl}$  approaches a minimum.**

Critical nuclei form on surface patches, or on nucleant particles, with spherical cap geometry as described by the theory in section 1.3. When  $d_p \gg 2r^*$ , this process can proceed via lateral spreading of the spherical cap. However, in the case that the diameter of the patch/particle  $d_p < 2r^*$ , continued lateral growth is

not possible, and the cap may only grow outwards, reducing the radius of curvature of the solid-liquid interface  $r_{sl}$  (Figure 1-7c i). When  $r_{sl} = r^*$ , continued growth cannot proceed and is energetically unfavourable unless the **undercooling** is increased, which reduces the critical radius  $r^*$ .

A critical condition is reached if the spherical cap becomes a hemisphere on the particle/patch surface, i.e.,  $2r_{sl} = d_p$  (Figure 1-7c ii) Further growth beyond this point causes an increase in  $r_{sl}$ , and is thus energetically favourable and can proceed without a further increase in undercooling (Figure 1-7c iii). This condition is called **free growth**. The free growth model has been formalised by Quested and Greer [15] and successfully applied to the Al/TiB<sub>2</sub> industrial case [16], [17]. As the theory suggests, there exists a critical undercooling for the onset of free growth, defined as follows:

$$\Delta T_{fg} = \frac{4\gamma_{sl}}{\Delta S_v d_p} \quad [19]$$

where  $\Delta T_{fg}$  is the undercooling required for free growth,  $\gamma_{sl}$  the solid-liquid interfacial energy,  $\Delta S_v$  the entropy of fusion per unit volume and  $d_p$  the diameter of the nucleant patch or particle. The critical condition is also defined by the point at which  $r_{sl}$  attains a minimum and is equal to  $r^*$  as follows:

$$r^* = \frac{2\gamma_{sl}}{\Delta T \Delta S_v} \quad [20]$$

Free growth implies that solidification can proceed spontaneously at an undercooling which is inversely proportional to the diameter of heterogeneous nucleant particles/patches. As undercooling increases, substrates of smaller size are progressively ‘activated’ as nucleant sites.

The free growth model is inherent to an approach to nucleation termed **athermal** nucleation. The term was originally defined in the 1940’s by Fisher *et al* [18] describing it as a situation in which embryos (i.e. clusters of atoms which have a radius smaller than the critical radius  $r^*$ ) are “*automatically*

*promoted to nuclei*” when the critical radius  $r^*$  decreases past their own size. In the classical theories described in 1.2 and 1.3, nucleation proceeds through a thermal activation; i.e. it requires a temperature reduction in order to overcome an energy barrier, beyond which nucleation proceeds at a rate determined by the overall contributions as indicated in Figure 1-3. It is a stochastic process, in that nucleation events occur randomly once appropriate conditions exist in the melt, and is thus time-dependent. In contrast, athermal nucleation is a deterministic process, meaning nuclei are produced only once conditions are changed such that the critical size is lowered, and is thus dependent only on the present undercooling in the system.

In the case study of nucleation of aluminium on  $\text{TiB}_2$  particles, it has been demonstrated that thermal nucleation is insignificant and athermal nucleation is the dominant mechanism [15], [19]. As such, in this system, nucleation is governed entirely by the applied undercooling according to the free growth condition in equation [19]. Modelling grain refinement in Al alloys using this approach has given good quantitative predictions of grain size [20] and good fits to experimental data from TP-1<sup>2</sup> tests [16]. It is worth qualifying, however, that the mechanism assumes a spatially isothermal melt; a condition which is likely more applicable for comparison with small-scale experiments such as TP-1 than to large castings which will experience higher thermal gradients; although, in the latter case, reasonable temperature uniformity is likely to exist for *individual* nucleation events within the melt.

---

<sup>2</sup> A standard test procedure for Al alloy grain refiners using a small conical mould [159]



## 1.5 Nucleation by adsorption

The spherical cap model for heterogeneous nucleation provides a suitable understanding for a number of nucleation cases. However, studies began to reveal problems when attempting to apply the theory to potent catalysts [21]. When either or both  $r^*$  and  $\theta$  are very small, the structural definition of the spherical cap breaks down as it begins to approach atomic-scale dimensions. To clarify, in situations where  $\theta$  is small, the supposed nucleus may only be a few atoms thick ( $\theta < 20^\circ$ ) or even a monolayer of atoms ( $\theta < 10^\circ$ ). Under these conditions a spherical cap is no longer a suitable model for describing the onset of nucleation, not least because it implies a physically unrealistic situation in which part of the cap would be less than 1 atomic diameter in height. Researchers were inclined to suggest more appropriate models for nucleation at these scales.

Sundquist [22] considered the nucleation of tin in a system with low undercooling (i.e. on a potent catalyst, with a small  $\theta$ ), proposing that the nucleus should be described as “*a monolayer of atoms occupying the atomic sites on the catalyst surface*”, i.e. that liquid atoms were **adsorbed** onto the surface of the inoculant forming a 2D monolayer. This was later clarified by Chalmers [23] who made the following statement:

*“A monolayer of atoms on the surface of a substrate cannot be regarded as a cluster of atoms brought together by a fluctuation in the liquid; it is more reasonable to regard it as an adsorbed layer in which the atoms can be arranged in many ways. The groupings of the atoms in the adsorbed layer play the same part as the embryo in the liquid; some have the structure of the crystal and, if large enough, can provide the starting point for further growth.”*

This proposal developed into a model for nucleation which was formalised by Kim and Cantor [24]. This model treats nucleation as an **adsorption** process. Adsorption refers to the adhesion of atoms or molecules onto a solid surface. Nucleation is modelled as an atom-by-atom adsorption process at the surface of

the catalytic heterogeneous particle. According to Kim and Cantor [24] a prediction of the surface energy of the catalyst is given by summing the influence of properties atom-by-atom and point-by-point on the surface. In experimental validation of the model, good predictions of nucleation undercooling were made, with the added benefit of predicting faceting of the adsorbed material at the surface. Model predictions could now be validated against experimental studies [25]. Nucleation in the systems investigated (Al-Si [26] and Al alloys [27]) was predicted/observed to be instigated by a so-called catalytic **monolayer** on the surface of a heterogeneous particle; a layer which then itself served as the catalyst for nucleation of the bulk material. These events could be studied in solid samples thanks to the melt-spinning technique; allowing molten alloy to pour onto a rapidly spinning wheel, which quenches rapidly, creating an amorphous bulk microstructure; a 'metallic glass'. Nucleation events which have occurred on heterogeneous impurities are frozen into this bulk structure at an early stage of their growth, allowing the morphology to be observed using HRTEM. This process, while imperfect (the glass-forming properties requiring the alloy composition to be different to industrial equivalents), allows investigation of early-stage nucleation without the difficulty of *in-situ* observation.

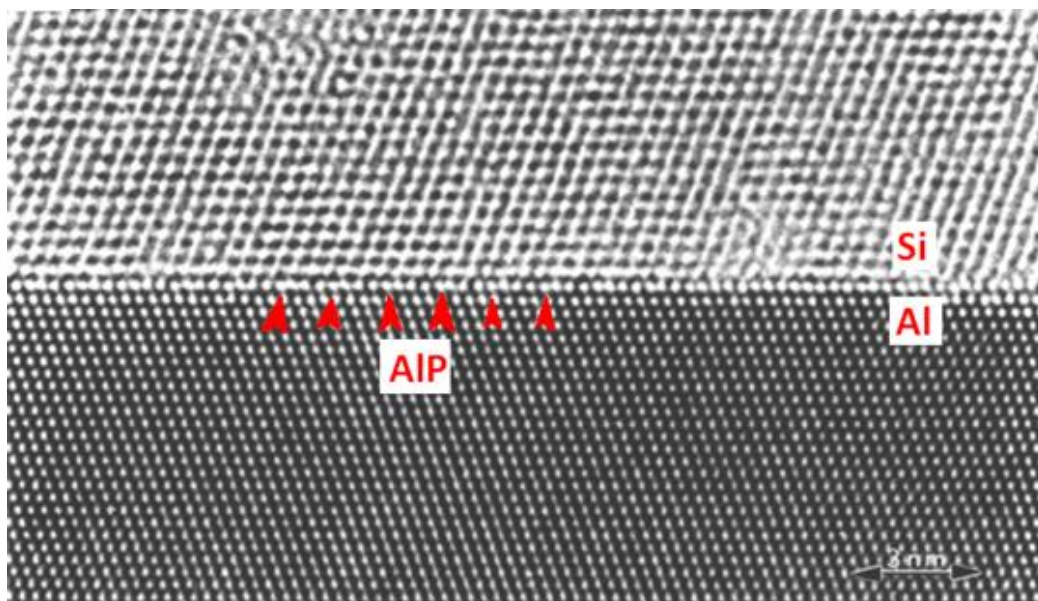
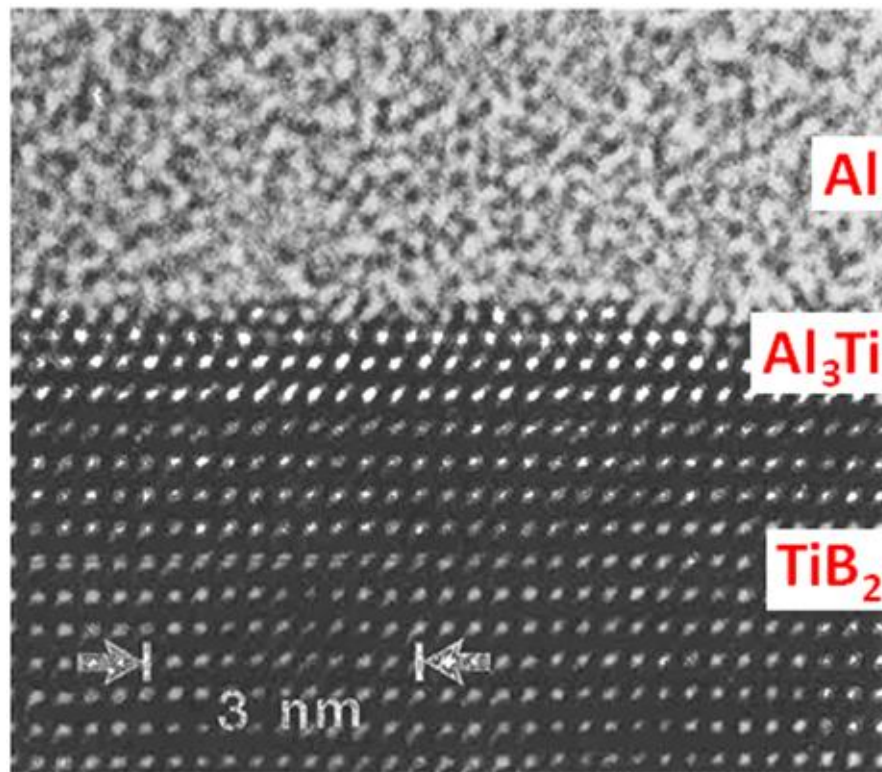


Figure 1-8 - HRTEM image of AIP layer on Al catalyst nucleating solidification of Si.

Modified from [25]; original image from [26]



**Figure 1-9 - HRTEM image of Al<sub>3</sub>Ti layer on TiB<sub>2</sub> nucleating solidification of Al. Modified from [27]**

Figure 1-8 and Figure 1-9 give an insight into the appearance of solid-liquid interfaces at the atomic scale. The case for Figure 1-8 was that of solidification of Si catalysed by the presence of an Al (111) surface. Al is observed to be a poor catalyst for Si, with undercooling between 45-60K [26]; however doping with P is shown to improve catalysis significantly. As stated by Cantor in his review [24] “*P is adsorbed onto the Al surface to form a catalytic AlP layer*”. Figure 1-9 shows Al on TiB<sub>2</sub>, a mechanism of great importance in the processing of aluminium. Titanium diboride (TiB<sub>2</sub>) particles are introduced to molten Al for grain refinement purposes. This will be explored in detail in section 1.7; for now it suffices to say that the particles are intended to provide sites for heterogeneous nucleation of Al to occur. In this scenario, a catalytic layer is observed to adopt the structure of a distinct phase – Al<sub>3</sub>Ti – which acts as a transition between the titanium diboride (TiB<sub>2</sub>) crystallites and crystalline Al (in this case, the quenching of the metallic glass has generated an amorphous structure in the Al, giving an impression of how the interface may appear *in-*

*situ*). Note that the ‘streaking’ apparent within the  $\text{Al}_3\text{Ti}$  layer likely results from imaging artefacts.

The proposed adsorption method raises interesting questions as to the structural compatibility between the catalyst and the solidifying material. In the majority of cases, there will be a degree of **mismatch** between the lattice parameters of the catalyst and solid, which would lead to residual **strain** in the interfacial structures on cooling. The magnitude of the mismatch would of course be dependent on the relative crystal orientation of the two materials. It has been long understood that catalytic efficiency is reduced by increasing lattice mismatch [28]. Tóth *et al* demonstrated using density functional theory that adsorption of the solidifying phase, the effective contact angle and the size of the nucleation barrier itself are in fact functions of the lattice constant of the substrate [29]; their work also verified the validity of Greer’s free growth model in this theoretical approach [16]. It should be noted, however, that other work has shown the high sensitivity of the nucleation process to the presence of impurities in the system, showing that chemical effects play a significant role [30], and in some cases are dominant over structural effects [31]. However, as will be demonstrated fully in section 1.7.2, in the relevant industrial case of  $\text{Al/TiB}_2$ , lattice mismatch certainly appears to be the dominant factor in determining nucleation potency.

Cantor’s adsorption model for nucleation defines a specific **undercooling**  $\Delta T_{ads}$  which is a prerequisite for adsorption and thus, for nucleation. The model predicts that adsorption will take place when the undercooling increases above this level. Complementary to this is a recent study by Fan [32] in which he specifies that nucleation on the atomic scale takes place by “*epitaxial growth of a pseudomorphic layer on the surface of the substrate*” once the undercooling is decreased beyond a critical value.

## 1.6 Liquid Ordering at the Liquid/Solid interface

Adsorption mechanisms bear strong relevance to a recently observed phenomenon in liquids adjacent to solid surfaces [6], [33], [34], whereby atoms in the liquid adopt a degree of order seemingly influenced by the presence of a hard 'wall'. The arrangement of atoms into a structure similar to that of the solid surface bears clear relevance to the adsorption of a layer of atoms onto the surface structure of a nucleating particle. It is fair to suggest that ordering of atoms in the liquid adjacent to a solid surface may be a precursor to the formation of catalytic monolayers as seen in Figure 1-8 and Figure 1-9.

It has been observed through various methods [34] that the presence of a solid surface induces atoms in an adjacent liquid to form multiple layers parallel to the surface, which become more diffuse – i.e. less well ordered – with increasing distance from the interface. A degree of in-plane order is also observed under certain conditions. Liquid atoms arrange over the adatom sites of the underlying solid lattice forming an essentially quasi-solid arrangement. The periodic potential of the solid surface induces these structures to form; their characteristics are influenced by a range of different factors. Figure 1-10 provides a visual, schematic reference of the ordered structures.

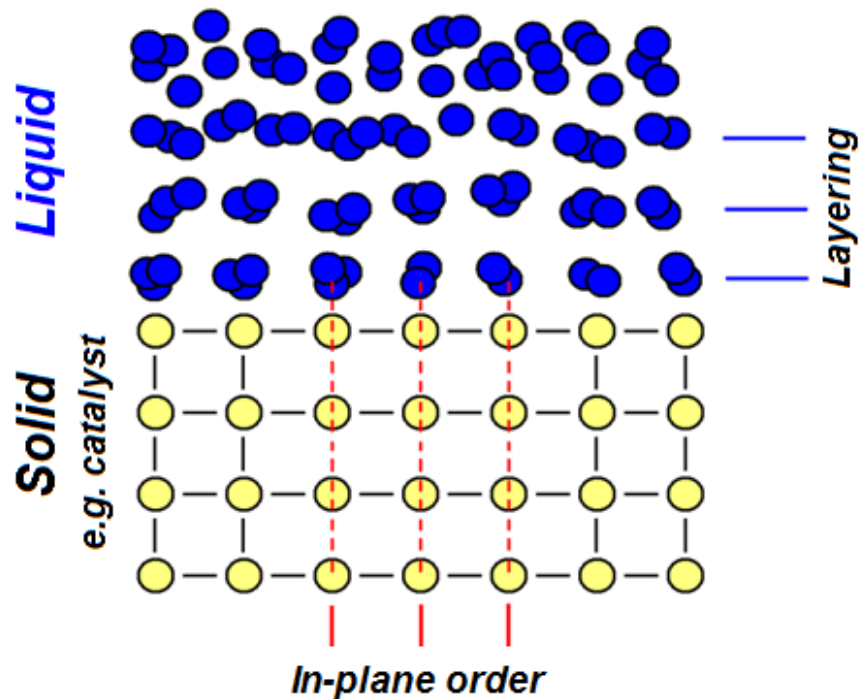
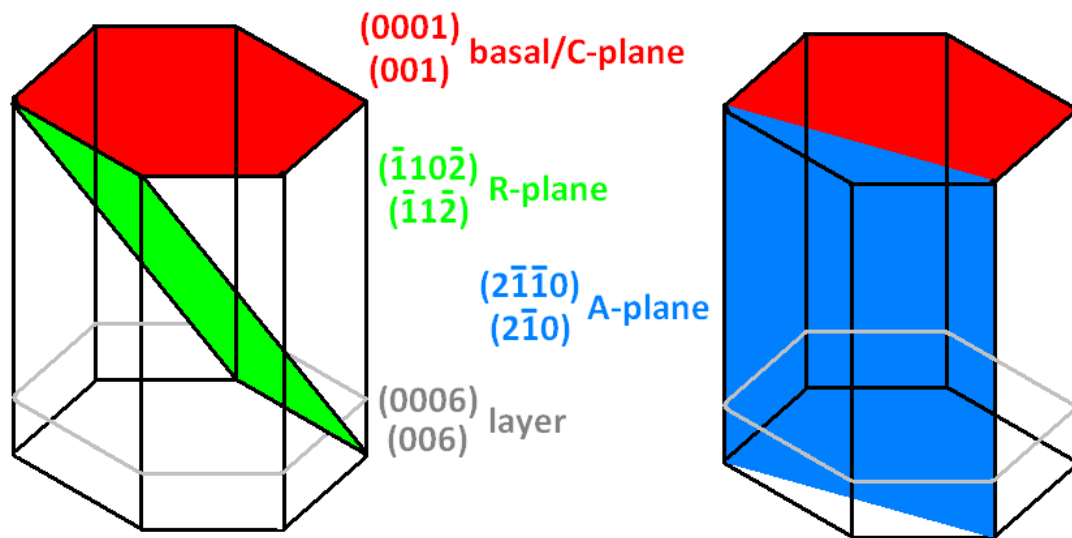


Figure 1-10 – Schematic representation of atomic-scale ordering in liquid adjacent to solid substrate

A number of articles [4], [6], [35], [36], letters [37], [38] and reviews [34] have explored the liquid ordering phenomenon. For the scope of the current work, the relevance to material processing is the most important aspect; particularly the influence of the phenomenon on the undercooling required for the initiation of nucleation.

HRTEM studies understandably provide the clearest perspective on the atomic-scale layering effect. Donnelly *et al* [39] were the first to report evidence for layering using this method. Fluid xenon was observed to form ordered layers when confined within faceted cavities in aluminium, the layering taking place against the flat facets. More recently, work by Oh *et al* [6] has found more distinct evidence of layering, in a system of liquid aluminium in contact with sapphire (single crystal alumina,  $\text{Al}_2\text{O}_3$ ). This system is ideally suited to TEM work as Al droplets can be formed on the surface of the crystal under irradiation from the electron beam combined with heating. The different displacement energies of the Al and O atoms means that Al diffuses to the surface and forms an atomically flat interface with the underlying crystal; oriented in this case to the (001) basal plane or 'C-plane'. The (001) plane is the basal of the  $\alpha\text{-Al}_2\text{O}_3$

unit cell, which has an HCP lattice. The cell comprises a number of planes of this form stacked above each other; so-called (006) planes. To avoid confusion, this thesis will use the standard 3-index Miller indices throughout; however, some of the following studies in this review use the 4-axis Miller-Bravais convention. Figure 1-11 shows schematically the orientation of the planes of interest in the  $\text{Al}_2\text{O}_3$  unit cell giving both the 3- and 4-index designation to assist the reader.



**Figure 1-11 – Schematic of  $\text{Al}_2\text{O}_3$  HCP unit cell showing various crystallographic planes referred to in studies under review**

Ordering of Al atoms in the liquid state adjacent to an  $\text{Al}_2\text{O}_3$  (006) interface was observed by Oh *et al* in a 2005 study [6]:



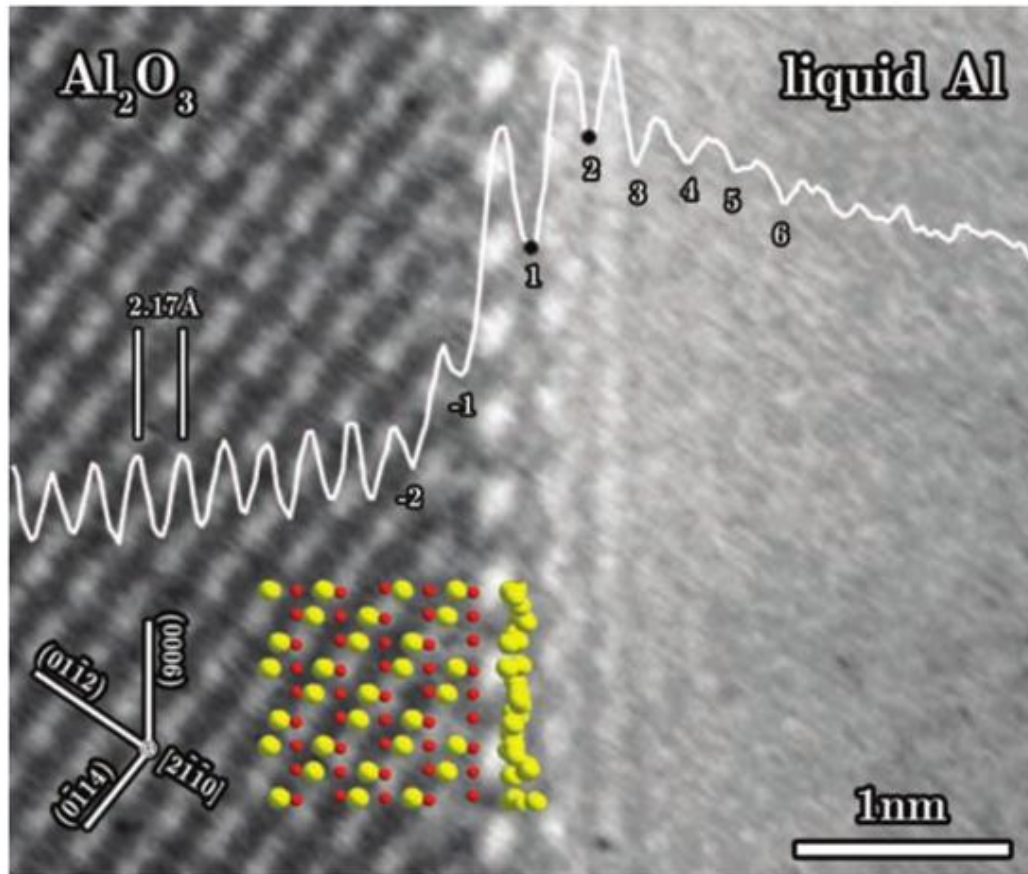
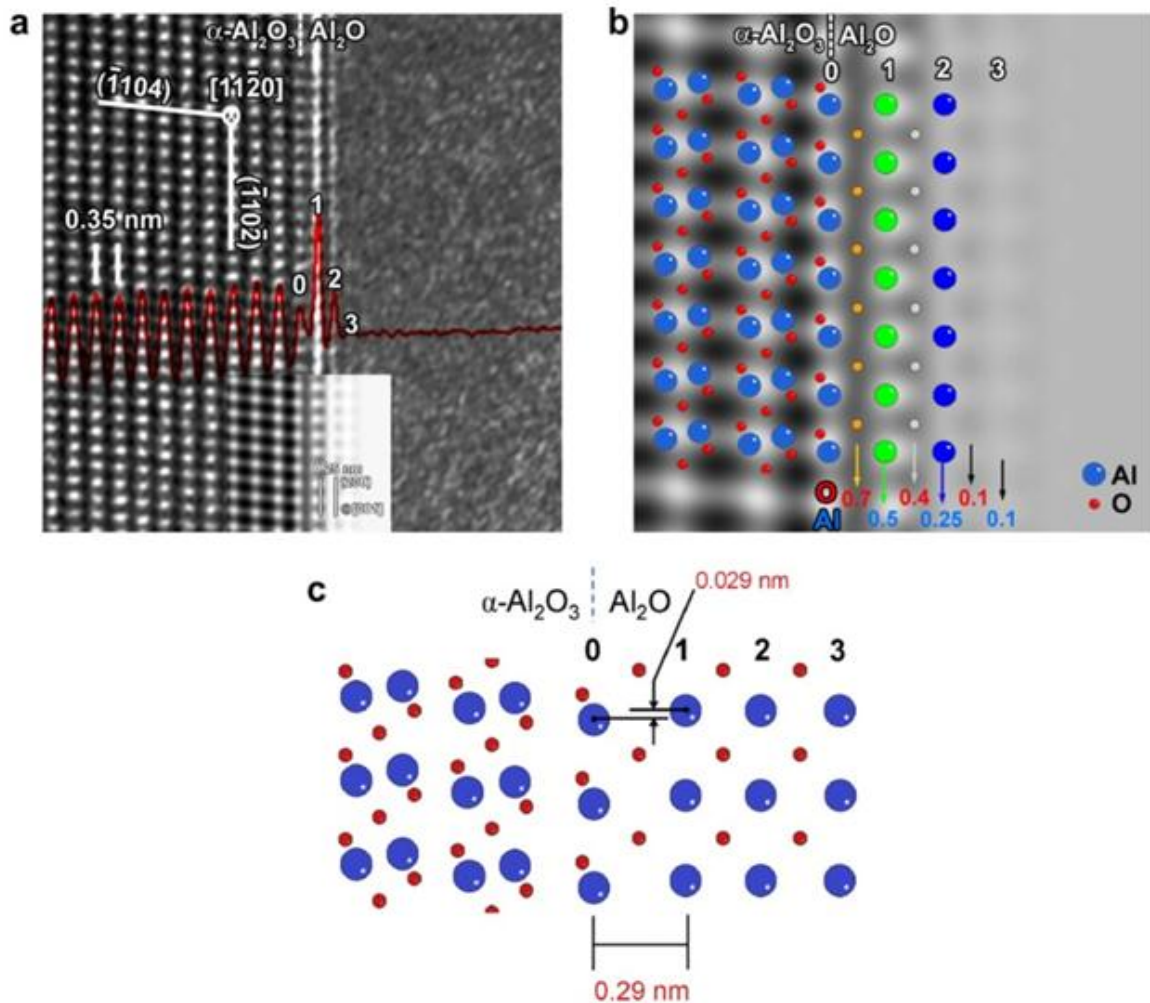


Figure 1-12 – HRTEM image of liquid Al in contact with solid  $\text{Al}_2\text{O}_3$  (006) plane at  $\sim 750^\circ\text{C}$  ( $T_m$  for Al =  $660.4^\circ\text{C}$ ). White line indicates scan of average intensity across interface; minima in intensity corresponding to positions of identified liquid layers at 1 and 2. Inset shows a schematic of  $\text{Al}_2\text{O}_3$  crystal and first layer of Al atoms. Reproduced from [6]

After comparison with simulated HRTEM images to eliminate imaging artifacts from the analysis, the validity of the observed ordering was confirmed. Similar studies focused on assessing whether any discernable in-plane order was present in the Al liquid layers. Lee *et al* [5] performed work using both the (001) ‘C-plane’ and  $(\bar{1}1\bar{2})$  ‘R-plane’ (see Figure 1-11) orientations of the  $\text{Al}_2\text{O}_3$  crystal. In the former, liquid layers were observed to have a spacing of  $2.20 \pm 0.25 \text{ \AA}$ , corresponding well with the spacing of (006) planes in  $\text{Al}_2\text{O}_3$  suggesting an influence of the solid lattice on the ordering. This contradicts the analysis of Figure 1-12; Oh *et al* reported spacings of  $3.50 \pm 0.25 \text{ \AA}$  and  $2.85 \pm 0.25 \text{ \AA}$  in the first and second layers respectively. However, they commented that this large change at the interface “*may be caused by delocalisation (an imaging artefact inherent in HRTEM studies) and/or the formation of a transient phase caused by oxygen transport along the interface*”.



The second point is especially interesting, as the ordering observed against the  $(\bar{1}1\bar{2})$  'R-plane' exhibited a slightly different character:



**Figure 1-13 - a) HRTEM image of liquid Al in contact with solid  $\text{Al}_2\text{O}_3$   $(\bar{1}1\bar{2})$  R-plane. Inset shows a simulated image (from MD) used for comparison. b) Inset from a) enlarged and overlaid with atomic structure; atom positions based on the assumption of a transient  $\text{Al}_2\text{O}$  phase. c) Enlarged view of atomic structure from b). Modified from [5]**

Lee *et al* [5] observed interplanar spacings which did not correspond to  $(\bar{1}1\bar{2})$  planes of  $\text{Al}_2\text{O}_3$ , but instead indicated the formation of an interfacial layer of an entirely different phase. The spacing was noted to be similar to that of the lower oxide  $\text{Al}_2\text{O}$ ; subsequent image simulation based on this assumption confirmed this and supported the suggestion of Oh *et al* [6] that larger spacings observed in these regions are likely to be caused by formation of a transient phase. It is also suggested that the relative positions of atoms at the  $\text{Al}_2\text{O}_3$  surface and in the first liquid layer indicates a degree of in-plane order; Lee *et al*

propose that this is due to the effect of the orientation of the  $\text{Al}_2\text{O}_3$  crystal influencing the structural correlation between the solid and liquid. The apparent formation of a transient phase at the interface is interesting, and accords well with the observations from Figure 1-8 and Figure 1-9 of transient phases forming at the interfaces; AIP at the interface of solid Al and liquid Si; and  $\text{Al}_3\text{Ti}$  at the interface of liquid Al and solid  $\text{TiB}_2$ ; respectively.

Another study on the Al/ $\text{Al}_2\text{O}_3$  system which is worth consideration was performed by Kauffmann *et al* in 2011 [36]. The motivation for this work was to reduce or eliminate the influence of imaging artefacts from HRTEM studies through a newly developed reconstruction procedure. Both in-plane and out-of-plane ordering were observed in this work. In-plane order appears to decay more rapidly than the layering, persisting only in the first three layers of Al in this case whereas 5-6 individual layers are discernable. These observations agree with those in studies on other materials; for example in water against KDP crystals [40], [41], wherein the two layers nearest the crystal surface exhibited in-plane order and were termed ice-like, and subsequent layers were more diffuse.

Kauffman suggests [36], the “*in-plane ordering measured in the current study is a result of both the interactions of the Al atoms with the periodic structure of the underlying substrate and an ordered adsorbate located within the layers of ordered Al.*”. Oh *et al* [6] observed that the adsorption of oxygen along the interface in this material system results in growth of new (006) sapphire layers. Modelling studies have provided support for this claim [42]. Environmental oxygen accesses the interface via the junction of solid  $\text{Al}_2\text{O}_3$ , liquid Al and the vacuum, and is therefore likely to be confined only to the first liquid layers; thus in-plane order decays more rapidly than out-of-plane (see Figure 1-10).

Another useful conclusion from the Kauffmann *et al* study is the spacing observed in the liquid Al layers. The first three spacings are measured to be  $\sim 2.00 \pm 0.10 \text{ \AA}$ , increasing to  $\sim 2.85 \pm 0.10 \text{ \AA}$  in the fourth. The latter value is close to the distance between nearest-neighbours in bulk liquid Al, according to the radial distribution function of this material. The smaller spacing in the first layers

matches more closely to the spacing of (006) planes in  $\text{Al}_2\text{O}_3$  of 2.165Å. This correlation leads the authors to conclude *“liquid atoms at the interface are influenced by the structure of the crystal and further away the ordering of the liquid atoms gradually disappears until they adopt the characteristics of the bulk liquid.”* This agrees well with the general impression formulated in studies on other materials [40], [43] that interfacial structures gradually transition from solid-like to liquid-like. The characteristics of liquid layers close to and far away from the interface are influenced by the crystal structure and bulk liquid parameters respectively; the first layer spacings are observed to correspond to crystal plane spacings from the solid lattice, more distant spacings are closer to the separation distances between near-neighbours indicated by the liquid density function.

Huisman *et al* investigated ordering in liquid gallium adjacent to a diamond (111) surface [33]. Using synchrotron X-ray scattering techniques, the atomic density across the interface was recorded. This was observed to have an oscillatory character which decayed with increasing distance from the interface; i.e. following the behaviour noted by Kauffmann *et al*. The layer spacing in this instance was approximately 3.8Å, which is similar to the spacing between (001) planes in solid Ga. It was thus concluded that the liquid Ga adopted a solid-like structure which *“is likely to trigger heterogeneous nucleation of the solid”*. Modelling studies by the same team supported this concept [44].

The liquid ordering phenomenon has also been extensively studied through molecular dynamics (MD) modelling. Returning to the case of aluminium, the most comprehensive investigation into the atomistic structure of solid-liquid interfaces thus far has been performed by Hashibon and co-workers [45], [46]. This research investigated ordering in liquid aluminium adjacent to solid aluminium; i.e. a crystal in contact with ‘its own melt’. This scenario is difficult to achieve experimentally due to the very low undercooling expected for solidification and the lack of contrast achievable between like materials in TEM. However, it does represent a mechanism of growth which occurs in real systems; i.e. solidified regions of Al acting as substrates for further crystal growth. In the model, solid Al is represented by atoms pinned to an FCC lattice;

this can be set up at various orientations to align particular crystal planes with the liquid. The liquid comprises the same atoms; however these are free to move under the influence of the inter-atomic potentials. Following an embedded atom method (EAM), Hashibon found evidence for pronounced layering of liquid aluminium in contact with solid Al crystal. Against (110) and (111) Al orientations, liquid layers adopted a spacing reflecting that of the underlying substrate; i.e. appearing to adopt a 'solid-like' character. Against the (100) surface, the spacing in the liquid layers did not adopt that of the (100) planes, but instead gradually altered to adopt that of the (111), suggesting a preference for a (111) orientation of the Al structure. Further work investigating ordering against a BCC (100) surface even found indications of liquid atoms being adsorbed onto the terminating plane of the substrate, effectively transforming it into an FCC (100) surface [47] and potentially indicating that it could act as a substrate for further crystal growth. However, it is fair to note that this transformation may have been favoured by the interatomic potentials employed, rather than being reflective of realistic Al behaviour. This highlights the fact that although MD modelling studies are extremely valuable, they are limited by the accuracy of the interatomic potentials employed, and as such should only serve as an indicator for material behaviour rather than considered to be solid evidence.

More recently, Men and Fan [48] used MD simulations to analyse the effect of lattice mismatch on the ordering in liquid Al atoms. Their results indicate that ordering becomes less pronounced with increased mismatch, and accord with the observations of Oh *et al* [6] that liquid Al against an  $\text{Al}_2\text{O}_3$  {006} surface exhibits ordering within 2-3 atomic layers. They also claimed that the solid-like layers *"could serve as a template for the growth of the new phase on the substrates"* i.e. act as a precursor to nucleation.

Somewhat counter-intuitively, ordering has in some cases been shown to impede, rather than assist, the solidification process, resulting in a larger undercooling than predicted for the bulk material. For example, Schulli et al [35] demonstrated that in AuSi droplets on a Si {111} surface, solidification occurred more than ~120K below the equilibrium freezing temperature, and attributed this

to a stabilisation induced on clusters of atoms in the liquid by the surface structure of the Si {111}; i.e. in-plane order. Greer commented on these results [38] noting that in-plane order is what would be expected for a liquid in contact with a substrate serving as an effective catalyst for solidification, and that the apparent suppression of solidification temperature by this in-plane ordering effect is particularly surprising. Other studies have observed this apparent impeding of the nucleation process; the suggestion being that local ordering imposes non-crystalline symmetries on the interfacial region, which must be broken – hence an energy barrier is created – for growth to proceed [40], [49]. Conversely, many studies concluded that the formation of ordered layers is likely to act as a trigger for heterogeneous nucleation [33], [44] and noted that the layered structures gradually transition from more ‘liquid-like’ to more ‘solid-like’ as the temperature is decreased [43]. These aspects are of great interest to a study of nucleation, particularly considering the adsorption/free growth framework which is strongly applicable to the important engineering case study of Al nucleation on  $\text{TiB}_2$  particles; intended to achieve grain refinement in the cast components.

## 1.7 Practical Application: Grain Refinement

### 1.7.1 Grain Refinement Theory

The scientific community is clearly still some way from a complete and comprehensive understanding of the nucleation process. However, in a practical sense, solidification is still harnessed and controlled in manufacturing processes. The production of aluminium is an appropriate case study; the material being of great importance to today's economy, with wide and increasing usage in transportation, aerospace and other industries.

As stated in the introduction section, a uniform and small sized **grain structure** is often desired for aluminium. Grain boundaries act to inhibit the movement of **dislocations** (crystal defects which cause deformation to the bulk material as they move under load), so a larger number of grains means a greater density of grain boundaries and thus a stronger material, by the Hall-Petch equation [50]:

$$\sigma_y = \sigma_0 + \frac{k_y}{\sqrt{d}} \quad [21]$$

where:  $\sigma_y$  is the yield stress for a material,  $\sigma_0$  a material-dependent constant for the starting stress,  $k_y$  a material-dependent strengthening coefficient, and  $d$  the average grain diameter in the sample.

The **grain refinement** effect is achieved via heterogeneous nucleation. If a large number of appropriate sites are present in the melt, nucleation will initiate (at low undercooling) at these numerous sites, with each event generating an individual grain. The size, number and distribution (amongst other parameters) of the heterogeneous particles thus influences the resulting grain structure. Grain refinement is also referred to as **inoculation** in the literature; the particles added to generate the refinement effect are correspondingly often termed **inoculants**.

### 1.7.2 Grain Refinement Practice

In industry, **grain refiner master alloys** are added to the molten Al in the form of rods, tablets or other dispersed morphologies. According to McKay and Schumacher [51] there are four types of grain refiner in common usage: Ti; Al-Ti; Al-Ti-C, and Al-Ti-B. The latter remains the most widespread and is commonly produced in the composition Al – 5 wt% Ti – 1 wt% B. The master alloy is added to an Al melt in the form of a rod or as pellets. After dissolution in the melt, the boron constituent manifests as  $\text{TiB}_2$  (titanium diboride) particles, which are intended to provide nucleation sites for Al. The widespread use of this approach in industry confirms that the process works, and gives appropriately refined grain structures in the final product; however, there remains considerable debate as to the exact mechanism through which this occurs. Reviews by McCartney in 1989 [52], Murty *et al* in 2002 [53], Greer *et al* in 2003 [54] and Quested in 2004 [55] detail the weight of theoretical and experimental work which has explored the process. In the context of the current project, the interest is focused on what happens in the nucleation event – i.e. at the interface between the inoculant  $\text{TiB}_2$  particles and the Al melt – and the influence of this particular process on grain refinement. Continuing post-nucleation growth and texture development in the solidifying Al is also of great importance to the resulting grain structure, but these aspects are not under investigation here and so will not be fully reviewed.

The ongoing debate as to the exact mechanism by which grain refinement occurs in Al processing revolves around the differing nucleation potential of two characteristic phases which are present in the Al-5Ti-B master alloy. These are titanium diboride,  $\text{TiB}_2$ ; and an aluminide phase,  $\text{Al}_3\text{Ti}$ . Both of these phases exist as particles within the master alloy. Upon addition to the melt, the Al in the master alloy dissolves, leaving  $\text{TiB}_2$  particles. The overall titanium content is diluted such that  $\text{Al}_3\text{Ti}$  is also expected to fully dissolve. The  $\text{TiB}_2$  particles then theoretically provide nucleation sites for crystalline Al. The debate stems from the fact that these particles do not always appear active nucleation sites. For example, work by Guzowski and Sigworth [56] showed that microstructural studies of master alloys observed  $\text{TiB}_2$  at the boundaries of Al grains; rather than the centre, where one would expect a nucleating particle to reside. In these

cases  $\text{Al}_3\text{Ti}$  particles were observed at grain centres suggesting they in fact provided the nucleation sites. Correspondingly, crystallographic analysis identified that  $\text{Al}_3\text{Ti}$  has a greater number of planes possessing a favourable orientation relationship with Al compared to  $\text{TiB}_2$  [53], [57].

Experimental studies by Mohanty and Gruzleski [7] were key in progressing understanding of the nucleation mechanism. Here, synthetic  $\text{TiB}_2$  particles were directly added to an Al melt (rather than allowing them to disperse from a grain refiner) and their nucleation behaviour investigated. Crucially, the study considered the effect of the presence of Ti in the melt; a relevant point due to the existence of a peritectic reaction in the Al-rich end of the binary Al-Ti phase diagram as shown in Figure 1-14:

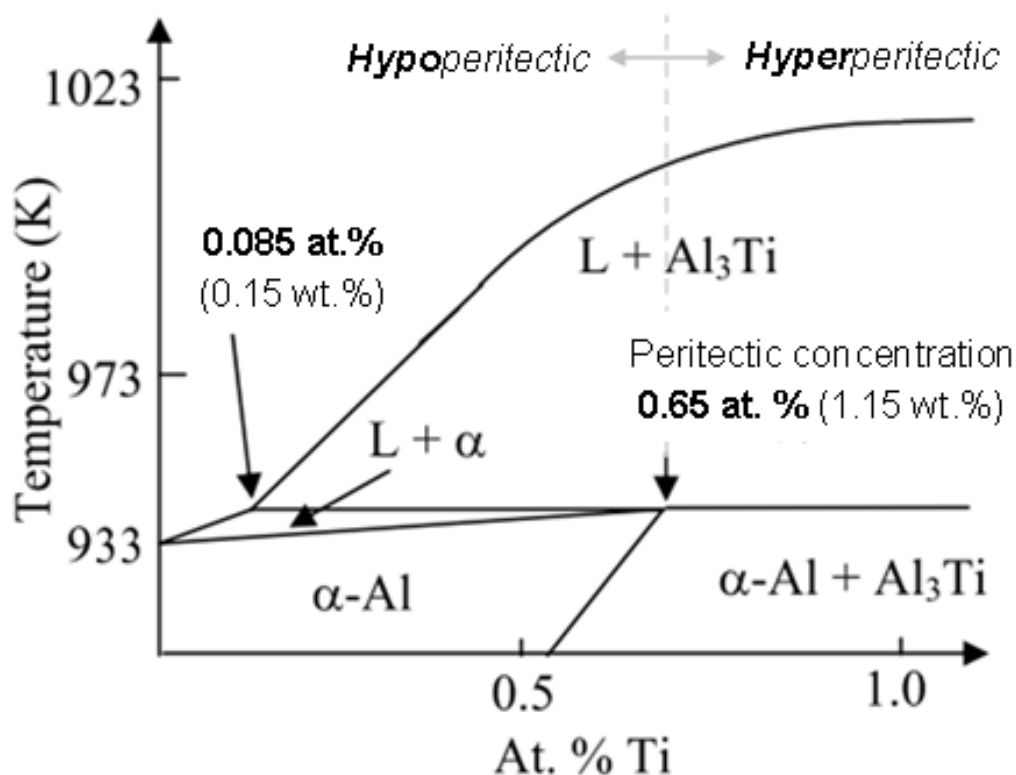
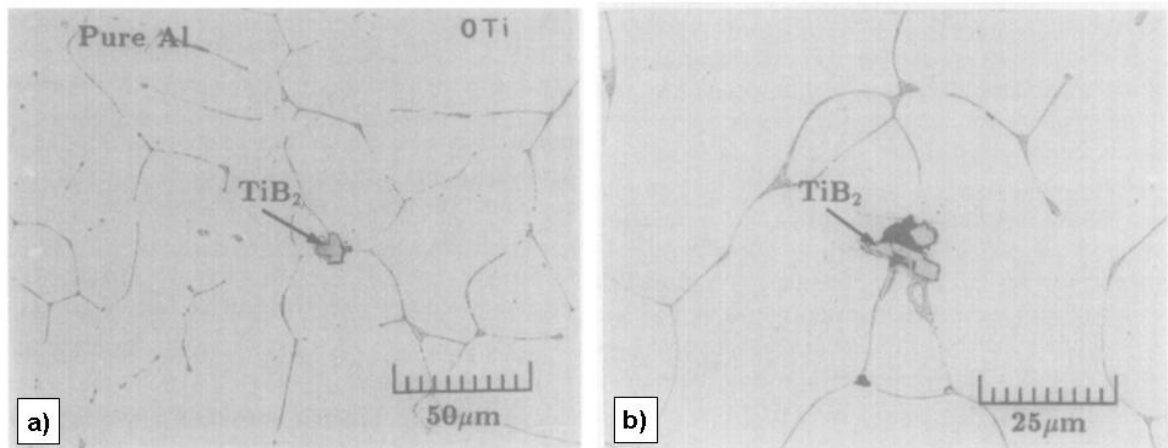


Figure 1-14 - Schematic of binary Al-Ti phase diagram. Modified from [51]

Mohanty and Gruzleski [7] and Pearson and Kearns [58] found that the presence of Ti in excess of that required for  $\text{TiB}_2$  stoichiometry was critical for achieving grain refinement. Mohanty and Gruzleski found that the presence of Ti appeared to determine the location (and therefore the nucleating potential) of

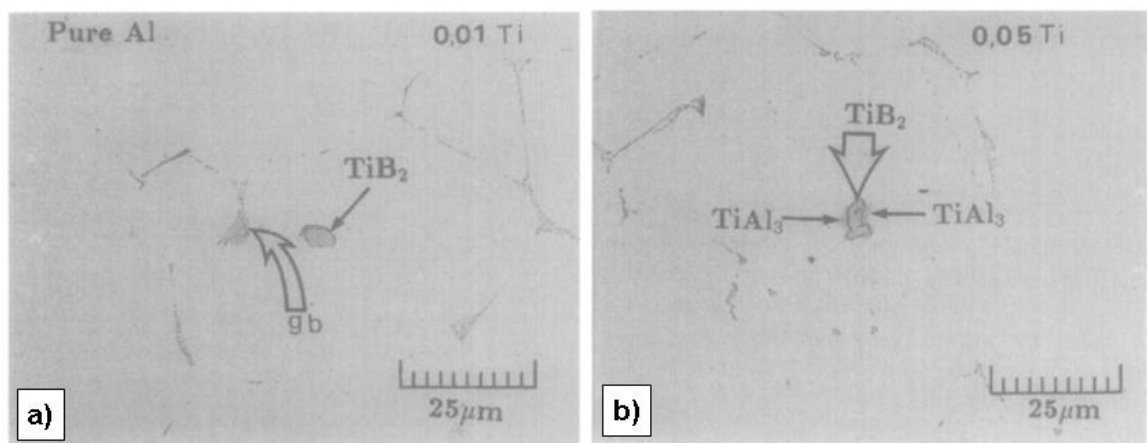


TiB<sub>2</sub> particles. As per the indications from Guzowski and Sigworth, the absence of solute Ti in the melt resulted in a microstructure in which TiB<sub>2</sub> particles were located at Al grain boundaries:



**Figure 1-15 - Indicating TiB<sub>2</sub> particles in solidified Al matrix without solute Ti. a) shows a single TiB<sub>2</sub> particle while b) shows a cluster present at the grain boundaries. Reproduced from [7]**

Following this, grain refinement practice was simulated via the addition of an Al-6%Ti alloy, ensuring the presence of solute Ti in the melt. The resulting microstructure showed TiB<sub>2</sub> residing at the centre of solid Al grains:



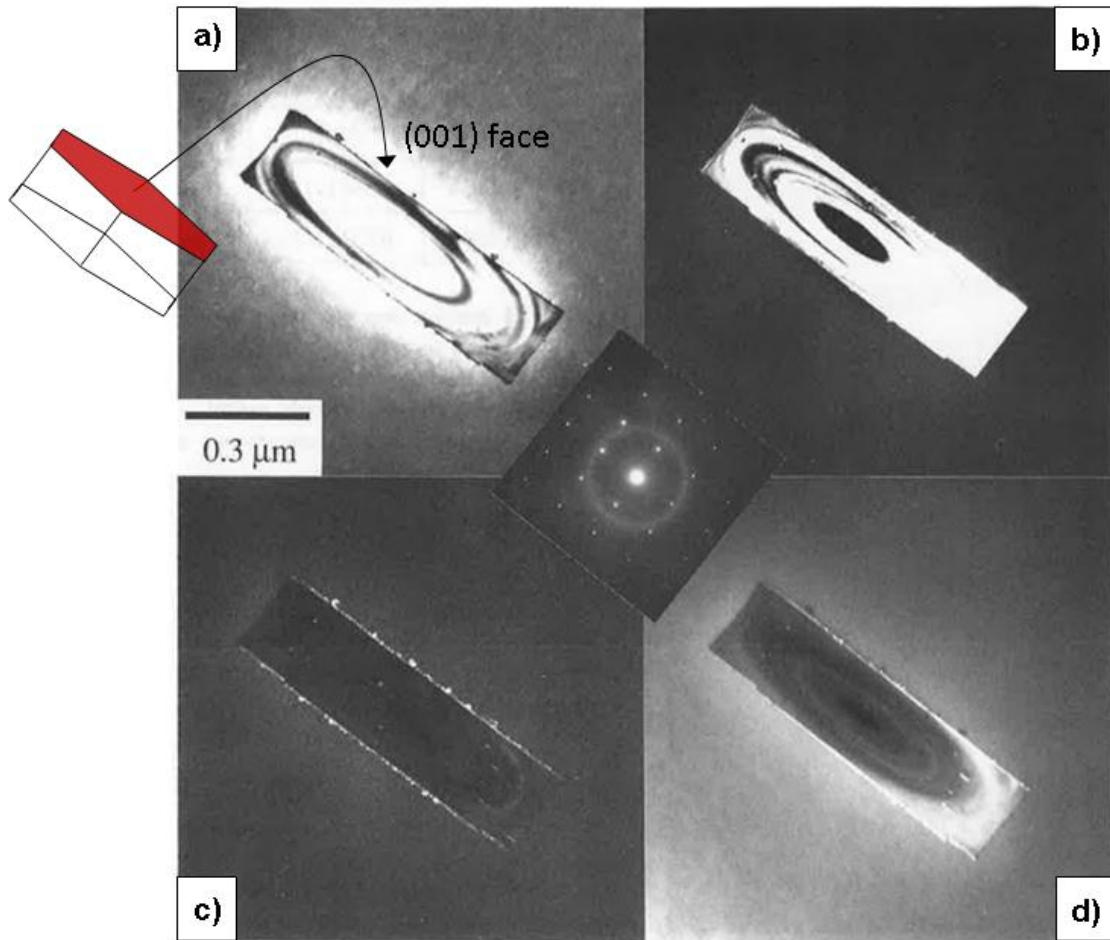
**Figure 1-16 - Indicating TiB<sub>2</sub> particles in solidified Al matrix with solute Ti at concentration a) 0.01%wt and b) 0.05%wt. Reproduced from [7]**

Clearly the addition of solute Ti somehow renders the TiB<sub>2</sub> particles suitable nucleation sites for crystalline Al. Interestingly, in Figure 1-16b, the authors noted the presence of a thin layer surrounding the boride, which through further

analysis they deemed to be  $\text{Al}_3\text{Ti}$ . It is suggested that the presence of this layer 'activates' the  $\text{TiB}_2$  particles as nucleation sites, resulting in their location in the centre of Al grains; following this hypothesis, the authors theorised that there must also be an  $\text{Al}_3\text{Ti}$  layer at lower wt% Ti concentrations, too thin to observe at the magnification used in Figure 1-16a. Interestingly, the existence of  $\text{Al}_3\text{Ti}$  is observed at wt% Ti concentrations significantly lower than the peritectic composition indicated in Figure 1-14. Increasing the Ti concentration even further resulted in larger amounts of  $\text{Al}_3\text{Ti}$ ; crucially it was still observed to preferentially nucleate on  $\text{TiB}_2$  particles despite the fact that, at such Ti concentration, it is thermodynamically feasible for  $\text{Al}_3\text{Ti}$  to exist in isolation in the melt. This suggests that there is a propensity for  $\text{Al}_3\text{Ti}$  to be associated with boride surfaces.

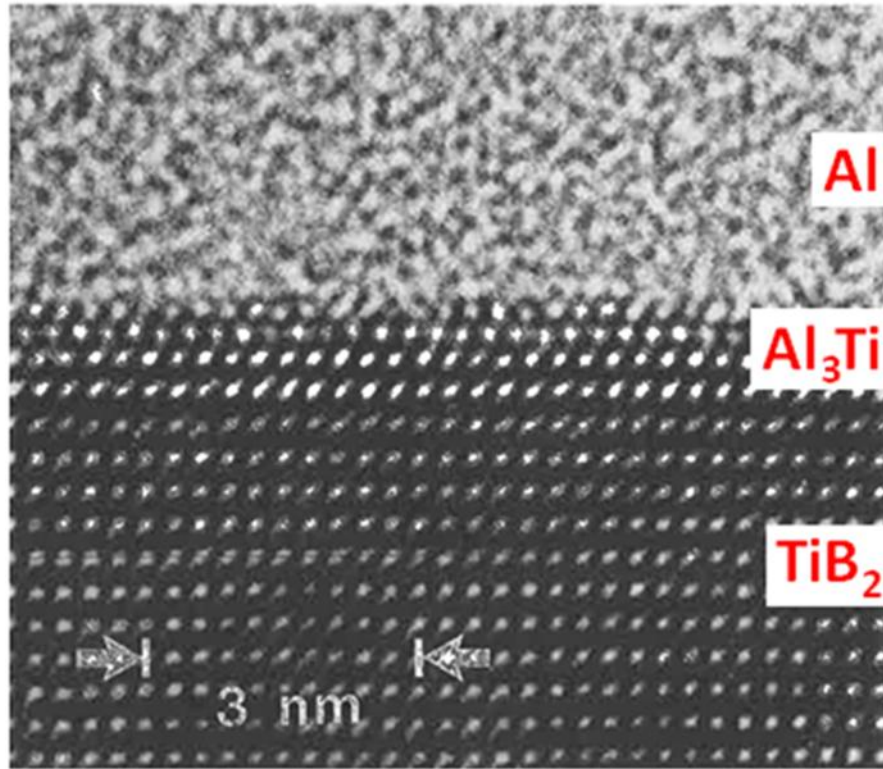
Other researchers independently identified the existence of a metastable phase on boride particles. Johnsson *et al* [59] described the formation of a metastable Al solid which, with hyperperitectic additions of the grain refiner alloy, was observed at temperatures 2-5°C above the equilibrium peritectic temperature. This observation is interesting in the context of liquid ordering, suggesting that the formation of an ordered layer of a transient phase is a precursor to nucleation in the case of Al.

Advances in electron microscopy permitted significantly more detailed investigations to be made at the boride-melt interface. The seminal studies by Schumacher *et al* represented significant progress in terms of spatial resolution [14], [27]. This was facilitated by the use of a 'metallic glass', an Al-based alloy (composition  $\text{Al}_{85}\text{Y}_8\text{Ni}_5\text{Co}_2$  by %wt) with grain refiner additions, which was rapidly quenched from the liquid state via melt spinning. This allows the solidification of Al to be arrested at a very early stage; i.e. just after the nucleation events occur. The resulting samples could then be investigated via TEM to observe the morphology around the boride particles roughly as it would appear *in-situ*.



**Figure 1-17 – TEM images of a  $\text{TiB}_2$  particle in quenched Al-based metallic glass with schematic of  $\text{TiB}_2$  crystal structure. a) Bright-field image. Remaining images are dark-field, showing b) the boride particle. c) Al crystals nucleated on  $\{001\}$  boride faces. d) Layer on  $\{001\}$  boride faces suggested to be  $\text{Al}_3\text{Ti}$ . Inset shows selected area diffraction pattern used to orient electron beam to run parallel to  $\langle 110 \rangle \text{TiB}_2$  direction. Modified from [27]**

Within the same study, HRTEM studies of the interface between the  $\text{TiB}_2$  particle and Al matrix permitted direct measurement of the atomic positions in the identified layer. These were consistent with  $\text{Al}_3\text{Ti}$  confirming the veracity of the claim. To clarify, we revisit Figure 1-9.



**Figure 1-18 – HRTEM image of Al<sub>3</sub>Ti layer on TiB<sub>2</sub> nucleating solidification of Al. The layer between the boride surface and Al matrix has atomic spacing consistent with those of Al<sub>3</sub>Ti. Modified from [27]**

Interestingly, the authors also note that longer holding times at high temperature, prior to quenching, did not lead to increased thickness of the layer; the presence and resulting thickness of the layer appears to be independent of this processing parameter. It is also notable that, as with the work of Mohanty and Gruzleski, the overall content of Ti is hypoperitectic (~0.05 %at) yet the Al<sub>3</sub>Ti layer forms readily and reproducibly.

Based on previous metallic glass studies [60], [61] and confirmed by analysis of HRTEM images such as the above, Schumacher and co-workers identify the orientation relationships between close-packed planes in Al, Al<sub>3</sub>Ti and TiB<sub>2</sub>, shown in Table 1-1:

<b>TiB<sub>2</sub></b>	<b>Al<sub>3</sub>Ti</b>	<b>Al</b>
$\langle 110 \rangle (001)$	$\langle \bar{1}\bar{1}0 \rangle \{112\}$	$\langle \bar{1}\bar{1}0 \rangle \{111\}$
$\langle 110 \rangle (001)$	$\langle 0\bar{2}1 \rangle \{112\}$	$\langle \bar{1}\bar{1}0 \rangle \{111\}$

**Table 1-1 - Orientation relationships in materials of interest. Note that the parallel planes are the same in both cases; there are two close-packed directions for the Al<sub>3</sub>Ti which satisfy the orientation relationship.**

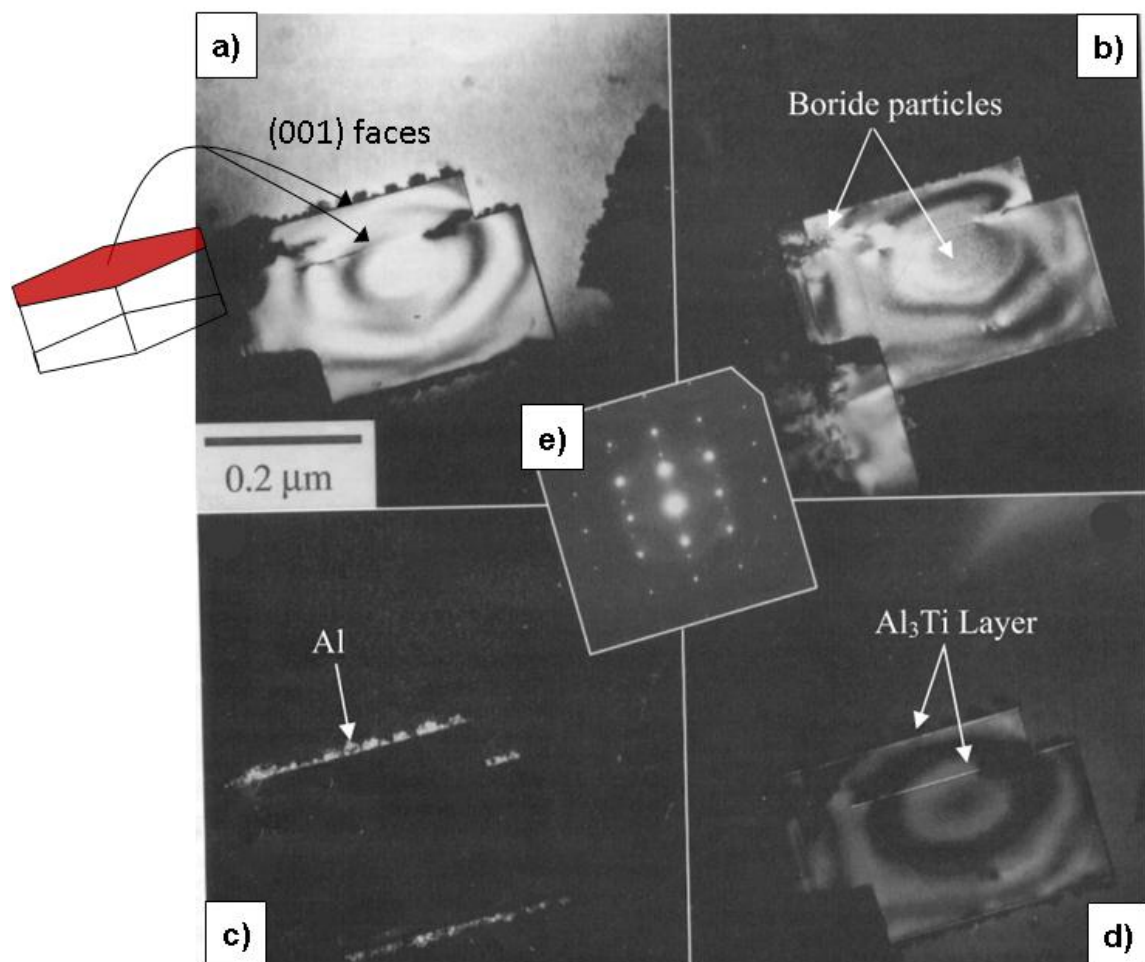
Interestingly, Al<sub>3</sub>Ti {112} is a non-equilibrium face, appearing to be stabilised by its relationship with the boride substrate. As previously discussed, one of the main factors associated with effective heterogeneous nucleation is the degree of mismatch between the crystal lattice of the nucleant and nucleated solid. Indeed, the fact that TiB<sub>2</sub> was known to have a relatively poor lattice match to Al was a key element of its effectiveness as a nucleant being questioned, despite years of industrial application. Using the identified orientation relationships, the mismatch is assessed as follows:

<b>Relationship</b>	<b>Direction</b>	<b>Lattice mismatch</b>
TiB <sub>2</sub> (001) // Al {111}	Al: along $\langle 110 \rangle = 2.86\text{\AA}$ TiB <sub>2</sub> : along $\langle 110 \rangle = 3.03\text{\AA}$	<b>5.9%</b>
Al <sub>3</sub> Ti (112) // Al {111}	Al: along $\langle 110 \rangle = 2.86\text{\AA}$ Al <sub>3</sub> Ti: along $\langle \bar{1}\bar{1}0 \rangle = 2.71\text{\AA}$ Al <sub>3</sub> Ti: along $\langle 0\bar{2}1 \rangle = 2.88\text{\AA}$	<b>2.1%</b> (based on average spacing in Al <sub>3</sub> Ti)

**Table 1-2- Detail of lattice mismatch along planes of interest**

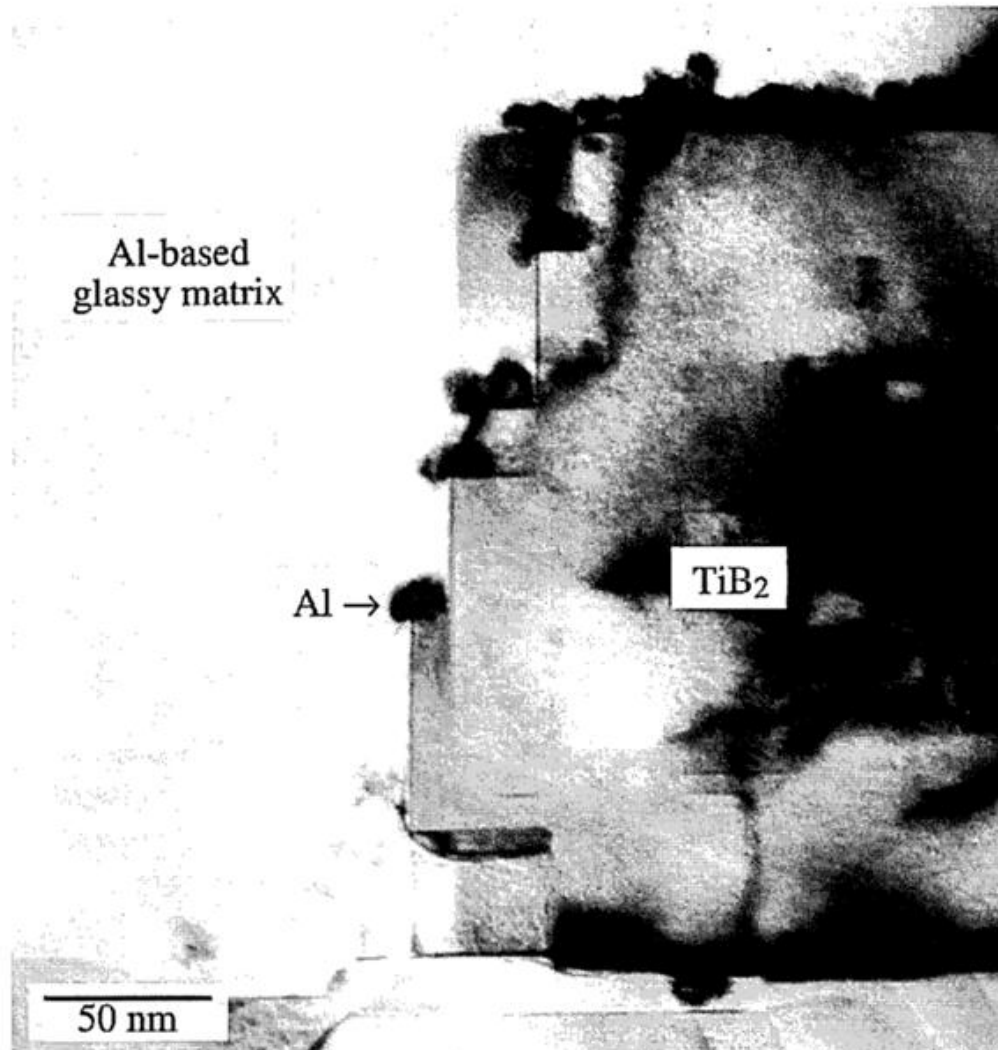
While thermal expansion improves the Al/TiB<sub>2</sub> mismatch, the effect is small over the relatively small temperature range required for Al processing. It is clear that the Al<sub>3</sub>Ti has a smaller mismatch with Al than TiB<sub>2</sub>, supporting the claim that it is in fact the aluminide phase which provides the potent substrate for nucleation of Al. It appears that it provides a kind of transitional medium between the lattices of the boride particle and crystalline Al, 'smoothing' the lattice disregistry between the two materials. Interestingly, as seen in Figure 1-18, the Al<sub>3</sub>Ti layer appears to be entirely coherent with the structure of the boride. This implies that the structure of the layer is under tensile **strain**. In fact, slightly increased lattice

spacing would also improve the match to the Al structure. The HRTEM indicates that the  $\text{Al}_3\text{Ti}$  is not a monolayer but consists of 3-4 layers of atoms; and as stated by McKay and Schumacher in commentary on the current work in 2005 [51] “As the thickness of the aluminide layer increases the lattice relaxes thereby reducing the interatomic spacing closer to that of the Al”. In thicker layers, this relaxation would be expected to result from interfacial dislocations or other misalignment, but there is no evidence for such mechanisms here. The coherency, and thus the strain, appears to be present throughout the layer. In a 1998 review Schumacher *et al* provided further strong evidence for the formation of  $\text{Al}_3\text{Ti}$  on boride surfaces [14]:



**Figure 1-19 – TEM images of  $\text{TiB}_2$  particles in quenched Al-based metallic glass with schematic of  $\text{TiB}_2$  crystal structure. a) Bright field image. Remaining images are dark-field, showing b) the boride particle, c) Al crystals nucleated on (001) boride faces, and d) the thin  $\text{Al}_3\text{Ti}$  layer on the boride surfaces. Inset shows selected area diffraction pattern. Beam axis is parallel to  $\langle 110 \rangle \text{TiB}_2$  direction. Modified from [51] (originally presented in [14])**

An important observation from Figure 1-17 and Figure 1-19 is the fact that Al appears to nucleate only on particular faces of the boride particles – specifically those with (001) orientation. This was further clarified through a close-up investigation of the presence of nucleated Al on small ledges/steps on the edges of boride particle. Crystalline Al is observed only on the faces with (001) character; no crystals are observed on other prismatic faces:



**Figure 1-20 – Bright-field TEM image showing close-up of boride particle. Crystalline Al is observed only on faces/ledges/steps which have a (001) orientation – no crystalline Al is observed to have nucleated on any other surfaces. Reproduced from [14]**

Despite the apparent clarity of TEM investigations the legitimacy of the  $\text{Al}_3\text{Ti}$  layer nucleation mechanism continued to be questioned. The relatively complex composition of the metallic glass alloys raises questions as to whether their behaviour can be considered an appropriate analogue for Al and its alloys in

industrial applications. Through the years of research, the continued debate has led to the proposal of a number of 'competing' mechanisms for the nucleation of Al by  $\text{TiB}_2$  particles. These were formalised by Easton and St John [62], [63] and are briefly described as follows. Some of these theories were effectively superseded by the more modern studies presented in the current section, but are presented here for completeness. All are based specifically on the use of Al-Ti based master alloys.

1. **Carbide/boride theory:** Formulated and proposed in the 1950's by Cibula [64] this theory expresses the idea that borides or carbides are definitively the nucleating sites for Al, via TiC carbides (the presence of carbon effectively being impossible to avoid in practical cases) or  $\text{AlB}_2/\text{TiB}_2$  borides (when using an Al-Ti-B master alloy). This older theory has effectively been discredited by the results shown in this section; poor lattice matching [57], borides being observed at grain boundaries when no Ti is present [7], and TEM studies [14], [27], [51], [65].
2. **Peritectic theory:** First proposed by Crossley and Mondolfo in the 1950's [66], this theory is based on the Al-Ti phase diagram (see Figure 1-14) suggesting that  $\text{Al}_3\text{Ti}$  nucleates Al by a peritectic reaction. The problem with this proposal is that according to the phase diagram the liquid Al melt should contain 0.15 wt.% Ti, whereas the normal content resulting from master alloy addition is around 0.01 wt.%. The peritectic reaction alone is thus not sufficient to explain the mechanism. It was suggested that the presence of boron effectively modifies the phase diagram in such a way that the peritectic reaction can take place at a lower Ti content [67] but there has been little evidence for this. Another important element of this theory is the assumption that  $\text{Al}_3\text{Ti}$  particles in the master alloy would fully dissolve into the melt such that the Ti would be in solution – were this not the case, the  $\text{Al}_3\text{Ti}$  particles themselves would provide potent nucleating sites for the Al.
3. **Peritectic hulk:** Proposed by Backerud and Yidong [68], [69] this theory suggests that  $\text{Al}_3\text{Ti}$  persists in the melt thanks to a 'shell' of borides forming around the aluminide particles, slowing down their dissolution and permitting them to act as nucleating sites for Al. Experimental work effectively discredited this mechanism; for example by the investigations of Johnsson



*et al* [59] demonstrating that refining efficiency remains constant over multiple melting and solidification cycles; were the peritectic hulk theory operative, the efficiency would be expected to decrease due to gradual diffusion of Ti from the aluminides over repeated cycles.

4. **Hypernucleation:** Proposed by Jones [70] this theory suggests that nucleation is facilitated through segregation of Ti to the boride/melt interface. Ti, having a similar atomic size to Al, helps to form a “*pre-existing solid aluminium with high titanium from which solid aluminium grows*” [53]. Conceptually, this fits with the suggestion that ordering in the liquid state acts as a precursor to nucleation; however, no experimental evidence exists to support the theory.
5. **Duplex nucleation:** Originally proposed by Mohanty and Gruzleski [7] this is the theory for which the studies presented in the current chapter [14], [27], [51], [65] provide strong evidence. Effectively, this theory states that Ti in the melt segregates to the boride/melt interface, allowing the formation of an  $\text{Al}_3\text{Ti}$  layer on  $\text{TiB}_2$  surfaces, which then provides the nucleating substrate for crystalline Al. Mohanty and Gruzleski showed the importance of Ti by demonstrating that  $\text{TiB}_2$  particles were present at grain boundaries when no Ti was present in the melt (Figure 1-15) and in the centre of grains when Ti was present (Figure 1-16). The work of Schumacher *et al* [14], [27], [51], [60], [61], [65] provides experimental evidence for this mechanism through imaging and characterisation of a distinct layer present on  $\text{TiB}_2$  {001} surfaces. The effect appears to occur at both hypo- and hyperperitectic concentrations of Ti, which thermodynamically is somewhat unexpected. Thus, whilst there is strong support for the existence of the  $\text{Al}_3\text{Ti}$  layer, the question remains as to exactly how and why it forms, and how it is apparently able to exist outside the normal concentration range.
6. **Solute theory:** Easton & St John [62], [63] recognised problems with the preceding theories, questioning, for example, the applicability of results from metallic glass experiments to a foundry alloy. They suggested that the fundamental issue with the preceding theories of grain refinement is that they focused almost entirely on the nucleation event. Classing the preceding 5 theories as belonging to a ‘nucleant paradigm’, they proposed a ‘solute paradigm’ wherein the effect of solute segregation was considered as a

primary mechanism for grain refinement. St John *et al* formalised this process in the so-called interdependence theory [71] but in a basic sense, the proposed mechanism is as follows. Solute (Ti, in our current case) segregates to the solid-liquid interface upon solidification of the melt, resulting in a constitutionally undercooled zone ahead of the interface. The lower temperature activates further nucleants ( $\text{TiB}_2$  particles) within this zone, which in turn interrupts growth of the previous grain. This theory clearly addresses the excess Ti content noted to be required for effective refinement (no Ti = no solute, hence no constitutional undercooling). However, it is fundamentally based on an assumption that  $\text{TiB}_2$  particles, despite the presented evidence to the contrary, *are* in fact potent nucleating sites for Al. In Table 1-2 the lattice mismatch between Al and  $\text{TiB}_2$  was shown to be 5.9% - a larger mismatch than Al and  $\text{Al}_3\text{Ti}$  – but notably still below the 10-12% suggested as a margin for effective promotion of nucleation [72].

Easton & St John make the important observation that whether the  $\text{TiB}_2$  or an  $\text{Al}_3\text{Ti}$  layer provides the actual nucleating substrate for Al, the boride particles themselves remain “*the prime nucleant particle*”. Some mechanism is operative at the (001) faces of these boride particles which plays a role in the subsequent grain refinement. The importance of solute for the ongoing growth of grains is emphasised in theory 6, however, this is not necessarily relevant to the initial nucleation event. There is clearly still scope for an improved understanding of the mechanism immediately at the interface between a solid  $\text{TiB}_2$  (001) surface and liquid Al.

More recently, a series of experiments by Iqbal *et al* [73]–[78] have provided evidence for the indication of  $\text{Al}_3\text{Ti}$  in the system in question via the use of synchrotron X-ray scattering techniques. In the first study [73] X-ray diffraction was performed through a sample comprising an aluminium alloy with solute titanium (around 0.1 wt.% - less than the peritectic composition of 0.15 wt. %) and  $\text{TiB}_2$  particles. In this experiment, diffraction spots which could not be indexed as Al were instead ascribed to an  $\text{Al}_3\text{Ti}$  phase; interestingly, the formation of  $\text{Al}_3\text{Ti}$  was observed at temperatures about 10K above the freezing

point for aluminium (i.e. while Al was still liquid). A concurrent experiment on a sample with solute titanium but no  $\text{TiB}_2$  particles lacked the  $\text{Al}_3\text{Ti}$  diffraction spots, and had a less well-refined grain structure on completion of solidification. A later study [74] found that  $\text{Al}_3\text{Ti}$  formed in samples at both hypo- and hyperperitectic compositions, with no  $\text{Al}_3\text{Ti}$  observed in samples containing only solute titanium *or* only  $\text{TiB}_2$ . The results thus provide further evidence for the formation of  $\text{Al}_3\text{Ti}$ , the importance of excess titanium, and indicate their significance to nucleation and subsequent grain refinement in Al alloys.

Another indicator of the likely importance of  $\text{Al}_3\text{Ti}$  to the nucleation process arises from work by Bunn *et al* [79]. This study was designed to investigate so-called *poisoning* of the grain refinement process, an action which renders the grain refiners less effective. When additions of zirconium were made to an Al melt with Al-Ti-B refiner, the authors noted that Zr can preferentially substitute for Ti in both the boride and aluminide, forming mixed phases. In the former case, the lattice parameter of the boride particles is increased, making formation of the aluminide layer more difficult, thus degrading their effectiveness in nucleating Al. In the latter case, the resulting mixed aluminide layer is suggested to be *“a different and possibly less potent composition for the nucleation of aluminium”*. In summary, then, the fact that poisoning of the grain refining effect results when adding elements which may substitute for Ti in the system supports the claim that the formation of an uncontaminated  $\text{Al}_3\text{Ti}$  layer on boride surfaces plays a key role in determining nucleation potency.

## 1.8 Synchrotron X-ray Scattering

### 1.8.1 Introduction

Investigating nucleation and solidification using HRTEM has been revealing, but it remains difficult to monitor the processes *in-situ*. Synchrotron X-ray facilities offer scientists novel ways to approach this issue. Probing samples with X-ray radiation allows structural information to be drawn out in a non-destructive, non-contact way; this means that X-ray scattering can be collected *in-situ* allowing solidification phenomena to be assessed as they occur. Synchrotron X-ray radiation has high brilliance, i.e. can produce a high concentration of photons; high collimation, i.e. the beam has a small angular divergence; high polarisation; and crucially for X-ray crystallography, can be almost perfectly monochromatised to produce a beam of a specific energy/wavelength. Typical X-ray wavelengths range between 0.1-10Å *i.e.* on the same length scale as atomic bonds and lattice parameters, making them ideal tools for investigating structures at the atomic scale.

Synchrotron radiation is produced via the acceleration of electrons to relativistic speeds in a particle accelerator. These particles circulate in an enclosed storage ring, confined via magnetic fields to travel in a circular path. This process causes the particles to emit radiation in the form of X-ray photons travelling tangentially to the storage ring. Beamlines built at these tangents capture and focus the X-ray beams onto an experimental sample. Detectors are positioned to record and measure the scattered and diffracted X-rays from the sample.

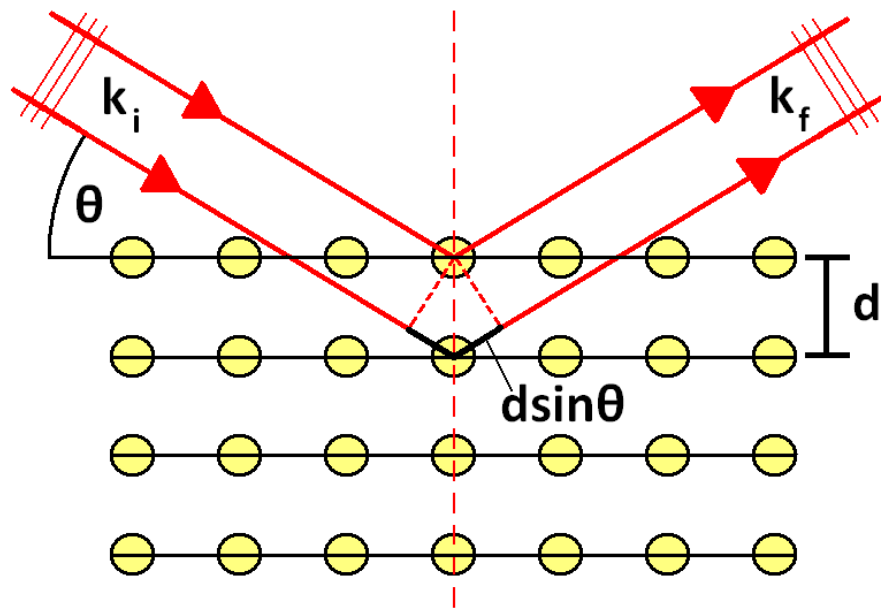
### 1.8.2 X-ray Crystallography

This section is intended as a broad overview of the X-ray diffraction theory [80]–[82] which is relevant to the current work.

X-ray crystallography is a tool for revealing the internal structure of crystalline materials. X-ray beams are diffracted by the atomic structure of a material in a way which is characteristic of the crystal lattice. At a synchrotron source, X-rays scattered from a sample strike detectors which record their positions and

intensities, generating a diffraction pattern which can be understood as a representation of the structure of the sample. For the current project, the overarching concept is that one may observe the changes to the diffraction pattern as changes are made in the sample – i.e. as solidification takes place – to observe *in-situ* the changes to the structure which are occurring.

An intuitive, concise understanding of X-ray diffraction is permitted through the use of Bragg's Law. This can be understood visually as shown in Figure 1-21:



**Figure 1-21 - Schematic representation of Bragg's Law.  $k_i$  and  $k_f$  are the wavevectors of the incident and scattered beams respectively. Physically,  $k_i$  and  $k_f$  are planar front waves with wavelength  $\lambda$ .  $d$  is the interplanar spacing between planes of atoms within a single crystal. For constructive interference to occur, the path difference  $2d \sin \theta$  must be equal to an integer number of wavelengths  $n\lambda$ .**

Consider X-rays as waves of electromagnetic radiation. When these waves strike atoms secondary waves are produced via elastic scattering from the electron shells of the atoms. These scattered waves propagate spherically from the atom, and in most directions destructive interference means they cancel out. However, in a few specific directions, the scattering constructively interferes to produce intense scattered beams, which are collected by the X-ray detectors. Bragg's law, defining the conditions in which diffraction takes place, is expressed in the following succinct equation:

$$2d \sin\theta = n\lambda$$

[22]

where  $d$  is the spacing between crystal planes,  $\theta$  the incident angle of the incoming and scattered X-ray beam,  $\lambda$  the wavelength of the X-ray beam and  $n$  an integer value. Diffraction only takes place under these conditions, i.e. when the path difference between the parts of the incident beam striking different layers of the crystal structure is equal to an integer number of wavelengths. As Figure 1-21 indicates, this is equal to the product of the crystal spacing and sine of the incident angle.

Within crystal structures, different crystal planes are defined by their Miller indices ( $hkl$ ). A total **family** of planes with the same character (for example, (111) and  $(\bar{1}\bar{1}\bar{1})$ ) are denoted with curled brackets  $\{hkl\}$ . For a given family of planes, the lattice spacing  $d$  is common, and for a cubic crystal system can be defined as such:

$$d_{hkl} = \frac{a}{\sqrt{h^2 + k^2 + l^2}}$$

[23]

where  $a$  is the lattice parameter for the material in question.

In a classical X-ray diffraction experiment, a single crystal of the material under investigation is mounted on a device called a **diffractometer**. This rotates the sample around various axes while maintaining alignment with the X-ray beam. As it moves, different crystal planes move into the Bragg condition and generate scattered beams which strike detectors. The result is a **pattern** of individual spots of scattered intensity, known as **Bragg peaks**. These are referred to as **diffraction patterns**, and they are effectively an impression of the internal structure of the sample in **reciprocal space**. This is a tricky but important concept in diffraction theory. To understand its importance, we introduce the concept of the **momentum transfer** in diffraction.

In Bragg diffraction the scattering is perfectly elastic, meaning the energy of the incident wave  $k_i$  is entirely conserved. The only difference is a direction change. The scattering vector  $Q$  is defined as  $Q = k_f - k_i$  as shown in Figure 1-22.

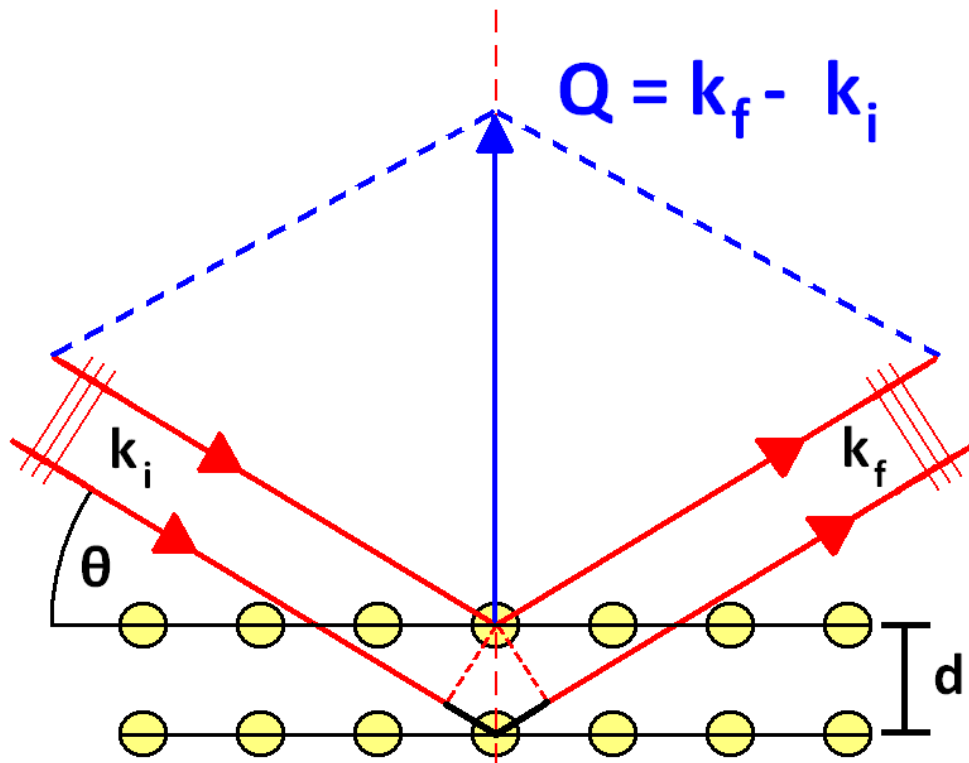


Figure 1-22 - Schematic indicating the formation of momentum transfer  $Q$

Diffraction patterns are effectively plotted in ' $Q$ -space', which can also be referred to as **momentum** or **reciprocal** space.

Any crystal structure is fundamentally based on one of 14 Bravais lattices; the number, type and positions of the atoms in relation to the lattice defining the material itself. Due to the diffraction condition, the values in momentum space at which diffraction occurs also forms a lattice; as such any lattice in real space has an equivalent reciprocal space lattice. These can often be relatively straightforward; e.g. the reciprocal of a simple cubic lattice is also a simple cubic lattice; the reciprocal of an FCC lattice in real space is BCC in reciprocal space, and vice versa.

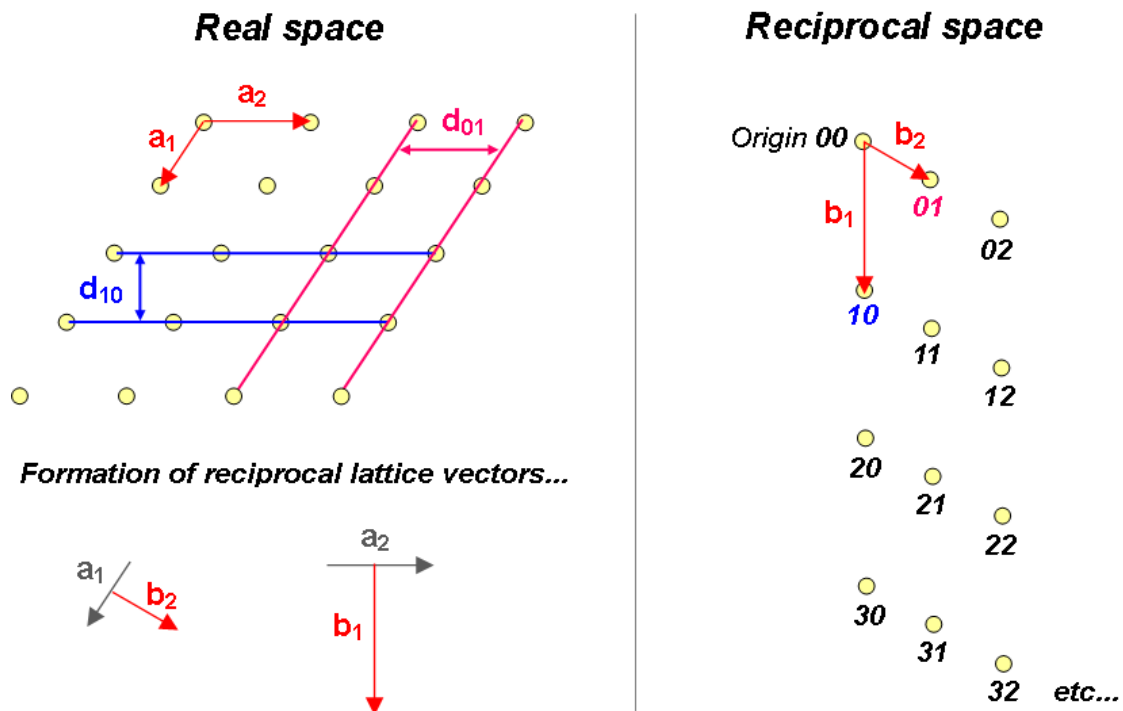
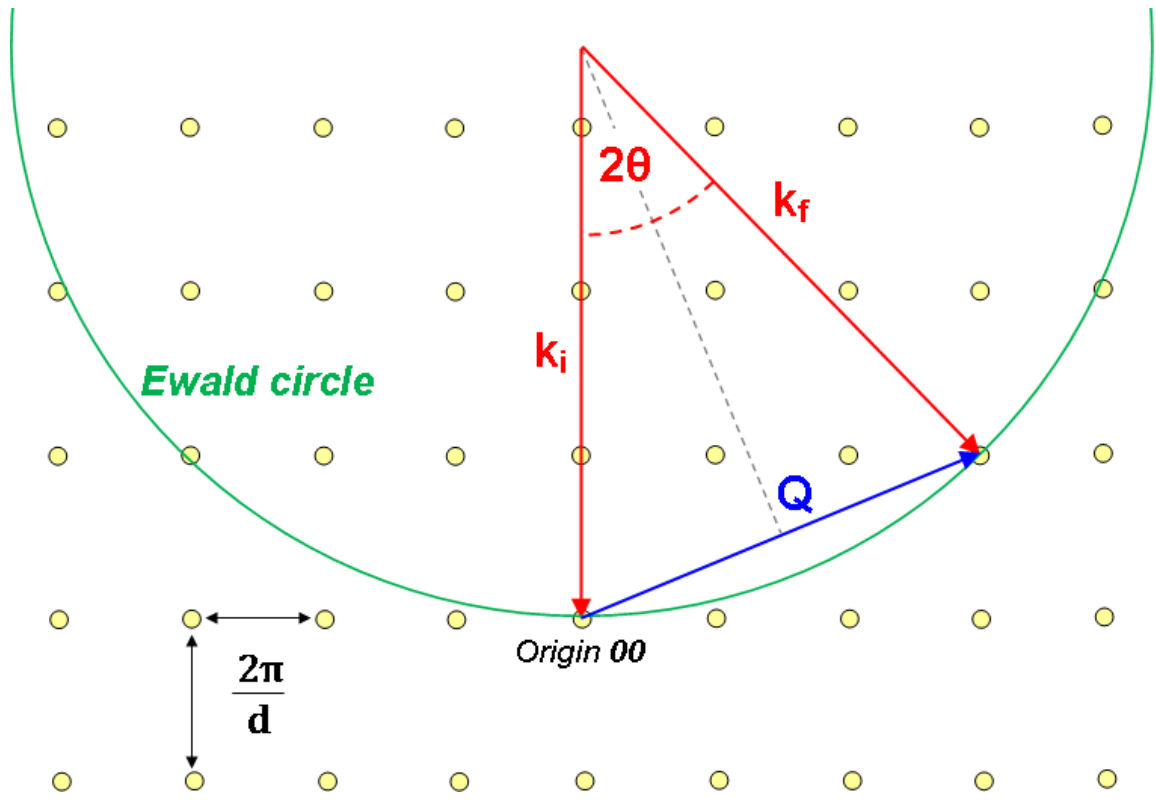


Figure 1-23 – Schematic showing the generation of the reciprocal lattice. Shown in 2D for ease of understanding (assume  $a_3/b_3$  are 'out of page')

For a real space lattice, defined by vectors  $\mathbf{a}_1$ ,  $\mathbf{a}_2$ ,  $\mathbf{a}_3$ , there is an equivalent reciprocal lattice defined by  $\mathbf{b}_1$ ,  $\mathbf{b}_2$ ,  $\mathbf{b}_3$ . Crystal planes in real space lattices are defined by their Miller indices  $(hkl)$ . The directions of the reciprocal lattice vectors correspond to the directions normal to the crystal planes in real space, and the length of the reciprocal lattice vectors correspond to the d-spacing of the crystal planes in real space. So, in the above,  $\mathbf{b}_1$  has magnitude  $1/d_{10}$  and is perpendicular to the (10) planes; and  $\mathbf{b}_2$  has magnitude  $1/d_{01}$  and is perpendicular to the (01) planes. The consequence is that **each point in the reciprocal lattice corresponds not to a single real space lattice point but to an entire family of crystal planes.**

We may now introduce the concept of the Ewald sphere, a construction which links the wavevector of the incident and diffracted X-ray beams, the diffraction angle  $\theta$ , and the reciprocal lattice. This construction helps to indicate the conditions required for diffraction:





**Figure 1-24 - Ewald construction in 2D.** The reciprocal lattice is set up such that the spacing between lattice points is  $2\pi/d$  where  $d$  is the real space interplanar distance. This reflects the periodicity in the wave and simplifies later calculation

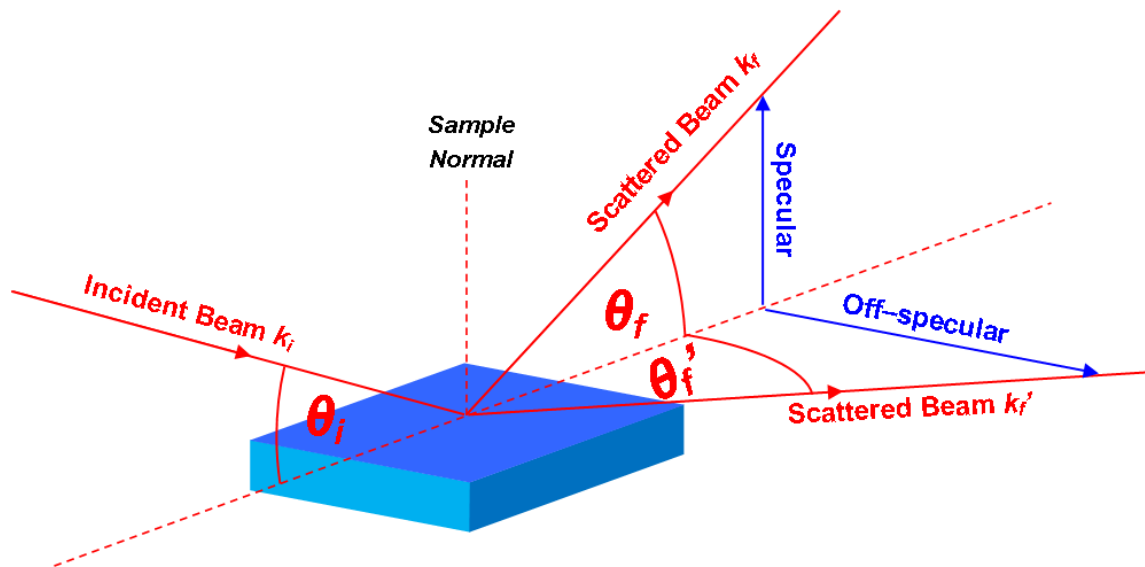
In the above,  $k_i$  (and  $k_f$ ) are given as  $2\pi/\lambda$  where  $\lambda$  is the wavelength of the incoming X-ray. The factor  $2\pi$  reflects the periodicity of the wave, and  $k_i$  is positioned such that it points to the origin of the reciprocal lattice. Because  $k_i = k_f$ , the scattering vector  $\mathbf{Q} = \mathbf{k}_f - \mathbf{k}_i$  lies on the surface of a sphere of radius  $2\pi/\lambda$ . For diffraction to occur, this vector must be equal to a reciprocal lattice vector  $\mathbf{G}_{hkl} = 2\pi(h\mathbf{b}_1 + k\mathbf{b}_2 + l\mathbf{b}_3)$ ; i.e.  $\mathbf{G} = \mathbf{Q} = \mathbf{k}_f - \mathbf{k}_i$ . This is the **Laue condition** for diffraction.

Typically for synchrotron studies the X-ray wavelength  $\lambda$  is fixed; as such the sample must be rotated about various axes in order to bring different reciprocal lattice points (representative of different crystal planes in the various materials in a given sample) into the diffraction condition. The detector must be set in the direction of  $k_f$  (i.e. at the angle  $2\theta$ ) to record the scattering. If we substitute the expression for  $d$  from equation [23] into the Bragg's law [22], it is clear how a scan should be performed:

$$\frac{\lambda^2}{4a^2} = \frac{\sin^2 \theta_{hkl}}{h^2 + k^2 + l^2}$$

[24]

For a given experiment, the left hand side of the above equation is constant. The right hand side indicates that as  $h, k, l$  increase,  $\theta$  also increases. A diffraction experiment thus usually proceeds by scanning through  $2\theta$  to find different  $(hkl)$  reflections, either in a **specular** direction (i.e. coplanar with the incident beam and sample normal) or an **off-specular** direction. The result is a **diffraction pattern** comprising a series of intense Bragg peaks. These patterns can be **indexed** to identify the presence of different materials, their crystallography, and, in the case that multiple materials are present in the sample, their relative crystallographic orientation. For reference, the directions are indicated in Figure 1-25.



**Figure 1-25 - Schematic showing the specular and off-specular directions in scattering geometry in relation to the incident beam and sample normal. Note that  $\theta$  refers to the scattering angle in both the specular ( $\theta_f$ ) and off-specular ( $\theta_f'$ ) directions.**

The preceding theory relates to diffraction from single crystals, i.e., assuming the ordered crystal structure is present throughout the entire volume of the sample illuminated by the X-ray beam. In polycrystalline materials, grains exist at multiple, random orientations; in a large enough sample they will exist at all

possible orientations. This means that for a particular incident wavelength, scattering is produced in all directions along a 'cone' emanating from the sample; the opening angle of the cone defined by the Bragg condition. The detector records a 2D 'slice' through this cone such that the resulting feature appears as a ring (or section thereof). This is also the fundamental process behind powder diffraction.

The preceding section encompasses the theoretical understanding required for one major aspect of the current project. Diffraction data will comprise a series of features at different positions relative to the diffraction angle  $2\theta$ . By indexing these patterns, information about the sample materials, their phase state, their crystallinity and their relative orientation can be drawn out. Monitoring the behaviour of the diffraction patterns as the sample is modified (i.e. by heating) will give information about how these properties change under different conditions. The shape of the diffracted features will also provide information on the morphology. A ring-like feature, for example, is indicative of polycrystalline morphology with a random grain orientation; whereas a single spot is indicative of an ordered crystal. These aspects will be explored in depth during the presentation of results in chapters 3 and 5.

### 1.8.3 Scattering from atoms

Bragg's law permits a good understanding of the use of diffraction data to infer unit cell parameters, atomic spacing and determining the orientation of crystallographic planes in a sample. It does not, however, deal with the relative intensities of the scattered features, which can give further information about the structure of the sample under investigation.

A lattice of atoms can be understood as a map of the electron density  $\rho(\mathbf{r})$  within a particular crystal, where  $\mathbf{r}$  is a vector  $= (x\mathbf{a}_1 + y\mathbf{a}_2 + z\mathbf{a}_3)$  defining a position within that crystal. A diffraction operation with a momentum transfer  $\mathbf{Q}$  on an electron at position  $\mathbf{r}$  multiplies the wave amplitude by a phase term  $e^{-i\mathbf{Q}\cdot\mathbf{r}}$ . The total scattering amplitude is then:

$$A(\mathbf{Q}) = \int \rho(\mathbf{r}) e^{-i\mathbf{Q}\cdot\mathbf{r}} d\mathbf{r} \quad [25]$$

summed over all values of  $\mathbf{r}$ . Equation [25] holds for the general case of an individual unit cell. For a specific crystal,  $\rho(\mathbf{r})$  is in fact a convolution of the electron density in the unit cell with a series of delta functions defining the atomic positions for that material. This combination results in an expression for the scattering from a specific crystal:

$$F(\mathbf{Q}) = \sum_j^{atoms} f_j(\mathbf{Q}) e^{-i\mathbf{Q}\cdot\mathbf{r}_j} \quad [26]$$

$F(\mathbf{Q})$  is called the **structure factor** for the crystal in question, and is the sum of individual **atomic scattering factors**  $f(\mathbf{Q})$  for all  $j$  atoms in the **unit cell**, taking account of the **phase** of each scattering event.  $F(\mathbf{Q})$  applies for a crystal represented by repetition of this unit cell. We know from the previous analysis that for diffraction to take place  $\mathbf{Q}$  must be equal to  $\mathbf{G}$ . The above equations hold when this condition is satisfied.

$F(\mathbf{Q})$  is a complex number with a magnitude and phase term. Diffraction experiments measure the **intensity** of the features in a diffraction pattern against  $\mathbf{Q}$  (i.e., for a specific  $hkl$ ), but give no information about the phase of each reflection. This is the root of the **phase problem** in crystallography. The intensity is related to the square of the magnitude of  $F(\mathbf{Q})$  through the following equation:

$$I_{hkl} = |F_{hkl}|^2 P \cdot L \cdot A \quad [27]$$

This equation is in reality more complex [83], but reduces to the above for our case.  $P$ ,  $L$  and  $A$  are correction factors for polarisation, a Lorentz factor<sup>3</sup> and geometrical area correction respectively, and are applied according to Vlieg [83]. Because the indices ( $hkl$ ) describe both crystal planes in real space and reciprocal lattice vectors  $\mathbf{G}$ , when diffraction is satisfied and  $\mathbf{G} = \mathbf{Q}$ , the Fourier representation of the scattering  $F(\mathbf{Q})$  is equal to  $F_{hkl}$ .

Obtaining a complete map of the electron density in the sample, and thus, a complete map of the structure, requires resolution of the phase problem. There are various methods to achieve this but they are complex and outside the scope of this project. If the phases are known, then the electron density in a sample could theoretically be constructed by using the Fourier transform. However, this is rarely possible in practice as phase information is lost in data collection. Typically, and in the case of the current work, the solution is model dependent; measured structure factors are compared with those calculated from a model of the predicted structure. As such, in the current project, the calculation of  $|F_{hkl}|$  (i.e. the *magnitude* of  $F(\mathbf{Q})$ ) is the primary goal of analysis. *Relative* intensities of the various peaks in  $|F_{hkl}|$  can give information as to the strength of (metallographic) texture within a sample.

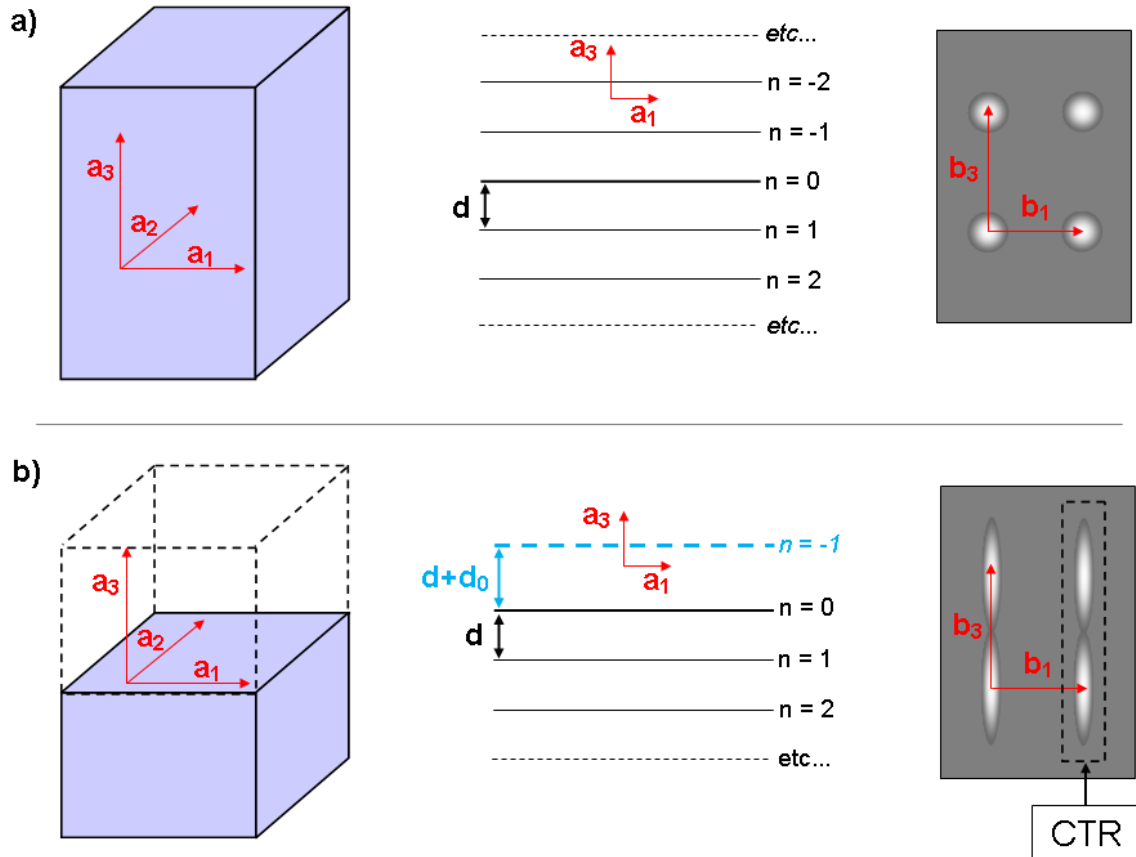
---

<sup>3</sup> The Lorentz factor is a geometrical correction for the way in which the scattered intensity, which has a finite width, intercepts the curved surface of the Ewald sphere

#### 1.8.4 Surface XRD and Crystal Truncation Rods

X-ray diffraction can be optimised for the study of surfaces and interfaces. To achieve this, the X-ray beam is aligned such that it approaches the sample at a very shallow angle. If the beam focus is suitably small, less of the **bulk** sample beneath the region of interest – i.e. the surface or interface – is illuminated, thus suppressing the scattering from this bulk region. A careful and correctly designed experiment may then be tailored such that the scattering is surface or interface sensitive. The structure factor  $F$  is then a reciprocal space representation of the structures in these regions. These techniques fall under the umbrella of **surface X-ray diffraction** (SXRD). Basic diffraction from a surface in the specular direction (refer to Figure 1-25) is often referred to as **X-ray reflectivity** (XRR).

As described in 1.8.2, diffraction from a single crystal produces a pattern of Bragg peaks at values where  $\mathbf{Q} = \mathbf{G}$ . The ideal model assumes a crystal which is infinitely large in all 3 directions, and in this scenario the Bragg peaks are point-like (although in reality, a crystal with a finite size results in Bragg peaks of finite width). This is shown in Figure 1-26a. When diffraction is performed from a crystal with a truncated surface, **streaks** of scattering appear in the direction normal to the surface, as shown in Figure 1-26b. These are termed **Crystal Truncation Rods (CTR's)**.



**Figure 1-26 – Schematic showing generation of diffraction patterns from a) an ‘infinite’ crystal and b) the same crystal but cleaved to produce a surface from which scattering takes place. The respective diffraction patterns for each situation are shown on the right hand side of the figure. In the case of b) streaks of scattering, called crystal truncation rods, are produced in the direction perpendicular to the surface and link the Bragg peaks.**

To explain how these rods arise we consider the sum from equation [25] in the  $\mathbf{a}_3$  direction only (i.e. along the normal to the sample surface). In the  $\mathbf{a}_1$  and  $\mathbf{a}_2$  directions the crystal repeats to infinity, but in  $\mathbf{a}_3$  the crystal is **truncated** at the surface. The crystal can therefore be treated as a stack of layers denoted  $n$ , whereby the truncated surface is at  $n = 0$ , separated by the layer spacing  $d$ , as shown in Figure 1-26. The scattering from this stack of layers is as follows:

$$F_{CTR} = A(\mathbf{Q}) \sum_{n=0}^{\infty} e^{i\mathbf{Q}_z d n} = \frac{A(\mathbf{Q})}{1 - e^{-i\mathbf{Q}_z d}} = \frac{A(\mathbf{Q})}{1 - e^{-i2\pi l}}$$

[28]

where  $\mathbf{Q}_z = 2\pi l/d$ ; i.e. the momentum transfer in the direction of  $\mathbf{a}_3$ , along the normal to the sample surface. The intensity, being proportional to the square modulus of the structure factor, varies as follows:

$$I_{CTR} = |F_{CTR}|^2 = \frac{A(\mathbf{Q})}{(1 - e^{-i2\pi l})(1 - e^{-i2\pi l})} = \frac{A(\mathbf{Q})}{4\sin^2(\pi l)} \quad [29]$$

This expression describes how the intensity varies in between Bragg peaks. When  $l$  is an integer, the denominator goes to zero and the intensity tends to infinity; i.e. a Bragg peak. Returning to equation [28], we define  $\mathbf{Q}_z = \mathbf{q}_z + 2\pi/d$  where the new term  $\mathbf{q}_z$  defines a small deviation from the Laue condition  $\mathbf{Q} = \mathbf{G}$ . In an infinite crystal this would result in zero intensity, but inserting it into the current expression demonstrates that the intensity is proportional to  $1/\mathbf{q}_z^2$ . This results in an intensity variation 'along' a CTR similar to the example shown in Figure 1-27 below:

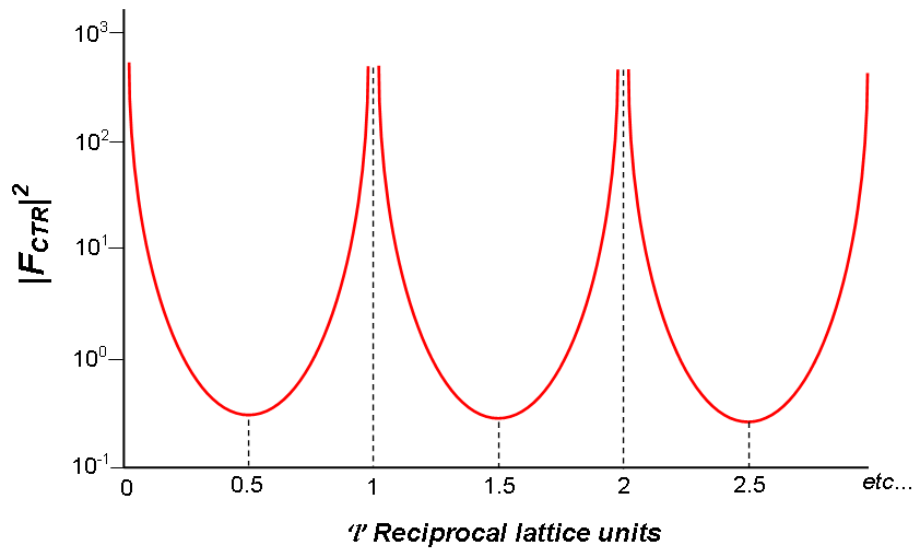


Figure 1-27 - Schematic of intensity variation along Crystal Truncation Rod

CTR's are excellent tools for the study of surfaces and interfaces due to the fact that the intensity distribution is highly sensitive to the atomic structure in these regions. This can be examined by considering an extra layer at  $n = -1$  in equation [28] with a lattice spacing in the  $\mathbf{a}_3$  direction that is different from the



bulk structure by a value  $d_0$  (see Figure 1-26b). The scattering is then formulated as follows:

$$F_{TOTAL} = F_{CTR} + F_{SURFACE} = \frac{A(Q)}{1 - e^{-i2\pi l}} + A(Q) e^{-i2\pi(1+d_0)l}$$

[30]

When  $d_0 = 0$  (i.e. the lattice spacing in the surface is the same as in the bulk) the intensity distribution is the same. However, if  $d_0 \neq 0$ , the surface term generates a different intensity distribution, which interferes with that from the bulk. The resulting  $F_{TOTAL}$  is a sum of the contributions of these profiles, examples of which are shown in Figure 1-28 below:

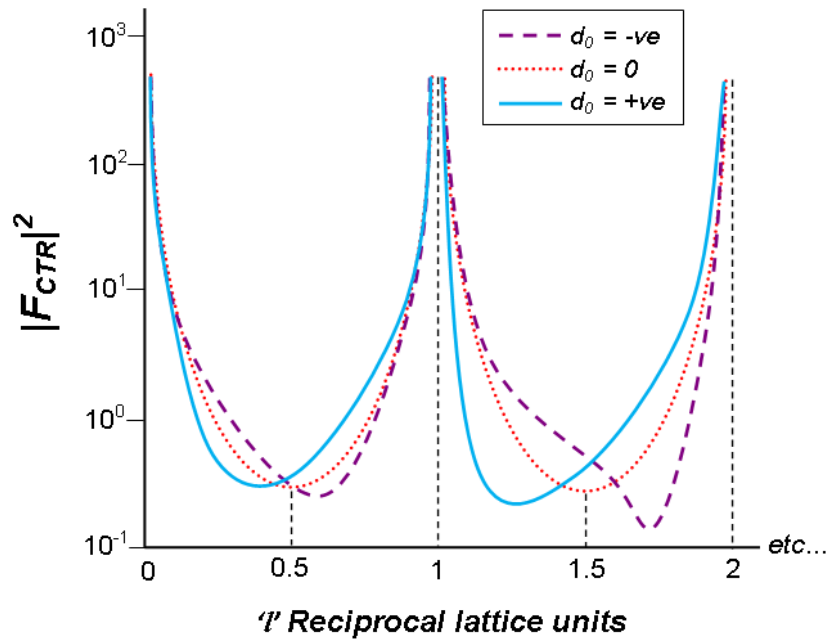


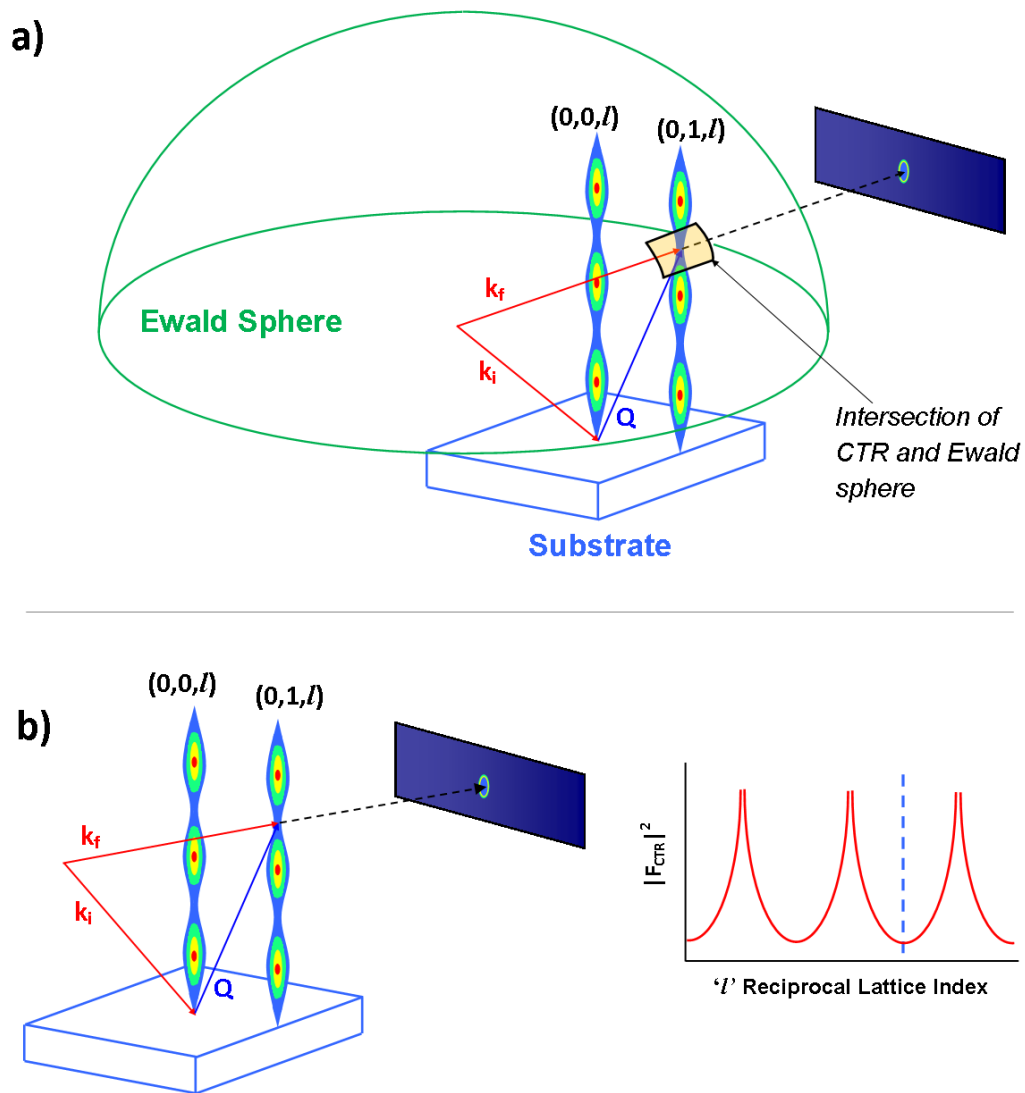
Figure 1-28 - Schematic of intensity variation to CTR from sample with extra layer at  $n = 1$

1

It is this property which renders CTRs a profitable tool for the study of surfaces. A small modification to the surface layer produces a readily observable change to the intensity profile. This is clearly of great merit to study of interfaces in the context of liquid ordering and nucleation, particularly to the case of adsorption; adsorbed atoms may effectively create a surface layer if there is good registry with the terminating plane of the substrate.

A less beneficial aspect of CTR study is the effect of surface roughness. This has the effect of reducing the intensity in the anti-Bragg positions [84], [85] which can be problematic if the signal-to-noise ratio is low; the data is obscured by and therefore is indistinguishable from background noise.

As described previously, scattering can only be recorded when the region of interest in reciprocal space intersects the Ewald sphere. Thus, in a diffraction experiment, the diffractometer must move the sample and detector simultaneously such that the origin of the Ewald sphere is moved so it intersects the rod at a different location. This process permits scanning 'up' the CTR and records the variation in intensity along it. The process is pictured in Figure 1-29.



**Figure 1-29 - Schematic indicating how CTR intensity profiles are recorded. a) indicates the condition that the diffractometer geometries must create; i.e. the Ewald sphere intersects with the CTR generated from the surface. b) indicates that the intensity profile is progressively recorded as the scan proceeds up the rod.**

Once CTRs have been collected, the analysis proceeds through a model fit procedure. Approximate models of the structure predicted within the sample are produced, from which predicted CTR profiles are generated [86]. These are compared with the experimental data, and a least-squares fitting procedure begins which, through the alteration of various parameters, aims to fit the predicted profile to the data points by modification of the model structure. A software package called ROD [86], developed by Vlieg and co-workers, is the primary tool for this process in the current project. It is described in greater depth in section 2.6.

Individual CTR's are classified by their  $(h,k)$  indices. Due to the symmetry of crystal structures, some rods will be equivalent to each other; i.e. the Bragg peaks are at the same values of  $l$  and similar intensity variation is observed between them. These are called **symmetry-equivalent** rods. The collection of numerous rods, including those at symmetry-equivalent positions, gives a higher quality data set; permitting greater confidence in the data and thus greater confidence in the resulting structure determination.

### 1.8.5 Relevance to current project

Previous studies using synchrotron X-ray scattering techniques have permitted new insight into the liquid ordering phenomena which appear to be a key aspect of the nucleation process. A large range of studies have investigated ordering at liquid surfaces [87]–[94]; in this project the interest is geared towards solid/liquid interfaces, which have been less extensively studied. Such experiments are noted to be challenging due to the deleterious effect of surface roughness [95] and background scattering from the solid [90], [96].

Depending on the material system, ordering is suggested either to impede [35], [40], [49], or to assist, the nucleation process. The previously discussed studies by Huisman *et al* [33], [97] are perhaps of greatest interest due to the author's assertion that ordering may act as a trigger for heterogeneous nucleation. This is particularly relevant as the scattering took place from a solid/liquid interface. A review by Fenter and Sturchio [98] provides extensive detail on the study of ordering in mineral-water interfaces by synchrotron X-ray scattering, highlighting the validity of surface-sensitive techniques such as CTR's. Reedijk and co-workers have used CTR's to demonstrate that ordering takes place in a variety of material systems, resulting in 'ice-like layers' in water [40], [41] and layering in liquid Sn on Ge (111) [43].

CTR's arise from all the surface Bragg peaks and are denoted by their  $(h,k)$  index. The (0,0) rod, which runs through the origin of reciprocal space, is collected using a specular scattering geometry and is thus known as the specular rod. Other rods are collected at different  $(h,k)$  indices and thus have an associated in-plane momentum transfer. According to Reedijk *et al* [40], an ordered liquid adjacent to a solid surface will contribute most strongly to CTRs with a small in-plane momentum transfer (i.e. low  $h$  and  $k$ ); conversely a completely disordered liquid will contribute only to the specular (0,0) rod. This is a useful point for the current study, suggesting efforts are best concentrated on rods such as the  $(1,0,l)$  and  $(0,1,l)$  for analysis of any ordering in the liquid state.

## 1.9 Remaining Challenges

Grain refinement in processing of Al and its alloys presents a useful practical case to explore nucleation and solidification behaviour. Theoretical and experimental studies continue to shed new insight into the exact mechanism by which this important industrial process operates; however, there remain a number of associated challenges:

1. Experiments such as those by Schumacher and co-workers [14], [27], [51], [65] using metallic glasses necessarily require post-hoc investigation, meaning the results lack *in-situ* detail of the process. Also, in metallic glass studies, all of the observed  $\text{TiB}_2$  particles appear to nucleate Al, whereas in industry it is commonly observed that less than 1% of the particles actually succeed in this task [17].
2. The use of synchrotron X-ray scattering techniques has been recently explored to examine nucleation in bulk Al with grain refiner additions by Iqbal *et al* [73]–[78]. These do give *in-situ* detail; the phase transformation is recorded and observed in real-time. However, the diffraction is here performed on a bulk sample, representative of a bulk ‘melt’; it does not specifically target the Al/ $\text{TiB}_2$  interface where nucleation occurs and thus while the formation of  $\text{Al}_3\text{Ti}$  is indicated it does not necessarily verify that it forms as a layer on  $\text{TiB}_2$  particles. More importantly, these experiments do not reveal the orientation relationship at the solid/liquid interface.
3. While  $\text{Al}_2\text{O}_3$  is readily available ‘off the shelf’ in single crystal form,  $\text{TiB}_2$  is not; single crystals are difficult and expensive to manufacture [99]. To study the Al (111) //  $\text{TiB}_2$  (001) interface therefore presents a great challenge in terms of sample preparation.
4. The Al/ $\text{TiB}_2$  system is expected to exhibit very low undercooling (<1K) [53], which presents a great challenge in terms of temperature control.

### 1.10 Aims of this work

The overall goal of this project is to explore new ways to probe interactions at a solid/liquid interface and gain useful knowledge about nucleation and solidification phenomena. Two material systems are chosen as appropriate case studies for this task:

#### 1. Al on $\text{Al}_2\text{O}_3$

- Widely studied model system
- $\text{Al}_2\text{O}_3$  readily available in single crystal form with defined orientation
- Expected to exhibit large undercooling, permitting a large 'window' of temperature over which Al can be expected to remain liquid; literature suggests between 40-50K [100] to a maximum of 175K [37], [101]
- Recent research has indicated that grain refinement of Al alloys by  $\text{Al}_2\text{O}_3$  may be possible through entrainment of surface oxides [102], [103]; this project may offer some insight into this possibility

#### 2. Al on $\text{TiB}_2$

- Highly relevant industrial case for grain refinement
- Continuing debate as to the exact mechanism of nucleation in this system
- Opportunities to explore novel methods for sample preparation and temperature control (address challenges 3. and 4. in 1.9)

Using these case studies, the intended outcomes for the project are detailed as follows:

1. Assess the feasibility of using novel X-ray scattering techniques to probe a solid ( $\text{Al}_2\text{O}_3$  or  $\text{TiB}_2$ ) / liquid (Al) interface
2. Observe and record the nucleation **undercooling** required to initiate solidification of Al against a specific crystal plane of the substrate ( $\text{Al}_2\text{O}_3$  or  $\text{TiB}_2$ )

3. Observe the **orientation relationship** which develops between solidified Al and the substrate
4. Observe changes to the material structure which arise from melting and subsequent solidification of Al (e.g. **thermal expansion**, residual **strain**)
5. Use CTR analysis where appropriate to observe modification of substrate surface structure

It is hoped that the above will lead to a better understanding of nucleation and associated phenomena.



## 2 Experiments

This section details experimental procedures, equipment and samples used to investigate the issues described in 1.10. Multiple experiments were performed during 4 individual blocks of beamtime; hereafter referred to as ‘Experiment 1’ (E1), ‘Experiment 2’ (E2); etc. This chapter describes these in full; they are detailed in brief below.

Experiment	Primary Goals	Samples and Materials	Why changes from previous experiment?
<b>E1:</b> Diamond Light Source Beamline <b>I07</b> Experimental Hutch 1	<ol style="list-style-type: none"> <li>1. Characterisation</li> <li>2. Monitor Al/Al<sub>2</sub>O<sub>3</sub> interface structure</li> <li>3. Assess nucleation undercooling</li> <li>4. Observe orientation relationships on solidification</li> </ol>	Sputter-deposited pure <b>Al</b> layer <i>on</i> 10 x 10 x 1mm <b>Al<sub>2</sub>O<sub>3</sub> (0001)</b> single crystal substrate	<i>First attempt at experiment:</i> <ol style="list-style-type: none"> <li>1. Gain knowledge and understanding of beamline</li> <li>2. Feasibility study for intended experiments</li> <li>3. Data collection</li> </ol>
<b>E2:</b> DLS Beamline <b>I07</b> EH1	<ol style="list-style-type: none"> <li>1. Commissioning micro-furnace</li> <li>2. Monitor Al/Al<sub>2</sub>O<sub>3</sub> interface structure</li> <li>3. Assess nucleation undercooling</li> </ol>	Sputter-deposited pure <b>Al</b> layer <i>on</i> 3mm x 1mm ‘disc’ <b>Al<sub>2</sub>O<sub>3</sub> (0001)</b> single crystal substrate	<ol style="list-style-type: none"> <li>1. Heater device developed to allow extremely fine control over temperature</li> </ol>
<b>E3: Part 1</b> ESRF Beamline <b>ID03</b> EH2	<ol style="list-style-type: none"> <li>1. Revisit undercooling study from E1 and clarify validity of the recorded values</li> <li>2. Record high quality CTR data</li> <li>3. Explore the use of evaporation to deposit Al <i>in-situ</i></li> </ol>	<b>X:</b> Sputter-deposited pure <b>Al</b> layer <i>on</i> 10 x 10 x 1mm <b>Al<sub>2</sub>O<sub>3</sub> (0001)</b> single crystal substrate  <b>W:</b> Clean 10x10x1mm <b>Al<sub>2</sub>O<sub>3</sub></b> substrate	<ol style="list-style-type: none"> <li>1. Problems with wetting with E2 samples</li> <li>2. Move to a new and unfamiliar facility</li> </ol>
<b>E3: Part 2</b> ESRF Beamline <b>ID03</b> EH2	<ol style="list-style-type: none"> <li>1. Characterisation</li> <li>2. Monitor Al/TiB<sub>2</sub> interface structure</li> <li>3. Assess nucleation undercooling</li> <li>4. Observe orientation relationships that form on solidification</li> </ol>	<b>A:</b> Sputter-deposited pure <b>Al</b> layer <i>on</i> sputter-deposited <b>TiB<sub>2</sub></b> layer <i>on</i> prepared 10 x 10 x 2mm <b>Mo</b> substrate	<ol style="list-style-type: none"> <li>1. Attempt to investigate the Al/TiB<sub>2</sub> system.</li> <li>2. Investigate success of methods used to prepare TiB<sub>2</sub> samples.</li> </ol>
<b>E4</b> DLS Beamline <b>I07</b> EH2	<ol style="list-style-type: none"> <li>1. Characterisation</li> <li>2. Monitor Al/TiB<sub>2</sub> interface structure</li> <li>3. Obtain evidence for Al<sub>3</sub>Ti</li> <li>4. Assess nucleation undercooling</li> <li>5. Observe orientation relationships that form on solidification</li> </ol>	<b>V:</b> Sputter-deposited <b>TiB<sub>2</sub></b> <i>on</i> <b>Ti</b> interlayer <i>on</i> prepared 10 x 10 x 2mm <b>Mo</b> substrate  <b>VIII:</b> As above but with sputter-deposited pure Al layer on top	<ol style="list-style-type: none"> <li>1. Focus on industrially relevant case</li> <li>2. Ensure desired (001) texture achieved in TiB<sub>2</sub> samples</li> <li>3. Investigate evaporation of Al onto TiB<sub>2</sub></li> </ol>

**Table 2-1 – Brief summary of experiments E1 – E4**

## 2.1 General methodology

The use of synchrotron X-ray radiation presents opportunities for novel approaches to investigation of nucleation and grain refinement. Experimental studies of these phenomena are usually limited to post-hoc investigations via microscopy [14], [27], [51], [65]. Synchrotron X-ray techniques offer the opportunity to study them *in-situ* and gain unprecedented insight into the behaviour of the materials involved, permitting focus directly on the interface between the Al and substrate. The aim is to gain a physical description of the nucleation process by studying liquid aluminium in contact with a substrate surface.

Synchrotron X-ray radiation is appropriate in this case for a number of reasons (also see 1.8.1):

- The high intensity of the beam allows data to be collected rapidly and resolve information even from weakly scattering elements of a sample. A high intensity is a requirement for collecting high-quality Crystal Truncation Rod (CTR) data; CTR's are valuable tools in the study of interface structures and as such are essential for this work.
- The beam is highly collimated, has high stability and is monochromatised; thus the scattering is sensitive to structures at micro- to atomic-scale.
- In a practical sense, synchrotron beamlines offer the ability to investigate samples in a range of environments; permitting the collection of data *in-situ* over the course of the heating/cooling processes required to instigate solidification.
- The beamlines visited for this study are specifically designated for the study of surfaces and interfaces, which are of interest in study of nucleation.

The basic methodology of the experiments described herein is as follows:

1. A sample of the nucleating substrate is prepared to an appropriate size (approx. 10mm x 10mm footprint). This guarantees that the available surface

for nucleation exceeds the critical radius  $r^*$ , but is a suitable size for existing equipment at I07 and ID03.

2. The surface of the substrate ( $\text{Al}_2\text{O}_3$  or  $\text{TiB}_2$ ) is prepared to achieve the best possible flatness, smoothness, and cleanliness.
3. Pure aluminium is deposited onto the prepared surface.
4. At beamline, the sample is mounted into the appropriate sample chamber to allow it to be moved into the X-ray beam.
5. Beam alignment is performed such that X-ray scattering is collected from the region of the sample comprising the interface between the aluminium and the substrate.
6. Heating and cooling is applied to the sample to melt the aluminium and thus generate an interface between the solid nucleating substrate and the liquid aluminium.
7. X-ray scattering data are collected before, during and after these heating and cooling processes.
8. Scattering data are analysed to explore the structural and morphological behaviour of the aluminium, the substrate, and of the interactions between the two.

The general setup is indicated visually in Figure 2-1:

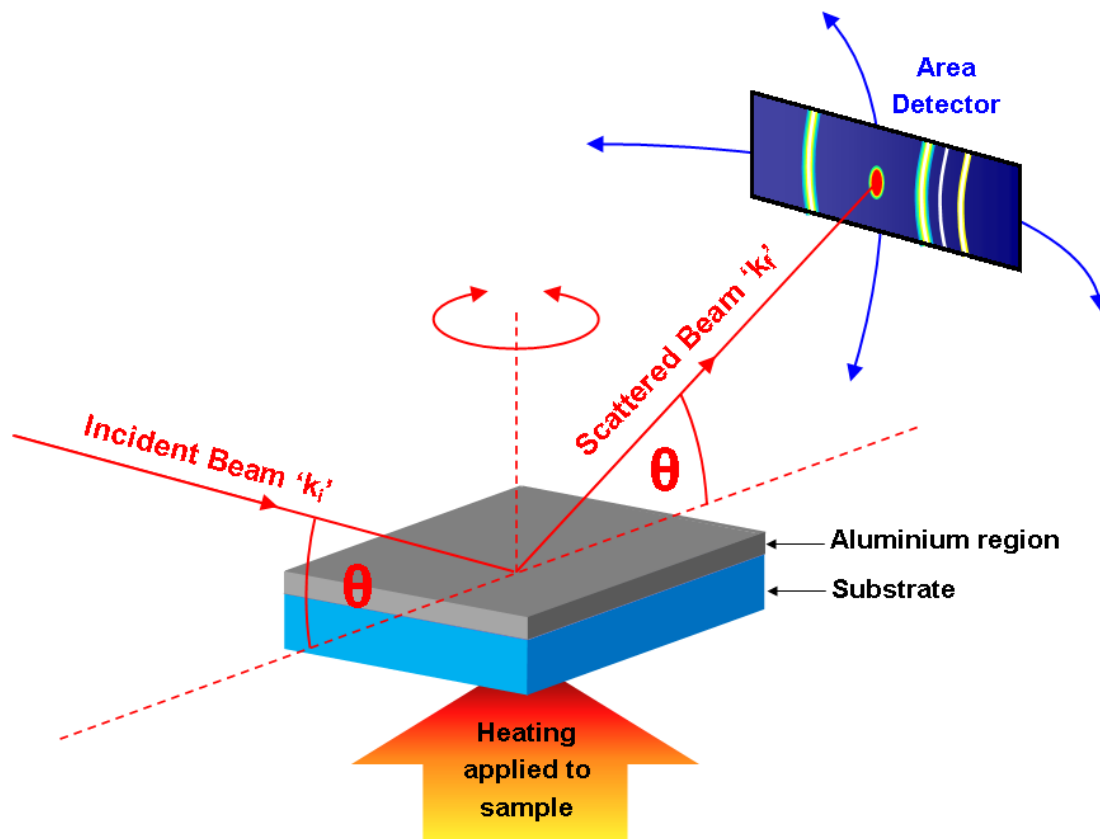


Figure 2-1 – General overview of experimental setup

The 'area detector' is a CCD array which is sensitive to and thus facilitates the collection of scattered X-rays. The sample and detector are mounted on a device called a diffractometer, which a) permits movement of the sample and detector to permit collection of scattering in all directions and b) ensures that the correct conditions for X-ray scattering (i.e. Bragg's law) are maintained throughout a given experiment.

Diffraction patterns comprise reflections corresponding to different  $(hkl)$  planes within the sample materials. These serve as an indicator of the materials present and the relative orientations of their crystal structures. Applying thermal profiles to the samples will change the material structures; and in turn the diffraction patterns. As such, the presence of materials at different temperatures, their phase, and their relative orientations; can all be monitored throughout the thermal profile by observing changes to the diffraction pattern.

## 2.2 Beamlines

The primary location for experiments over the course of the project was beamline I07 at Diamond Light Source [104] ; E1, E2 and E4 all took place here. I07 is the designated 'surface and interface diffraction' beamline and as such was the obvious choice for this project. Low incident angle techniques were considered to be of particular importance, as these are particularly sensitive to changes at the interface, so had potential to reveal in-plane structure. General surface X-ray diffraction (SXRD) is a useful characterisation tool for identification of different phases and structures within the samples, and would reveal more 'out of plane' detail.

I07 comprises two experimental 'hutches' allowing for the setup of different sample environments. Pilatus 100k area detectors were available in both hutches allowing for exploration of a wide region of reciprocal space.

E1 and E2 were operated in experimental hutch 1 of I07. This hutch permits users to run experiments with a wide range of sample environments. In this case, the samples were mounted within a 'baby' chamber; a small vacuum chamber which allowed for off-line setup of samples and equipment. For E1, the sample was fixed to a 'transfer plate' allowing it to be brought into contact with an in-built sample heater without compromising the high vacuum ( $\sim 6.5 \times 10^{-9}$  mbar) established prior to beamtime. For E2, the in-built heater was replaced with an in-house designed heater device (see 2.4), in an attempt to facilitate finer control over sample temperature. The baby chamber itself was topped with a beryllium dome to allow penetration of the X-ray beam to the sample surface and exit of the scattered X-rays. Because of the low density and atomic mass of beryllium, it permits the transit of X-rays without significant attenuation; any scatter which is produced is weak and easily distinguishable from other materials.

Experiment E3 took place at beamline ID03 of the European Synchrotron Radiation Facility (ESRF) in Grenoble, France. ID03 is the effective equivalent

of I07 at this facility, designated as the ‘surface diffraction beamline’ and offering the same range of scattering techniques [105].

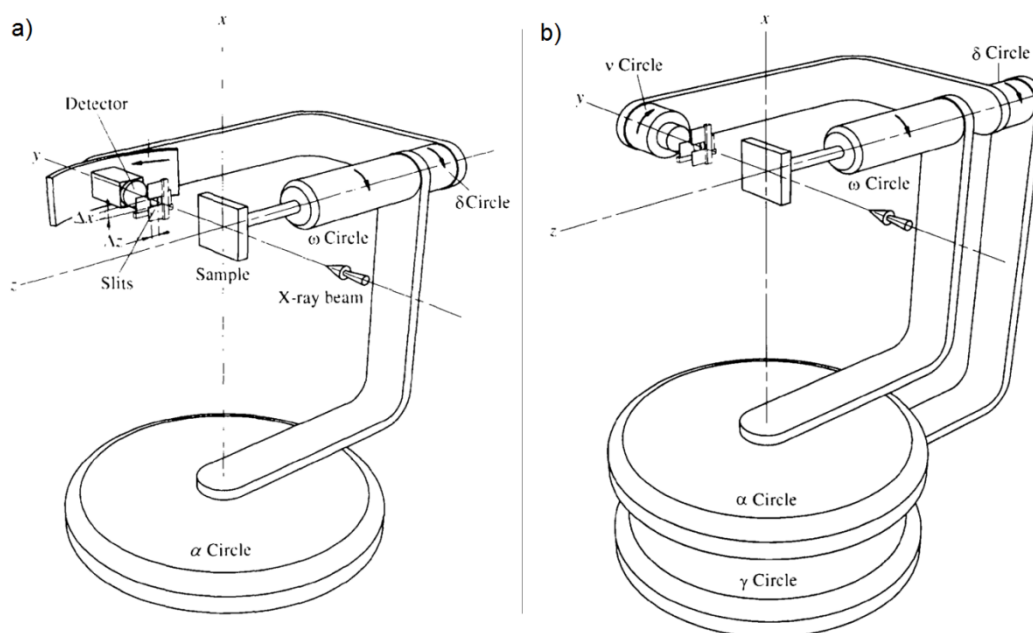
For both E3 (at ID03) and E4 (at I07) experiments took place using the purpose-built Ultra High Vacuum (UHV) chambers, which are specifically designed to facilitate experiments at very high vacuum ( $\sim 10^{-9}$  mbar). Scattering from airborne elements is effectively eliminated, and the extremely low pressure reduces (though does not eliminate) the potential for sample oxidation. For both E3 and E4, samples were directly mounted to chamber-specific sample heaters. Compared with the baby chamber used in the preceding experiments, the UHV chamber approach affords less flexibility in terms of sample positioning but offers the benefits and reliability of a standardised setup.

There are slight differences between each of the diffractometers used in the experiments; i.e. in experimental hutches 1 & 2 at I07 and in experimental hutch 2 at ID03. The designations are described in Table 2-2. The term ‘circle’ in this context refers to the individual axes of rotation about the sample or detector positions.

<b>Beamline/Hutch</b>	<b>Diffractometer</b>	<b>Experiment</b>
I07/EH1	2+3 circle – used horizontal scattering geometry for E1 and vertical scattering geometry for E2	E1, E2
I07/EH2	2+3 circle – horizontal scattering geometry	E4
ID03/EH2	z-axis diffractometer – horizontal scattering geometry	E3

**Table 2-2 - Diffractometer specification**

Figure 2-2 shows schematically the slight differences between these diffractometer types:



**Figure 2-2 – Schematic representations of a) z-axis and b) (2+3) circle diffractometers. The geometries are fundamentally similar, the only differences being that for the (2+3), a v-circle is added for the detector azimuth, and the  $\gamma$ -circle rotates the whole detector arm rather than just the detector itself. Reproduced from [106]**

The z-axis and (2+3) diffractometers are in fact special cases of the classic six-circle geometry, the corrections for which are described fully by Vlieg [83] and are applied to data accordingly. For the purposes of this study the differences between the various geometries are of little consequence; rotations about the various angles would have the same effect in either of the above geometries or in the six-circle. Indeed, the additional v-circle on the (2+3) is not used in these experiments; thus the differences between the two types are trivial for the current work.

It should also be noted that a 6-axis mounting called a hexapod is used at both I07 and ID03, onto which the sample is mounted. This allows for minor corrections to the sample position and facilitates rocking scans used for initial sample alignment. It does not affect the diffractometer geometry directly, but of course is accounted for in later calculation.

The following figures are photographs from the experiments themselves. These are included to assist the reader in understanding the diffractometer geometry.

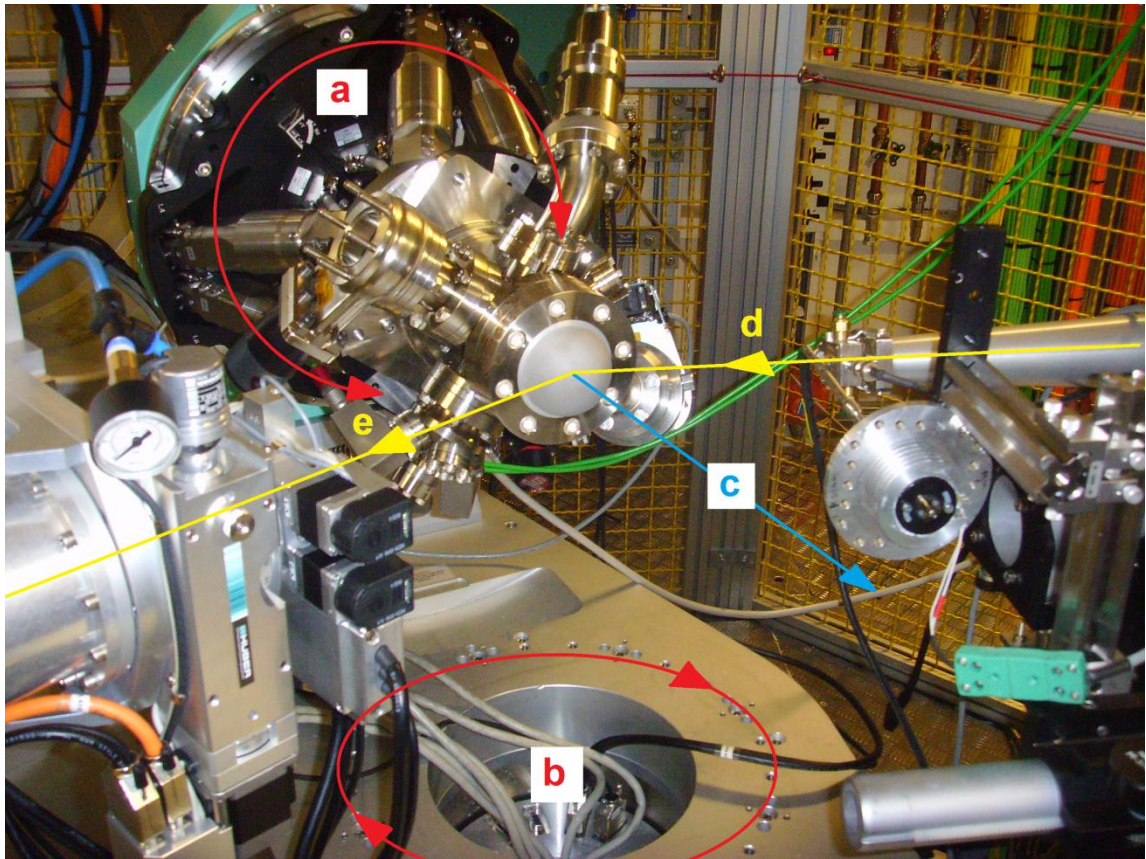
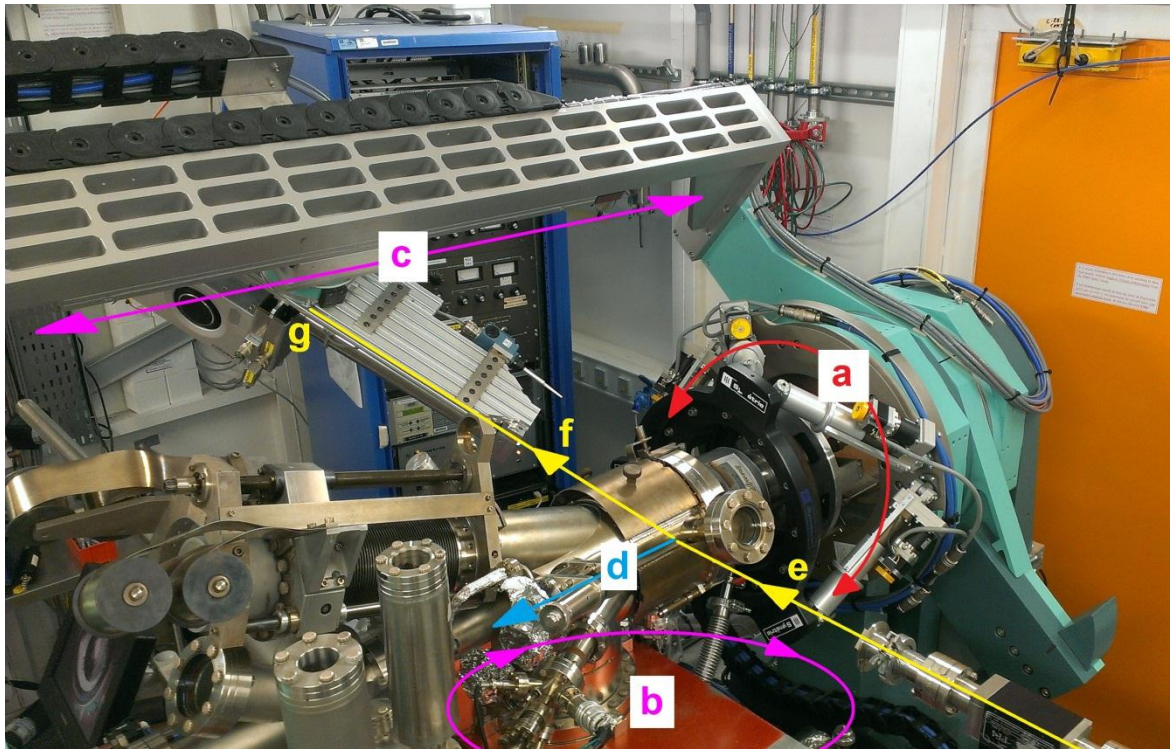


Figure 2-3 – Sample position for E1 at I07: a)  $\delta/\omega$  rotation circle b)  $\alpha/\gamma$  rotation circle c) sample normal d) X-ray beam in e) diffracted X-ray beam out (to detector, out of shot).

Refer to Figure 2-2 to clarify alignment of rotation circles.





**Figure 2-4 - Sample position for E3 at ID03: a)  $\delta/\omega$  rotation circle b)  $\alpha$  rotation circle c) detector moves along this linear track and is rotated in place to create  $\gamma$  rotation d) sample normal e) X-ray beam in f) diffracted X-ray beam out to g) detector. Refer to Figure 2-2 to clarify alignment of rotation circles.**

## 2.3 Materials and Sample Preparation

In the present study two key material systems were identified:

1. Al/Al<sub>2</sub>O<sub>3</sub>. This system was identified as a key model system in literature, having been shown to exhibit atomic-scale layering for Al in the liquid state [1,2]; a potential precursor to nucleation in which there is significant interest. The most important aspect of this system, however, is the expectation of high undercooling between Al liquid and solid Al<sub>2</sub>O<sub>3</sub>. Al<sub>2</sub>O<sub>3</sub> is a relatively ineffective nucleant for crystalline Al and undercooling as high as 175K has been observed [37]. As such, the use of this material system affords a large 'temperature window' within which to work.
2. Al/TiB<sub>2</sub>. This is the system of greater interest in an engineering context. As described in the introduction, TiB<sub>2</sub> particles are an extremely important component in processing of aluminium. The mechanism through which they initiate (or otherwise) the nucleation of crystalline aluminium remains a matter of considerable debate [14], [53], [62], [63]. It is hoped that these experiments will reveal new information about this system, contributing to the increasing body of knowledge surrounding this important industrial process. The undercooling obtained for nucleation of crystalline Al on TiB<sub>2</sub> is expected to be small (<1K) so this system will present a greater challenge in terms of temperature control.

Sample preparation differed for each experiment, and it is sensible to discuss these individually.

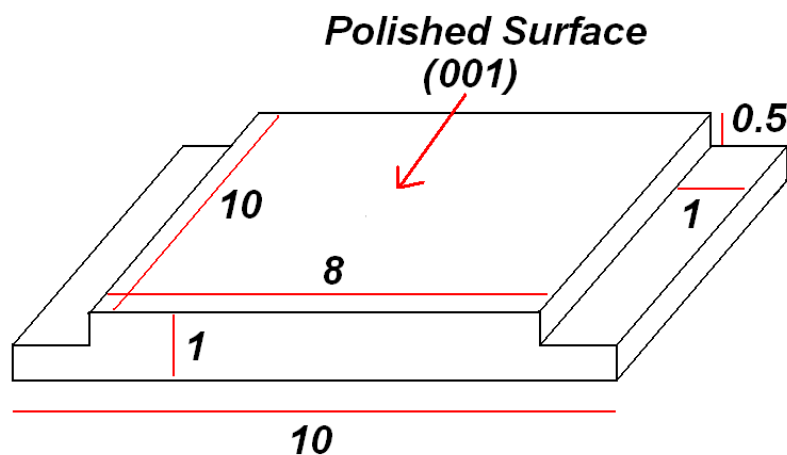
### 2.3.1 Experiment One

E1 was the initial study and the author's first experience of synchrotron X-ray facilities. The Al/Al<sub>2</sub>O<sub>3</sub> system was used. Single crystals of alumina – otherwise termed sapphire – were used, permitting a specific crystal plane to be chosen for the substrate. For this study, the crystallographic orientation of the samples was chosen such that the basal or 'C' plane (001)<sup>4</sup> was aligned with the substrate surface. Single crystal Al<sub>2</sub>O<sub>3</sub> substrates were supplied by Surfacenet

---

<sup>4</sup> Or (0001) in the 4-index Miller-Bravais system, preferred in some literature

GmbH and grown using the Czochralski method along the [001] direction such that the top surface was aligned with the (001) basal plane of the  $\alpha\text{-Al}_2\text{O}_3$  unit cell. The relative orientation of the [001] axis and the normal to the substrate surface was subject to a tolerance of  $\pm 0.5^\circ$ . The size of the substrates was 10x10x1mm; with 1mm ‘steps’ machined into two sides to allow the sample to be mounted firmly. These steps ensure that samples can be held in place while ensuring that the working surface remains proud of any clamping or fixing device. This allows the X-ray beam a direct path to the working surface at any angle of approach or sample rotation. A schematic of the basic sample geometry is shown in Figure 2-5.

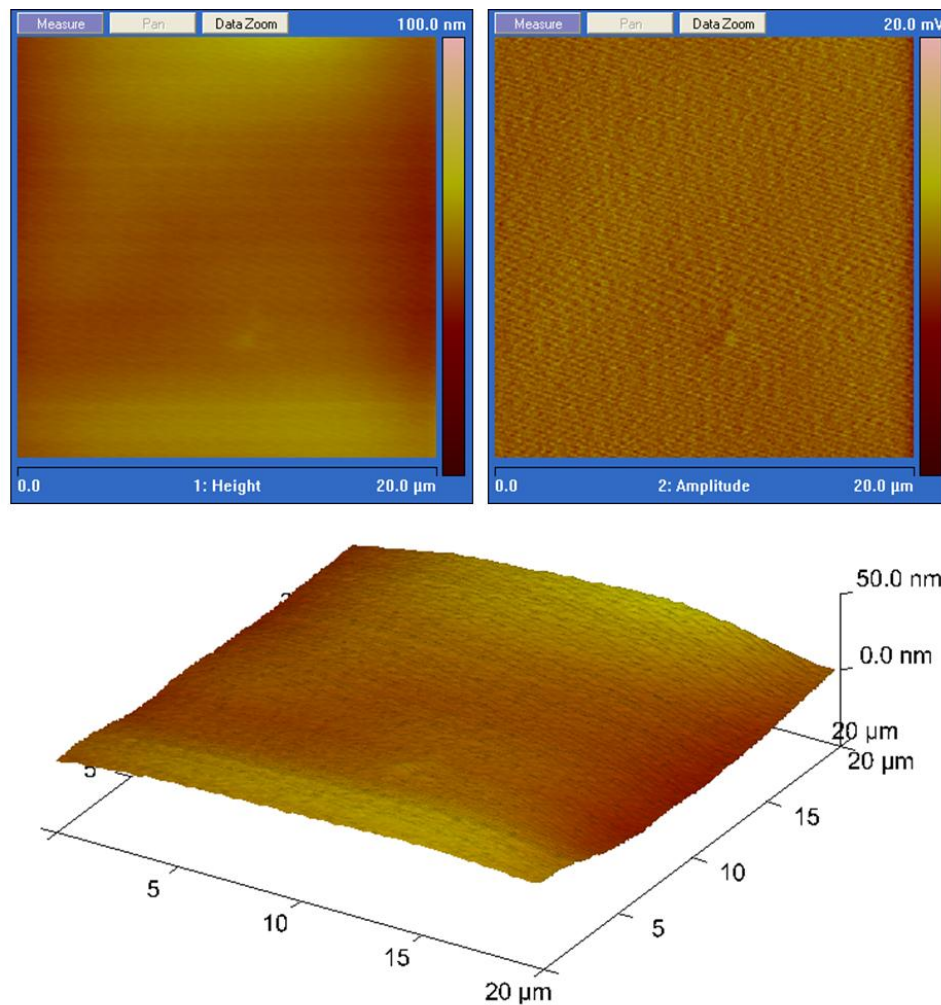


**Figure 2-5 – Basic substrate geometry. Dimensions in mm**

Taking account of the steps, the resultant working surface of the substrate was sized 8x10mm. This surface was chemo-mechanically polished leaving roughness only on nano-metre scale ( $R_a < 1$ ), confirmed by AFM investigations<sup>5</sup> shown in Figure 2-6. Minimal interface roughness is desirable for successful diffraction experiments. Various annealing schedules to further improve the surface quality were investigated based on study of supporting literature [107]–[110]. Overall, these did not produce significant improvement over the as-received samples. However, it was noted that a 20h anneal in air did consistently reduce the sharpness of peaks in the surface profile; thus the final sample was prepared in this way prior to the next stage of sample preparation.

<sup>5</sup> Veeco Dimension 3100 Scanning Probe Microscope, Advanced Microscopy Centre, University of Leicester

It was noted that while HRTEM studies on this material system were able to focus on regions of atomic flatness [5], [6], [33] this was neither achievable over samples of this size nor would it be representative of inoculant and/or oxide surfaces in real scenarios [102]. Roughness at the interface would not prevent or preclude the collection of X-ray scattering data, but would require consideration in further analysis and in comparison with the HRTEM studies [5], [6].



**Figure 2-6 – AFM investigation of E1 Al<sub>2</sub>O<sub>3</sub> single crystal (001) sample surface.**

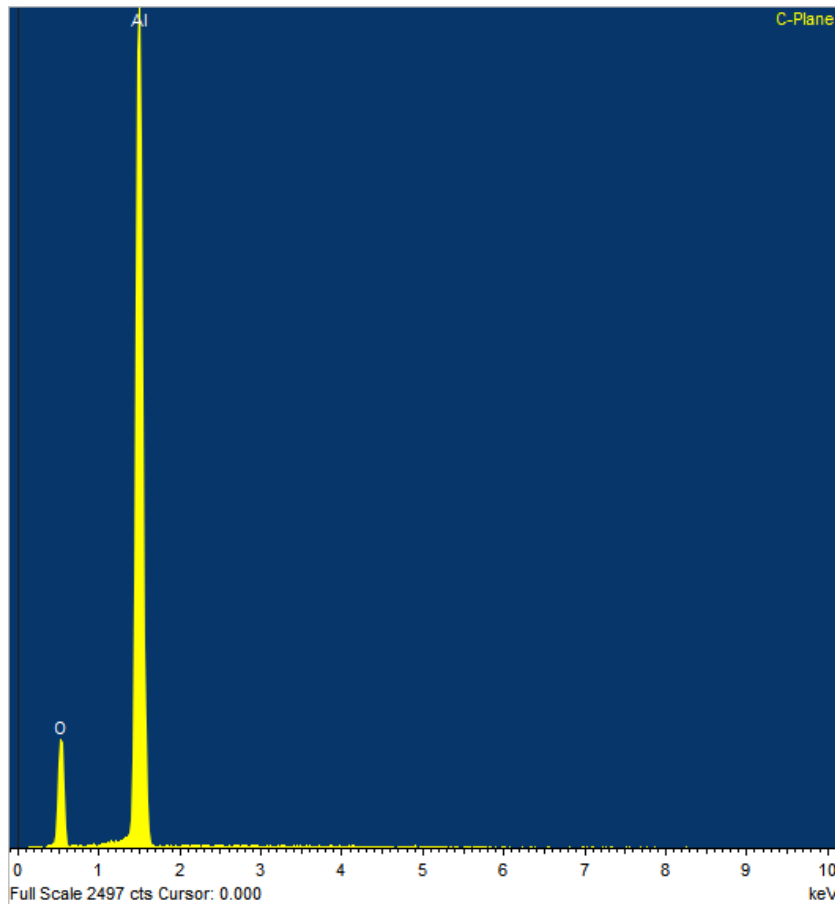
The introduction of liquid aluminium to the substrate surface presented a difficult problem. Studies of wetting dynamics between Al<sub>2</sub>O<sub>3</sub> and Al mostly used sessile drop apparatus to directly introduce liquid Al onto the substrate surface [111]–[114] but it was not feasible to incorporate this into the existing beamline vacuum equipment in a timely manner. Instead, a simpler approach was proposed. A layer of pure Al was sputter-deposited onto the Al<sub>2</sub>O<sub>3</sub> substrate

surface using a d.c. magnetron sputtering system. At the beamline, the Al/Al<sub>2</sub>O<sub>3</sub> sample would be mounted on a small sample heater, which would be used to heat the sample such that the Al layer would melt, forming a liquid drop or droplets on the Al<sub>2</sub>O<sub>3</sub> surface thus creating the interface between the two materials. Apart from thermal expansion, the Al<sub>2</sub>O<sub>3</sub> would be unaffected by the heating; its melting temperature of ~2072°C [115] being well above the expected 660.4°C [116] for pure Al. The benefit of sputtering the Al layer is that it is performed under vacuum, avoiding – though not preventing – oxidation of the Al adjacent to the Al<sub>2</sub>O<sub>3</sub> surface, and rendering the deposition a relatively clean process. A thin (1-5nm) oxide passivation layer would form on the final exposed Al surface. The overall Al layer thickness would need to be significantly larger than this, such that the passivation layer would be remote from the Al/Al<sub>2</sub>O<sub>3</sub> interface under investigation, and avoid contributing to the scattering. However, the layer would also need to be sufficiently thin that the X-ray beam would not be completely attenuated by the Al.

Al<sub>2</sub>O<sub>3</sub> substrates were prepared prior to deposition by cleaning in ultrasonic baths using alkali wash followed by ethanol. Sputter deposition took place under argon working gas pressure of  $1 \times 10^{-2}$  mbar; the base pressure of the system was  $\sim 6 \times 10^{-7}$  mbar to further minimise the potential for contamination. For deposition itself a high purity (5N) Al target was operated at 120W. An in-built crystal thickness monitor (XTM) indicated a deposition rate of approximately 2.7nm/s<sup>6</sup> and deposition continued until a thickness of ~500nm was achieved. This thickness was chosen to obtain a quantity of material sufficient to form a liquid region of reasonable size upon melting whilst ensuring that the X-ray beam would not be completely attenuated as it travelled through the sample. Post-deposition EDX analysis detected only Al and O in the sample – this primarily indicated the purity of the layer and the lack of external impurities – clearly the technique would not distinguish between the Al and O in the substrate and sputtered layer. Figure 2-7 shows the EDX profile.

---

<sup>6</sup> The accuracy of the XTM was later noted to be somewhat limited; as such the quoted values may not be entirely accurate. The intention to deposit a suitably thick layer for effective melting was nonetheless achieved.



**Figure 2-7 - EDX analysis of the E1 sample, confirming presence of Al and O and lack of impurities**

### *2.3.2 Experiment Two*

For E2, a small heater device was developed (described in 2.4). This was designed to accommodate new  $\text{Al}_2\text{O}_3$  samples, but due to time and financial restrictions substrates were instead prepared from existing pieces of single crystal  $\text{Al}_2\text{O}_3$  which had been purchased for testing purposes prior to E1. A diamond core drill was used to machine discs of 2.8mm diameter and 1mm thickness; these were then cleaned in alkali wash followed by ethanol before deposition of Al following the same procedure as in 2.3.1. Samples representing both C-plane (001) and R-plane (-11-2) orientations of  $\text{Al}_2\text{O}_3$  were prepared.

### *2.3.3 Experiment Three*

Prior to E3 it was decided that an attempt would be made to investigate the Al/TiB<sub>2</sub> system alongside the present Al/ $\text{Al}_2\text{O}_3$ . For the latter system the sample

from E1 was prepared for re-use; first an etching process<sup>7</sup> was used to remove residual Al from the surface, followed by an alkali wash/ethanol cleaning process. After annealing, Al was re-deposited following the sputtering process described in 2.3.1 to a thickness of  $\sim 5\mu\text{m}$ ; an increased thickness compared to the E1 samples as results had indicated the attenuation of the X-ray beam would be minimal.

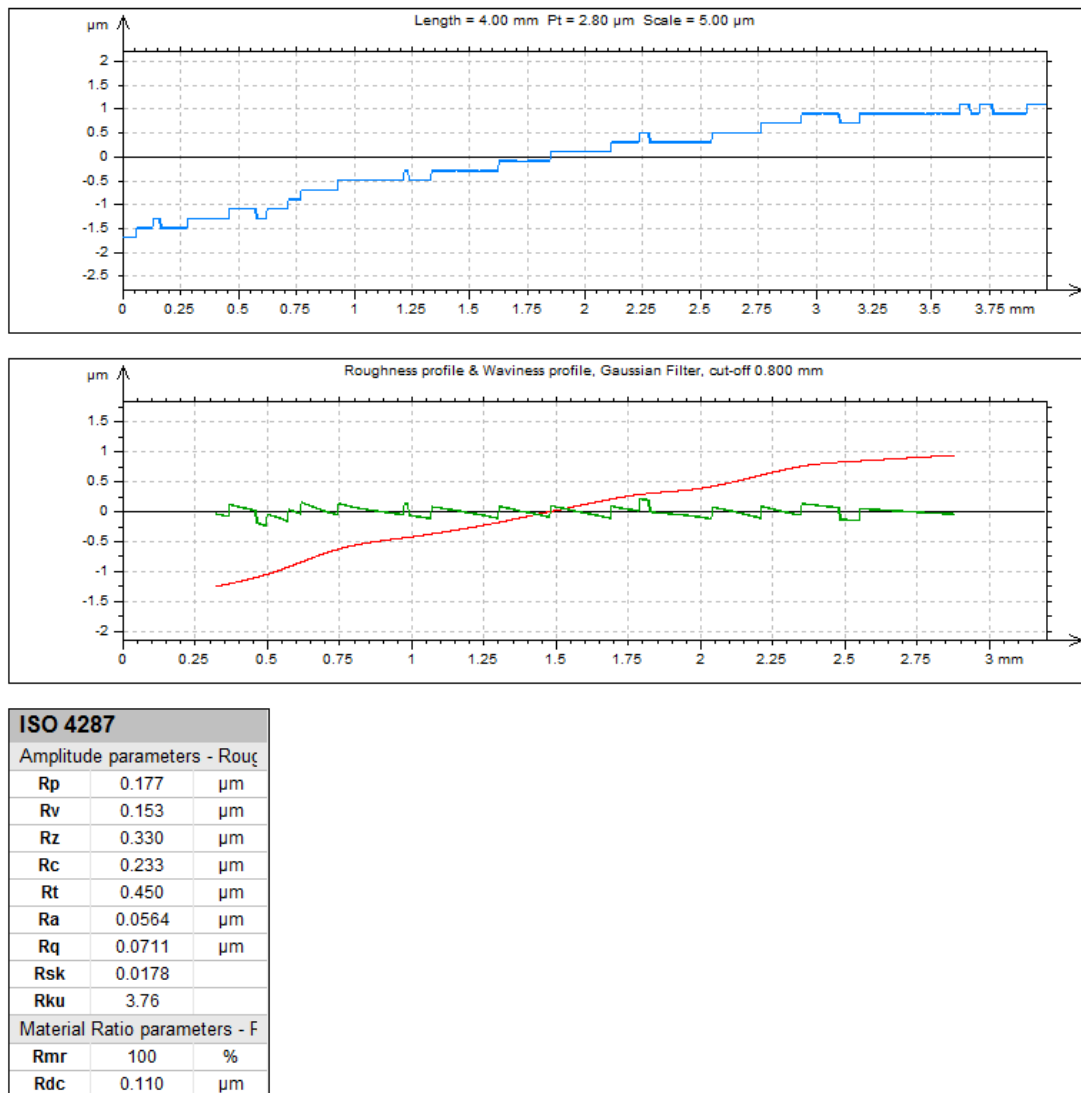
For the  $\text{TiB}_2$  sample, a different approach was required. Despite indications that it was possible to grow single crystals of  $\text{TiB}_2$  [99] these were not commercially available within budget. As discussed in section 1.7, TEM studies showed that crystalline Al nucleated preferentially on the (001) basal plane of the  $\text{TiB}_2$  particles. Various literature [117]–[121] regarding sputter deposition of  $\text{TiB}_2$  (for applications such as hard tool coatings) indicated that the deposited material would develop a strong (001) texture. The initially deposited material would form a fine grained region of a mixed texture; as the thickness increased the (001) texture would develop, suggested to be due to the fast growth rate along the [001] direction [117]. The texture development also appeared to be reasonably independent of sputtering parameters [117], [119]. It was thus suggested that a suitable sample could be made by sputter depositing  $\text{TiB}_2$  such that the surface would have a (001) texture and approximate the characteristics of the (001) faces of actual boride particles. While a single crystal substrate would be preferable, and would permit the use of more complex diffraction techniques, this approach was considered to be a practical way to investigate the problem in hand.

Based primarily on the work of Berger *et al* [117]–[119], [122] sputter deposition of  $\text{TiB}_2$  was performed to create samples for E3. The boride material was deposited onto molybdenum substrates prepared by mirror polishing of the top surface followed by the alkali wash/ethanol cleaning process. Surface profilometry measurements indicated excellent smoothness was achieved ( $R_a < 0.06\mu\text{m}$ ) as shown in Figure 2-8.

---

<sup>7</sup> As recommended by Pi-Kem, a solution of 3 parts  $\text{HNO}_3$  and 1 part  $\text{HCl}$  was used to etch and remove residual Al from the crystal substrate





**Figure 2-8 - Surface Profilometry measurements on Mo substrates prepared for E3**

Substrate geometry was fundamentally similar to that of the Al<sub>2</sub>O<sub>3</sub> samples - i.e. a top surface of approx. 8x10mm with 'steps' machined into opposing sides for clamping. The thickness of the pieces was approximately 2mm. Mo was selected for its ready availability and because, being a single element, the resulting diffraction signal would be less complex and simpler to index than other possibilities (cemented carbide or high-speed steel). The TiB<sub>2</sub> sputtering target was 99.5% pure and operated at 120W for the course of the deposition; attempts to operate it at higher power caused cracks to appear, though it was still functional. Due to a non-functioning XTM an educated assessment of the deposition rate was made based on parameters used in other studies [117]–[119], [122]. A rate of ~1nm/s was assumed, resulting in an *expected* layer



thickness of  $\sim 7\mu\text{m}$  after 2 hours deposition<sup>8</sup>. Post deposition EDX detected Ti on the surface, confirming the presence of  $\text{TiB}_2$  (boron, having low atomic mass, is not readily detectable by EDX).

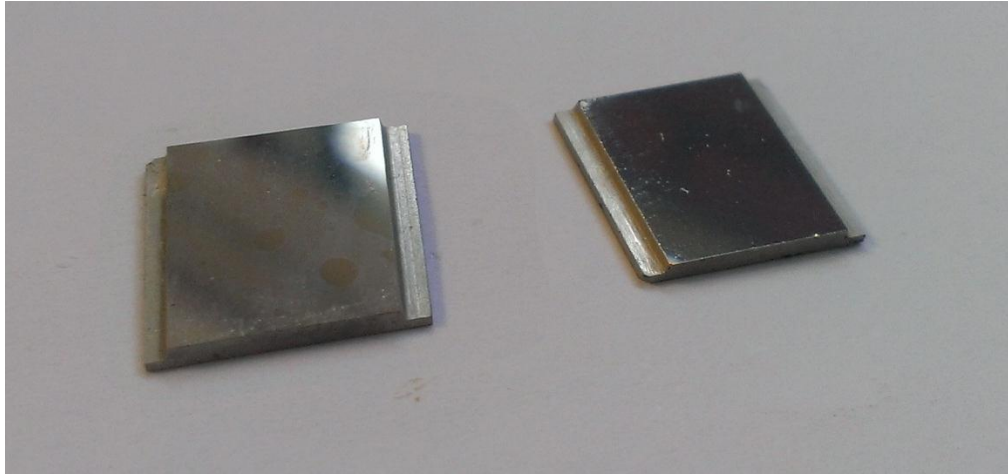
Of interest in the work of Berger *et al*/ was the application of a bias voltage to the substrates during deposition, particularly the improvement in coating adherence and residual stress achieved through the use of a positive bias [119]. The coater was set up to accommodate this by attaching a bias lead to an Al plate to which the substrates were mounted. A positive bias of +10V was applied over the course of the  $\text{TiB}_2$  deposition. The literature suggested around +50V, however it became apparent that the power supply used did not have sufficient capacity to dissipate the excess charge generated by the sputtering plasma, and +10V appeared to be a 'safe' value.

Following the completion of the  $\text{TiB}_2$  'substrates' the coater was set up to deposit a layer of Al on the surface as before. The Al deposition again followed the same procedure as in 2.3.1; this time using a target power of 150W. The deposition rate was assumed to be  $\sim 0.7\mu\text{m}/\text{min}$  resulting in a final assumed Al layer thickness of  $\sim 10\mu\text{m}$  after 15 minutes.

The following image shows the final prepared samples for E3, denoted sample 'X' (Al on  $\text{Al}_2\text{O}_3$ ) and 'A' (Al on  $\text{TiB}_2$ ). This nomenclature will be revisited in the results chapters.

---

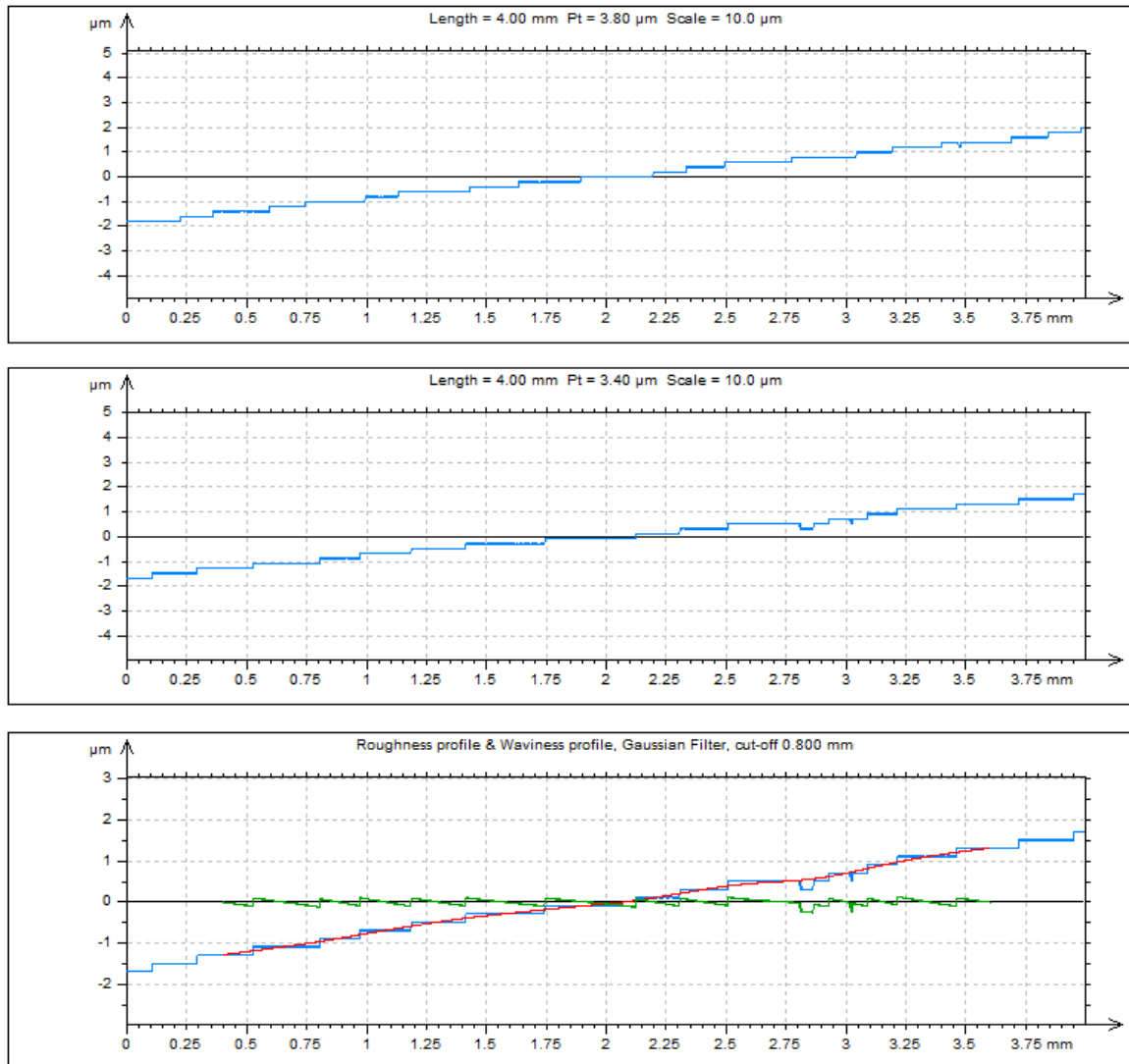
<sup>8</sup> Characterisation at E3 indicated this thickness may have been significantly less than expected – further detail in 2.3.4



**Figure 2-9 - Samples prepared for E3. Left - sample X, Right – sample A**

#### *2.3.4 Experiment Four*

For E4 efforts were concentrated entirely on the Al/TiB<sub>2</sub> system. Results from E3 had indicated that the TiB<sub>2</sub> layer had in fact retained a mixed texture (with a slight (101) bias) despite indications from literature that the (001) texture development should be independent of sputtering parameters. It was suggested that the deposited thickness may simply not have been sufficient to allow the development of the (001) texture; the assumed deposition rate of ~1nm/s was likely over-estimated, so this TiB<sub>2</sub> deposition was allowed to run for a longer time to encourage texture development to occur. As in E3, Mo pieces were used as substrates for TiB<sub>2</sub>; these pieces were prepared through machining, polishing and cleaning as detailed in 2.3.3, and exhibited similarly smooth surface profiles ( $R_a < 0.05\mu\text{m}$ ), as shown in Figure 2-10.



ISO 4287		
Amplitude parameters - Roughness		
Rp	0.113	μm
Rv	0.110	μm
Rz	0.223	μm
Rc	0.219	μm
Rt	0.390	μm
Ra	0.0439	μm
Rq	0.0532	μm
Rsk	0.122	
Rku	2.14	
Material Ratio parameters - Function		
Rmr	100	%
Rdc	0.110	μm

**Figure 2-10 - Surface Profilometry measurements on Mo substrates prepared for E4**

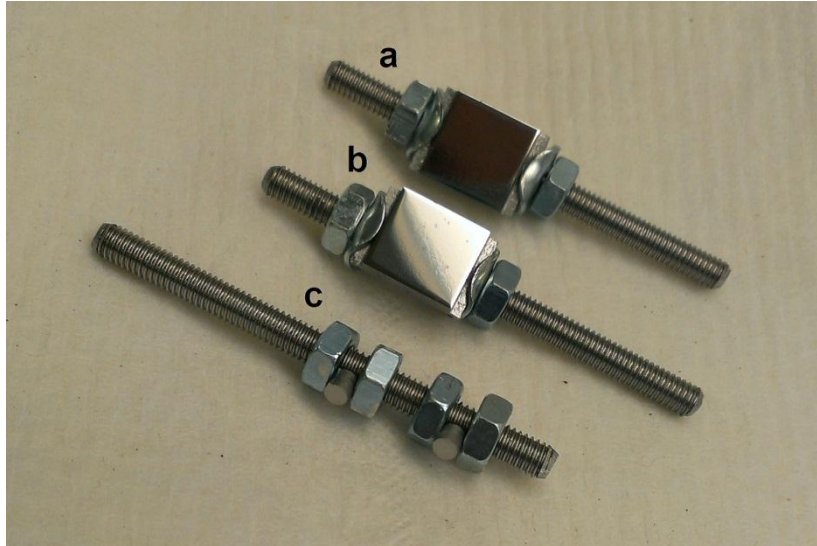
A study by Sricharoenchai *et al* accessed after E3 presented some solutions to the issues observed with the E3 TiB<sub>2</sub> samples [123]. Many of the TiB<sub>2</sub> coatings prepared in this study were observed to have a general (101) texture; with the

(001) texture only produced under certain conditions. The key aspects to promote the desired (001) texture appeared to be a) reducing target-substrate distance and b) increasing substrate temperature. Both of these options would increase the mobility of the sputtered atoms on the target surface and thus encourage fast growth along [001] as well as having a positive effect on the adherence of the  $\text{TiB}_2$  layer. The set-up of the in-house sputter coater would only allow for either substrate bias or heating to be applied. It was decided that the latter would be prioritised, based on indications from Sricharoenchai's work and on the fact that the substrate bias used in E3 sample preparation had not resulted in a strong (001) texture in the  $\text{TiB}_2$ .

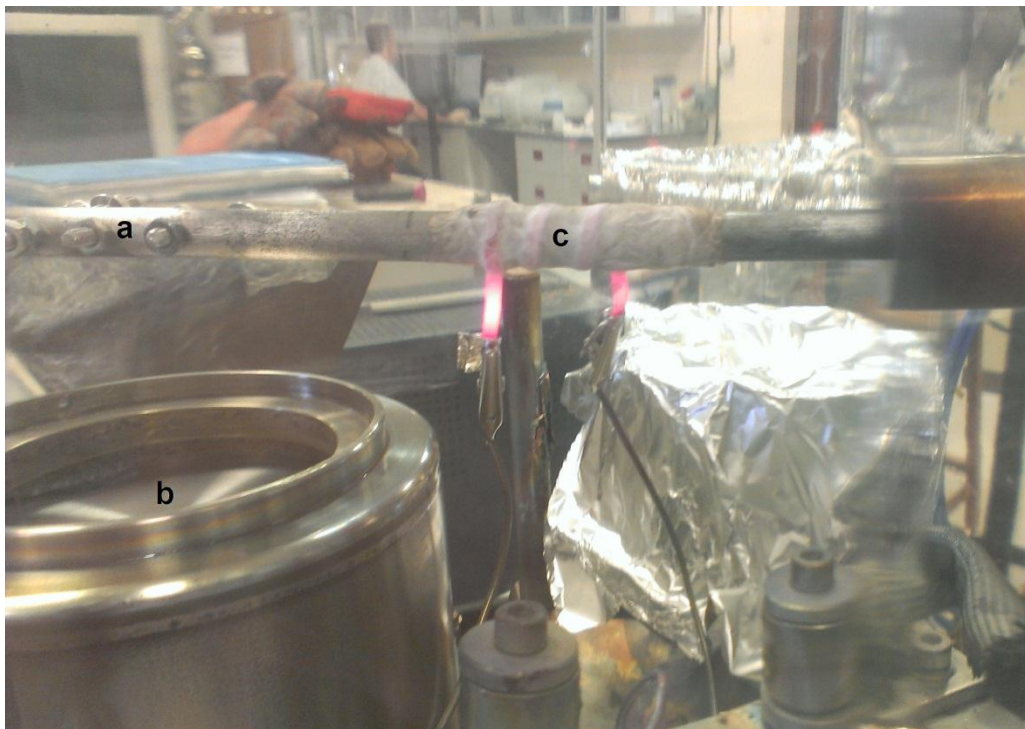
The intention was now to replicate the deposition process from the aforementioned study as closely as possible, to ensure the development of a (001) texture. Based on this study, and discussions with colleagues in UoL Physics, it was decided to first deposit a thin ( $\sim 0.1\mu\text{m}$ ) layer of pure Ti; this would assist adhesion between the Mo and  $\text{TiB}_2$  and reduce the risk of delamination. A heater device was designed to allow the substrates to be held at elevated temperatures during deposition. This was a simple piece of apparatus comprising a steel bar to which Mo pieces could be firmly clamped. A heating element cut from Sigraflex<sup>9</sup> graphite foil was wrapped around a section of the bar coated with a high-temperature alumina-silica based ceramic adhesive (Ceramabond 668 [124]) for electrical insulation. Applying a voltage across this element caused the whole system; bar with substrates attached; to be heated. While inefficient in terms of direct heating of the substrates, the large thermal mass of the bar resulted in good temperature stability once heated. The following figures show the sample mounting and the use of the heater device inside the sputter chamber.

---

<sup>9</sup> Sigraflex is a tradename for a laminated graphite foil product which was used throughout the project. It was primarily used in the construction of the micro-heater described in 2.4.



**Figure 2-11 - Molybdenum pieces prepared and fixed for deposition of Al. Polished pieces a) and b) are clamped to threaded rods which are then fixed into the heater assembly. The two smaller cylindrical pieces c) on the bottom rod are samples prepared for the micro-furnace (see section 2.4)**



**Figure 2-12 – Setup for deposition of  $\text{TiB}_2$  on E4 samples. Samples are mounted at a); the threaded rods are rotated such that the sample surfaces directly face the  $\text{TiB}_2$  sputtering target located at b). The sample and mounting assembly is heated during deposition via the potted heating element located at c).**

The guiding study [123] suggested a substrate temperature of  $\sim 400^\circ\text{C}$ ; in practice this proved difficult to achieve due to radiative losses from the bar and

limitations of the power supply. Substrates were heated both via the bar and through being in close proximity to the actual sputter target which heats during the process. The recorded substrate temperature was  $\sim 250^{\circ}\text{C}$  when deposition was begun and reached  $\sim 295^{\circ}\text{C}$  during the process. As this was somewhat below the suggested  $\sim 400^{\circ}\text{C}$  the target-substrate distance was reduced from 60 to 40mm to attempt to compensate (while ensuring the substrates remained above the plasma surrounding the target).

For final deposition the Ar working gas pressure was maintained around  $1 \times 10^{-2}$  mbar throughout. Initial deposition of the Ti interlayer took place using a high purity (4N) target operated at 200W for 10 minutes; following the same specification as in [123] to produce an interlayer of thickness  $\sim 0.1\mu\text{m}$ . For  $\text{TiB}_2$  it was noted that it was possible to operate the target also at 200W; the cracking which had occurred previously likely relieved residual stresses in the target thus meaning it would be unlikely to crack again. As such it was again possible to replicate the process of Sricharoenchai *et al*; the process was run for 3 hours to produce an assumed layer thickness of  $\sim 0.5\mu\text{m}$ . These deposition rates/expected resulting thickness appeared to be somewhat more realistic than the assumed rates in E3 sample preparation.

Initial characterisation at E4 showed that the  $\text{TiB}_2$  substrates had indeed been produced as intended – with a strong (001) texture.

E4 incorporated the use of an Al evaporator to directly deposit aluminium on the prepared samples *in-situ*. As such, most of the prepared  $\text{TiB}_2$  samples were left as-is. However, for contingency, one of the samples (denoted ‘VIII’) had a layer of Al pre-deposited via sputtering, following the same procedure as for E3, to a thickness of approx.  $10\mu\text{m}$ .

The Al/ $\text{TiB}_2$  system has never before been investigated in this manner. Studies by Iqbal *et al* [73]–[77] explored X-ray diffraction from a sample which replicates the bulk conditions of an Al alloy melt; this has proved useful in determination of, for example, the phase fraction within the solidifying system. The current

experiments, however, are designed to directly probe the interface between the materials, with an ordered substrate designed to approximate on a larger scale the morphology and behaviour at the  $\text{TiB}_2$  particle/crystalline Al interface, and reveal in greater detail the physical behaviour and orientation relationships which arise. To the author's knowledge, this is the first time that this specific type of study has been attempted on this important material system.

## 2.4 Heater Design

For E2 the intention was to create a device which would permit extremely fine temperature control and thus allow the investigation of systems with very low undercooling. The concept was developed upon discussions with individuals from the German Aerospace Centre (or ‘Deutsches Zentrum für Luft- und Raumfahrt’ / “DLR”) followed by a visit to their site in Cologne. The process was driven by their development of a ‘micro-furnace’ device for investigating diffusion in micro-gravity conditions [125]. The key technology of interest was a laminated graphite foil material called Sigraflex used to make heating elements which could attain the temperatures required for our experiments with low power demand. Preliminary testing at DLR indicated temperatures of  $\sim 800^{\circ}\text{C}$  were readily achievable with a standard 10A/30V laboratory power supply (under vacuum conditions;  $3 \times 10^{-3}$  mbar), as shown in Figure 2-13.

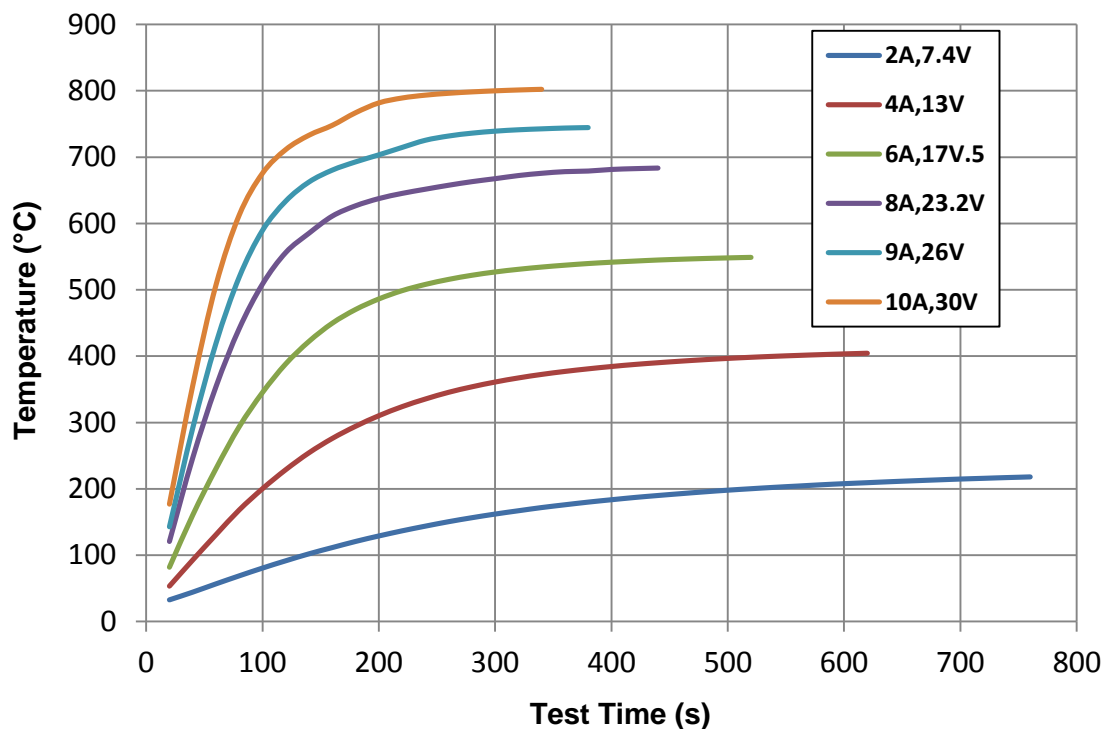


Figure 2-13 - Heater prototype testing at DLR

The device specification was broadly as follows:

1. Heat sample to temperatures up to approx.  $800^{\circ}\text{C}$
2. Maintain temperature stability of  $\pm 0.1^{\circ}\text{C}$  over this range



3. Allow X-ray transit to sample
4. Fit within existing equipment on beamline I07
5. Modular construction – i.e. design to accommodate alternate sample geometries for future experiments

Through a process of discussion, materials selection, prototyping and testing, a device was created for E2. The final design is shown in Figure 2-14. A complete breakdown of the materials used in the heater, with relevant properties, follows in Table 2-3.

The protruding section of the graphite crucible block holds the substrate sample. Pure Al is then placed above and the heater is operated to melt the material in this region. The crucible section allows penetration of the X-rays through to the substrate/melt interface while containing the melt and securely supporting the substrate beneath. This principle of operation is shown in Figure 2-14b.

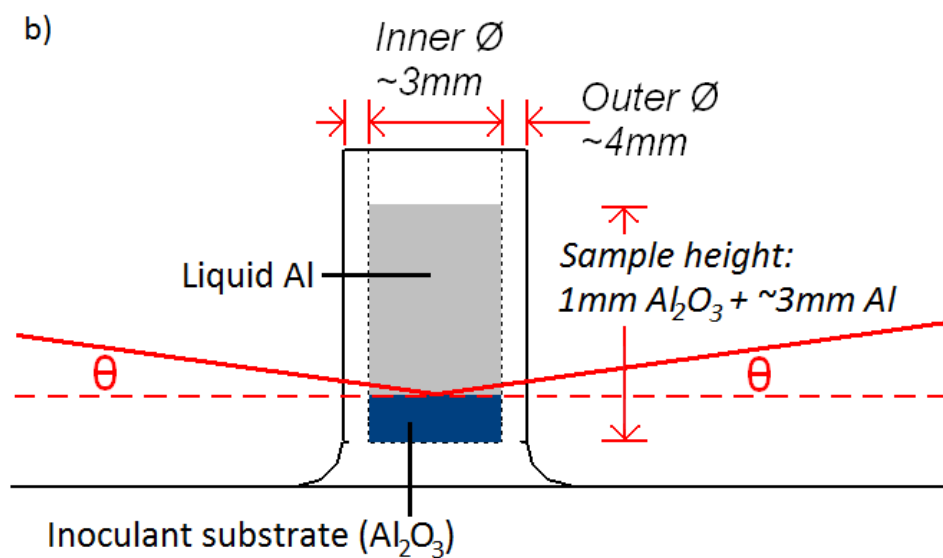
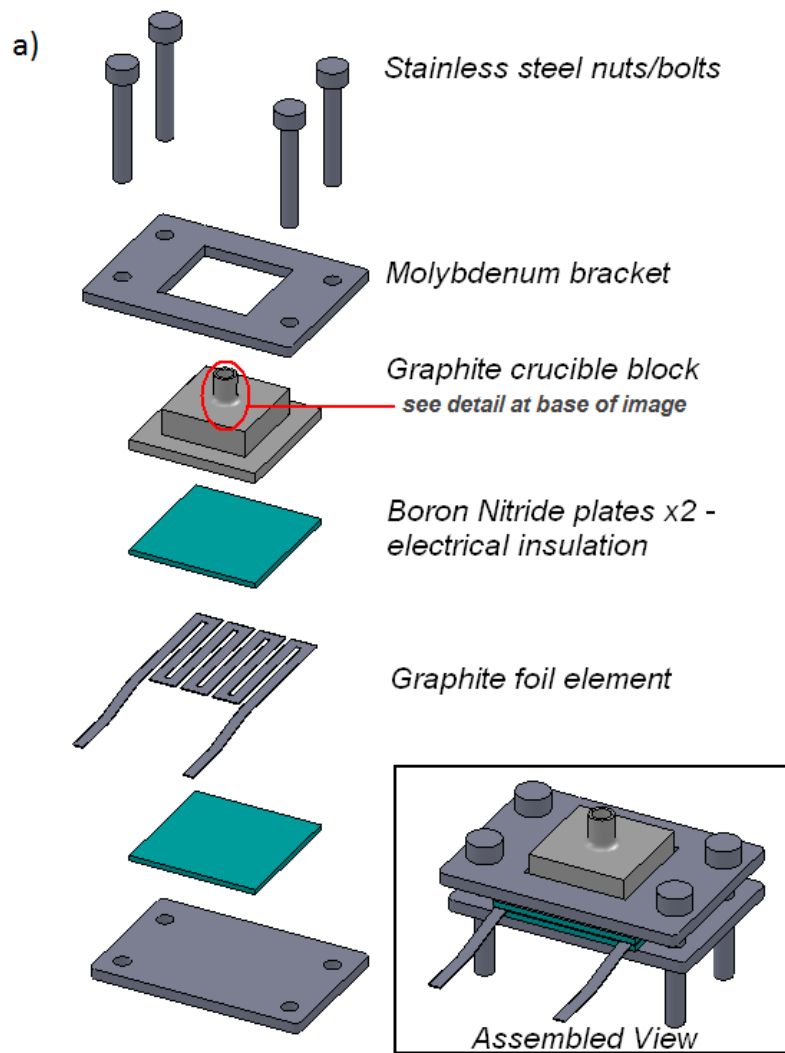


Figure 2-14 - Heater Design for E2. a) Exploded view of heater assembly. b) Operating principle

Material	Thermal Conductivity	Thermal Expansion	Specific Heat	Density	Notes/ Supplier
<b>Al<sub>2</sub>O<sub>3</sub></b> samples	At 20°C <i>Properties in relation to C-axis</i> Parallel: <b>23.1 W/(K·m)</b> Perp: <b>25.2 W/(K·m)</b>	<b>6.66 x 10<sup>-6</sup></b> parallel to optical axis <b>5 x 10<sup>-6</sup></b> perpendicular to optical axis	At 20°C <b>0.761 kJ/K·kg</b>	<b>3.98 g/cm<sup>3</sup></b>	<b>Pi-Kem</b> N.B. samples machined from existing material
<b>Sigraflex</b> (Graphite foil heating element)	At 20°C Parallel: <b>180-200 W/(K·m)</b> Perp: <b>4-6 W/(K·m)</b>	20-1000°C Parallel: <b>~1x10<sup>-6</sup>/K</b> Perp: <b>~30x10<sup>-6</sup>/K</b>	At 20°C <b>0.7 kJ/K·kg</b>	Bulk density <b>1.0 g/cm<sup>3</sup></b>	<b>SGL Group</b> Sigraflex TH
<b>Molybdenum</b> (bracket)	At 20°C <b>142 W/(K·m)</b>	At 20°C <b>5.2x10<sup>-6</sup>/K</b> At ~700°C (from graph) <b>5.6x10<sup>-6</sup>/K</b>	At 20°C <b>0.254 kJ/K·kg</b> At ~700°C (from graph) <b>0.285 kJ/K·kg</b>	At 20°C <b>10.22 g/cm<sup>3</sup></b>	<b>Special Metals Fabrication Ltd</b>
<b>Graphite</b> (crucible block)	Assume at 20°C <b>90 W/(K·m)</b>	Assume at 20°C <b>4.7x10<sup>-6</sup>/K</b>	Assume at 20°C <b>0.71 kJ/K·kg</b> (engineering toolbox; olmec grade may slightly differ)	Assume at 20°C <b>1.85 g/cm<sup>3</sup></b>	<b>Olmec</b> Grade 'Y459'
<b>Boron Nitride</b> (insulation)	At 20°C <b>50 W/(K·m)</b> At 400°C <b>40 W/(K·m)</b> At 700°C <b>30 W/(K·m)</b>	20-1000°C <b>4.4x10<sup>-6</sup>/K</b>	At 25°C <b>0.794 kJ/K·kg</b>	Assume at 20°C <b>2.0 g/cm<sup>3</sup></b>	<b>Henze BNP</b> HeBoSint D100
<b>Steel</b> (nuts&bolts)	At 100°C <b>42.7 W/(K·m)</b> At 300°C <b>40.7 W/(K·m)</b> At 1200°C <b>30.1 W/(K·m)</b>	At 20°C <b>11.2x10<sup>-6</sup>/K</b>	50-100°C <b>0.477 kJ/K·kg</b> 150-200°C <b>0.523 kJ/K·kg</b> 750-800°C <b>0.837 kJ/K·kg</b>	At 20°C <b>7.83 g/cm<sup>3</sup></b>	<b>RS Components</b> (Engineering Workshop)

**Table 2-3 - Bill of Materials used in Heater**

As is clear from the table, materials with broadly similar properties were selected, especially in terms of thermal expansion, to avoid issues with

differential expansion on heating which could lead to cracking. The device was manufactured in-house at UoL and further testing revealed that it was capable of reaching the required temperatures using standard 10A/30V power supplies.

The intention for E2 samples was to purchase new  $\text{Al}_2\text{O}_3$  substrates with rod geometry (diameter  $\sim 3\text{mm}$  as indicated, but with a length of  $\sim 5\text{mm}$ ) as this shape would locate neatly in the cylindrical crucible and reduce the risk of lateral movement. Unfortunately this was not possible and so thin ( $\sim 1\text{mm}$ ) disc-shaped substrates were instead prepared, as described in 2.3.2. Small dabs of the Ceramabond 668 adhesive were used to secure the discs to the base of the crucible sections.

Initial testing of the heater operation took place in the chemistry department at UoL using a vacuum chamber. The heater sat on a platform adjacent to a sapphire window allowing progress to be observed throughout. A thermocouple was mounted within the crucible section to record the temperature which would be achieved at the sample location. As Figure 2-15 shows, the heater offered the ability to attain the required temperature range with low power requirements, confirming that it would be operable using a standard laboratory power supply.

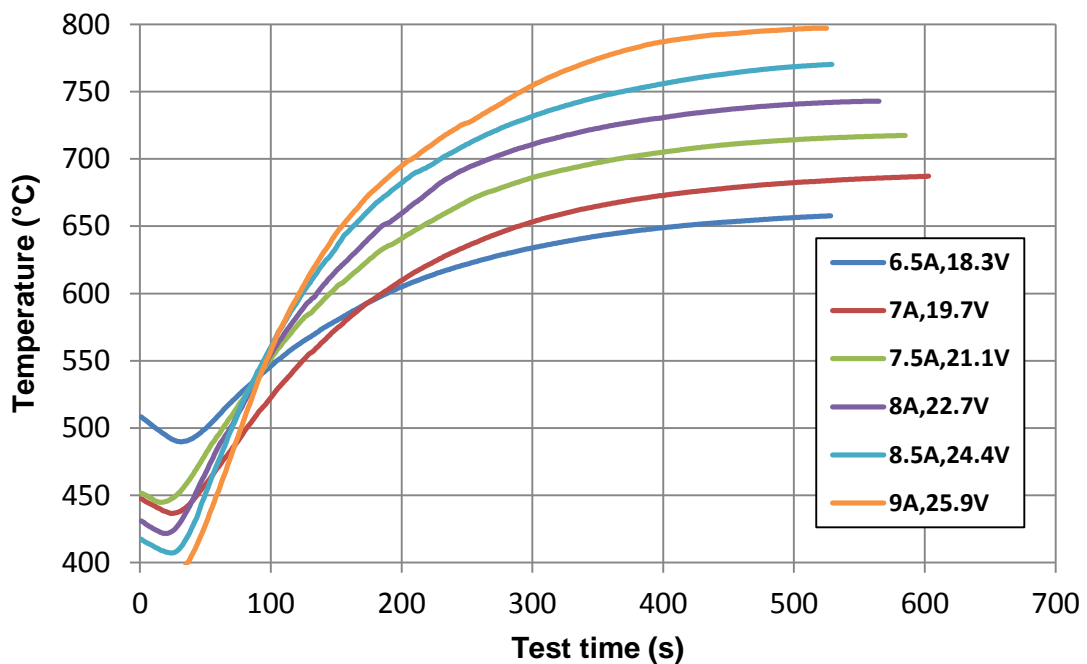


Figure 2-15 - Assembled heater testing

Commissioning of the heater took place during E2 at Diamond I07. An extra baseplate was designed to mount the device within the baby chamber and to facilitate connection of existing power and thermocouple connections. The heater was positioned such that the centre of rotation of the baby chamber was aligned with the sample position within the crucible. Height was adjusted such that the incident and scattered X-ray beams could freely travel to the sample surface through both the dome and graphite crucible section, even at low incident angles.

For temperature control the heater was connected to a Eurotherm 2704 temperature controller which was interfaced with the I07 network to provide measurements directly to recorded datasets. PID parameters were selected through the in-built 'autotune' function; the continued commissioning process found that these automatically generated values were appropriate and resulted in excellent temperature stability.

Complementary to this a number of heat transfer simulations were performed to clarify the likely temperature discrepancy between thermocouple and sample positions. Parameters of importance in the simulation were entered from Table 2-3. The following shows the result of one of these simulations; the node positions indicate the points at which the thermocouples were attached in E2. The range of simulations, of which the following figures are a sample, indicated that there would be a discrepancy of only  $\sim 1^{\circ}\text{C}$  even at the upper range of temperatures required.

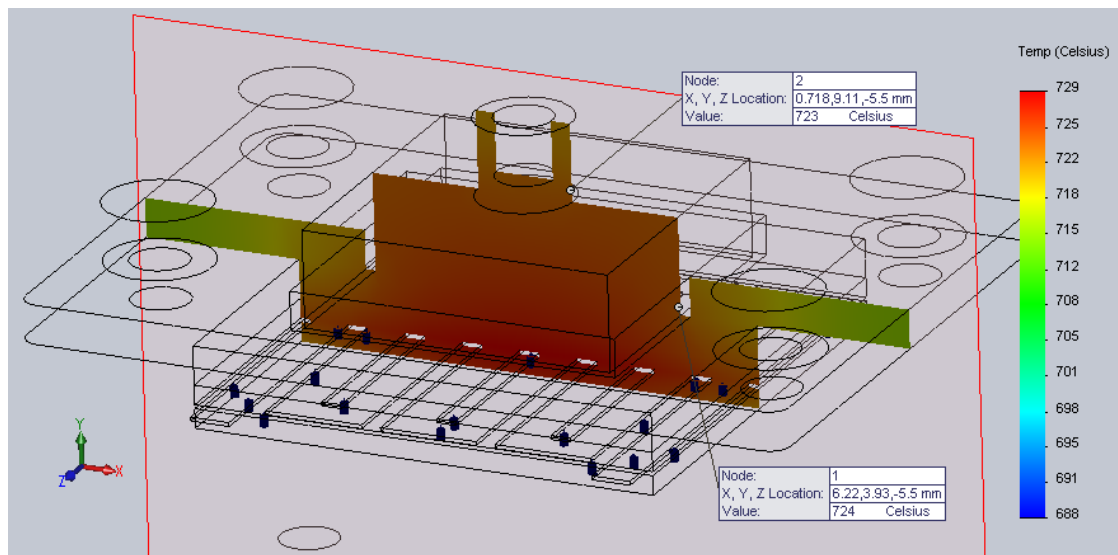


Figure 2-16 - Heat transfer simulation for heater, performed using SolidWorks. Node 1: 724°C; Node 2: 723°C

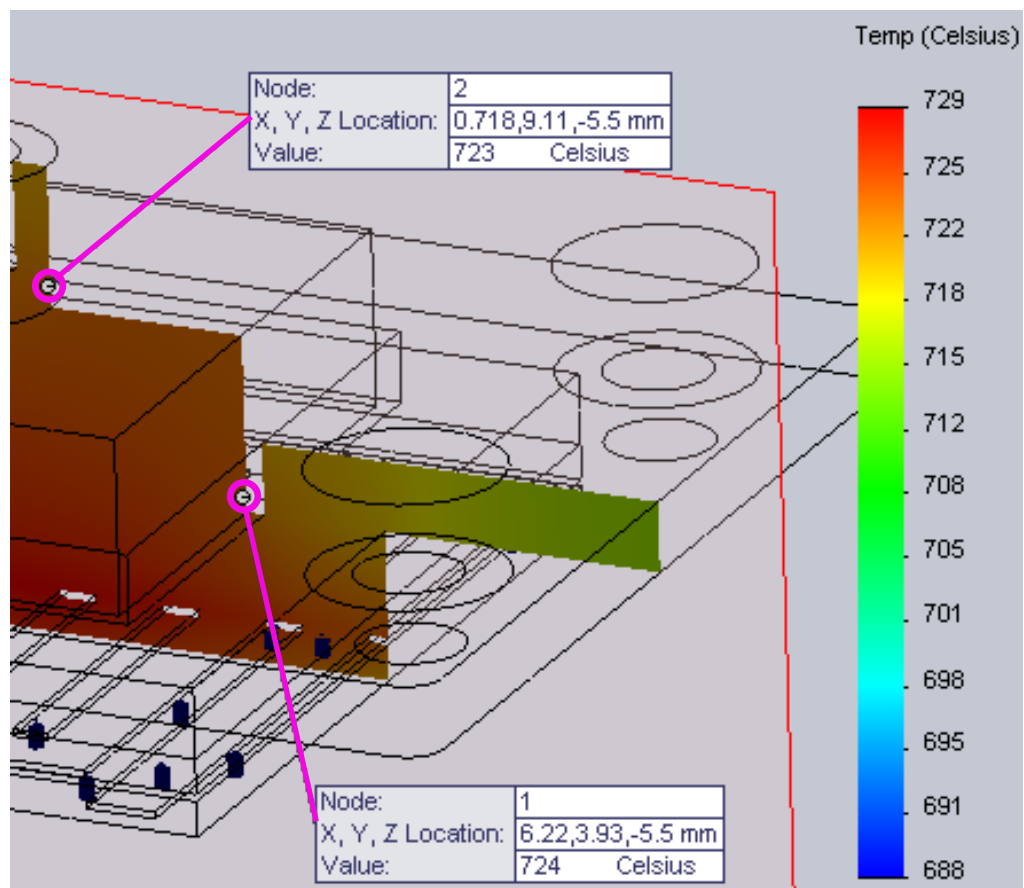


Figure 2-17 – Zoom in on Figure 2-16 to highlight node positions (i.e. intended thermocouple positions on heater).

## 2.5 Experimental Procedure

The following section will detail the operation of each experiment from E1 to E4. Experimental techniques and the relevant parameters used will be explained. Each experiment required significant time to set up and align samples such that they were situated at the centre of rotation of the diffractometer circles. This was first done geometrically (aligning the beam with the sample surface) and then, where possible, crystallographically (aligning the beam with the internal crystal structure of the sample, to account for miscut with the surface).

### 2.5.1 *Experiment One*

Experiment one took place October 2011 at Diamond Light Source, beamline I07. For this run the sample was a single crystal  $\text{Al}_2\text{O}_3$  substrate with sputtered Al layer prepared as detailed in 2.3.1. As stated, the concept was to heat the sample such that the sputtered layer would melt, forming a liquid film/population of droplets upon the surface. The sample was mounted on a transfer plate that could be located onto the substrate heater. A thermocouple located as close to the sample as practically possible provided temperature measurement and control via a temperature controller (Eurotherm 2704). Measured temperature data was calibrated by the melting point of the pure Al.

Objectives for E1 were to characterise the samples, apply heating and cooling and monitor how this altered the collected scattering, and assess the **undercooling** and **orientation relationships** in solidification. Throughout E1 X-ray energy of 15keV was used, corresponding to a wavelength  $\lambda$  of 0.826Å.

Disregarding alignment scans and those used to familiarise the team with beamline procedures, a total of 3 'complete scans' were performed during E1; hereafter referred to as S1, S2 and S3. In the interests of clarity and concordance with the results section, these are detailed separately in the order they were performed.

### 2.5.1.1 E1 S1

The initial challenge for E1 was to characterise the sample. To perform this, specular X-ray geometry was used. X-rays were incident on the sample at an angle  $\theta$  while the detector was set at an angle  $\theta$  from the sample surface. This  $\theta$ - $2\theta$  relationship maintains the Bragg condition.

The X-ray beam was focused to a spot size of approximately 250x200 $\mu$ m and aligned such that the detector collected scattering from both the Al<sub>2</sub>O<sub>3</sub> substrate and the Al layer. Beamline software recorded the position of scattering features against the angle  $2\theta$  at which they appeared. According to Bragg's Law, these  $2\theta$  values correspond to atomic spacing  $d$  in real space; these values could be correlated with known spacing of particular families of planes within the sample materials. Observed peak positions were validated against XRD spectra generated through crystallography package CaRIne 3.1 [126] and data from the ICSD [127].

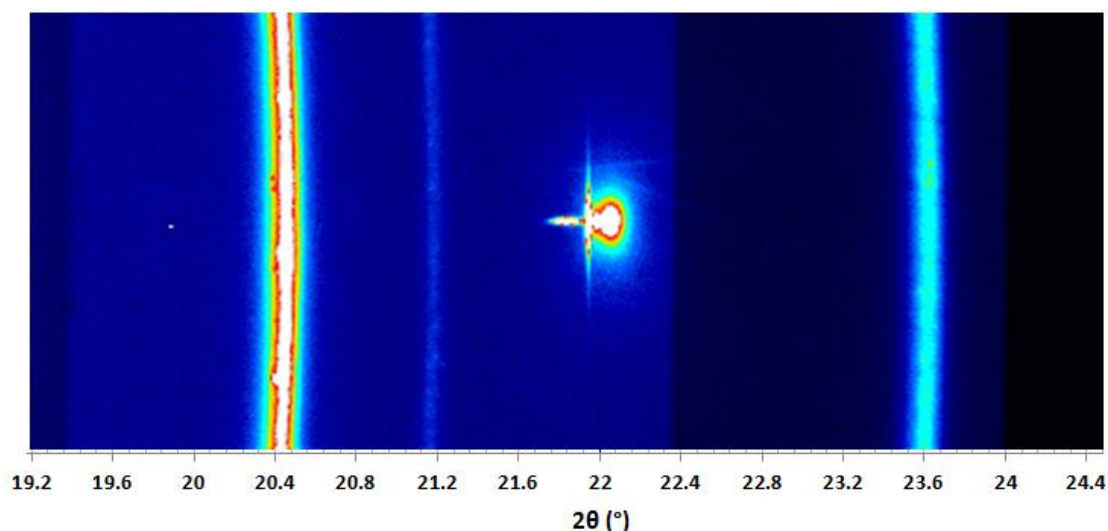
In setup for S1 it was noted that the angular acceptance of the detector was, at this X-ray energy and for this sample, sufficiently wide to collect scattering from 3 important scattering features in 'one shot'; i.e. no translation through  $2\theta$  was required to collect scattering from the different peaks. These features are given in Table 2-4.

Peak Position in $2\theta$ (°)	$\theta$ (°)	$d$ (Å)	Planar Family
20.4	10.2	2.338	Al {111}
22	11	2.165	Al <sub>2</sub> O <sub>3</sub> {006}
23.6	11.8	2.024	Al {200}

Table 2-4 - Peak positions and corresponding d-spacings from S1

To assist the reader the corresponding detector image – representing the initial condition of the sample – is shown in Figure 2-18.





**Figure 2-18 – Pilatus 100k detector image from E1 S1 showing initial condition (false colour map applied for clarity; actual images are greyscale)**

For S1, a heating and cooling process was applied to the sample over the course of approximately 9 hours. The substrate heater comprised filaments arranged in a spiral configuration. Heater surface area was sufficient to exceed the sample surface area and thus generate good temperature uniformity over the sample. Images were collected throughout the thermal cycle to monitor any structural transition in the Al. To capture sufficient intensity, the detector was exposed to the beam for 4 seconds, and total time between each image was approximately 64s. In order that the images would capture changes in the scattering, isothermal holds at particular temperatures were used rather than a continuous heating/cooling profile. Around temperatures of primary interest – between around 500°C and the maximum of ~700°C – steps between these isothermal holds gave a temperature resolution of approximately  $\pm 10^\circ\text{C}$ . This was deemed sufficient for detecting the nucleation undercooling in the Al/Al<sub>2</sub>O<sub>3</sub> system (expected to be on the order of tens of °C) while allowing preliminary verification of the technique itself. The portion of reciprocal space shown in Figure 2-18 – i.e.  $2\theta$  from 19.2 to 24.4 – was monitored throughout the thermal cycle. This allowed observation of the changes to the morphology of the sample as it was heated and cooled. Changes in the scattering pattern displayed above were observed and these are discussed in chapter 3.

### 2.5.1.2 E1 S2

S1 gave useful indications of the behaviour of the sample under thermal cycling, but the relatively small range of  $2\theta$  used limits the potential to draw out detailed structure. To explore this, S2 was set up to collect crystal truncation rods (CTR's). A script was written in the beamline software to record the (0,1, $l$ ), (1,0, $l$ ) and (0,0, $l$ ) rods consecutively, and in that order. The (0,1) and (1,0) rods were collected from  $l=0.5$  to  $l=14$  in increments of  $l=0.1$ . For the specular (0,0) rod, effectively an XRR scan, data points were recorded against  $2\theta$  from  $3^\circ$  to  $40^\circ$  in  $0.2^\circ$  increments.

After manual heating to approximately  $450^\circ\text{C}$ , the script was run at a range of pre-defined temperature levels such that all 3 rods were collected at each temperature. For the chosen increments in  $l/2\theta$  scanning each individual rod required approximately 20 minutes; continuous heating/cooling was thus not used as it would result in significant temperature variation over collection of a single rod. Steps between temperature levels were initially large ( $\sim 50^\circ\text{C}$ ) but were finer around the expected melting temperature of the aluminium layer. During the cooling phase, steps were initially of  $\sim 10^\circ\text{C}$ , increasing to  $20^\circ\text{C}$  after cooling to  $\sim 660^\circ\text{C}$  was reached. This approach was chosen as the CTR scans were primarily an attempt to capture any structures present in the aluminium layer while it was in the liquid state. The overall process for S2 took approximately 20 hours.

### 2.5.1.3 E1 S3

S3 was effectively a repeat of S2, again collecting the (0,1, $l$ ), (1,0, $l$ ) and (0,0, $l$ ) rods. The thermal profile was altered to reflect a more rapid heating and cooling process and thus observe the different behaviour under these conditions. The overall process took approximately 15 hours.

## 2.5.2 Experiment Two

Experiment two centred on the use of the micro-heater device, constructed and mounted within the baby chamber as described in 2.4. Samples were pre-

loaded into individual crucible sections. Two thermocouples were used, situated at the node positions indicated in Figure 2-16. T/C 2 (at Node 2) was mounted using the Ceramabond 668 into a small hole drilled into the side of the crucible section. This was intended as the measurement point for the Eurotherm temperature control feedback loop; however, during the early part of E2 it became apparent that this did not have good thermal contact with the device; readings were significantly different to expectations and to the other thermocouple. The T/C 1 (Node 1) was then used instead as the 'control' thermocouple. As shown previously, simulations (and testing experience) had indicated that the thermal gradient between the thermocouple and sample positions would be negligible and could be accounted for in analysis.

Objectives for E2 were to fully commission the heater device, and use it to investigate scattering from the Al/Al<sub>2</sub>O<sub>3</sub> interface with greater control over temperature. Throughout E2 X-ray energy of 20keV was used, corresponding to a wavelength  $\lambda$  of 0.62Å. This was an increase from the 15keV used in E1, to maximise beam penetration through the relatively thick crucible section.

Tests were conducted 'off-line' prior to E2. The intention was to 'pre-melt' a small volume of Al into the crucible section to ensure a sizeable liquid region would be generated on heating as indicated in Figure 2-14b. Small lengths of high purity (5N) Al wire were placed in the crucible prior to assembly of the chamber. To allow observation of the pre-melting the Be dome was replaced with a steel cylinder with a sapphire window. Careful heating via the Eurotherm brought the system above the Al melting temperature. Upon heating the Al pieces softened and then joined to form a continuous 'blob', which then joined with the sputtered Al layer on the surface of the sample. The Al then quickly assumed a roughly spherical shape; this sphere sat on the substrate and appeared to remain solid even as the heater temperature was raised to 750°C. It is well understood that Al does not readily wet Al<sub>2</sub>O<sub>3</sub> (001); contact angles recorded via sessile drop experiments are reasonably high, ranging from around 90° [128] to 130° [112] at the stated temperature level; though there appears to be some debate as to whether the contact angle increases[112],

[129] or decreases [130] with time. In this case, however, it was apparent that the Al almost instantly had *completely* de-wet from the  $\text{Al}_2\text{O}_3$  surface. The subsequent spherical geometry resulted in a minimal contact point between the Al and the substrate; as such the thermal transfer was reduced and the Al failed to melt.

It became apparent that these problems – de-wetting and subsequent lack of thermal contact – would recur throughout E2. Each sample had a pre-sputtered Al layer which could be heated and cooled, but on melting this appeared to be subsumed into the larger droplet. In hindsight it is apparent that oxidation effects may have contributed to the Al droplet failing to wet the  $\text{Al}_2\text{O}_3(001)$  surface [128]; while some degree of oxidation was of course expected due to the high reactivity of Al, the terminal effect on the experiment was unforeseen.

Sample problems and the difficulties associated with commissioning new equipment made the collection of useful data from E2 a significant challenge. After solving many issues a final overnight scan was initiated. Over the course of 14 hours, XRR was performed between 1.5 and 25.5 in  $2\theta$ , with a concurrent heating/cooling profile applied. After manual heating to 500°C, the profile applied a ramp rate of  $\sim 1^\circ\text{C}/\text{min}$  for both heating and cooling; ramping up to 750°C then down to 400°C. The heater device performed extremely well, exhibiting excellent responsiveness and temperature stability to within  $\pm 0.1^\circ\text{C}$ . Within the context of the wider project this represented a great success – the heater device was fully commissioned and demonstrated the required characteristics for future implementation. Unfortunately, the overnight scan in question was problematic, due to a simple error. To maintain the Bragg condition, the I07 diffractometer requires the angle  $\gamma$  to be twice  $\alpha$ ; i.e.  $\gamma = 2\alpha$ . In writing the script the condition was incorrectly entered as  $2\gamma = \alpha$ . As such, the diffractometer angles were misaligned throughout the entire scan and the dataset could not be accurately indexed.

While E2 suffered from many problems it was a useful learning exercise and offered many lessons for future experimentation. It also allowed demonstration

of the capabilities of the heater device, which as later results will show, exhibited superior temperature control and stability.

### 2.5.3 Experiment Three

Experiment three necessitated a change of approach due to the move to an alternative beamline; ID03 at the ESRF, France. This experiment involved both the continued investigation of the Al/Al<sub>2</sub>O<sub>3</sub> system and an initial investigation of Al/TiB<sub>2</sub>. Due to the difficulties experienced with E2, and the move to an unfamiliar beamline, E3 adopted the simpler setup which had proved successful in E1; i.e. the use of a 10x10x1mm substrate with 'steps' for mounting to a sample heater built into an existing sample chamber.

Samples for both material systems were prepared as detailed in 2.3.3. Individual samples used in the experiment were designated as follows:

**X:** Al on Al<sub>2</sub>O<sub>3</sub>. The re-prepared substrate from E1, with an Al layer pre-deposited through sputtering.

**A:** Al on TiB<sub>2</sub>. Detailed description of preparation in 2.3.3.

**W:** Al<sub>2</sub>O<sub>3</sub>. A single 10x10x1mm piece of single crystal Al<sub>2</sub>O<sub>3</sub>, originally purchased for testing purposes, was brought to ID03 to allow exploration of the possibility to evaporate Al *in-situ* onto a crystalline substrate. This sample did not have the 'stepped' profile and was not subjected to any treatment apart from a cleaning with alkali wash and ethanol.

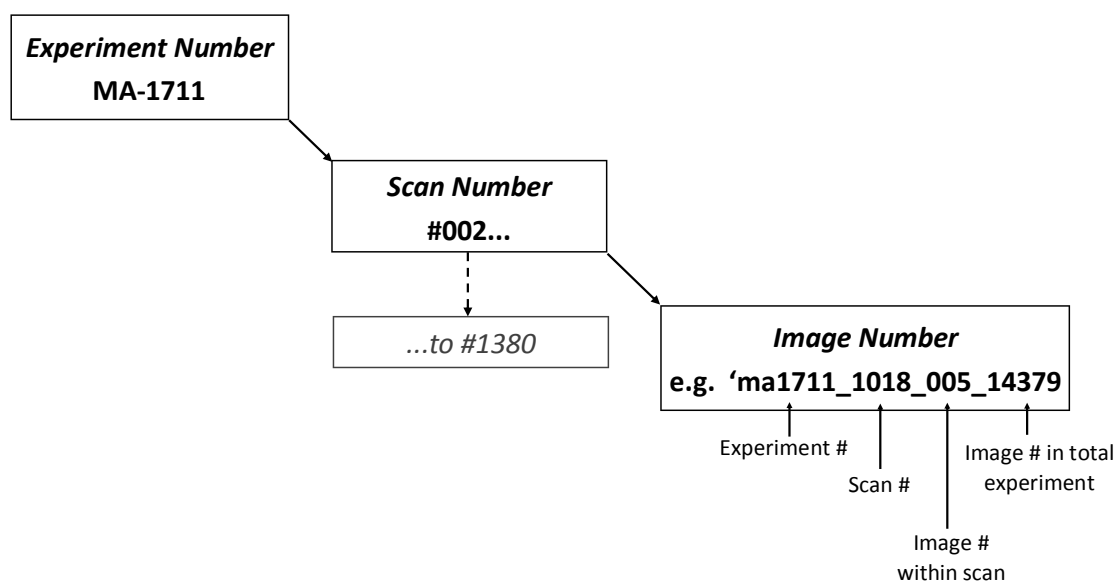
Samples were mounted to small sample heaters designed for direct integration to the ID03 UHV chamber. As sample W lacked the 'steps', a small amount of Ceramabond 668 was used to secure it to an existing Mo block which was affixed to a sample heater. The adhesive is rated up to 1371°C [124] and was unaffected by the heating and cooling during the experiment.

The initial objective for E3 was to obtain high-quality data for the Al/Al<sub>2</sub>O<sub>3</sub> system. Based on results from E1 (detailed in chapter 4) this would primarily be investigated through the collection of the (1,0,*l*) CTR. An additional objective

was characterisation of the TiB<sub>2</sub> sample, followed by monitoring of the change to the scattering profile during heating and cooling. The option of *in-situ* evaporation of Al onto a crystalline substrate was suggested during the experiment itself. X-ray energy of 20keV was used for sample 'X'; upon moving to sample 'A' it was noted that X-ray fluorescence of the Mo substrate was an issue at this energy so it was reduced to 19.9keV, giving  $\lambda = 0.623\text{\AA}$ . This energy was retained for the remainder of the experiment.

The team was able to acquire significantly greater quantities of data at E3 than in previous experiments. The data were recorded as a series of scans, numbered consecutively. For this reason it is sensible to present the experimental process in a broken-down fashion; first sample-by-sample and then scan-by-scan. Where numbers are omitted, the scan in question was either an alignment scan (containing no useful data) or aborted. Following the run with sample 'X' attempts were made to clean and re-use it; however it quickly became apparent that the scattering was messy and would likely lead to poor quality data. This series of scans is therefore omitted.

Due to the large quantity of data collected at E3 and subsequently at E4, the automatically assigned scan and image numbers are used to present the data. The following diagram should assist the reader in understanding the naming convention.



**Figure 2-19 – Naming convention for E3**

#### 2.5.3.1 Sample 'X' procedure

Following the naming convention described above, the operations on sample 'X' were as follows:

- Scan 002-930: Initial alignment followed by characterisation of sample structure. Some heating & cooling was performed and changes monitored through observing images at constant angular position.
- 933-937: Specular reflectivity.
- 939-1075: Collection of (0,1) rod over a heating & cooling cycle. Between each rod scan, alignment scans were performed to counteract any sample motion under thermal expansion and maintain the beam at the correct position.
- 1076-1089: Symmetry-equivalent CTRs collected.

#### 2.5.3.2 Sample 'A' procedure

- 1090-1111: Sample alignment.
- 1112-1121: Characterisation of structure.
- 1122-1257: Continued characterisation over a heating & cooling cycle. The script was designed to collect scattering in both the in-plane and out-of-plane directions to identify orientation of the structures within.

#### 2.5.3.3 Sample 'W' procedure

The ID03 team had pointed out that an Al evaporator was incorporated into their setup allowing *in-situ* deposition of Al onto a substrate under UHV conditions. This would result in an exceptionally clean and consistent layer of Al with which to perform further investigations.

- 1329-1337: A range of CTR scans with different (h,k) indices:  
(0,1), (1,0), (1,1), (2,0), (2,1), (1,2), (0,2), (0,3), (3,0)
- 1346: A generic 'timescan' used during initial attempts to evaporate Al. The detector was set to a constant angular position to allow monitoring of the appearance of features indicative of deposited material. Evaporation parameters were such that a deposition rate of approximately 0.4Å/min was achieved. The substrate was heated for the duration of the process as it was felt this would assist in mobility of the evaporated material on the Al<sub>2</sub>O<sub>3</sub>

surface. The temperature climbed from  $\sim 466^{\circ}\text{C}$  to  $\sim 477^{\circ}\text{C}$  over the course of  $\sim 25$  minutes.

- 1350-1351: (1,0) and (0,1) rods immediately following deposition.
- 1356-1364: Range of CTR scans as in 1329-1337.
- 1367: Timescan for further deposition of Al, as no significant changes to the CTRs were observed. This time the deposition was done 'cold' – i.e. no heating was applied to the substrate. Under natural cooling the substrate temperature dropped from  $\sim 38.1^{\circ}\text{C}$  to  $\sim 37.5^{\circ}\text{C}$  over the course of  $\sim 10$  minutes.
- 1368-1370: Specular reflectivity.
- 1371-1380: Range of CTR scans:  
(0,1), (1,0), (1,1), (2,0), (2,1), (1,2), (0,2), and repeat (0,1), (1,1)

#### 2.5.3.4 General observations from E3

It was immediately apparent that the CTR data collected at E3 was of significantly higher quality than that from E1. Collection of symmetry-equivalent rods (not performed at E1) was intended to add clarity and confidence to the data. The analysis of these rods will be explored in detail in chapter 4.

E3 included the first investigations on the Al/TiB<sub>2</sub> system. As briefly described in 2.3.4, it was apparent from early scans that the TiB<sub>2</sub> layer on sample 'A' had in fact *not* adopted the desired (001) texture; but instead had a mixed orientation with a slight (101) bias. Despite this, heating & cooling of the Al layer on the sample led to some interesting observations; and the characterisation helped to guide a modified approach to sample preparation for E4.

Time constraints meant that the evaporation technique could not be fully explored. Material was deposited and data recorded during this process, but there were no investigations on subsequent heating and cooling of the deposited material. The inherent cleanliness of the technique renders continued investigation important and potentially beneficial to quality of data; as such it was decided that it would be explored again during E4.



#### 2.5.4 Experiment Four

For this experiment the decision was made to switch focus entirely to the Al/TiB<sub>2</sub> system, in view of its industrial relevance. The experiment returned to I07 at Diamond, this time using the UHV system rather than the baby chamber used in E1 and E2. This decision was made based on the recent experiences at E3; maintaining the same type of setup would allow more direct comparison with the results from the TiB<sub>2</sub> sample A. As contingency/preparation for future work, the heater device and appropriate samples were prepared concurrently, though limited beamtime meant that it was not possible to investigate using this as well as the UHV setup.

For E4 an Al evaporator was sourced from UoL Physics. This device was mounted to the I07 UHV chamber prior to the experiment.

Samples, prepared as detailed in 2.3.4, were as follows:

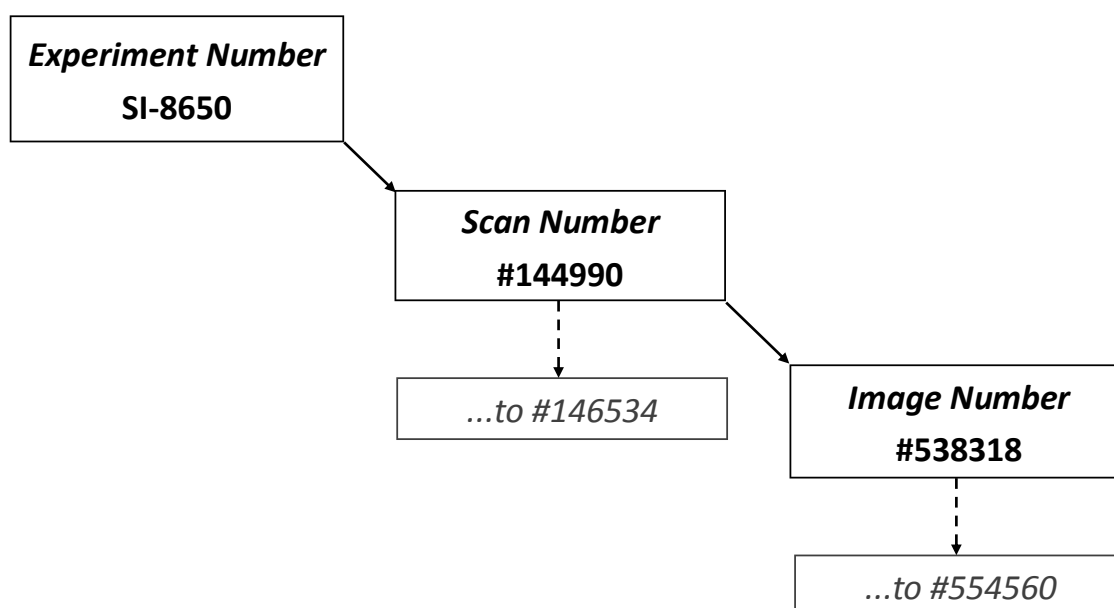
**V:** TiB<sub>2</sub> on a Mo substrate with a Ti interlayer. This sample was used as a base for *in-situ* Al evaporation.

**VIII:** Same as V but with a pre-deposited Al layer on the TiB<sub>2</sub> surface.

The first objective for E4 was to characterise the TiB<sub>2</sub> samples and verify that the (001) texture had indeed been generated in the material. Following this, the evaporator would be used to deposit a clean Al layer on sample V. The evolution of the structure of the sample would then be monitored over an applied heating & cooling profile. Sample VIII presented an opportunity to run similar tests to E1; this time on the Al/TiB<sub>2</sub> system.

##### 2.5.4.1 Sample V procedure

Figure 2-20 indicates the naming convention used for DLS experiments which differs slightly from the ESRF.



**Figure 2-20 – Naming convention for E4. Unlike E3, the scan and image numbers are not linked. Scan and image numbers at I07 are recorded from the start of the original beamline operation, rather than being ‘reset’ at the start of each users beamtime**

The scans are thus presented using the automatically assigned I07 numbering:

- 144990-145015: Initial alignment and characterisation.
- 145017-145034: Repeated out-of-plane scans to monitor Al deposition with evaporator.
- 145035-145038: In- and out-of-plane scans to characterise deposited structure.
- 145039-145253: Rather than full scans over a  $2\theta$  range, these scans comprised sets of images taken at 3 Al peak positions in  $2\theta$ ; corresponding to the (111), (200), and (220) families of planes. This was repeated during heating of the sample. The concept was to monitor the evolution of the Al structure as the layer increased in temperature.
- 145254-145255: In- and out-of-plane scans to characterise sample structure at high temperature.
- 145256-145673: Sets of images at (111), (200) and (220) positions as before, during cooling of the sample.

At this point, the sample was ‘flashed’ to a temperature of around 1200°C – this process was intended to remove the Al from the sample and leave a ‘clean’ surface for another deposition via the evaporator. Monitoring of the sample surface via video link showed no apparent surface deterioration up to this point.

- 145674-145678: In-plane scans to monitor Al deposition
- 145680-146425: In- and out-of-plane scans during heating and cooling through a range of temperatures, identified as being of interest through previous scans.

During the above the video link to the sample showed that the surface structure had deteriorated, exhibiting a 'crazy-paving' type appearance. At this point sample V was removed and sample VIII loaded.

#### *2.5.4.2 Sample VIII procedure*

- 146426-146503: Initial alignment followed by in- and out-of-plane scans for characterisation
- For the heating and cooling on sample VIII, the detector was positioned to monitor the Al (111) peak as heating proceeded. With careful monitoring the temperature was manually elevated up to ~600°C, following which a ramp of 1°C/min was applied. As soon as the (111) peak disappeared from the detector image (indicating the phase transition) the heater was switched off, effectively applying a quench to the sample. This process was designed to freeze the Al quickly and avoid significant migration of material to the edges of the sample (which had led to problems in E3; discussed in section 5.1).
- 146510-146534: Final in- and out-of-plane characterisation scans of the solidified structure.

#### *2.5.4.3 General observations from E4*

Following the challenging TiB<sub>2</sub> sample preparation (and the difficulties experienced with the TiB<sub>2</sub> sample at E3) it was extremely satisfying to observe the strong (001) texture which had been developed in the E4 samples. This immediately suggests that, with a formalised preparation procedure, this technique may have considerable potential for further investigations on TiB<sub>2</sub> as it appears to be considerably cheaper than obtaining single crystals.

Deposition using the Al evaporator generated some intriguing behaviour which will be explored further in chapters 4 and 5. Subsequent melting and re-freezing of the Al gave indications as to the orientation relationships established

between the Al and  $\text{TiB}_2$  on cooling. This will feed into current understanding of the nucleating potential of  $\text{TiB}_2$  in aluminium melts and provide supporting information about the mechanism.

## 2.6 Software used in Data Analysis

Scattering data, in its most basic sense, is collected as series of .tiff images. During each scan, beamline software concurrently records data about diffractometer angles, elapsed time, sample temperature etc; these are saved in large ASCII text files. Through selection of appropriate regions of interest (ROI's) on the detector window prior to each scan, the software can also record  $\theta$ - $2\theta$  plots and display them as the scan proceeds. While relatively crude, these offer valuable indications as to the progress of the scans and allow identification of phase and morphological changes *in-situ*.

At the beamlines, specific software packages were used to control equipment and display 'live' data. Equivalent packages are available which allowed the data to be loaded and viewed in a similar way 'off-line', which helped in understanding and initial assessment, though they offered little in terms of further manipulation and analysis. These packages are called DAWN (Data Analysis WorkbeNch) [131] and PyMca [132]; these were appropriate for viewing I07 and ID03 data respectively.

The ASCII text files, representing the most complete overview of the dataset for each experiment, were imported into Microsoft Excel. This allowed manipulation, calculation, and subsequent presentation of the data in a manner suitable for inclusion in the present document.

The .tiff image files represent the most 'raw' form of the data. On numerous occasions it was useful to view these images, to check the geometry of particular scattering features. A package called FIJI [133] was used extensively for this purpose; this is a distribution of the widely-used ImageJ package with extra tools appropriate for this work. FIJI facilitated more rigorous integration of the scattering intensity, where it was observed that the ROI's applied at beamtime were not sufficient to 'capture' the features identified as being of interest in the images.

A program called ROD permitted generation of expected scattering profiles for CTR's. Developed at the ESRF by Elias Vlieg, this is a valuable tool which also offered the ability to 'fit' collected experimental data to a model profile, leading to indications of the atomic structure within the sample. ROD is primarily used in the field of surface science, and in the context of the current work a full description is unnecessary – more detail can be found in the references [86], [134]. What follows is a description of the fundamental operation of the program geared towards the current materials science focus.

As described in section 1.8.4, CTR's arise from the presence of crystalline surfaces in X-ray diffraction. For a bulk crystal, diffracted intensity is concentrated in Bragg peaks; when a surface is present, additional intensity is found in between these Bragg peaks along a 'rod' in reciprocal space. The character and variation of this additional intensity arises from the particular character of the crystalline surface from which diffraction is taking place. As such, the intensity profile represents a kind of 'signature' of the surface structure, and is extremely sensitive to any changes thereof. If, as is theorised, the presence of liquid and/or crystalline aluminium causes any modification to the  $\text{Al}_2\text{O}_3$  surface, the CTR's should be modified accordingly.

The basic inputs to the ROD program are as follows:

- A 'bulk' file (\*.bul) defining the equilibrium atomic structure of the  $\text{Al}_2\text{O}_3$  crystal
- A data file (\*.dat) containing the structure factors recorded from experimental work in terms of the reciprocal lattice vectors  $h, k$  and  $l$
- A 'fit' file (\*.fit) defining the atomic structure of the top few layers of atoms in the *surface* of the  $\text{Al}_2\text{O}_3$  crystal

Based on the atomic structure defined in the bulk and fit files, and assuming a hard-sphere model of the atoms themselves, ROD calculates and produces a predicted CTR profile for the particular  $h, k, l$  index defined; for example, if the experimental data represents  $(0, 1, l)$  rod scattering, the predicted  $(0, 1, l)$  rod is calculated. A plot of the predicted and experimental scattering profile indicates how significantly the experimental values differ from the predicted. Then, the 'fit'

file is parameterised to allow the *occupancy* and *displacement* of surface atoms to change. ROD alters these parameters within defined limits to modify the surface structure in such a way as to produce a predicted scattering profile which fits as closely as possible to the experimental data. The user must then observe the values of the parameters to assess whether they are physically realistic. If so, the modified fit file can be understood as a possible representation of the actual surface structure in the experimental sample.

Due to the mathematical nature of the fitting process, there may be multiple routes (i.e. variations of the occupancy and displacement parameters) by which a reasonable fit can be achieved. It is up to the user to explore these and decide which are a) physically possible and b) most likely to have occurred in the real sample. The samples and methodology in the current work are quite different to those of more fundamental surface science experiments; as such the application of ROD is less straightforward and many assumptions must be made, e.g. the number of atoms in the surface layer (fit file). However, ROD probably represents the best method through which to obtain at least a basic understanding of the structural changes which may occur at the Al/Al<sub>2</sub>O<sub>3</sub> interface.

### 3 Results: In-situ Observation of Al/Al<sub>2</sub>O<sub>3</sub> Melting and Solidification

This chapter presents the results of investigations into melting and solidification phenomena in the Al/Al<sub>2</sub>O<sub>3</sub> system. Experiments 1, 2 and part of 3 focused on this case and recorded:

- In-situ observation of melting and solidification
- **Thermal expansion** during heating
- Nucleation **undercooling**
- **Orientation relationship** at the interface between Al<sub>2</sub>O<sub>3</sub> and Al
- **Strain** in solidified Al near the interface

In the following sections, the above observations will be made through presentation and analysis of results from experiments 1, 2 and 3. Finally, overall conclusions will be drawn in section 3.4.

#### 3.1 Experiment One

In experiment 1 three separate scans were made; the results will be reported in the order that they took place.

##### 3.1.1 S1

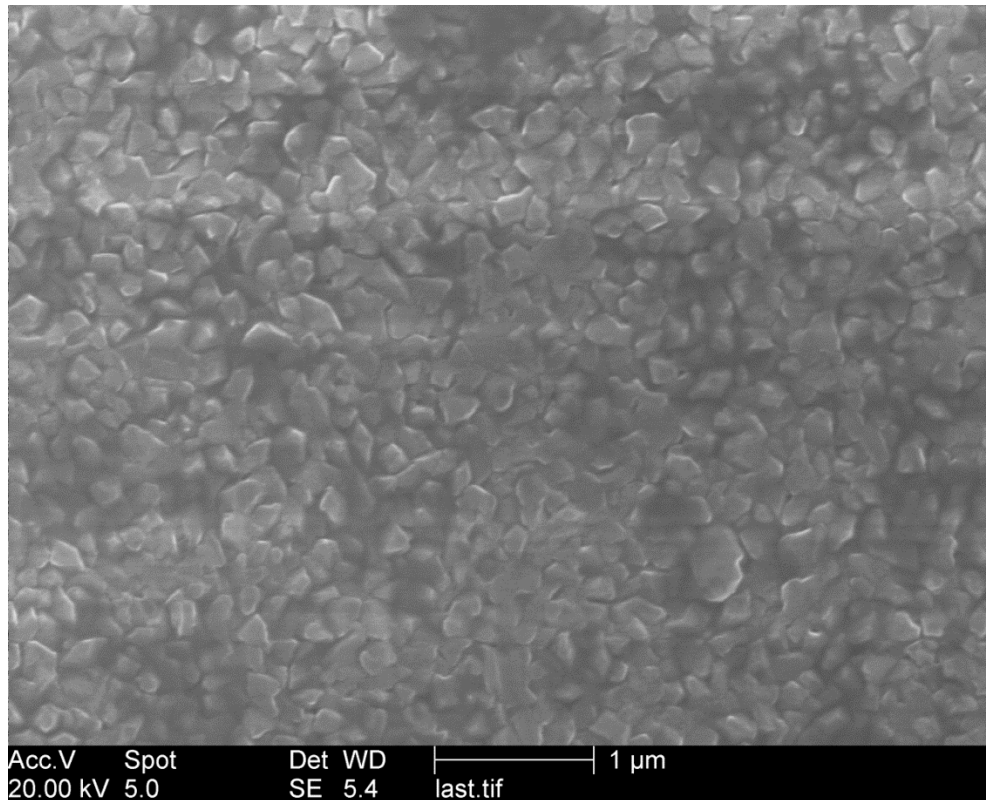
The Al/Al<sub>2</sub>O<sub>3</sub> system was a suitable candidate for preliminary work because it has exhibited large nucleation **undercooling**, as high as 175°C [10], [101], [135]. As previously stated, this permits a large ‘temperature window’ within which to work, facilitating an assessment of nucleation undercooling at this stage. On solidification, the following **orientation relationship** was identified as being likely to form between the Al<sub>2</sub>O<sub>3</sub> substrate and Al nucleus [136] and the experiment would also identify whether this occurred.

$$(001) \langle 110 \rangle \text{ Al}_2\text{O}_3 // (111) \langle 112 \rangle \text{ Al}$$

$$\text{or } (0001) \langle 11\bar{2}0 \rangle \text{ Al}_2\text{O}_3 // (111) \langle 112 \rangle \text{ Al}$$



It was important initially to understand the correlation between the morphology of the sample and the X-ray scattering produced from it. The sputter-deposited Al film was assumed to have a polycrystalline, granular-type morphology; verified by SEM analysis of the sample surface shown in Figure 3-1:



**Figure 3-1 - SEM micrograph of sample surface, showing granular morphology of sputter-deposited Al film. The size of individual granules is approximately 200nm.**

After completing alignment scans, the diffractometer was oriented such that scattering could be collected by the Pilatus detector from both the Al layer and  $\text{Al}_2\text{O}_3$  substrate in one image. The crystallography of the  $\text{Al}_2\text{O}_3$  substrate allowed the alignment to be performed relative to the  $(006)^{10}$  reflection, which was relatively close in  $2\theta$  to the features arising from two closed-packed planes in the Al layer. Table 3-1 shows this in detail:

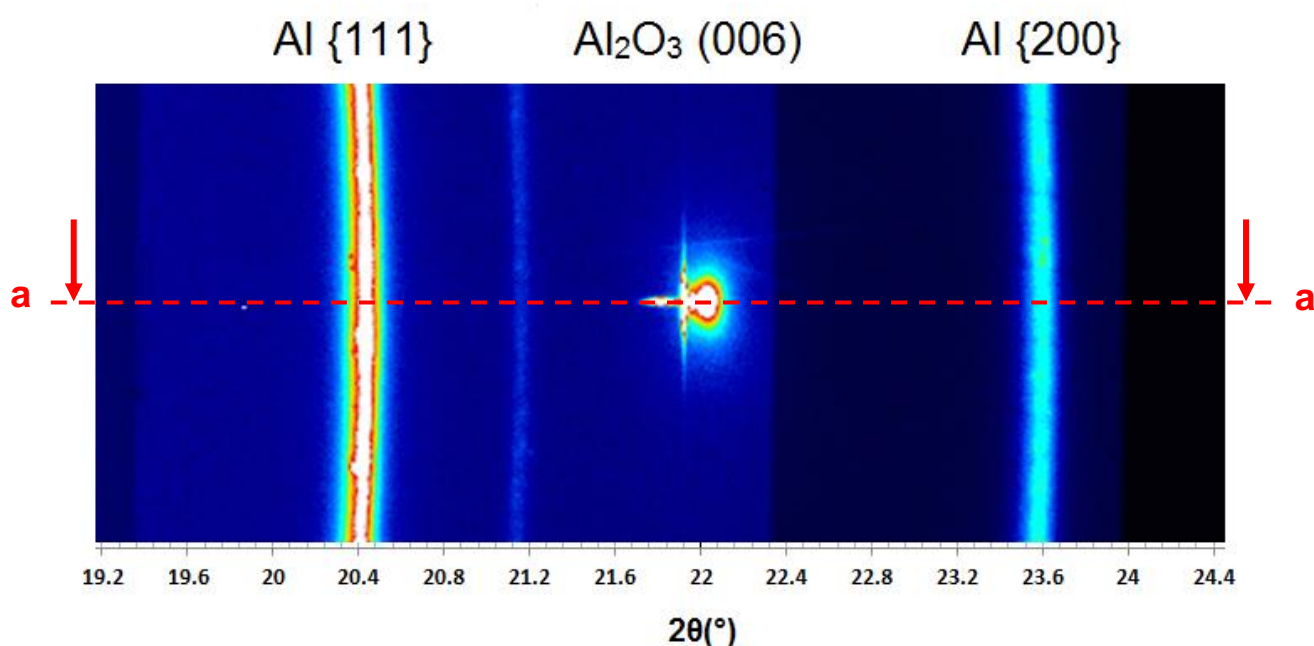
<sup>10</sup> As described in chapter 1, the  $\text{Al}_2\text{O}_3$  unit cell is made up of six planes with (001) character 'stacked' along the [001] direction; as such the individual planes are (006)

Peak Position in $2\theta$ (°)	$\theta$ (°)	d (Å)	Planar Family
20.35	10.2	2.338	Al {111}
22.00	11	2.165	Al <sub>2</sub> O <sub>3</sub> (006)
23.55	11.8	2.024	Al {200}

**Table 3-1 - Peak Positions and corresponding d-spacings with X-ray energy = 15keV ( $\lambda=0.826\text{\AA}$ ). Values of 'd' and ' $\theta$ ' are related through Bragg's Law.**

The initial state of the sample is shown in Figure 3-2. Here the single 'spot-like' central peak at  $2\theta = 22^\circ$  indicates the presence of the single crystal Al<sub>2</sub>O<sub>3</sub>. On either side of this feature, there are two intense streaks with a slight curvature, representing 2D sections through Debye diffraction cones. These arise from the randomly oriented crystallites in the polycrystalline structure of the Al layer. The continuous, unbroken nature of these features reflects the fine grain structure in the layer (observed directly in Figure 3-1). This morphology results from the sputtering process used to deposit the Al, and produces a scattering profile similar to that which would be expected in a powder diffraction experiment; the Al layer, being fine-grained and polycrystalline, could be understood as having a powder-like morphology.

Referring to the expected  $2\theta$  positions in Table 3-1, scattering features are indexed to the planar families to which they are associated. This is indicated for the reader by the  $2\theta$  scale along the base of Figure 3-2. It is notable here that the {111} feature is relatively more intense than the {200}; indicating a slight preference for a {111} texture in the sputtered film as expected [137], [138].

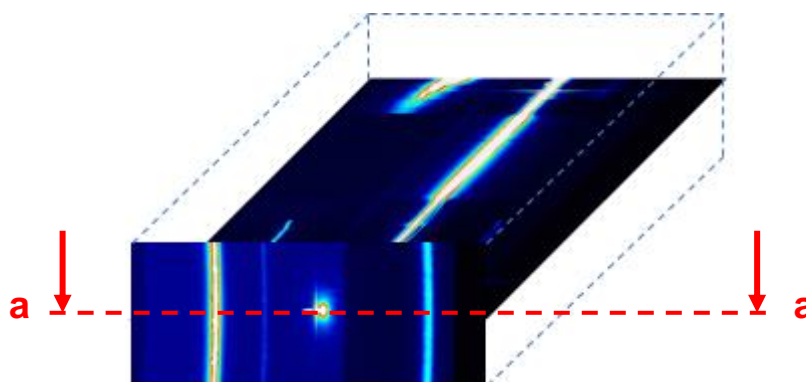


**Figure 3-2 – Initial detector image from Al/Al<sub>2</sub>O<sub>3</sub> sample at room temperature, showing the features of interest. Line ‘a-a’ indicates projection for Figure 3-4.**

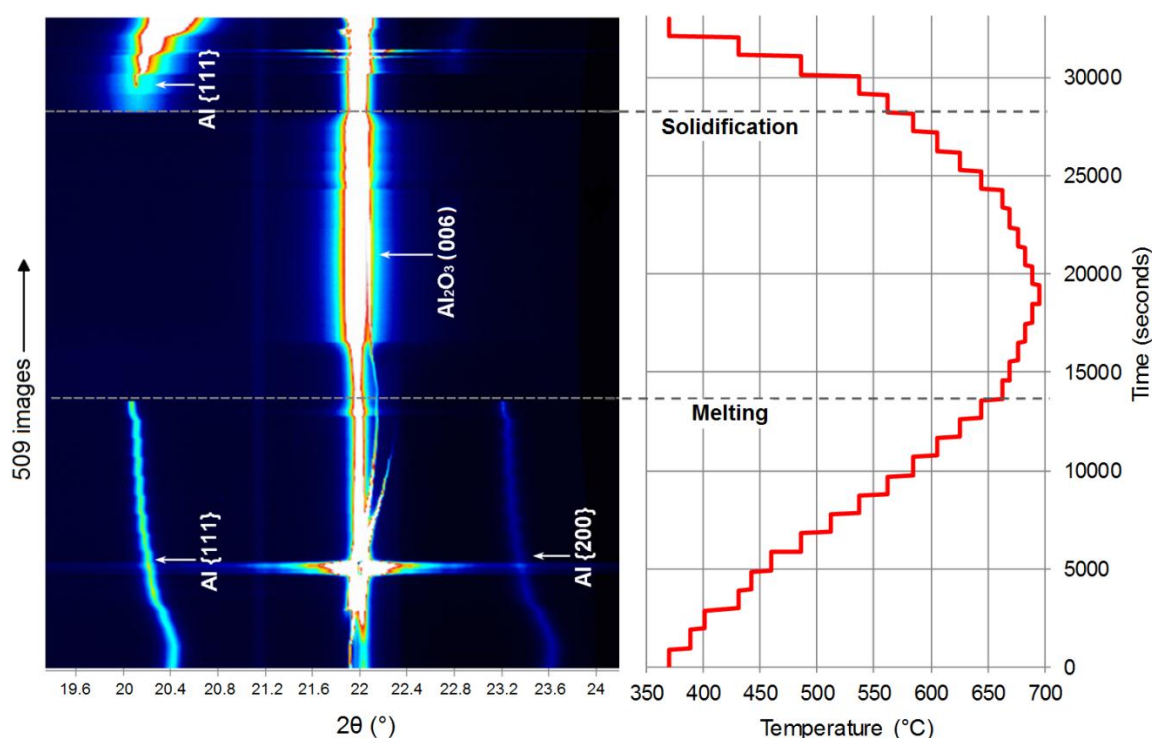
Heating and cooling cycles were applied to the sample using a substrate heater. This would alter the morphology in the sample; the changes would then be interpreted from the scattering pattern. The heating process comprised an initial manual heat to ~350°C, followed by an automated step-heating process using isothermal holds. Around temperatures of interest – between around 500°C and the maximum of ~700°C – steps between these isothermal holds gave a temperature resolution of approximately  $\pm 10^\circ\text{C}$ . This was deemed sufficient for detecting the nucleation **undercooling** of Al/Al<sub>2</sub>O<sub>3</sub> while allowing preliminary verification of the technique itself.

A total of 509 detector images akin to Figure 3-2 were collected over the course of the scan. Using FIJI [133] the total dataset was concatenated into a single ‘stack’ allowing the dataset to be manipulated in 3D. Orthogonal views can then be created to show the progression of the entire scan in a single image. This technique is a powerful tool for visualising diffraction data especially in the context of phase evolution [139], [140] and is presented in Figure 3-4.

Figure 3-4 shows the evolution of sample morphology over the course of the heating and cooling cycle. Referring to Figure 3-2, one can observe that all the features of interest are located along a central axis 'a-a'. Figure 3-4 is presented such that the viewer's perspective is to look 'down' on each image in the dataset as indicated by the arrows either side of axis 'a-a'; this is shown visually in Figure 3-3. By 'slicing' through the data in this way, all the relevant information (i.e. the 3 features) is retained with the change in perspective.



**Figure 3-3 – 3D volume indicating how the sequential plot in Figure 3-4 relates to the images collected from the Pilatus detector as shown in Figure 3-2**



**Figure 3-4 – *In situ* X-ray diffraction patterns for the Al/Al<sub>2</sub>O<sub>3</sub> system. The y-axis plots diffraction patterns sequentially through the heating and cooling cycle. Heating was manually ramped to ~350°C prior to the implementation of the displayed heating and cooling cycle using isothermal holds.**

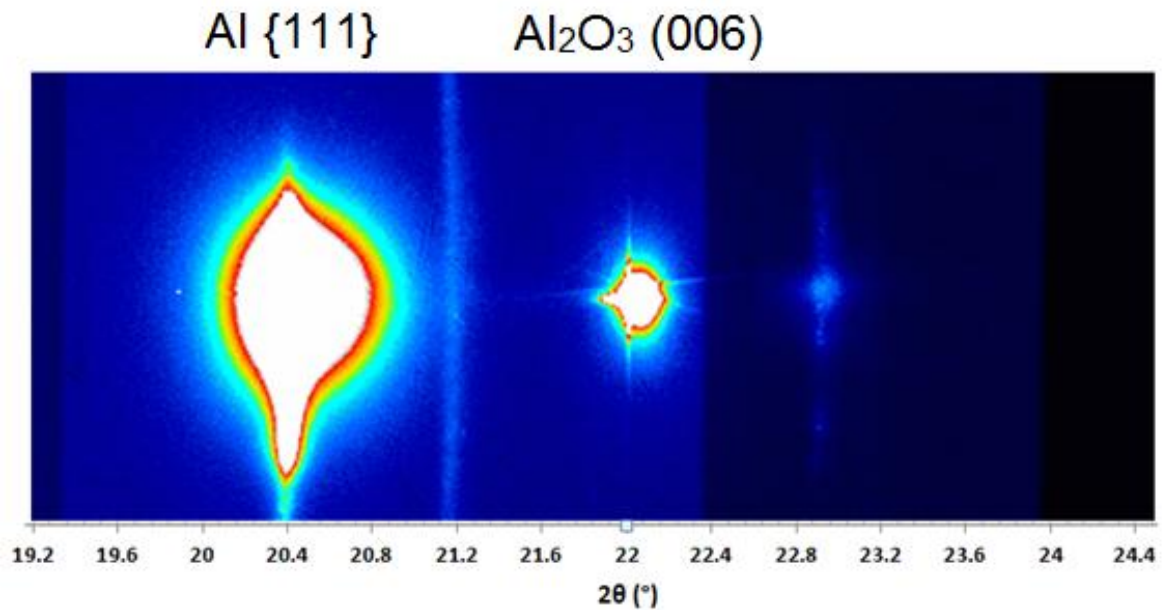
Referring to Figure 3-4: The 3 features, observed ‘face on’ in Figure 3-2, are seen ‘top down’ at the base of the left hand image. As heating is applied, Al features shift to (smaller  $2\theta$ ) larger  $d$ . At around 14000s, these features disappear, indicating that melting has taken place and that the Al is now in the liquid state<sup>11</sup>. The system continues through the thermal cycle, into the cooling stage. At approximately 28000s, a feature reappears, settling back to the original Al {111}  $d$  value as cooling proceeds.

The large ‘flare up’ of the Al<sub>2</sub>O<sub>3</sub> peak at approx. 5000s is not a structural change (the Al<sub>2</sub>O<sub>3</sub> would not be significantly affected by temperatures <1000°C), but results from slight sample movement under heating that brings the Al<sub>2</sub>O<sub>3</sub> (006) Bragg peak directly into the detector window. In normal operation the detector is

<sup>11</sup> liquids, lacking repeated structure or long-range order, do not strongly scatter in a particular direction like a solid; scatter from the short-range structure in the liquid is relatively weak, falling into background noise and/or not generating distinct peaks in this  $2\theta$  region

aligned such that it records the diffuse scattering just beside the actual peak, as exposure to the direct Bragg peak for too long can damage the CCD.

The features in Figure 3-4 are now analysed in greater detail. Firstly, note the shifting positions of the Al {111} and {200} features. Upon heating, they translate to larger  $d$ ; one may observe both gradual shifts (apparent in the early stages) and sharp transitions which reflect the jumps in between heating 'steps'. These changes in  $d$ , or atomic spacing, in these families of planes, indicates the **thermal expansion** taking place in the Al layer as the system is heated. In terms of  $d$ ; the {111} ring moves from its original value of 2.338Å to 2.369Å, and the {200} ring moves from 2.024Å to 2.054Å. We compare this percentage expansion – 1.59% and 1.69% in the {111} and {200} features respectively – with the predicted linear expansion of Al over the temperature increase applied. Using a linear thermal expansion coefficient of 23.5  $\mu\text{m/mK}$  [116] over a temperature increase of 628.3°C (melting temperature 660.37° - room temperature 32.07°C) the calculated percentage expansion would be 1.48%. This predicted value is close to the percentage expansion in lattice parameters observed on heating. This observation is straightforward but highlights the degree to which fine morphological changes can be recorded with this technique; the peak shift corresponds to a distance of only  $\sim 0.4\text{\AA}$  yet is readily observed from the images.

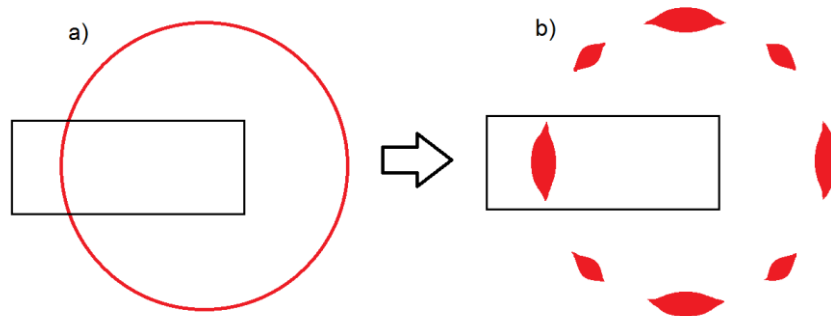


**Figure 3-5 - Detector image from endpoint of heating/cooling scan**

A number of further conclusions may be drawn from observation of Figure 3-4 and comparison with the detector images from the start and end of the thermal cycle (Figure 3-2 and Figure 3-5):

1. It is apparent that the Al {111} peak returns strongly upon solidification. This indicates that the aluminium has solidified with a preferred orientation. As the scattering geometry in this case is specular – i.e. the information relates to the *perpendicular* structure in the direction of the sample normal – the implication is that there is some alignment of {111} planes with the substrate surface. Figure 3-2 indicates that, prior to melting, the Al layer exhibited a bias to a {111} texture. However, the strength of the returning {111} feature on cooling (and the lack of an observable feature in the {200} position) indicates a significantly strengthened {111} texture in the solidified layer.
2. The final image in the cycle (Figure 3-5) highlights that the {111} feature appears as a large, broad spot, as opposed to the ‘streak’ in the initial state. The transformation of a consistent ring into a spot-like feature is indicative of a significant coarsening of the grain structure in the solidified layer with respect to the original. Compared with the perfectly spot-like Al<sub>2</sub>O<sub>3</sub> (006) feature, however, the {111} spot is slightly elongated along the path of the

original ring, and there are likely other similar features at various points around the transcribed 'ring' which are not captured in this detector image. This is indicated schematically in Figure 3-6. Overall, this suggests that there is a population of multiple larger grains, with {111} planes roughly parallel to the  $\text{Al}_2\text{O}_3$  surface, rather than a single Al crystal with {111} orientation.



**Figure 3-6 – Schematic showing transformation of the Al{111} feature from a) ring to b) spot-like. Rectangle indicates the field of view of the detector.**

3. A further observation can be drawn from the breadth of the returning {111} feature. There is a spread of scattering intensity across a range of  $2\theta$ , centred on the expected {111} position of  $20.4^\circ$ . Adjustment of the image brightness verifies that there is indeed a spread in intensity around this position; as such it is a real effect and not simply an imaging artefact. Peak broadening may be an indicator of inhomogeneous **strain** within the Al layer. A homogeneously or uniformly strained component would lead to a peak *shift*, whereas inhomogeneous strain can lead to peak broadening as seen in Figure 3-5 [141], [142]. Different regions of the Al may have solidified with different strain characteristics, leading to a spread of  $d$  values manifested as a broad diffraction feature. There are other possible sources of peak broadening, including:

- Instrumental contributions such as misalignment, beam divergence, etc
- Structural 'errors' such as stacking faults or twinning
- Small crystallite size (although this is only expected for nano-scale particles; solidified grains are likely to be larger)

While it is important to keep these various possibilities in mind, strain is judged to be the most likely candidate, primarily due to the large misfit of



lattice parameters between Al {111} and Al<sub>2</sub>O<sub>3</sub> (006). However, further analysis is required to conclusively demonstrate that strain is indeed the cause in this case.

4. A feature at  $2\theta = \sim 22.9$  is remote from the expected {200} position of  $\sim 23.6$ ; the size of this discrepancy indicates that this feature does not arise from the Al. There are a number of potential explanations for the origin of this feature, which are presented separately as follows:

4a) The feature may arise from oxidation of the Al, either at its surface or at the interface with Al<sub>2</sub>O<sub>3</sub>. Due to the high reactivity of aluminium, oxidation is inevitable, even under UHV conditions. The oxide layer is usually 3-6nm thick and has a predominantly amorphous structure [136] suggested to consist mostly of AlO<sub>4</sub> tetrahedra [143]. It is difficult to establish exactly which 'type' of Al<sub>2</sub>O<sub>3</sub> is present here, if any; some degree of crystalline structure would however have to be present in order for diffraction to take place and produce the feature seen in Figure 3-5. In the previously discussed HRTEM studies of the Al/Al<sub>2</sub>O<sub>3</sub> interface by Oh *et al*, oxygen is suggested to *"permeate the ordered liquid along the interface, and is then deposited as Al<sub>2</sub>O<sub>3</sub> by epitaxial growth, facilitated by the motion of interfacial steps"* [6]. In this case the implication is that Al atoms follow the hexagonal close-packing of the Al<sub>2</sub>O<sub>3</sub> substrate due to the strong Al-O interaction at the interface [4]; this however would lead one to conclude that this new oxide forming at the interface would simply contribute to the existing (006) scattering by replicating the structure. However, referring to published data [144], there is a strong  $\alpha$ -Al<sub>2</sub>O<sub>3</sub> peak expected at  $2\theta = 22.86^\circ$  arising from the {113} (or {11 $\bar{2}$ 3}) planar family. In the  $\alpha$ -Al<sub>2</sub>O<sub>3</sub> unit cell construction these planes are tilted approximately  $61^\circ$  away from the (006) – as such, if this feature does indeed arise from Al<sub>2</sub>O<sub>3</sub>, the implication is that this new oxide is forming with an in-plane structure approximating that along {113} planes.

4b) An alternative view is that the feature at  $2\theta = \sim 22.9$  arises from the passivation layer – oxide on the surface of the Al as it re-solidifies. This is

supported by the fact that the feature appears in the diffraction image some time *after* the Al {111} reflection (approximately 2000s); whereas oxide at the interface would be expected to appear simultaneously with the crystalline Al. Due to the high melting temperature and stability of  $\text{Al}_2\text{O}_3$ , the passivation layer on the Al would not be expected to melt on heating – instead, it would likely exist as ‘islands’ free to move on the liquid Al surface, or perhaps as small particles within the liquid. On cooling, this oxide would only produce a diffraction signal once a sufficient quantity was stationary, i.e., when the Al layer had solidified.

4c) One final possibility which merits consideration is that the feature does in fact arise from Al {200}, albeit from a small population of grains (indicated by the low intensity of the feature) and significantly strained (a large peak shift compared to the original Al {200} feature – the new  $2\theta$  value,  $\sim 22.9^\circ$ , implies a  $d$  of  $2.082\text{\AA}$ , compared to the equilibrium  $2.024\text{\AA}$ ), which gives a strain of 2.9%. The feature also appears to exhibit a degree of broadening (though this is far less apparent than in the {111} feature due to its lower intensity) which would indicate non-uniform strain as well.

Further analysis will be carried out to clarify which of the proposed mechanisms in 4) is correct. In any of the cases, the overall development of a strong {111} texture is undisputed, clearly indicated as it is by the dominating strength and shape of the {111} feature.

The nucleation **undercooling** can be derived from the presence of the peaks corresponding to Al crystals. During heating the Al layer remained in the solid state until the temperature reaches  $644.6^\circ\text{C} - 662.6^\circ\text{C}$ . During this transition the Al became liquid; according to the equilibrium melting temperature of Al ( $660.4^\circ\text{C}$ ). Only the  $\text{Al}_2\text{O}_3$  peak remains. After attaining a maximum temperature of  $\sim 700^\circ\text{C}$ , the system was cooled. At  $561.2^\circ\text{C}$  the {111} peak was observed indicating re-solidification of the Al. By correlating the dis- and re-appearance of the {111} peak during melting and solidification, an assessment of the

nucleation undercooling can be made. As stated previously, the thermal profile was applied to the sample through the use of approximately isothermal ‘holds’ at different temperatures around those theorised to be of interest (for example, either side of the expected melting temperature of 660.4°C). The reappearance of the {111} feature was observed at 561.2°C, however the solidification itself is likely to have occurred at some temperature between this and the 583.8°C hold which preceded it. With this in mind, the nucleation undercooling for Al in contact with (001) Al<sub>2</sub>O<sub>3</sub> is calculated:

$$\Delta T = 660^{\circ}\text{C} - (572 \pm 11^{\circ}\text{C}) = 88 \pm 11^{\circ}\text{C}$$

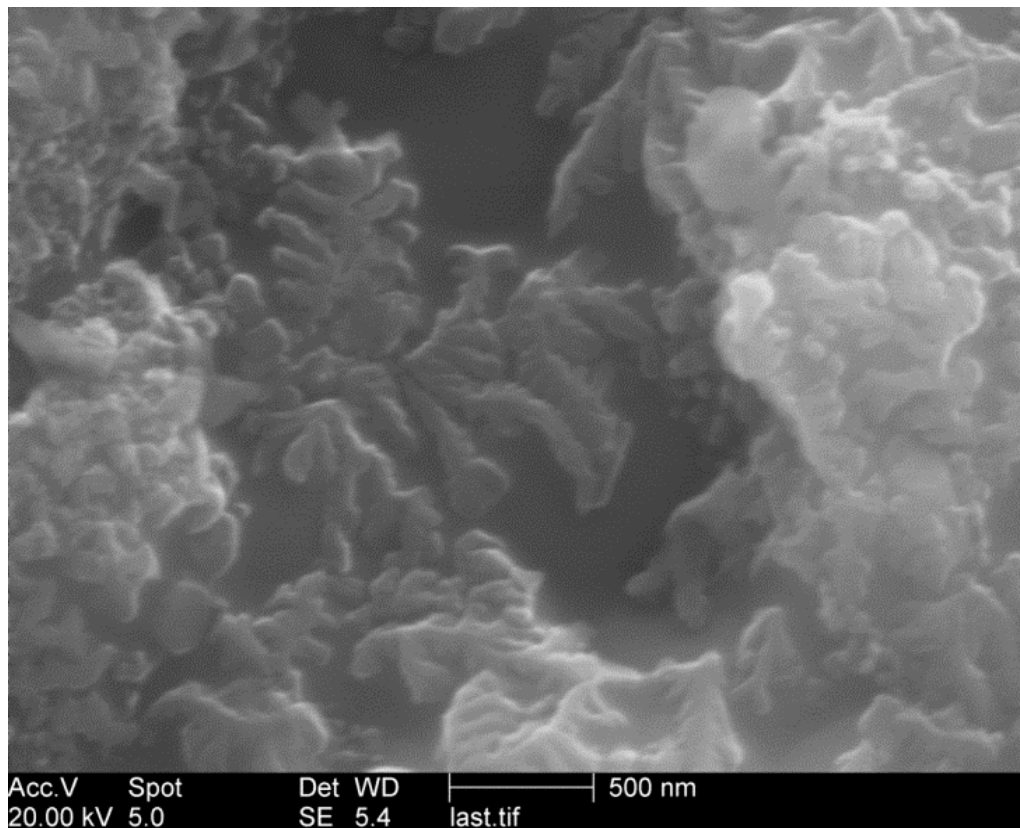
This measured value is within the broad range of those reported in studies of undercooling in aluminium droplets, in which the material system is the same due to the coating of Al<sub>2</sub>O<sub>3</sub> that naturally forms on the surfaces of such objects. Uttormark *et al* report a range  $40^{\circ}\text{C} \leq \Delta T \leq 50^{\circ}\text{C}$  from an experiment in which 845 individual nucleation events were recorded [100]. Under certain conditions<sup>12</sup>, however, values of up to 175°C [101] are reported. It should be noted that sample preparation in these experiments is significantly different, i.e. the undercooling was measured in aluminium droplets with an oxide skin, not against a specific crystal plane of the oxide.

The total volume illuminated by the X-ray beam is on the order of 0.03mm<sup>3</sup>; the volume within the aluminium layer itself is approximately 0.131x10<sup>-3</sup> mm<sup>3</sup> (following the method of Rowles [145]). Using the classical spherical cap model [11], [12] the estimated nucleation volume for Al is on the order of 660 nm<sup>3</sup> at the nucleation undercooling of 80K. Clearly the detected volume is far greater than that required for nucleation, but this ensures that a number of individual nucleation events, including early nucleation events, are captured. The time spent at each temperature level – approximately 15 minutes – is intended to promote growth of stable nuclei if the undercooling is sufficient: consequently an

---

<sup>12</sup> Various aspects including the production of extremely fine powders (i.e. very small droplets), cooling at extremely high rates, and from low superheats, are observed to contribute to a large  $\Delta T$

Al scattering feature is generated. These aspects in tandem ensure that the reported value for undercooling is unlikely to be an excessively large estimate.

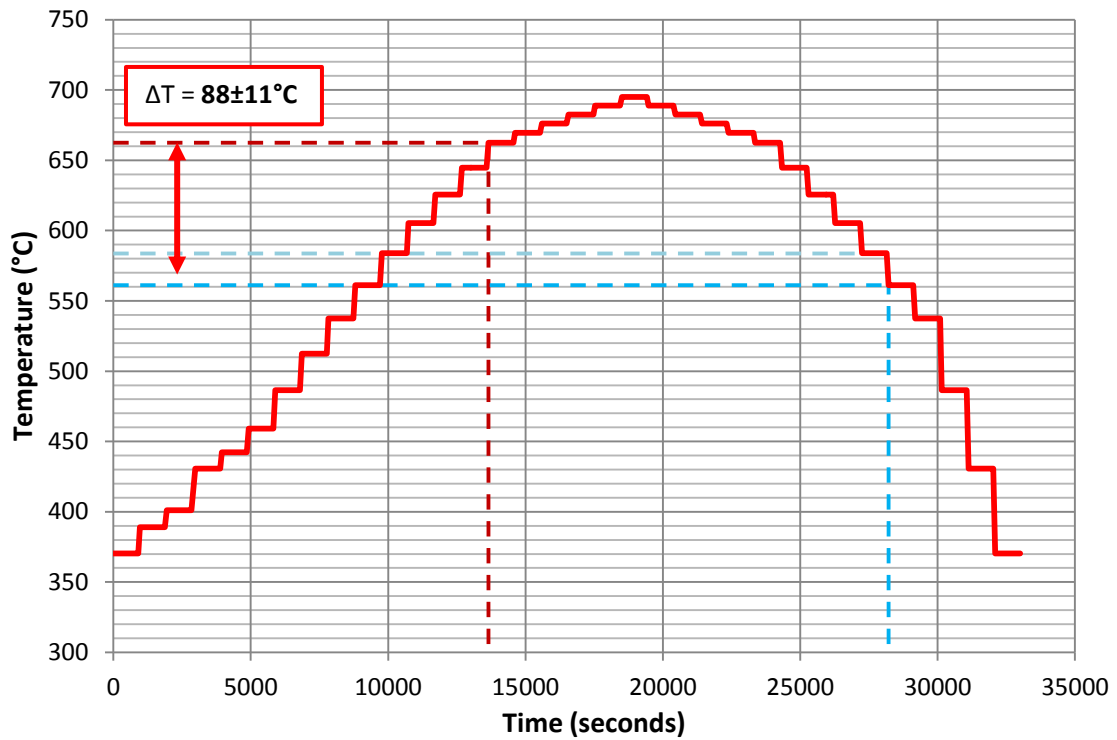


**Figure 3-7 – SEM micrograph of solidified Al. The featureless dark grey areas in the middle of the image are exposed regions of the  $\text{Al}_2\text{O}_3$  substrate surface. All other areas are Al. Primary Al dendrites are observed in the centre of the image.**

The SEM micrograph shown in Figure 3-7 gives some insight into the solidification geometry within the Al. A dendritic structure is observed to have grown parallel to the  $\text{Al}_2\text{O}_3$  surface. Therefore, if Al {111} planes are parallel to the surface as the results indicate, dendrite growth direction can be stated as  $\langle 112 \rangle$  i.e. along the {111} planes.

It was also observed that the Al layer appeared to ‘ball up’ on melting, forming a population of liquid droplets. The size of these droplets (estimated 20-30 $\mu\text{m}$ ) relative to the beam footprint means scattering from a number of them would have been captured during the scan. The results thus represent the average behaviour of individual droplets undergoing solidification. Figure 3-7 is a ‘zoom in’ to one of these droplet areas.

The  $(001) \langle 110 \rangle \text{Al}_2\text{O}_3 // (111) \langle 112 \rangle \text{Al}$  orientation relationship was indeed observed to form on solidification of the Al as anticipated. Figure 3-8 displays the assessment of the undercooling above superimposed on the temperature profile applied to the sample in S1.



**Figure 3-8 – Heating & cooling profile used for E1 S1. Dark red dashed line indicates temperature level at which Al features were observed to disappear. The blue dashed lines demarcate the scan in which the Al feature reappearance was observed.**

S1 demonstrated the potential of the X-ray scattering approach to the investigation of nucleation. The quoted value for nucleation undercooling in this system is subject to a particularly low temperature resolution; there is scope for significant improvement here. The range of other observations made demonstrates the potential of the technique to reveal qualitative information about the solidifying structure of the Al. Subsequent scans during E1 were designed to reveal these structures in greater detail. The E1 S1 results are reported separately in articles by the author of this thesis [146], [147].

### 3.1.2 S2

The second scan of the experiment was designed primarily to collect CTR scattering. CTR measurements contain detailed information about atomic structure at surfaces and as such represent an important tool to monitor the solidifying structure at the Al/Al<sub>2</sub>O<sub>3</sub> interface. A script was written to facilitate collection of the specular (0,0,*l*) and two off-specular (0,1,*l*) and (1,0,*l*) rods in one 'sweep'. This would be repeated at each isothermal temperature as defined by the aforementioned heater control. Due to the time required to collect each individual rod the steps between each isotherm were increased relative to S1. This again results in a poor temperature resolution and thus a poorly defined value for nucleation undercooling; however, it should still be comparable to the value measured from S1.

The (0,1,*l*) and (1,0,*l*) rods will be further discussed in chapter 4; any variation reflecting changes to the atomic structure at the interface tends to be concentrated in off-specular rods. Melting and solidification behaviour is more easily identified via specular scattering and it is this dataset which will be addressed first.

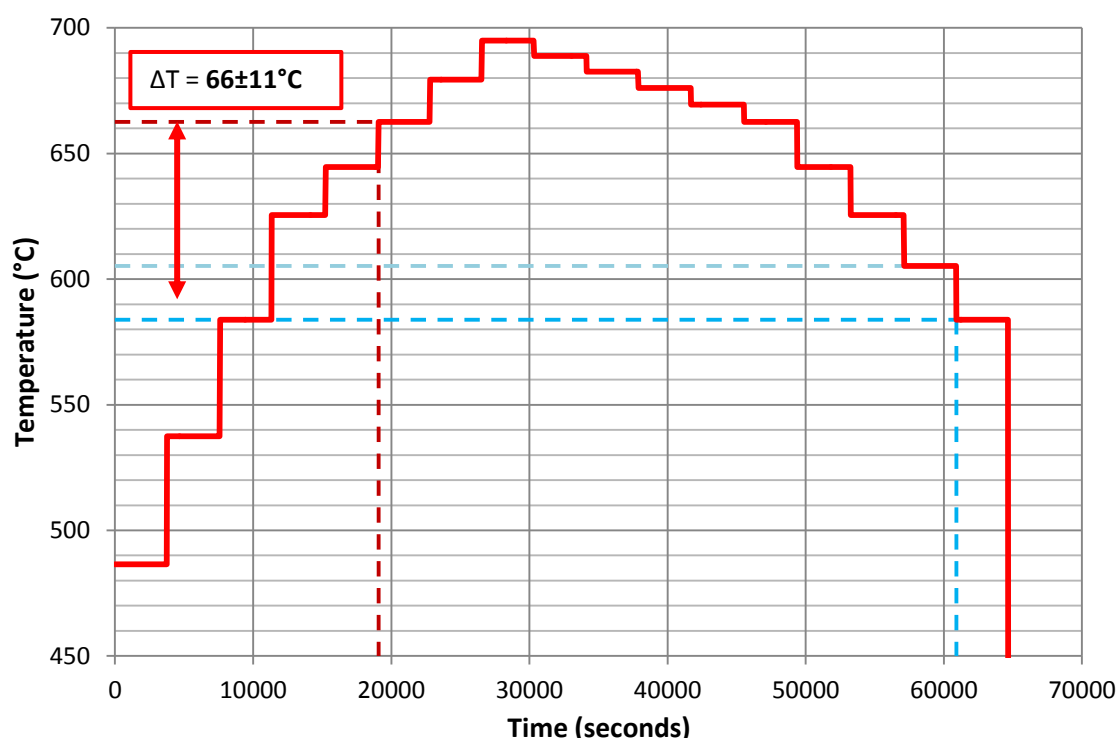
#### 3.1.2.1 Initial conditions

The same sample was used as for S1, therefore the resulting structure from the heating and cooling in S1 represented the initial condition in S2; i.e. a textured layer with strong {111} bias. This was manifest in the data by a strong {111} peak and the lack of any features corresponding to {200} or any of the next closest-packed families of planes, as Figure 3-10 later shows.

#### 3.1.2.2 Undercooling

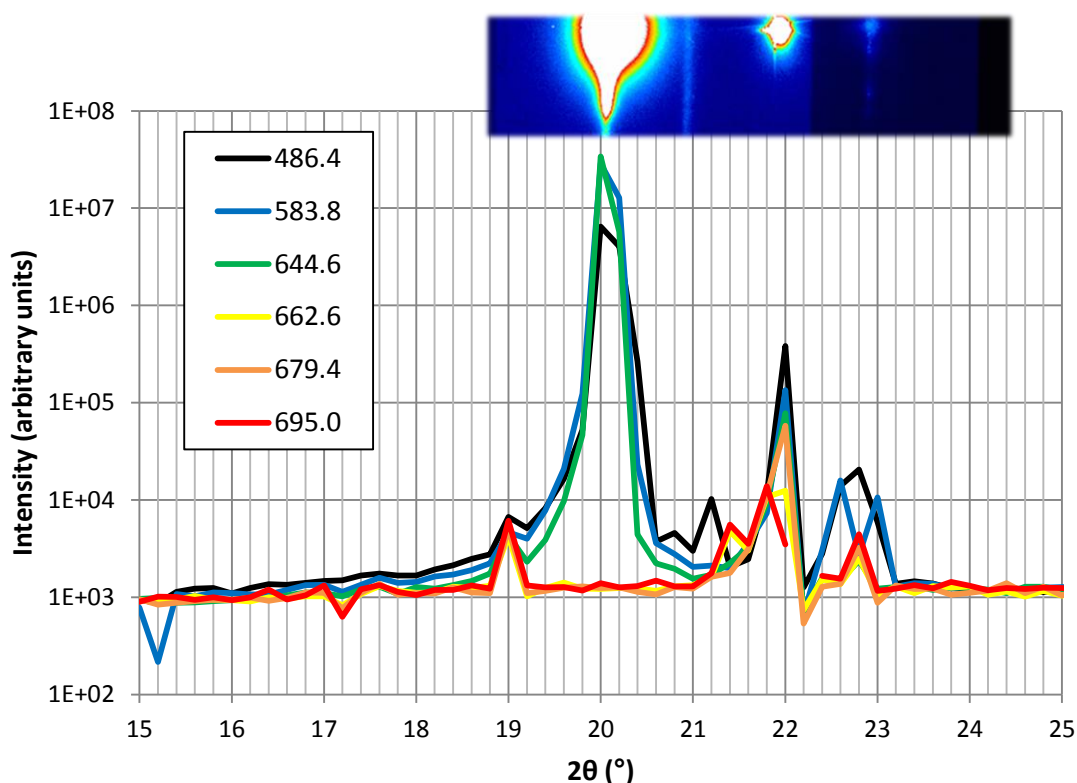
Using the (0,0,*l*) data a second assessment of the **undercooling** could be made. The following figures shows the temperature profile applied to the sample – note that this reflects the time taken for the *total* scan, not just for the specular scattering used in this initial assessment of undercooling – the aforementioned (0,1,*l*) and (1,0,*l*) CTR's were collected during the same scan. The overall duration of S2 was approximately twice that for S1. During the

cooling phase, steps between isothermal holds were designed to be finer while the Al was in the liquid region, and then increase in size below 660°C.



**Figure 3-9 – Temperature profile used for E1 S2. Dotted lines indicate temperature levels at which Al (111) peak disappeared (red) and reappeared (light blue – final scan showing no (111) feature; dark blue – (111) feature present)**

The following figures show a selection of the  $\theta$ - $2\theta$  plots which were generated from the (0,0, $l$ ) or specular data at every isothermal hold. The disappearance and subsequent re-appearance of the Al {111} peak is correlated with the temperature recorded to give an assessment of the required undercooling as in S1. Due to the significantly wider range of  $2\theta$  covered by these scans (compared with S1) the image concatenation technique used previously is not appropriate; plots of scattered intensity against  $2\theta$  position are more effective. The displayed intensity values have been background subtracted, however geometric corrections [106] are not applied as the relevant diffractometer coordinates were not recorded in the data; these corrections would however have no effect on the presence or location of characteristic peaks and the observation of these features stands as a method to assess the undercooling despite the non-idealised data.



**Figure 3-10 – Selected specular data from E1 S2 during heating. Large central peak at  $2\theta = 20.2$  arises from Al {111}. Smaller peak at  $2\theta = 22$  arises from  $\text{Al}_2\text{O}_3$  {0006}. Peak at  $2\theta = 22.8$  is suggested to arise from oxide. Part of the detector image is included to assist the reader in identifying the correlation between these and the  $I$  vs  $2\theta$  plot.**

It is worth reiterating that the endpoint of E1 S1 represents the initial conditions for S2. This is reflected in the plots above, and the final detector image from S1 (shown previously in Figure 3-5) is superimposed above to assist the reader in understanding this. As expected, the Al {111} peak is the dominant feature, confirming again the strong {111} texture generated in the solidified Al. The  $\text{Al}_2\text{O}_3$  (006) peak is also clear, and in Figure 3-10 is observed to persist throughout the heating process – note that the slight shift to  $2\theta \sim 21.8$  likely indicates thermal expansion in the substrate<sup>13</sup>. The third peak at  $2\theta \sim 22.8$  may, as suggested, arise from an oxide passivation layer formed on the Al – a claim lent credence by the fact that it also persists throughout the heating process – such an oxide layer would not melt, but would remain on the surface of liquid Al. A small but persistent feature at  $2\theta = 19$  may also arise from this passivation layer - a peak from  $\alpha\text{-Al}_2\text{O}_3$  {104} is expected at  $2\theta = 18.7$ . These observations

<sup>13</sup> This kind of slight peak shift is also observed in S1, but the imaging adjustments used to display Figure 3-4 correctly obscure this somewhat in the image



also appear to confirm that the features do not in fact arise from strained Al {200}; had they done, the features would have disappeared on melting. The hypothesis 4c) proposed from the S1 results can thus be eliminated, and it is apparent that the feature around  $2\theta \sim 22.8$  in both S1 and S2 likely arises from an Al oxide phase.

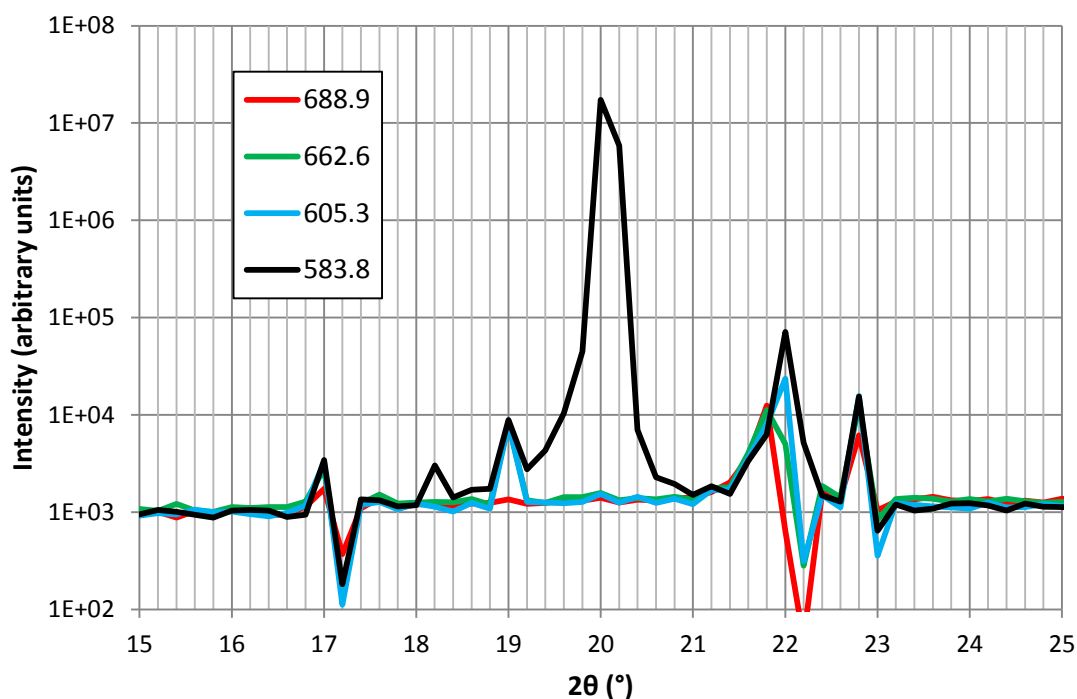
Regarding the issue of Al passivation, it is fair to point out that these structures, if they exist, are at such a small ( $\sim 5$  nm thickness) and localised scale that they may not adopt well-defined morphology or exhibit the exact behaviour of characteristic  $\text{Al}_2\text{O}_3$  phases. This may explain the discrepancy in the observed peak positions. The passivation theory is sensible due to the high reactivity of Al; its propensity to form an oxide layer is diminished yet not eliminated through being under UHV conditions.

An alternative view is that the features are not from a passivation layer at all, but arise from sample mountings or other surrounding material, which may have moved into the beam path as a result of thermal expansion or other movement. While it is important to keep these concerns in mind in all diffraction experiments, the alignment processes (and regular re-alignment scans throughout the thermal cycle) are intended to eliminate or at least reduce the risk of this occurring. In this specific case, tantalum wires are used to secure the sample to the heater surface - these would be the strongest candidate to move into the beam path as they are closest to the sample itself. Based on published crystal structure data, however, Ta [148] is not expected to produce peaks at the observed positions in  $2\theta$ . It is thus appropriate to consider the oxidation mechanism as the primary candidate for the appearance of the features in question.

Data from particular isothermal holds (rather than the entire set) have been selected for the above plot to highlight the clear phase transition that occurs in the Al. The extremely strong Al {111} peak apparent at the first 3 isotherms (at  $T = 486.4^\circ\text{C}$ ,  $583.8^\circ\text{C}$  and  $644.6^\circ\text{C}$ ) disappears completely on the transition to  $662.6^\circ\text{C}$  (which is the next isothermal hold in the sequence). Once again, the Al peak disappears around the expected equilibrium melting temperature. A further

two isotherms at higher temperatures were subsequently performed to clarify the peak disappearance and ensure the Al was indeed in the liquid state.

Following this, the temperature profile entered the cooling stage. Figure 3-11 shows selected data from this part of the experiment:



**Figure 3-11 - Selected specular data from E1 S2 during cooling.  $\text{Al}_2\text{O}_3$  (006) peak at  $2\theta = 22$  remains visible throughout. Central Al {111} returns on scan at 583.8°C.**

The initial 3 scans on the above (at  $T = 688.9^\circ\text{C}$ ,  $662.6^\circ\text{C}$  and  $605.3^\circ\text{C}$ ) exhibit only the peaks arising from  $\text{Al}_2\text{O}_3$  (006) and the suggested persistent oxide passivation layer. The scan at  $T = 583.8^\circ\text{C}$  clearly shows that the Al {111} feature has returned, indicating solidification. Applying the appropriate tolerance to the calculation as a result of the steps between isothermal holds, the undercooling can be calculated for S2 as follows:

$$\Delta T = 660^\circ\text{C} - (595 \pm 11^\circ\text{C}) = 65 \pm 11^\circ\text{C}$$

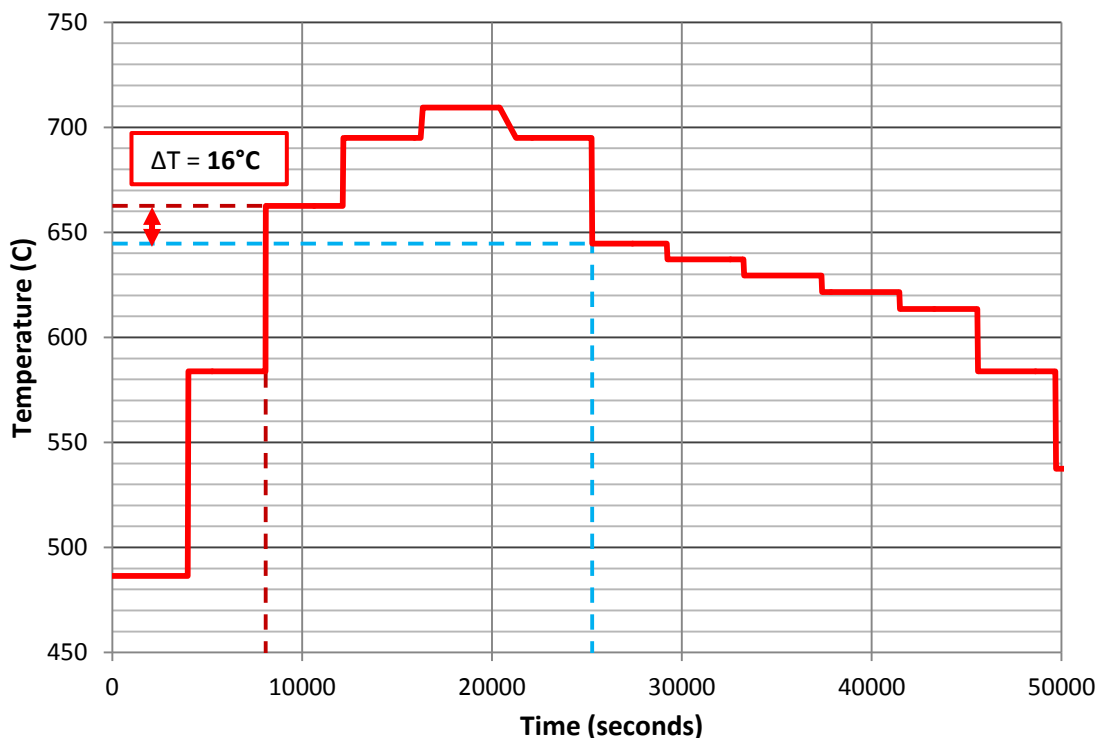
A lower undercooling is identified compared with S1; however there is overlap between the two cases when considering the large margins of error associated with the values that arise as a result of the steps between the isothermal holds.

**Thermal expansion** is less apparent in the results from S2; this is primarily due to the larger  $2\theta$  scale over which measurements are taken. A marginal peak shift can be observed on heating in Figure 3-10 but it is clear that the direct imaging method used for S1 is significantly more effective for studying this particular phenomenon.

The longer scans used in S2 were necessary for the collection of CTR's to a high  $l$ -index. For the specular scattering data the large  $2\theta$  range that results is perhaps unnecessary; although the intention was to try and observe a larger number of features, the Al {111}, {200} and Al<sub>2</sub>O<sub>3</sub> (006) reflections were dominant and in relatively close proximity.

### 3.1.3 S3

S3 was a repeat of S2 at slightly different temperature levels. Steps were significantly larger than in S1 and S2 to investigate the effect of rapid heating and cooling. The following shows the temperature profile applied in S3.



**Figure 3-12 – Temperature profile used for E1 S3. Dashed lines indicating dis- and reappearance of Al features as before.**

The sharp drop in temperature at approx. 7 hours is analogous to a quenching process; i.e. an instant reduction in temperature. This provides a strong driving force for nucleation and, as is clear from the data, the Al layer was indeed observed to have resolidified as a result. The resulting undercooling is significantly lower than that observed in S1 and S2. As the following graphic indicates, the characteristic Al {111} peak is observed at the 644.6°C isotherm:

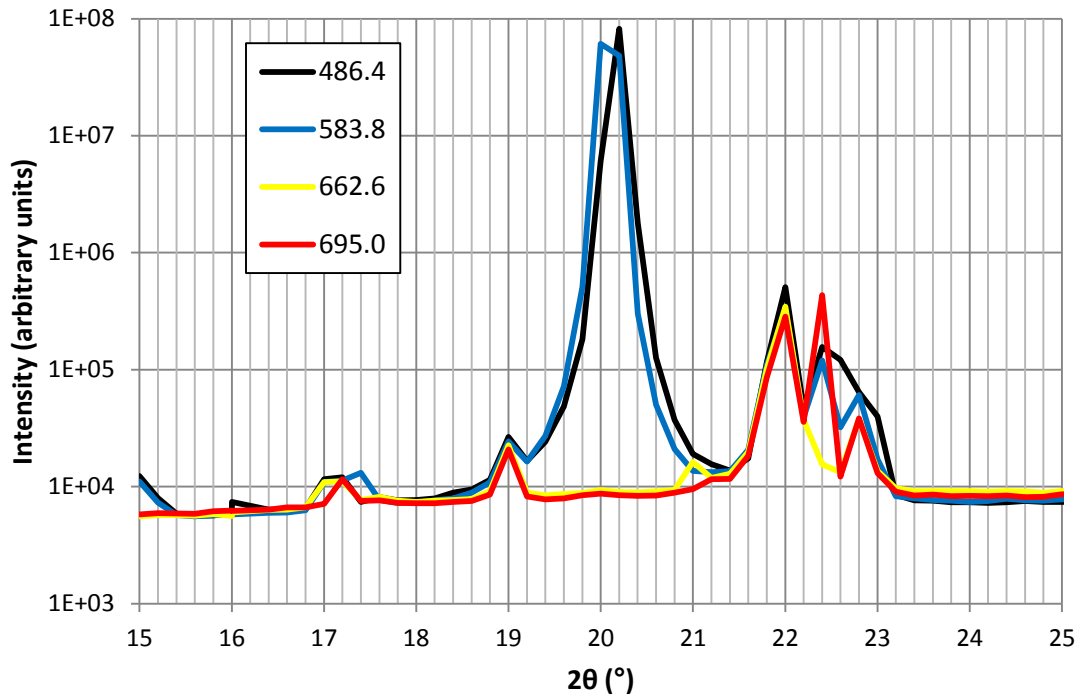
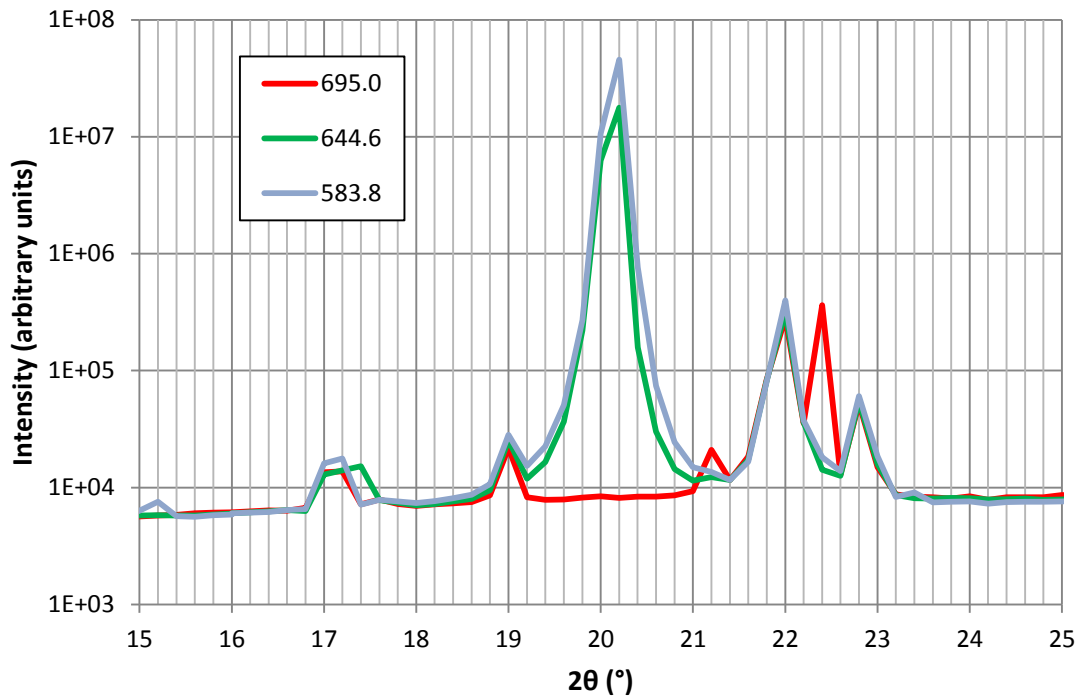


Figure 3-13 – Selected specular data from E1S3 during heating



**Figure 3-14 - Selected specular data from E1S3 during cooling**

Solidification takes place at some point between the equilibrium freezing temperature of ~660°C and the scan temperature of 644.6°C. The undercooling is therefore calculated as follows:

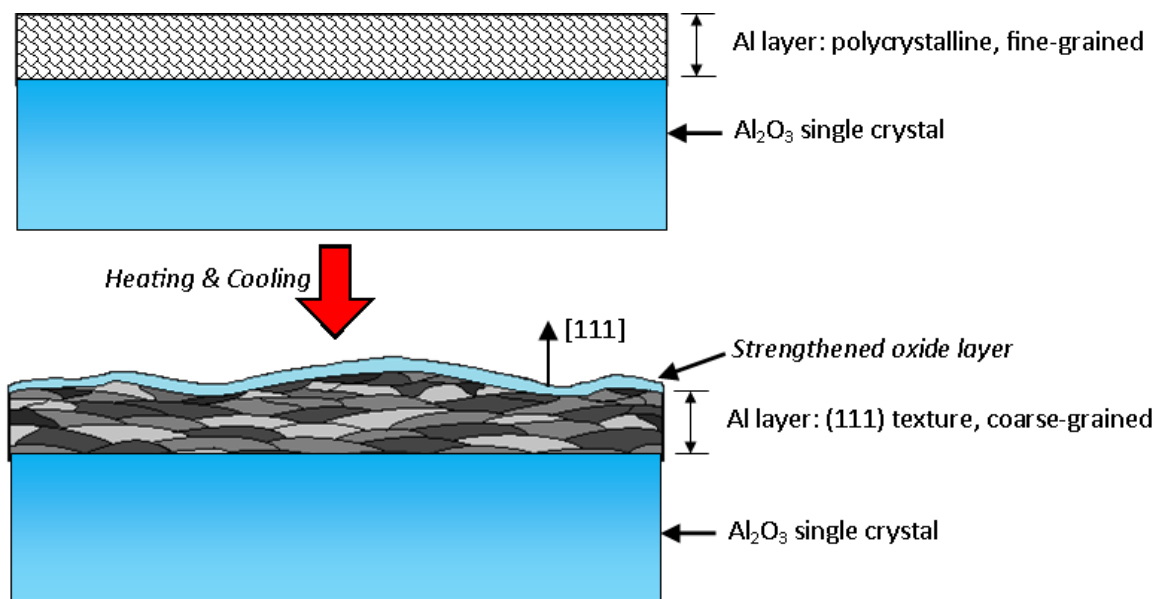
$$\Delta T = 660^{\circ}\text{C} - (652 \pm 7.9^{\circ}\text{C}) = 8 \pm 7.9^{\circ}\text{C}$$

It is unclear why this value is significantly lower than those recorded from S1 and S2. It is especially puzzling given that a fast cooling rate usually results in an *increased* undercooling. Compared with S1 and S2, the low  $\Delta T$  here implies that nucleation sites more potent than a clean  $\text{Al}_2\text{O}_3$  (001) surface are present. These may arise from: some contamination occurring between scans; an increased surface roughness, perhaps due to repeated thermal cycling; or the presence of oxide and/or passivation layers. In any case, the above result is deemed unreliable and so the results from S1 and S2 will be used in future analysis.

### 3.1.4 E1 Conclusions

In terms of melting and solidification, E1 provided useful information regarding both the nucleation undercooling and the orientation relationships which develop between Al and  $\text{Al}_2\text{O}_3$ . The persistence of the peak at  $2\theta = \sim 22.9^\circ$  suggests that it does indeed arise from an oxide layer. Having formed during S1, the feature remains throughout both S2 and S3 and appears to be unaffected by the thermal profile. The fact that it was not observed in the initial condition (i.e. prior to S1) indicates that some aspect of the heating/cooling processes has resulted in either the formation of a new oxide layer, or in the thickening/strengthening of an existing passivation layer, the structure of which was *initially* not sufficient to produce a diffracted signal.

Based on all the S1 observations, the following presents the *suggested* morphological transition in the sample as a result of heating and cooling:



**Figure 3-15 – Suggested morphological transitions in E1 sample resulting from heating and cooling cycles. Note that Al grains in the second image are shown ‘flattened’ but in reality may have a columnar or equiaxed morphology.**

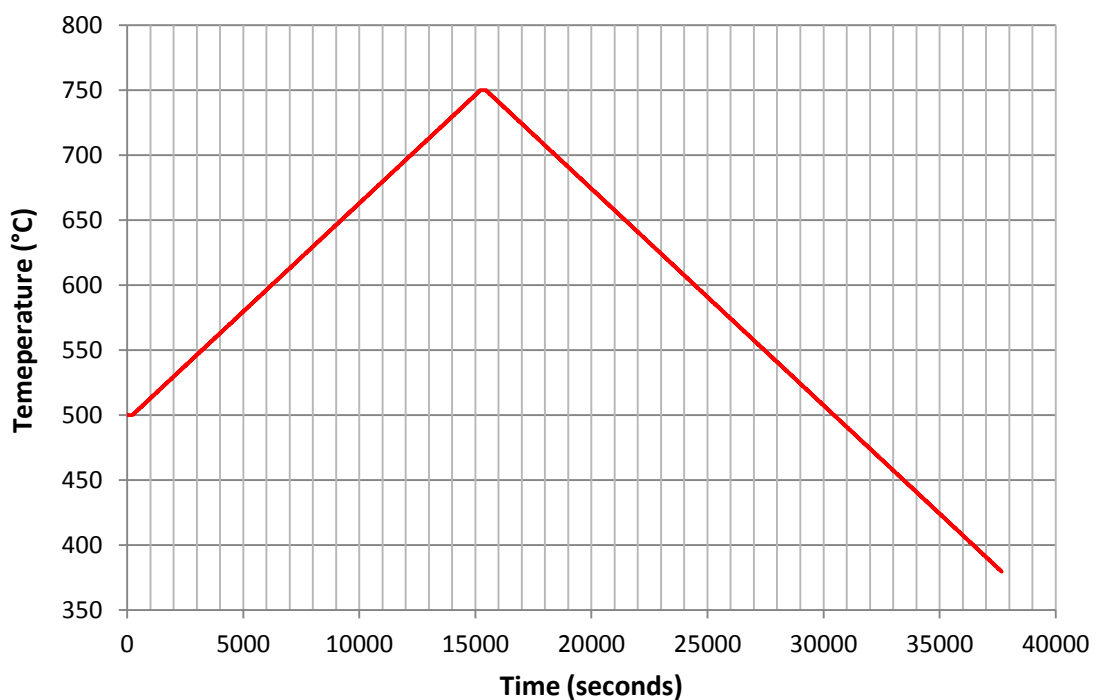
The above is suggested primarily as the transition during S1, in which the most dramatic transition was noted – from an as-sputtered, polycrystalline, fine-grained layer to the strongly textured, coarse grained morphology shown. This is supported by the microscopy shown in Figure 3-1 and Figure 3-7. During S2 and S3 the Al itself melts; however the morphology on cooling is suggested to

be effectively the same. The suggested oxide layer may however be more stable during these scans as suggested by the persistence of the corresponding features.

It is important to point out that the formation of a coarser grain size on cooling is likely influenced by the relatively slow cooling used in the scans. It is also fair to note that if the  $\text{Al}_2\text{O}_3$  surface is assumed to be the primary nucleating surface for the Al, most of the 'melt' is remote from it, which reduces the number of individual grains which are nucleated. As solidification proceeds, self-nucleation via existing solid Al crystal will come into play. The resulting higher density of available nucleation sites will likely lead to a decreasing grain size in the regions of the Al which solidify last (assumed to be those most remote from the substrate) as indicated schematically in Figure 3-15.

### 3.2 Experiment Two

As described in chapter 2, many problems were experienced in E2; primarily the difficulties in commissioning new equipment and de-wetting issues with the samples themselves. Consequently, the results are of little use in terms of a study of nucleation. Despite this, the heater device itself exhibited excellent temperature stability and control, potentially rendering it a useful tool in future experiments. Note the following profile recorded from the heater thermocouple over an approximately 11-hour scan:



**Figure 3-16 – Temperature profile achieved with heater device during E2**

Experiment 2 was beset by difficulties, but served to validate the performance of the heater as shown. It also offered an opportunity to observe scattering from a system comprising different materials; primarily the fine-grained graphite from which the heater crucible section was made. The issues experienced provided some of the motivation to return to standardised sample geometry for E3.



### 3.3 Experiment Three

Experiment three (E3) took place at beamline ID03 of the ESRF. It involved work on three separate samples, denoted X, A, and W. Chapter 2 details preparation in full; Table 3-2 acts as a quick reference:

Sample	Material	Description
<b>X</b>	Al/Al <sub>2</sub> O <sub>3</sub>	Al <sub>2</sub> O <sub>3</sub> single crystal with pre-deposited Al layer on surface
<b>A</b>	Al/TiB <sub>2</sub>	TiB <sub>2</sub> substrate prepared by sputtering onto molybdenum block; Al layer then pre-deposited onto TiB <sub>2</sub> surface
<b>W</b>	Al <sub>2</sub> O <sub>3</sub>	Clean Al <sub>2</sub> O <sub>3</sub> single crystal – no surface preparation or pre-deposition

Table 3-2 – Samples used in E3

This chapter details the observations on melting and solidification made using sample X. CTR scattering was collected from samples X and W and will be explored in chapter 4. Sample A represents a different material system and is discussed in chapter 5.

#### 3.3.1 Sample X

Two initial challenges were identified for this sample:

1. Clarify the **undercooling** in an Al/Al<sub>2</sub>O<sub>3</sub> system
2. Confirm and better characterise the morphological transitions in the Al/Al<sub>2</sub>O<sub>3</sub> system indicated by the E1 results  
(Collection of (0,1) CTRs at higher resolution was also performed using this sample; this is explored in chapter 4)

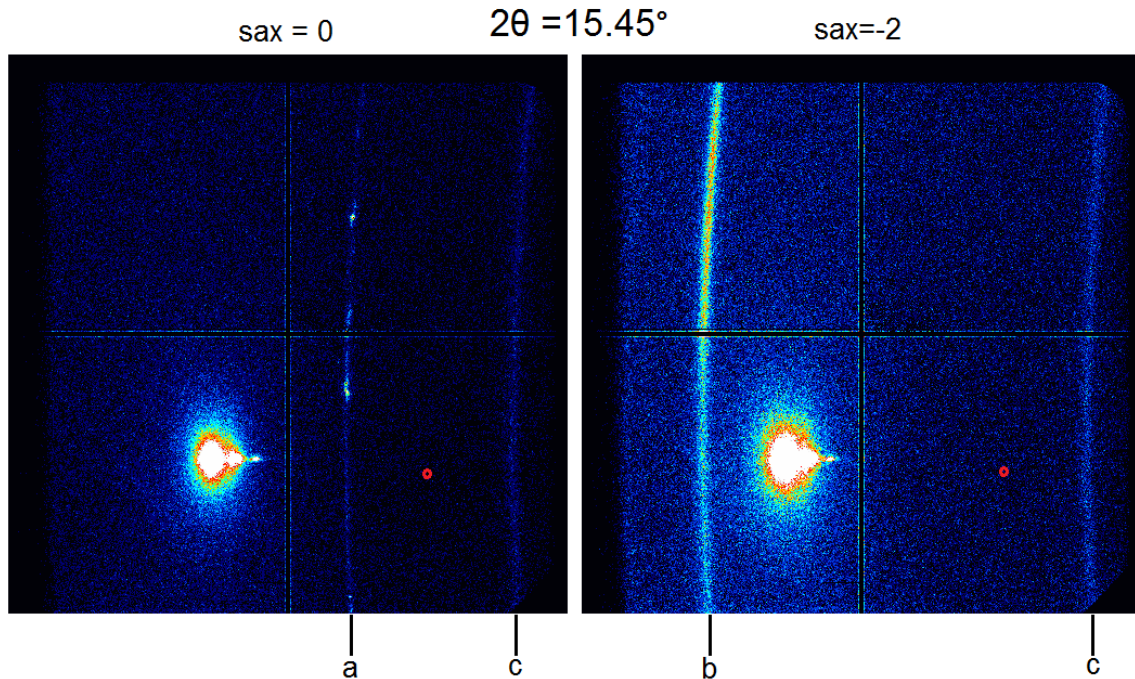
An X-ray energy of 20keV ( $\lambda=0.62$ ) was used for all scans on sample X. Table 3-3 shows expected peak positions for the 3 features of interest at this energy.

Peak Position in $2\theta$ (°)	$\theta$ (°)	d (Å)	Planar Family
15.24	7.62	2.338	Al {111}
16.46	8.23	2.165	Al <sub>2</sub> O <sub>3</sub> (006)
17.62	8.81	2.024	Al {200}

**Table 3-3 - Peak Positions and corresponding d-spacings with X-ray energy = 20keV  
( $\lambda=0.62\text{\AA}$ )**

### 3.3.2 E3 S1: Imaging approach

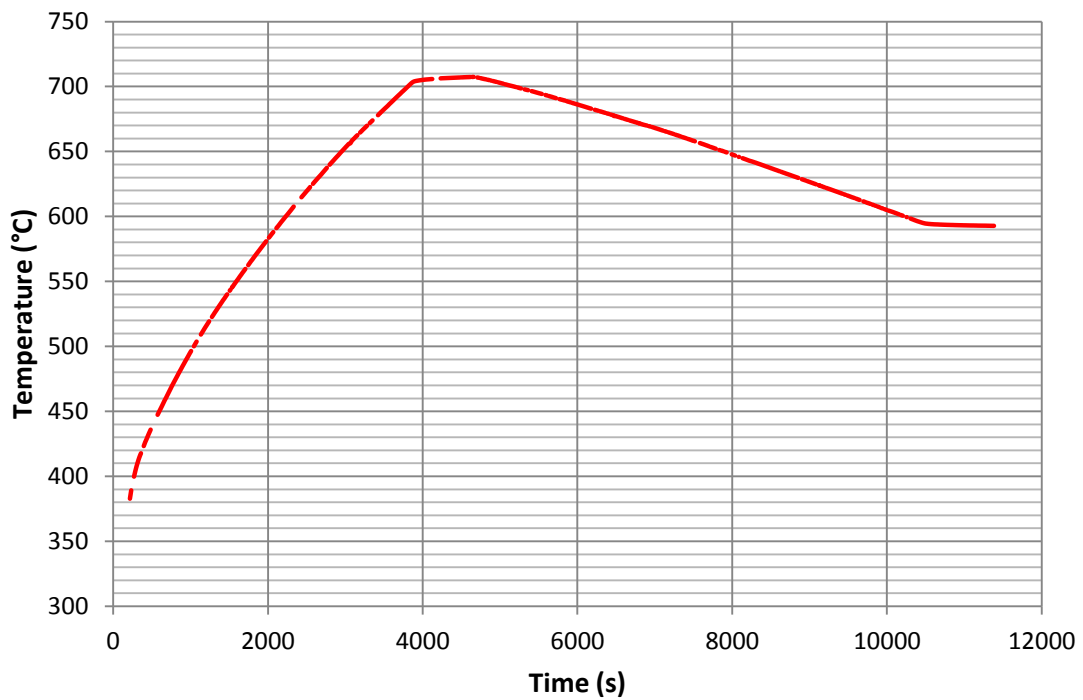
To address the first challenge, an approach similar to E1 S1 was adopted. A specular scattering geometry was implemented, and the diffractometer aligned such that scattering features from both the Al layer and Al<sub>2</sub>O<sub>3</sub> substrate could be recorded in the same window. Initial scans located the (006) peak from the Al<sub>2</sub>O<sub>3</sub> single crystal. A  $2\theta$  position of 15.45° was optimal to record scattering from this point as well as capturing a number of powder-like rings in the vicinity. As the sample was surrounded by different materials used for mounting (Ta wires, Mo baseplate etc) it was important to initially identify which powder rings arose from the Al layer, and which arose from these surrounding materials. For this a rocking scan was performed; tilting the sample about the x-axis in the diffractometer reference frame while maintaining the  $2\theta$  position. This was done through adjustment of the hexapod; the rotational axis, called 'sax', was cycled between sax=0 and sax=-2. The following image shows the comparison between the two positions (taken at room temperature).



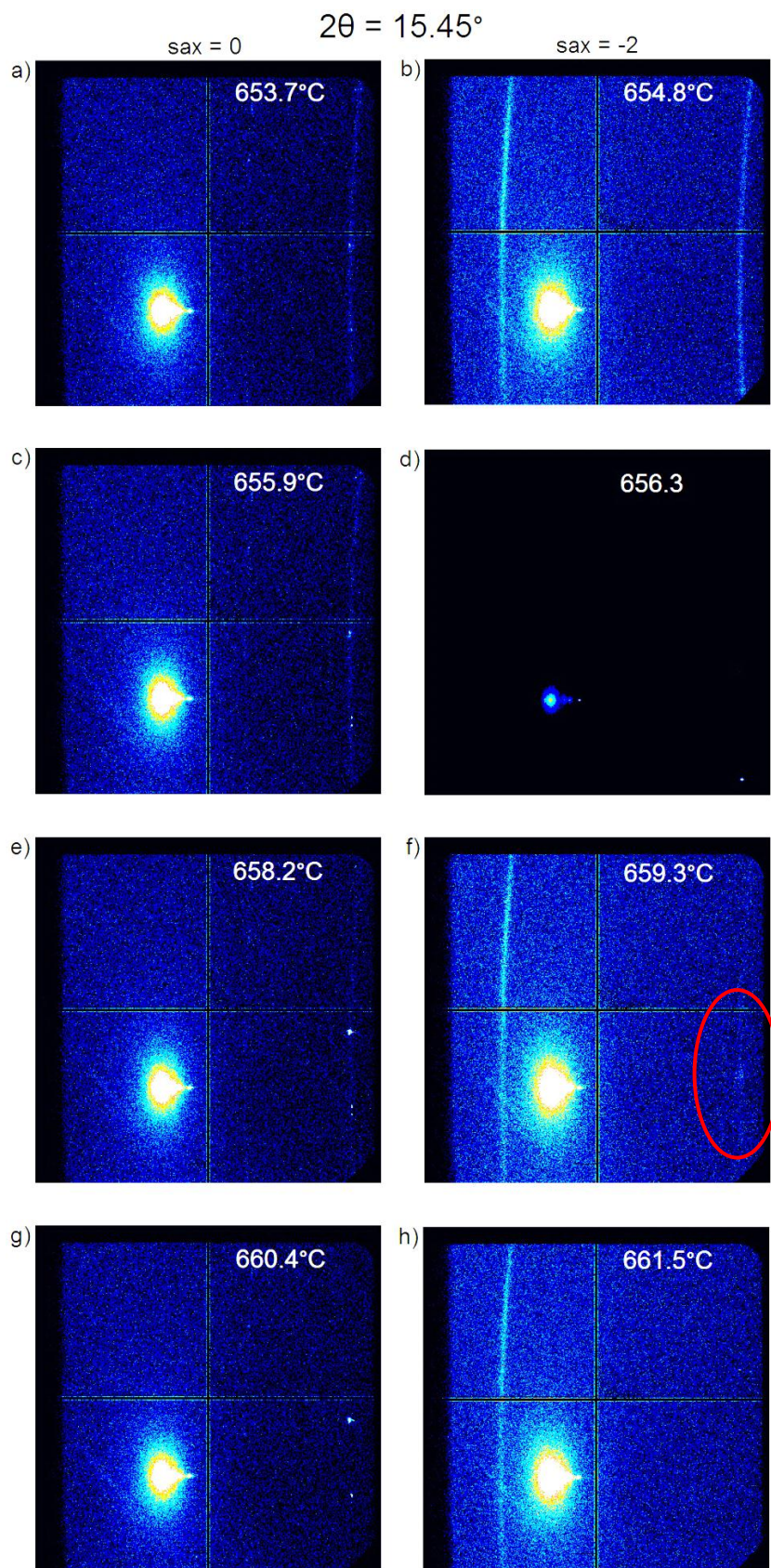
**Figure 3-17 – Images from Al/Al<sub>2</sub>O<sub>3</sub> sample indicating disparity of powder-like features at different sample rotations. Stated 2θ position (15.45°) is centred on the red dot in the lower right quadrant. Bright ‘spot’ on both images is the Al<sub>2</sub>O<sub>3</sub> {0001} feature. Within the image: a) feature only appearing at sax=0 b) feature only appearing at sax=-2 c) feature appearing at both sax=0 and sax=-2 therefore arising from the Al layer**

Figure 3-17 shows that the feature denoted ‘c’ occurs at both positions, whereas ‘a’ and ‘b’ appear only at sax=0 and sax=-2 respectively. It is clear then that features ‘a’ and ‘b’ arise from components of the heater or mounting; illuminated by the X-ray beam only at the corresponding ‘sax’ positions. Conversely, the Al layer and Al<sub>2</sub>O<sub>3</sub> substrate are in the beam path at both positions; thus features from these materials should appear in both images. This is exhibited by both the bright Al<sub>2</sub>O<sub>3</sub> feature and the powder ring at ‘c’. Due to the unambiguous nature (and therefore 2θ position) of the Al<sub>2</sub>O<sub>3</sub> feature, the position of the ring relative to it, and its curvature, the ring at ‘c’ is assuredly the {111} powder ring from the Al layer. This was further verified by using image measurement tools to clarify the exact positions of the features in terms of the 2θ index recorded in the image header. The detector comprises 4 quadrants, but the actual 2θ position refers to the centre of the lower right quadrant, indicated by the red dot in Figure 3-17.

Having identified the presence of the Al {111} ring, a temperature profile (Figure 3-18) was applied to the sample to observe the behaviour as the Al was heated and subsequently cooled. Images like those in Figure 3-17 were recorded approximately every 18s. Upcoming figures display selections of images which reveal phase transformations in the sample. The presentation of the whole detector image is most revealing in this case, rather than using the image concatenation technique from 3.1.1.



**Figure 3-18 – Temperature profile applied to sample X for initial imaging scans**



**Figure 3-19 – Detector images showing phase transition in Al layer. Ring is clearly visible to right hand side of image in a)-c), and a faint structure persists to f) as indicated. It is no longer present in g) and h). Image d) is blacked out due to an error.**

The disappearance of the Al powder ring can be correlated with the recorded temperature. Whilst there is a degree of subjectivity in identifying exactly when features disappear, imaging tools have been used extensively to amplify faint features and eliminate doubt as far as possible. Taking this into account, the disappearance occurs between images f) and h) in Figure 3-19. In Figure 3-19f, the ring structure is still present albeit very faint. In Figure 3-19g a pair of bright spots can be seen which lie along the path of the ring; however the overall ring structure has clearly broken down at this point, and is completely gone in Figure 3-19h. It could be argued that the small bright spots represent a small population of Al crystallites which remain solid while the majority of the material has transitioned to the liquid state. For the purposes of the experiment, the melting point is deemed to be the point at which the *ring* feature breaks down, as this likely represents the point at which the majority of the Al has transitioned to the liquid state. In E1 S1, this transition is sharp and obvious due to the large steps between the isothermal holds. In this case, the temperature ramp is continuous, thus the Al region can be expected to melt more gradually. Material directly adjacent to the Al<sub>2</sub>O<sub>3</sub> surface will likely melt first due to being in closer proximity to the heat source, leaving small platelets of solid Al on the liquid surface (Figure 3-19g) until they too are melted through conduction from the surrounding liquid.

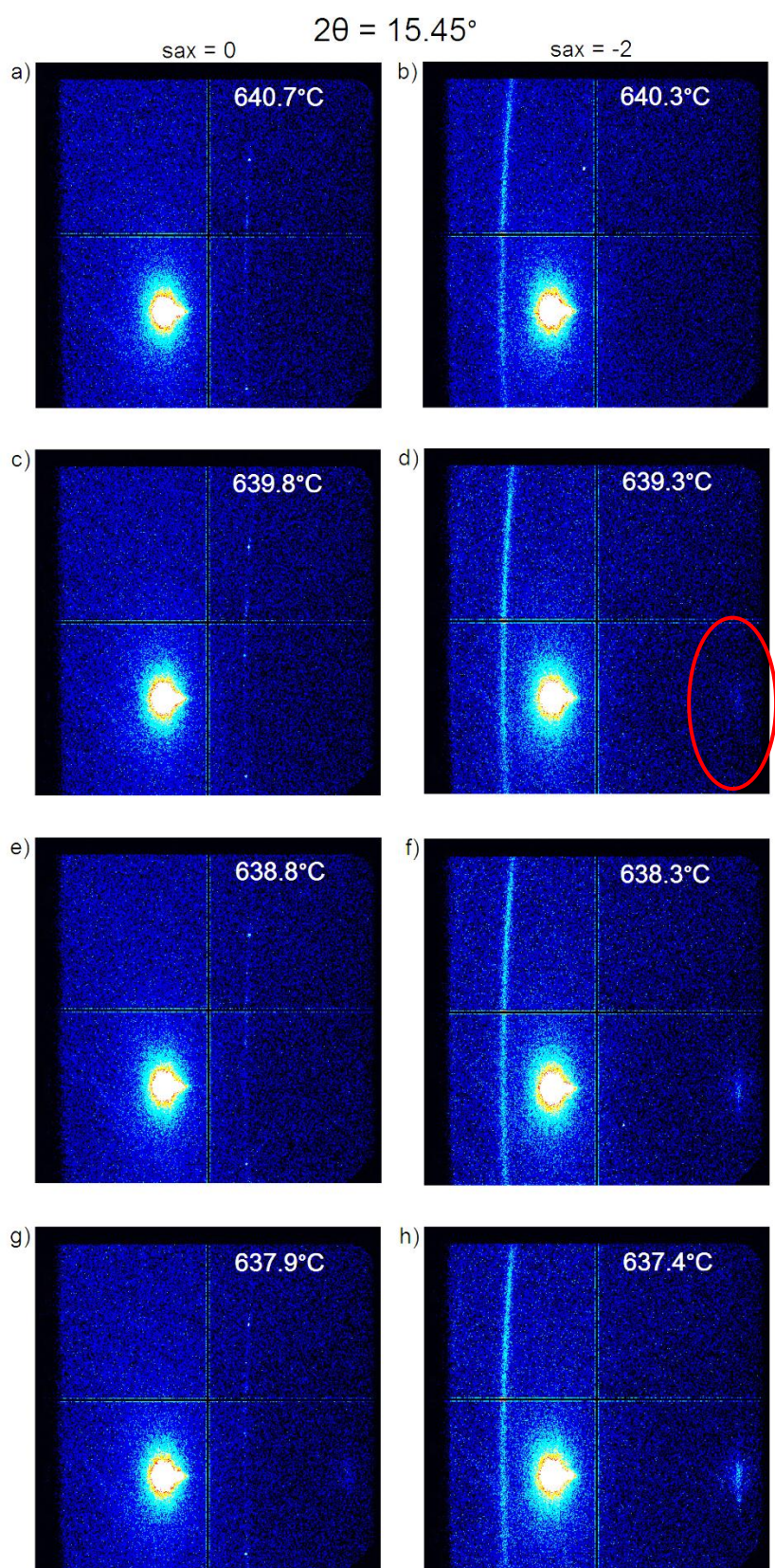
Taking Figure 3-19g as the actual melting point, the corresponding temperature is 660.4°C, coinciding with the expected equilibrium melting temperature of 660.37°C.

A separate image series recorded prior to melting shows the Al {111} feature, over the course of heating, translates to a smaller  $2\theta$  position; i.e., a larger d-spacing, exhibiting the **thermal expansion** occurring in the Al prior to melting. Over this series, the temperature ramps from 549.3°C to 654.9°C (increase of 105.6°C) while the translation amounts to a change in  $2\theta$  of  $\sim 0.025^\circ$ . The  $2\theta$  position of the Al {111} feature at the initial temperature of 549.3°C is  $15.06^\circ$ , showing thermal expansion has already taken place, as the expected room temperature position is  $15.24^\circ$ . The lattice spacing has shifted from 2.338Å ( $2\theta$



= 15.24°) to 2.366Å ( $2\theta = 15.06^\circ$ ) prior to the scan; followed by a shift from 2.366Å to 2.370Å ( $2\theta = 15.035^\circ$ ) over the image series. The percentage expansion in the lattice parameters from room temperature (taken here as 25°C) to 549.3°C is 1.2%. Applying the theoretical linear expansion [116] over this temperature range also gives a predicted percentage expansion of 1.2%. The change is similar to S1 E1, which exhibited an expansion of 1.48% over a 628.3°C rise. This further clarifies the veracity of the powder ring as the Al {111} feature and indicates that the sample is behaving in a similar fashion as in previous experiments.

Using the same image processing method, attention is now switched to the characteristic reappearance of a feature in the {111} position on cooling.



**Figure 3-20 – Detector images showing reappearance of Al {111} feature. Feature returns in image d) and develops in intensity over e)-h).**



The reappearance of a feature in the Al {111} position can be seen clearly in Figure 3-20. The transition is more apparent in this case – there is clearly no feature in Figure 3-20b, but at the same location in Figure 3-20d, there is some intensity present (indicated by the red oval). The returning feature has a markedly similar character to that in E1 S1, i.e., with a shape suggesting there is some transcription along the path of the original ring, but with a lateral breadth exceeding that of the original feature. This confirms previous conclusions about the morphological changes which occur when using this technique; i.e. an original sputtered layer, with a granular, polycrystalline, ‘powder-like’ morphology, transforms to a coarse grained morphology with a strong {111} texture. These observations address challenge 2), identified at the start of the experiment.

The breadth of the returning feature, as in E1, again suggests the possibility that **strain** exists in the solidified layer. The character of the transformation of the Al {111} feature – from a thin powder ring to an intense, broad spot – is very similar in both E1 and here in E3. This serves to verify the reproducibility of the result and of the consistency in the experimental technique (despite taking place at different beamlines). In terms of strain, the ‘spread’ in values does not appear as wide in these latest results, but this is likely just an issue of imaging adjustments. As discussed in 3.1.1, there are alternative reasons for peak broadening, but strain appears to be the most likely candidate

Correlating the observations above with recorded temperatures, a new assessment of the **undercooling** can be made. The feature does not appear in the  $sax = 0$  position until later in the scan, so solidification temperatures will be taken from the  $sax = -2$  images and tolerances applied accordingly.

$$\Delta T = 660.4^{\circ}\text{C} - (639.3 \pm 0.5^{\circ}\text{C}) = 21.1 \pm 0.5^{\circ}\text{C}$$

This value is noticeably lower than those recorded in E1; 88°C and 66°C from S1 and S2 respectively. It is unclear exactly why this is the case; although it may be related to the fact that E1 S1, S2 and S3 *and* the present E3 S1 run were all performed using the same sample. It is fair to question whether the

reported result of  $\sim 20^{\circ}\text{C}$  is indeed real. It is appropriate to suggest that a second assessment of the undercooling, from a second, separate batch of E3 data, should be made to impart greater confidence in the above and to more conclusively address challenge 1) identified at the start of the experiment.

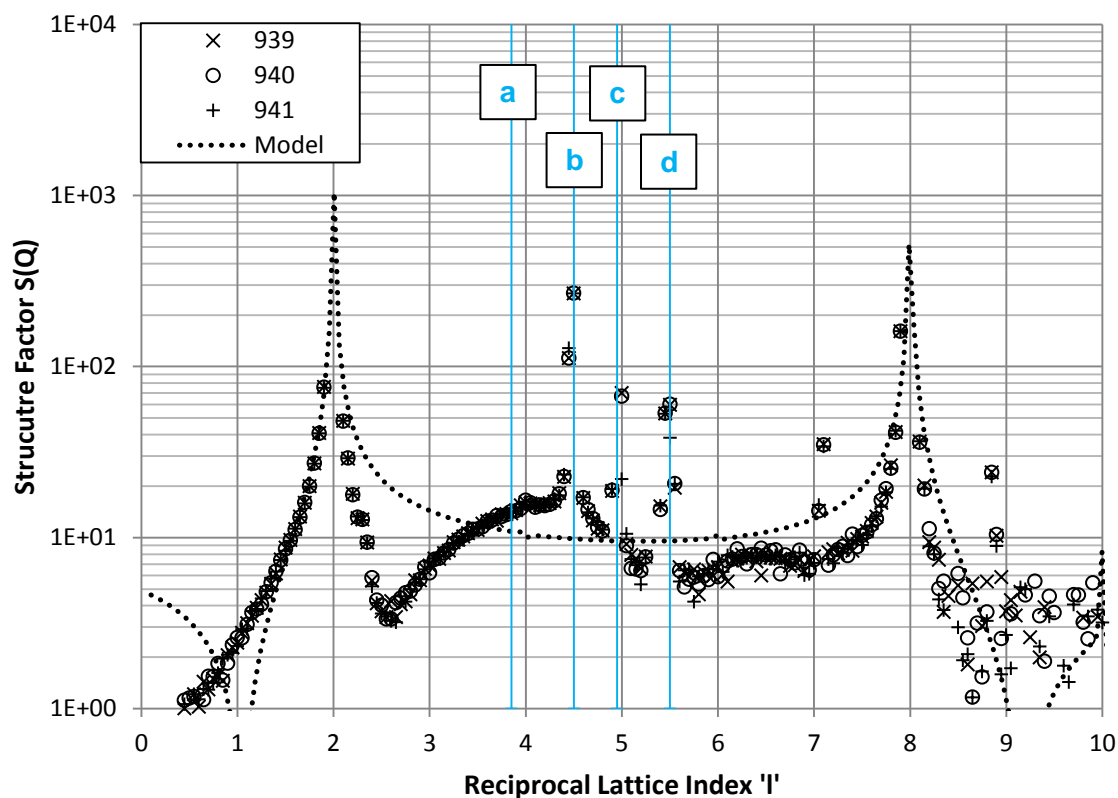
### 3.3.3 E3 S2: CTR profile undercooling assessment

The collection of CTR scattering permits detailed investigation of atomic structure at the  $\text{Al}/\text{Al}_2\text{O}_3$  interface. In collecting CTRs at E3, however, an unexpected opportunity arose to investigate solidification through similar means to those detailed in the preceding section. The following explores this particular aspect; the more in-depth structural analysis can be found in chapter 4.

The initial set of CTR measurements in E1 had indicated that the  $(0,1,l)$  crystal truncation rod demonstrated the most interesting characteristics in terms of possible temperature dependence. Therefore, E3 focused primarily on the  $(0,1,l)$  rod, and was set up to repeatedly record this from  $l = 0.5$  to  $l = 10$  as the sample was subjected to a temperature profile (Figure 3-24). This process, somewhat serendipitously, presented a means by which to observe the mesoscale phenomena of melting and solidification.

It is important to qualify that CTR data for experiment 3 has been fully background subtracted *and* had geometrical correction factors applied according to Vlieg *et al* [83]. All relevant diffractometer positions were recorded within the scan files and could thus be used to generate the corrections necessary at each data point. This allows the data to be presented directly as the structure factor modulus rather than an arbitrary intensity value.

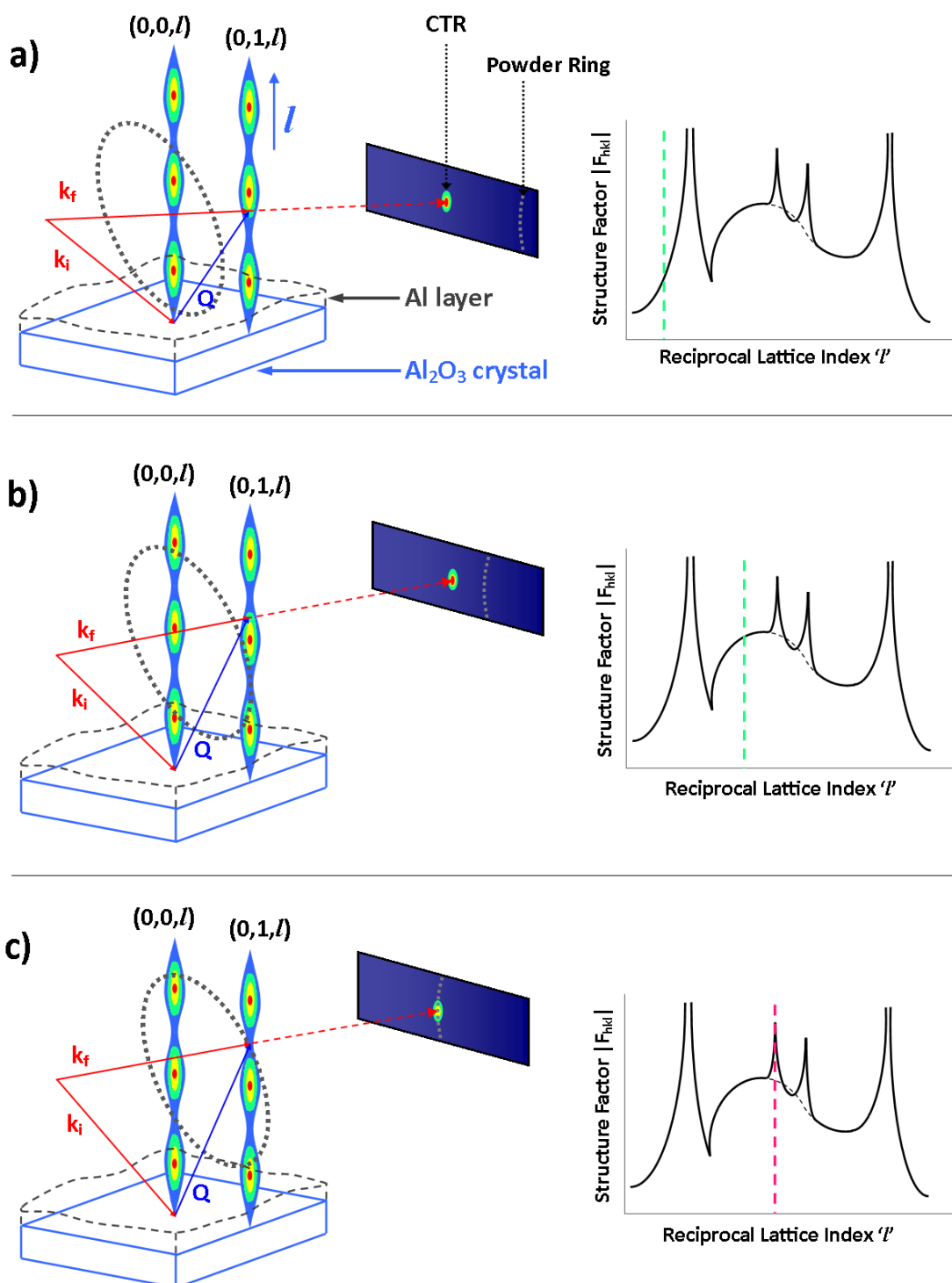
After alignment,  $(0,1,l)$  rods were collected to verify the orientation of the substrate. The first set of scans (at room temperature) revealed an interesting feature which would allow us to clarify our observations of the undercooling in the system.



**Figure 3-21 – Initial (0,1) rods from sample X. Note some of the data points around the Bragg peaks have been deleted to keep the y-axis within a reasonable limit. The numbers 939, 940 and 941 in the legend refer to the corresponding scan numbers from the ESRF data. Callouts a-d correspond to images in Figure 3-23.**

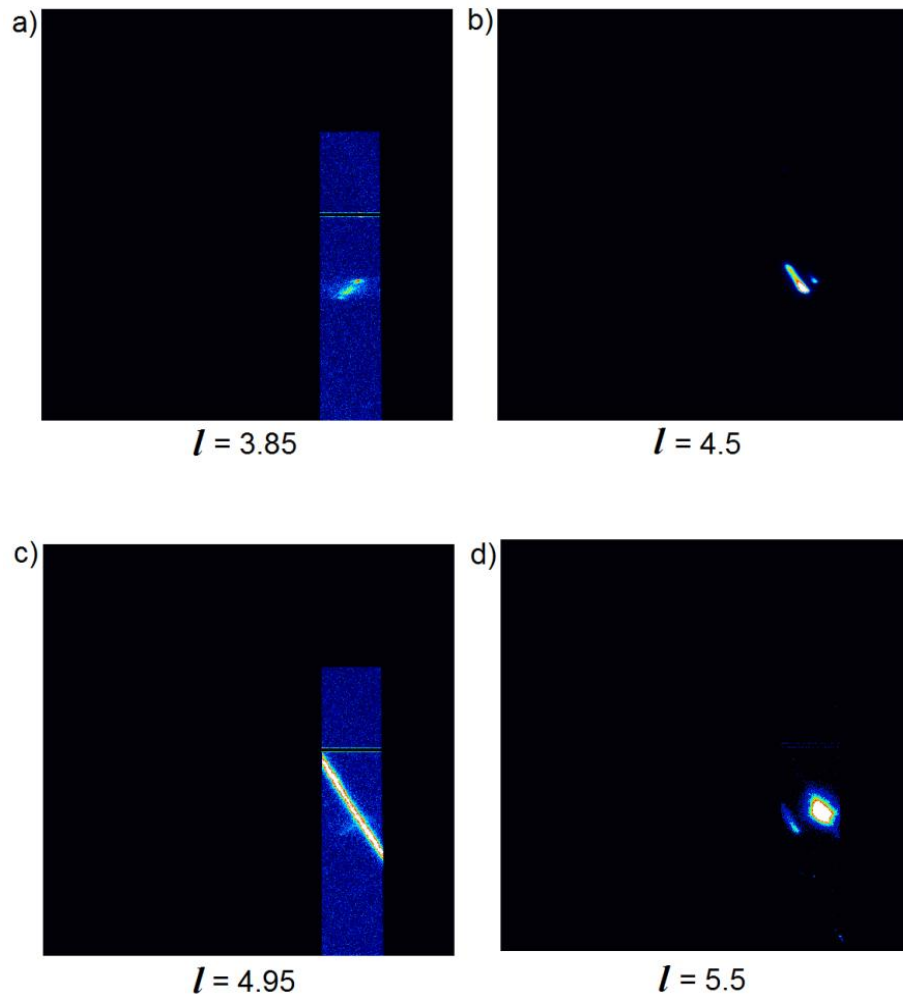
The general shape of the CTR is as expected, that is, with Bragg peaks at  $l=2$  and  $l=8$ . The shape of the profile between  $\sim l=2.5$  and  $l=7$  reflects an altered structure at the  $\text{Al}/\text{Al}_2\text{O}_3$  interface. Note how the data deviates from the predicted profile from a clean  $\text{Al}_2\text{O}_3$  {001} surface, shown as a dotted line in Figure 3-21. A fitting procedure must be followed to draw out detailed structural information, and is discussed in chapter 4. Initially, however, refer to the features located at  $\sim l=4.5$  and  $\sim l=5.5$ . These ‘peaks’ do not appear to arise from the rod itself. They are patently not Bragg peaks; they are not situated at integer values and are comparably extremely thin (comprising only 1-2 data points). They do not appear to follow the general arc of the actual CTR profile, and thus are likely a superposition of powder rings or other background scattering from the other materials in the system (i.e. the aluminium) which happen to intersect with the detector as it moves ‘up’ the crystal truncation rod. In regular CTR scanning the sample usually comprises a single material; the modification of the surface being reflected in the variation of the CTR profile. In the current work,

the  $\text{Al}_2\text{O}_3$  *single* crystal from which the CTR itself arises is topped with a *polycrystalline* layer of Al. Figure 3-22 defines how this arrangement can lead to superposition of powder peaks:



**Figure 3-22 – Schematic indicating how powder features can superimpose on CTR data. a)->b)->c) shows a scan ‘up’ the  $(0,1,l)$  CTR (increasing  $l$ ). Co-ordinated diffractometer motion keeps the rod in the centre of the detector as the scan proceeds. Powder features arise from the Al layer as it is also illuminated by the X-ray beam. As the diffractometer moves, the rod remains stationary, but powder features move relative to it. Thus at certain values of  $l$ , powder features are coincident with the position of the CTR in reciprocal space, and so are superimposed on the profile, as in c).**

Inspection of the detector images reveals that these peaks arise from small but extremely intense features, as shown below:

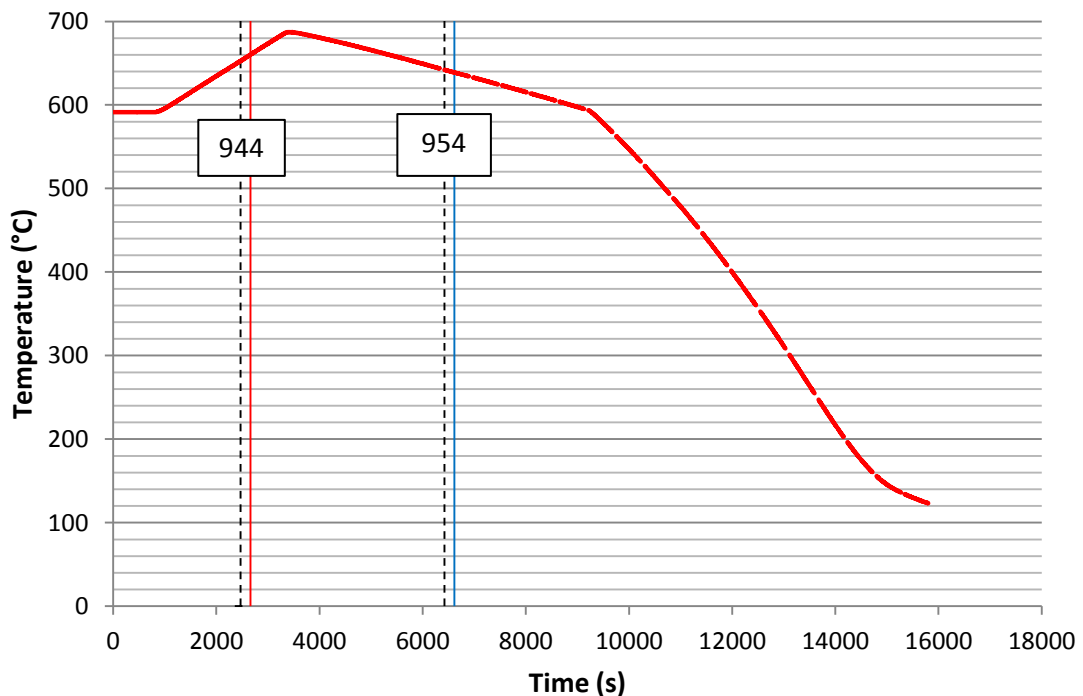


**Figure 3-23 – Direct detector images from scan #939. Refer to Figure 3-21 for corresponding locations within scan. Note that the detector slits have been closed to restrict background scattering. a) General image showing the CTR itself (intersection with Ewald sphere). b) peak at  $l = 4.5$  likely arising from Al. c) powder ring. d) peak at  $l = 5.5$  likely arising from Al. Note the brightness of image d) has been significantly increased to highlight the shape of the feature.**

Referring to the above; note that the features in images b) and d), recorded at the  $l$  values in question, are ‘spot-like’ but appear to be orientated at an angle. The very intense feature in image c), quite clearly a powder ring, has the same diagonal orientation. Compare this to the orientation of the CTR data itself in image a), angled in a different direction (due to intersection with the curved Ewald surface). The angle of the features in b) and d) have the same character as the powder ring in c).

The powder ring in c) is likely superfluous, arising from surrounding or supporting components; recall the similar rings in the previous detector images presented from E3 (Figure 3-17, Figure 3-19 and Figure 3-20) that exhibited no changes during processing. The powder ring here also exhibits no change over the entire temperature profile applied to the sample. We therefore conclude that this powder ring is not significant to the study in question, and that it is the features in Figure 3-23 b) and d) which must be observed. These features have the same angular orientation as the powder ring, and thus are considered to arise from powder-like scattering from sample materials – i.e. the Al layer – rather than the CTR itself, which in Figure 3-23 a) appears to have a markedly different geometry.

To understand the significance of the above we must observe what happens to these features on heating. (0,1) rods are recorded continuously throughout the heating and cooling process, beginning from scan #939 as indicated in Figure 3-21. The temperature profile applied is displayed in Figure 3-24:



**Figure 3-24 – Profile applied to sample X during collection of CTRs. Callouts indicate the scan number recorded at that point with dashed lines indicating the start of the scan. The red and blue lines indicate the exact time during the corresponding scan at which the Al {111} peak is recorded.**

The following figures (Figure 3-25, Figure 3-26, Figure 3-27, Figure 3-28) select specific pairs of CTR's, recorded consecutively, which exhibit important transitions. They plot both the CTR profiles and the corresponding temperature change during recording of each rod. The CTR data has been presented in a line plot, rather than using the convention of discrete data points, so that the peaks are more clearly defined. Note that for these figures, data is obtained while scanning over a temperature range to reveal phase transformations, and does not take place at an isothermal hold as in previous experiments.

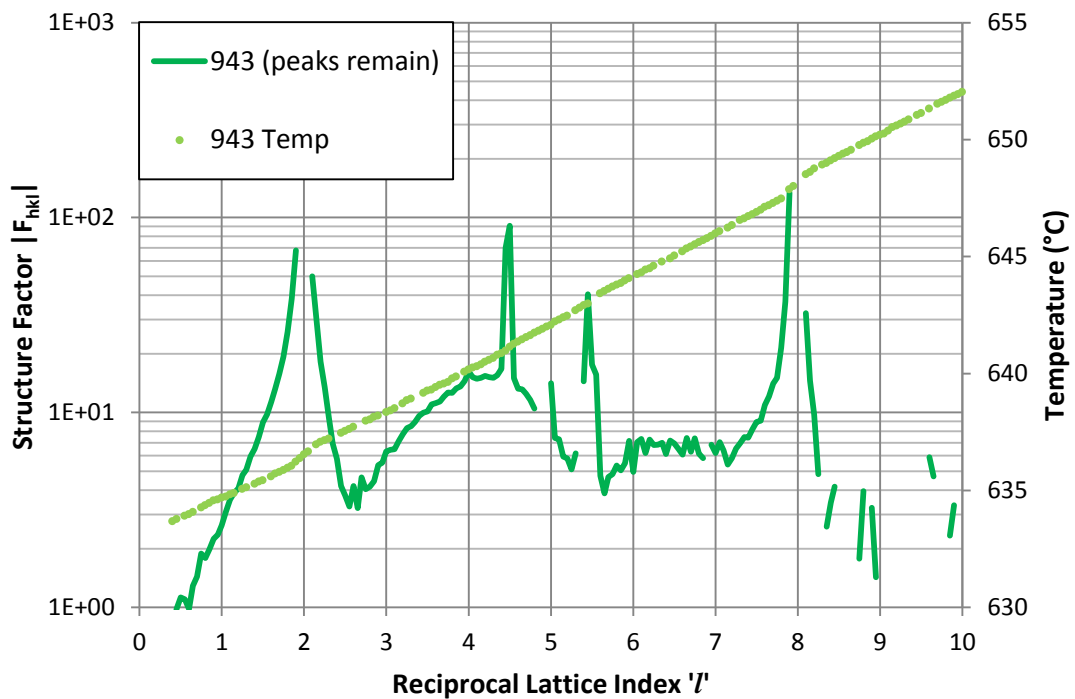


Figure 3-25 – (0,1,*l*) rods recorded in scan 943.



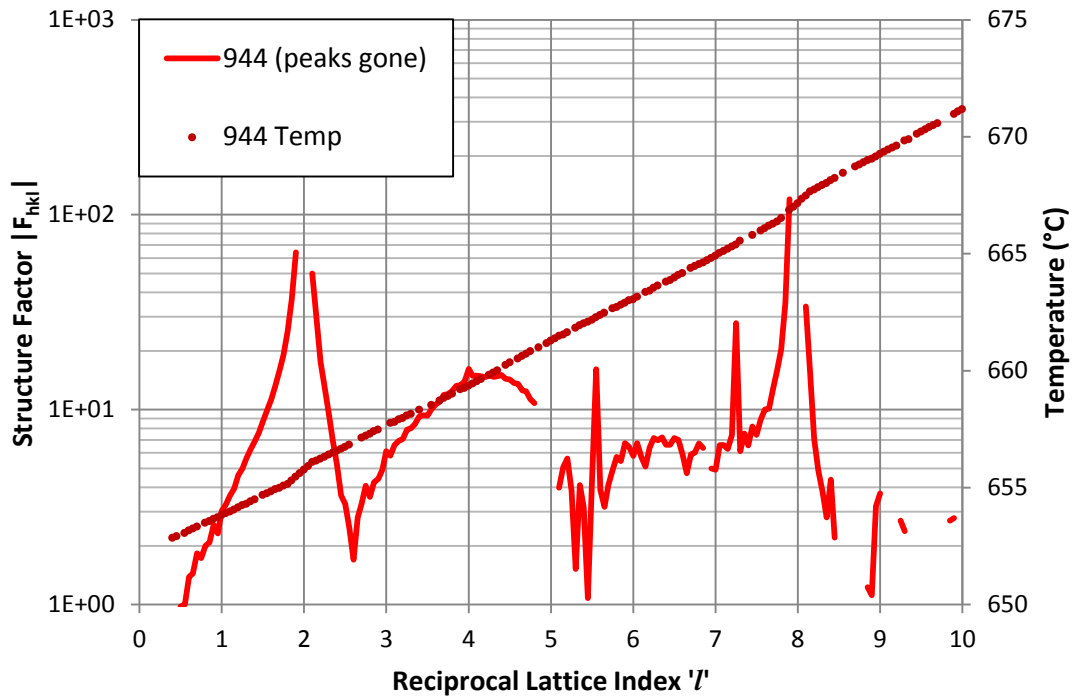


Figure 3-26 – (0,1,*l*) rods recorded in scan 944

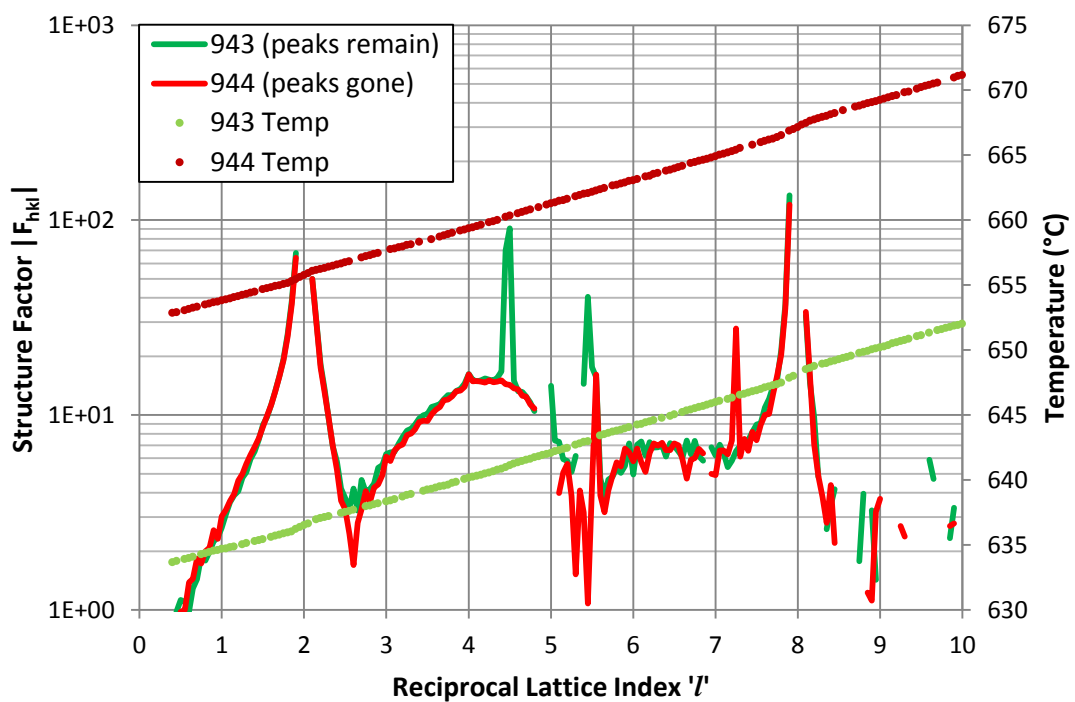
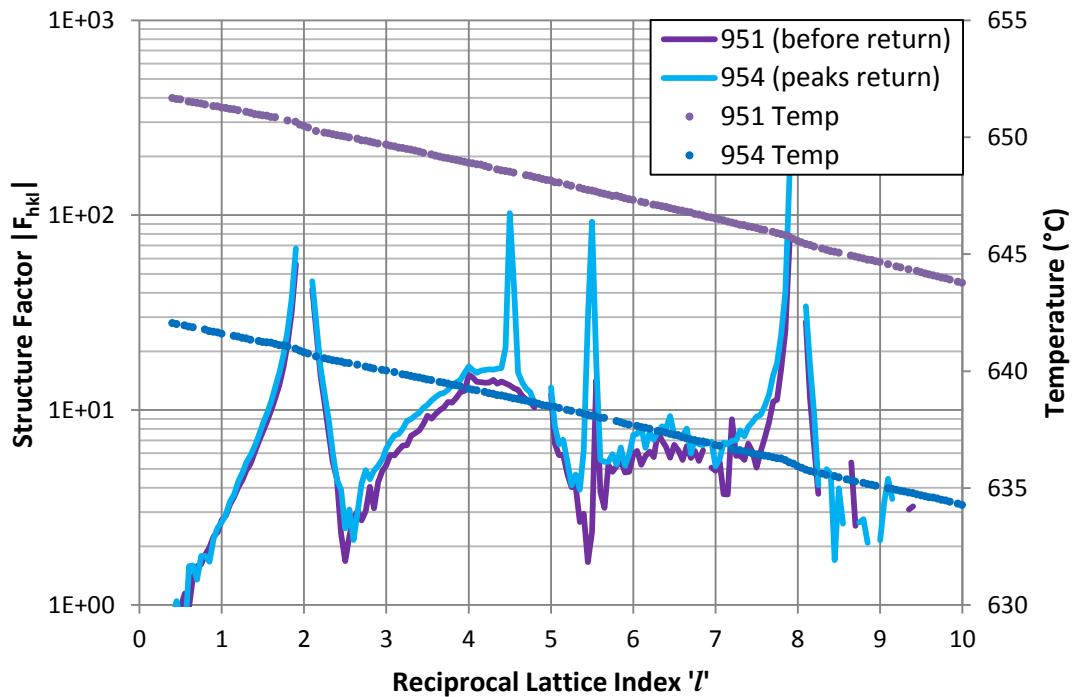


Figure 3-27 – (0,1,*l*) rods recorded in scans 943 and 944; presented as a combined figure

The significance of the above is immediately clear – the peaks at  $l = 4.5$  and  $5.5$ , which are present in 943, have disappeared in 944. The temperatures recorded during the collection of each rod are presented using a secondary y-

axis; this shows that, for scan 944, the temperature is approximately 660°C at the point at which the  $l = 4.5$  peak was previously recorded, and around 662°C at  $l = 5.5$ . These temperatures suggest that the features are indicative of solid Al which has transitioned to the liquid state during scan 944.

This assumption is rendered correct upon cooling of the sample, during which the following transition is occurred:



**Figure 3-28 – (0,1, $l$ ) rods recorded in scans 951 and 954; presented as a combined figure (N.B. these are consecutive scans; 952 was abandoned due to implementation of realignment scans from 953 on)**

The above displays the return of the characteristic peaks at  $l = 4.5$  and  $l = 5.5$  on cooling. Referring to the temperature profiles, the  $l = 4.5$  feature in scan 954 corresponds to a temperature of 638.9°C ( $l = 5.5$  corresponds to 638.1°C, though if this also, as expected, arises from Al, the solidification has of course already taken place).

This information permits another assessment of the undercooling required to instigate nucleation of crystalline Al. Taking the feature at  $l = 4.5$  as the ‘indicator’ of the presence (or otherwise) of aluminium, the following calculation is made:

$$\Delta T = 660.4^{\circ}\text{C} - (638.9 \pm 0.05^{\circ}\text{C}) = 21.5 \pm 0.05^{\circ}\text{C}$$

This value shows excellent agreement with that taken from assessment of the detector images in 3.3.1.

It is fair to qualify that the solidification of Al may have occurred at some temperature in between the final point at which it was categorically *not* present (i.e. at  $l = 5.5$  in scan 951;  $647.7^{\circ}\text{C}$ ) and subsequently detected (i.e. at  $l = 4.5$  in scan 954;  $638.9^{\circ}\text{C}$ ). Applying this to the undercooling calculation results in the following range of values:

$$\text{Lower bound: } \Delta T = 660.4^{\circ}\text{C} - (647.7 \pm 0.05^{\circ}\text{C}) = 12.7 \pm 0.05^{\circ}\text{C}$$

$$\text{Upper bound: } \Delta T = 660.4^{\circ}\text{C} - (638.9 \pm 0.05^{\circ}\text{C}) = 21.5 \pm 0.05^{\circ}\text{C} \text{ as before}$$

It should be noted that the first value of  $21.1^{\circ}\text{C}$  assessed in 3.3.1 is based on observation of detector images directly at the peak positions; as such the appearance of solid-like features is unequivocal. The fact that this second assessment gives a value – or at least, a range of values – which is very close to this imparts confidence that a) these features superimposed on the CTR do indeed arise from Al and b) that the values have been recorded accurately.

As an aside; it is clear that the CTR superpositions show *two* features reappearing on cooling. This contrasts with earlier experiments in which only one feature – indicative of Al {111} – would reappear. The imaging study in 3.3.1 showed that, as in E1, the Al layer re-solidified with a coarse-grained morphology having a {111} texture; this morphology thus represents the initial condition for the collection of CTRs which immediately followed, so it is unlikely that the two features at  $l = 4.5$  and  $5.5$  are indicators of Al {111} and Al {200}










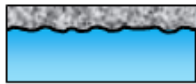

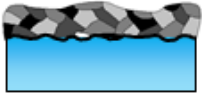
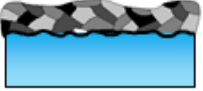

respectively. The scattering geometry for collection of CTRs is fundamentally more complex than the specular geometry used in the imaging scans, and it is likely that the same powder feature has simply intersected the CTR at two different points. The two features should thus be understood as *together* representing a 'signature' indicating the presence of Al. The preceding work thus serves as a useful repeatable measure of undercooling in the Al/Al<sub>2</sub>O<sub>3</sub> system, but cannot be used to reveal the orientation relationship between the two materials.

### 3.3.4 E3 Conclusions

The values for undercooling from the two parts of E3 described, S1 (3.3.2) and S2 (3.3.3), show excellent agreement. The first scan also clarified the **orientation relationship** after solidification. This imparts confidence in the validity of the suggested values. However as previously noted there is a significant discrepancy with the results from E1; (88°C and 65°C from S1, S2 respectively, discounting S3). While the *magnitude* of all the values (i.e. tens of degrees) is in agreement, there is sufficient discrepancy to suggest that some of these results are inaccurate.

An important consideration is that it was necessary to use the same Al<sub>2</sub>O<sub>3</sub> sample for both E1 and E3. Efforts were made to clean and re-prepare the sample thoroughly and by the same process, but there may have been minor differences in preparation. Also, E1 itself may have resulted in a permanent structural change or degree of contamination to the sample which may have had an influence on the behaviour of the sample during E3. The surface roughness of the substrate may have increased, either through damage to the surface directly or through the existence of residual material on the surface (possibly Al oxide, as suggested by E1 results). In either case, the resulting roughness would likely lead to a higher density of potent nucleating sites (due to the presence of cavities, pits etc) leading to reduced undercooling as seen in E3. While the character of the melting and solidification behaviour – the morphological changes, resulting texture etc – were relatively similar in E3 and E1, the discrepancy in the undercooling values is large enough to suggest that

this is the case. Figure 3-29 describes the suggested process leading to the lower  $\Delta T$  values in E3.

PROCESS	BEFORE	AFTER
<b>Experiment 1</b>		
<b>E1</b> Sample Preparation	Al <sub>2</sub> O <sub>3</sub> crystal 20h annealing in air 	Polycrystalline, 'powder-like' Al layer 
<b>E1 S1:</b> Heating & cooling with specular scattering		Polycrystalline coarse -grained Al layer 
<b>E1 S2 and E1 S3:</b> Heating & cooling with CTR collection		
<b>Experiment 3</b>		
Acid Etching and Cleaning		Residual damage to surface 
<b>E3</b> Sample Preparation	20h annealing in air 	
<b>E3 S1:</b> Heating & cooling with specular scattering		
<b>E3 S2:</b> Heating & cooling with CTR collection		

**Figure 3-29 – Schematic illustration of possible morphology changes in Al and Al<sub>2</sub>O<sub>3</sub> through E1 and E3**

### 3.4 Conclusions

The preceding work has demonstrated the feasibility of X-ray scattering techniques to reveal melting and solidification behaviour *in-situ*. The Al/Al<sub>2</sub>O<sub>3</sub> system has proved a useful test case for such work. Conclusions can be summarised as follows:

1. The high spatial resolution afforded by scattering techniques allows **thermal expansion** to be identified to a fine degree, including identifying expansion along individual crystallographic directions. In E1 S1 for example; over a temperature change of ~630°C, expansion of 1.59% and 1.69% was observed in the Al {111} and Al {200} features respectively; comparing well with the theoretical linear expansion of 1.48%.
2. Through monitoring the dis- and re-appearance of characteristic peaks, phase transitions within materials can be identified. By correlating this with temperature, solidification temperatures – and hence, **undercooling** – can be assessed. If isothermal holds are used these measures represent a good assessment of the undercooling required to instigate nucleation. Consideration must however be given to the modifications to the nucleating surface which may arise from multiple thermal cycles.  $\Delta T$  values of 88°C and 65°C are recorded for Al on Al<sub>2</sub>O<sub>3</sub> (001).
3. **Orientation relationships** between crystal and substrate near the interface during solidification can be identified by observing which features appear and in which scattering geometry. an orientation such that {111} planes are aligned parallel with the Al<sub>2</sub>O<sub>3</sub> substrate surface. This is due to a) the ‘spottiness’ of the returning {111} feature, and b) the strength of the {111} reflection/lack of {200} feature. This behaviour is observed again in the first part of E3.
4. Non-uniform **strain** exists in solidified crystals near the interface, evidenced/suggested by the breadth of the returning {111} features in experiments. The strain measured in the experiments is in the specular direction, i.e. along a direction normal to the substrate surface; the z direction. It

can be reliably assumed that this would be complemented by a corresponding strain in  $x$  and  $y$ , i.e., along the interface. CTR data should provide more detailed information as to the nature of the strain in the plane of the substrate surface.

5. Features which cannot be directly ascribed either to the Al or the single crystal substrate (and which do not appear to arise from surrounding materials or equipment) suggest the presence, and indeed the continued formation of, further aluminium oxide within the system. It remains unclear whether this 'new' oxide exists at the Al/Al<sub>2</sub>O<sub>3</sub> interface, within the Al structure, or on the surface of the Al layer. Residual oxide material on the substrate surface may, by contributing to surface roughness, influence the **undercooling** in the system.

#### 4 Results: Ordered structures at Al/Al<sub>2</sub>O<sub>3</sub> interface determined through Crystal Truncation Rod analysis

The preceding work revealed the range of morphological and structural information that can be obtained via specular scattering. Within the overall project it is the interfacial structure between materials which is of greatest interest. Analysis of crystal truncation rods (CTR's), described in section 1.8.4, can provide detail about the interfacial structure at atomic scale; permitting insight on any adsorption, relaxation, roughness or other phenomena which may be related to nucleation. Figure 4-1 follows as a reminder of the CTR collection procedure.

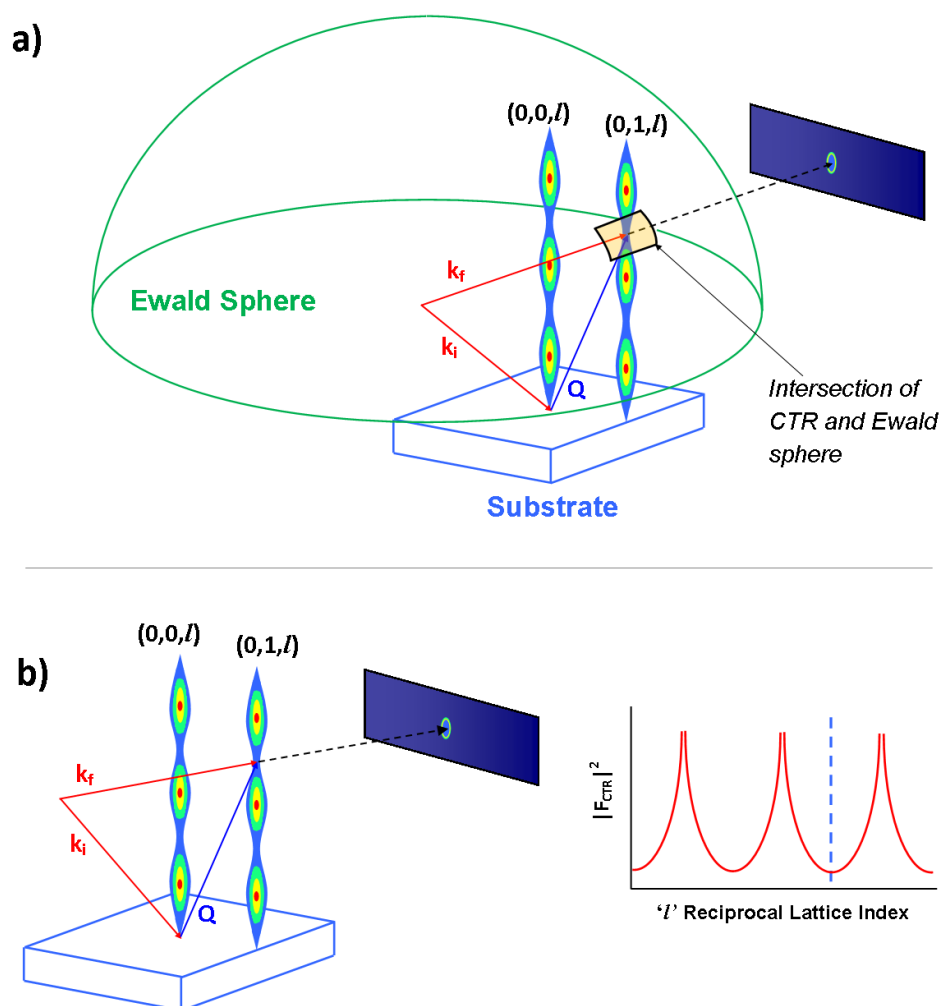


Figure 4-1 – Schematic indicating how CTR intensity profiles are recorded. a) indicates the condition that the diffractometer geometries must create; i.e. the Ewald sphere intersects with the CTR generated from the surface. b) indicates that the intensity profile is progressively recorded as the scan proceeds up the rod.



Diffraction by transmission through a single crystal results in a pattern of intensity concentrated in discrete points (Bragg peaks), but when diffraction takes place from a surface, additional intensity arises between the Bragg peaks, known as a CTR. The intensity is extremely sensitive to the surface structure of the sample. For the current work, the aim is to investigate the surface of the crystalline  $\text{Al}_2\text{O}_3$  substrate to ascertain how the presence of Al influences or modifies the surface structure. CTR's result from scattering by a crystal, and as such are only sensitive to features at the interface which adopt the structure and periodicity of that crystal. For the current project, one may consider the effect of liquid ordering described in section 1.6; specifically the case of adsorption of liquid atoms onto the solid surface [24], [25], which would adopt the periodicity of the solid and contribute to the CTR. As such, in the current case, only the  $\text{Al}_2\text{O}_3$  substrate, and any ordered material *associated* with the substrate (e.g. liquid layers existing at a constant separation from the substrate surface), contribute to the CTR; polycrystalline and liquid Al do not.

A CTR scan records intensity against the reciprocal lattice vector  $l$ . To perform a scan along a CTR, the sample is rotated such that the Ewald sphere intersects the rod at the desired locations in reciprocal space, as shown in Figure 4-1. The detector moves into the appropriate position to capture the intensity at this point. This is a complex process which requires extremely precise and co-ordinated motion of both sample and detector. Modern synchrotron facilities and equipment are capable of achieving this with a degree of automation requiring less specific knowledge on the part of the user. This is primarily thanks to the work of Vlieg *et al*, and full details of diffractometer geometry, angle calculations and correction factors can be found in his papers [83], [106].

## 4.1 Experiment One

As previously noted in 3.3.3 the (0,1,*l*) and (1,0,*l*) CTRs were collected from the sample during the application of the E1 S2 temperature profile shown in Figure 4-2. Similarly to the study of undercooling in the previous chapter, an individual rod is collected at each of the applied isotherms. The notion is to observe whether the rod profile changes as the sample is heated and cooled, which would suggest that the interfacial structure is changing. This is particularly relevant during cooling, as the Al transitions from the liquid to solid state.

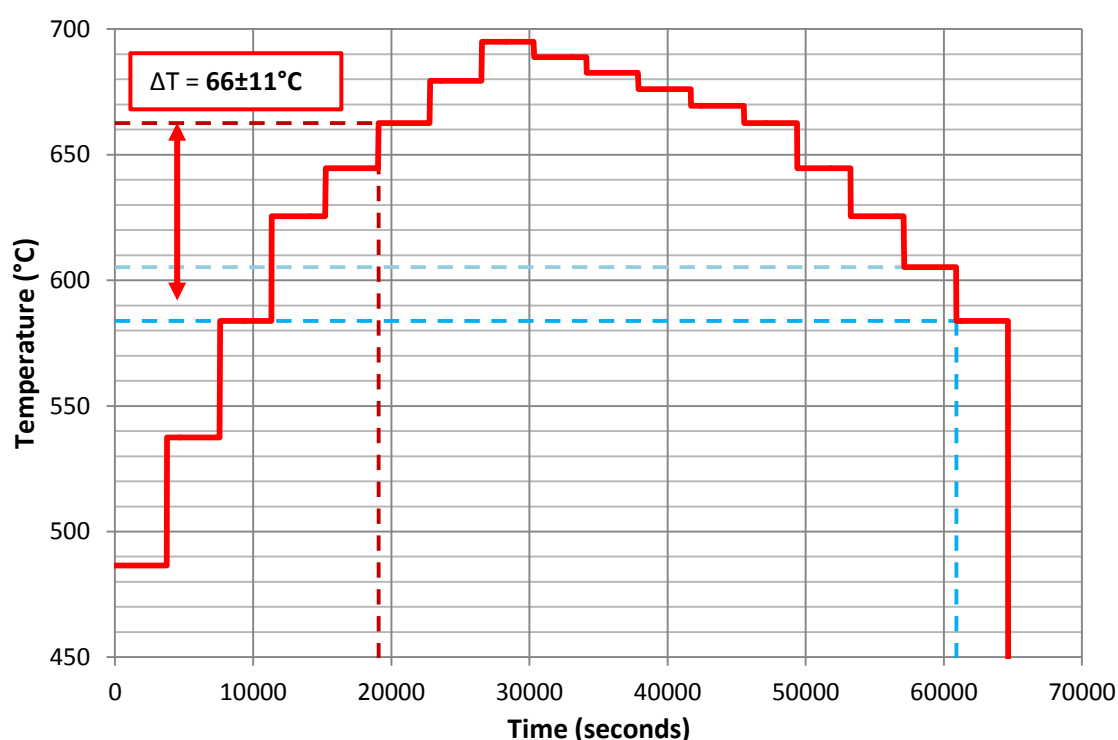


Figure 4-2 - Temperature profile for E1 S2

The (0,1,*l*) and (1,0,*l*) rods were collected in S2 at each of the isotherms displayed in Figure 4-2. A selection of these rods is displayed in the following set of figures. At the detector, the rod appeared to have a tendency to drift away from the centre, likely due to a slight miscut in the Al<sub>2</sub>O<sub>3</sub> substrate combined with thermal drift. Intensities directly recorded by beamline software were therefore inaccurate (particularly further up the rod in *l*). To solve this, intensity was directly integrated from the detector images themselves, using a process which adjusts the position of the ROI to compensate for the movement of the rod within the detector frame.

In each of the following 4 figures, the series 'Model' represents the predicted CTR from an ideal  $\text{Al}_2\text{O}_3$  {001} surface, generated using ROD [86].

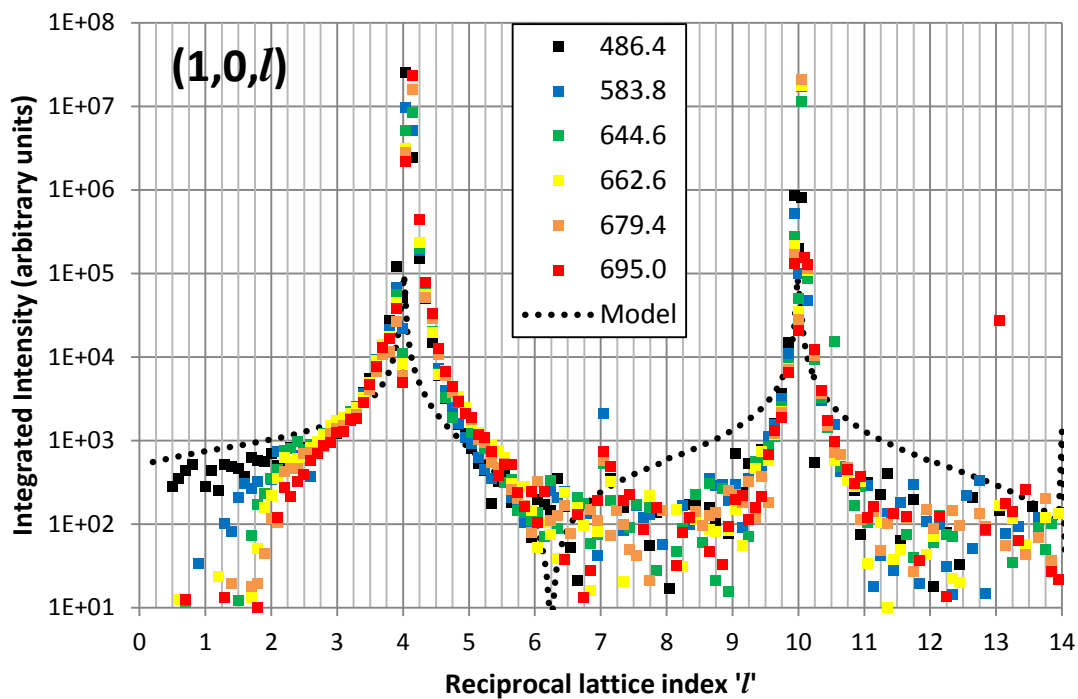


Figure 4-3 – Selected (1,0,*l*) rods during heating, showing the expected Bragg peaks at *l* = 4 and *l* = 10 and scattering intensity variation along the rod

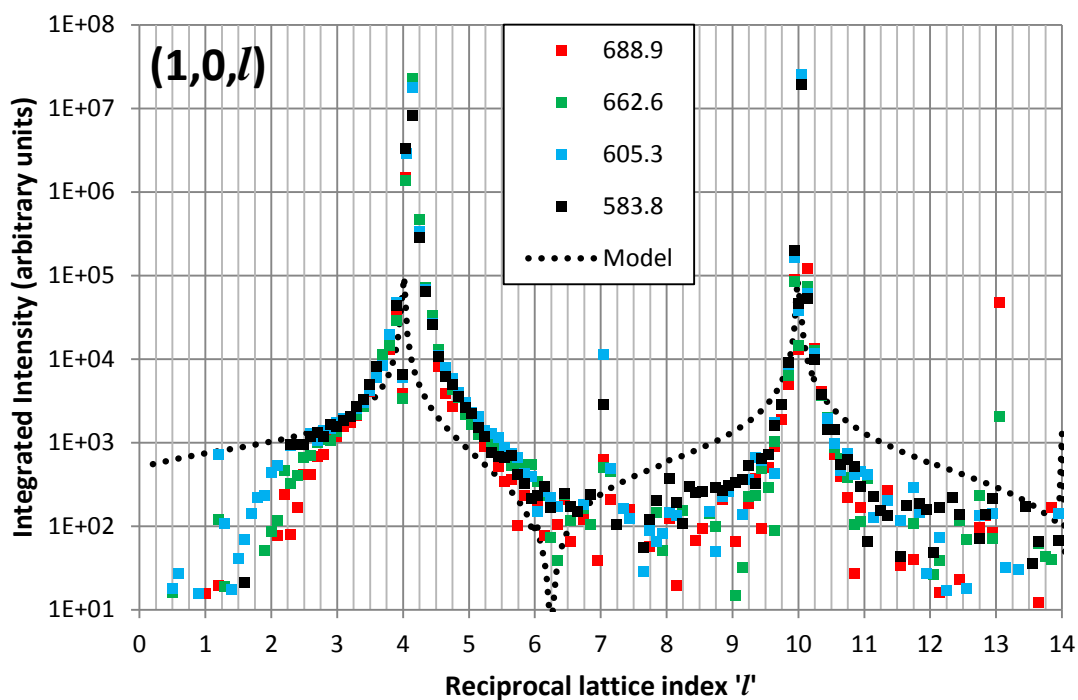


Figure 4-4 - Selected (1,0,*l*) rods during cooling

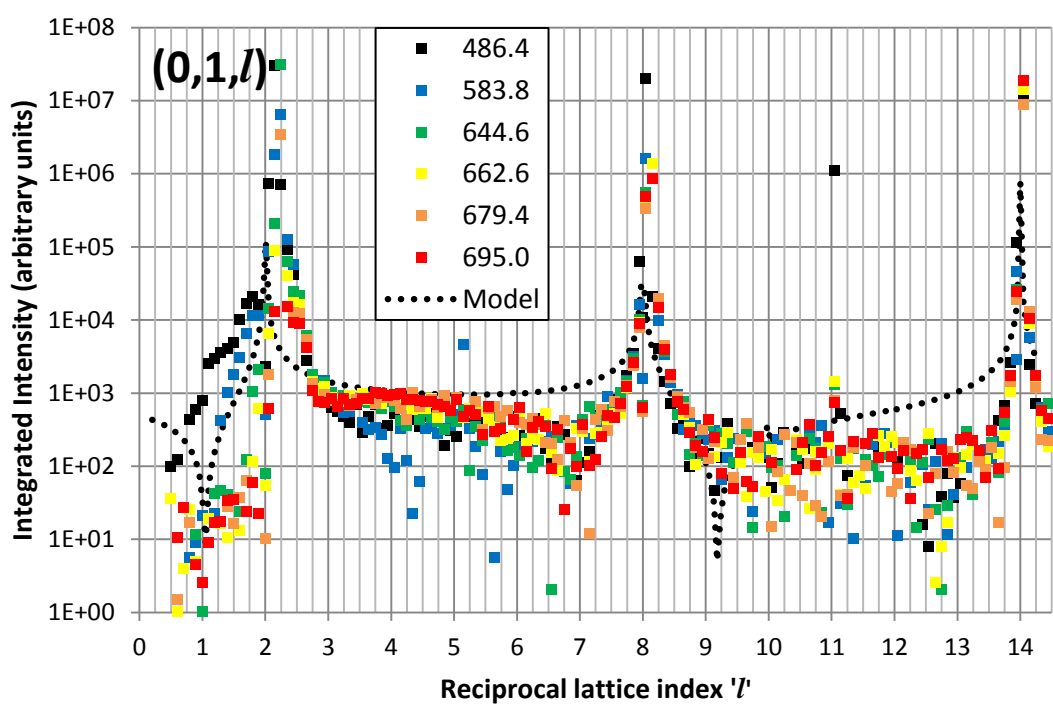


Figure 4-5 - Selected (0,1,*l*) rods during heating

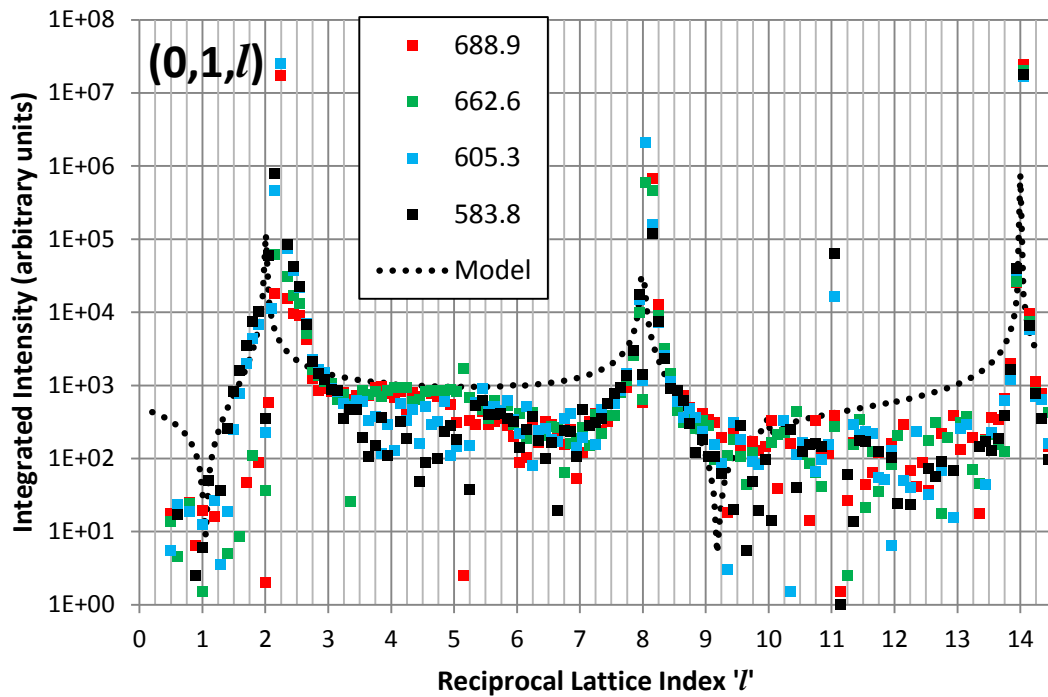


Figure 4-6 - Selected (0,1, $l$ ) rods during cooling

Initial observations are as follows:

1. Bragg peaks occur at the expected values of  $l$  verifying that the substrate crystal has the correct orientation.
2. The data appears to be of higher quality at lower values of  $l$ ; this is particularly apparent in the (0,1) rods. For  $l > 9$  there is a large degree of noise and it is difficult to transcribe the actual path of the rod.
3. The rods appear to be broadly similar at all isotherms. There are no strong, distinct changes with temperature (in contrast with to the obvious peak disappearance and re-appearance in the specular data)
4. Some slight temperature dependence may be seen in the (0,1) rods; between  $l = 1$  and  $l = 2$ , and after the Bragg peak at  $l = 3$  to  $l = 5$ . This is slightly subjective, but there does appear to be some relation between temperature level and intensity along the rod at these points. However, it is important to note that at low  $l$  values the scattering geometry is such that the incident and reflected X-ray beams are at very low incident angles. As a result, the system is here highly sensitive to misalignment and/or thermal drift, leading to inaccuracies in the data. X-rays may strike the edges of the sample or supporting structures and scatter in a way which is not

representative of the CTR profile itself. This is the likely cause for the large spread in values seen in the lowest  $l$  regions of both (1,0) and (0,1) rods.

It is well known [84], [85] that roughness at a surface or interface reduces the intensity at anti-Bragg positions, i.e. *between* the peaks at  $l = 4, 10$  in the (1,0) and  $l = 2, 8, 14$  in (0,1). The signal may be indistinguishable from background noise, and the character of the data in anti-Bragg positions in the figures appears to suggest that this has indeed occurred. It is difficult to conclusively state whether the intensity of the CTR itself is low due to interface roughness, or whether a high level of noise simply obscures the profile.

Attempts to fit this data proved challenging. In the important anti-Bragg positions, there is great inconsistency; both within individual rods and between rods at different temperatures. It is likely that the intensity in these positions is dominated by background noise, making it extremely difficult to generate a realistic fit. By extension, this means it is difficult to ascertain what (if any) effect changing temperature has on the profile. The only potential source of useful information is that described in point 4) on the previous page; i.e. a slight temperature dependence of the (0,1) rod. As suggested, geometric effects mean data at lower  $l$  may be unreliable, but overall, there is more in the (0,1) profiles which suggests a degree of temperature dependence (e.g. between  $l = 3$  and  $l = 5$ ).

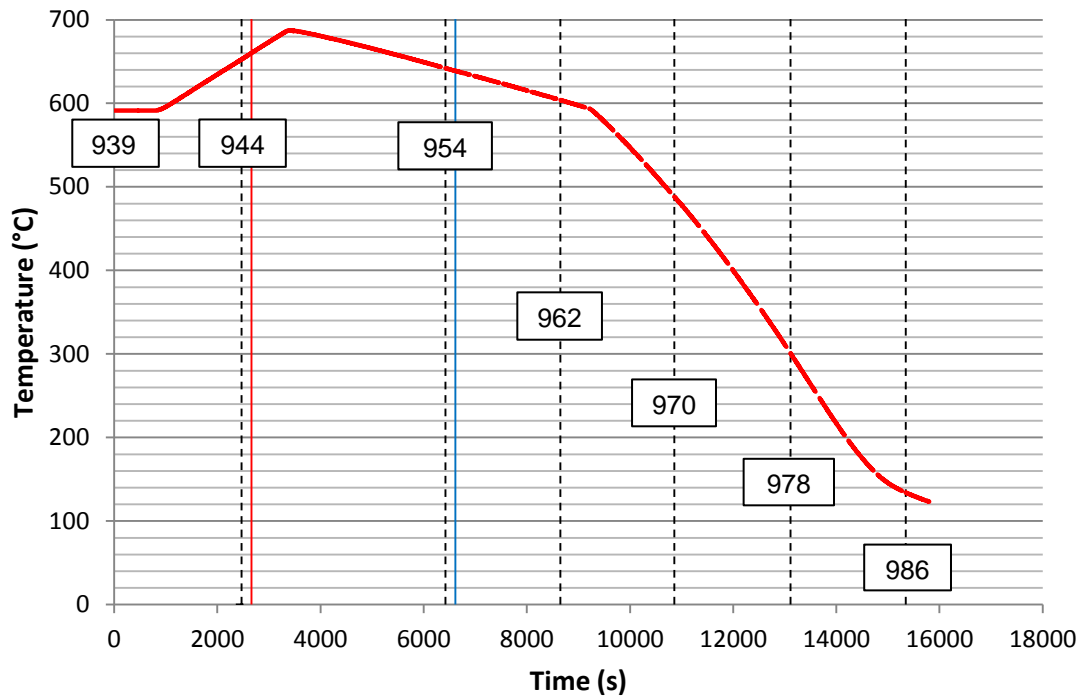
Future experiments were optimised based on these findings. The (0,1) rod was selected as the primary means of investigation, to observe whether the temperature dependence seen in E1 was repeatable. Improvements in the signal/noise ratio and the resolution in  $l$  were also necessary.

## 4.2 Experiment Three

Development of the E3 strategy was ongoing concurrently with attempts to analyse the E1 data. The decision was taken to focus primarily on the (0,1) rod for E3 – this having shown the most promise in E1 – to assess whether similar trends could be identified.

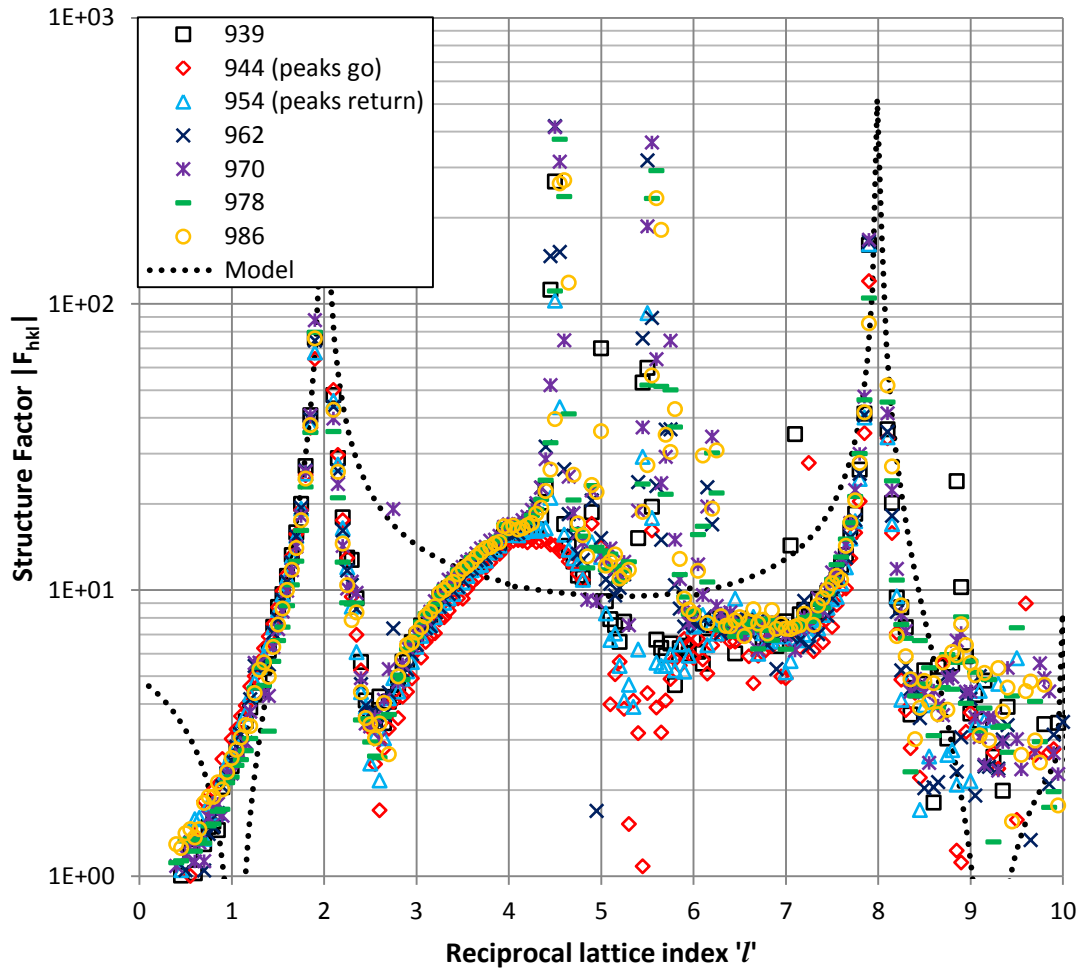
### 4.2.1 *Sample X: Al on Al<sub>2</sub>O<sub>3</sub>*

As discussed in 3.3.3, superposition of Al powder-like features on CTR's offered a useful means through which to observe melting and solidification in the Al/Al<sub>2</sub>O<sub>3</sub> system. This however is not the primary goal of the technique; CTR analysis is designed to give detailed measurements of the atomic structure at the interface. The data collected at E1 was of low resolution and was obscured by the background at anti-Bragg positions. For E3, the goal is to improve both of these aspects, and observe whether the CTR profiles alter over the course of a temperature profile applied to sample X, revealing any changes in the atomic structure at the Al/Al<sub>2</sub>O<sub>3</sub> interface that occur during or as a result of nucleation of solid Al. The temperature profile applied to the sample is shown in Figure 4-7. A number of callouts on this figure indicate individual CTR's collected during heating and cooling. These selected CTRs are displayed in the subsequent Figure 4-8.



**Figure 4-7 - Profile applied to sample X during CTR collection. Callouts indicate the scan number recorded at that point with dashed lines indicating the start of the scan. Melting was detected in 944, and solidification in 954. For these, red and blue lines indicate the specific point during the scan at which the Al {111} peak is recorded.**





**Figure 4-8 – Selected (0,1) CTRs collected from sample X during heating and cooling. Refer to legend and Figure 4-7 to observe the temperatures at which the rods were recorded. Bragg peaks at  $l = 2$  and  $l = 8$  with characteristic intensity in between. Sharp peaks between  $l = 4$  and  $l = 6$  arise from the superposition of powder-like features as described in 3.3.3.**

It is immediately clear that the data is of significantly better quality compared to E1. The signal/noise ratio has also been dramatically improved; there is more consistency both within and between rod profiles. In terms of the data itself, the most potent observation relates to the shape of the profile between the two Bragg peaks, particularly the presence of a characteristic 'hump' between  $l = 2.5$  and  $l = 5$ . The profile exhibits a clear deviation from the predicted scattering from a 'clean'  $\text{Al}_2\text{O}_3$  (001) surface (shown by the dotted line). This suggests that the surface structure of the  $\text{Al}_2\text{O}_3$  has been modified; and it is fair to suggest that this modification is due to the presence of the Al layer on the surface.

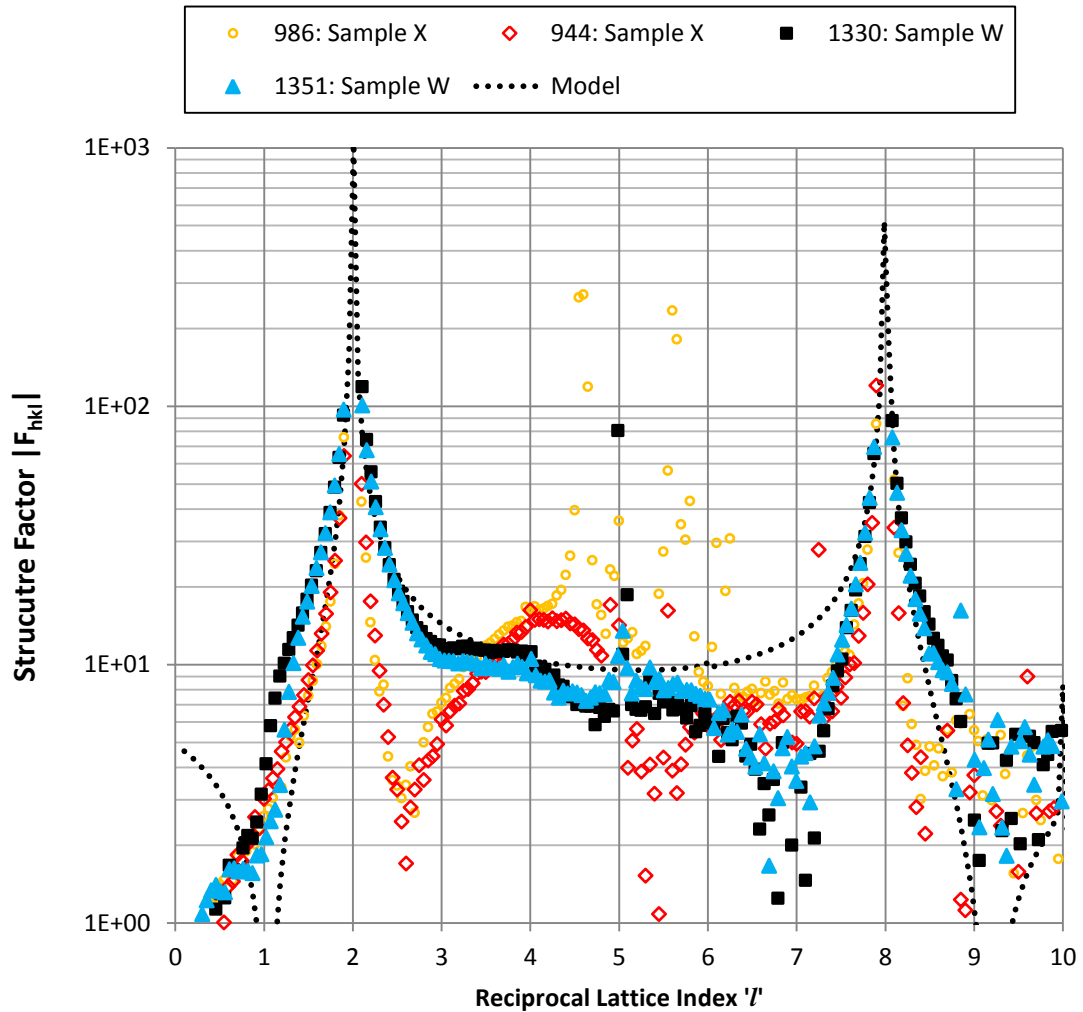
The other immediate conclusion here is that, apart from the dis- and re-appearance of Al powder peaks, the CTR's do not change significantly with temperature. The general profile shape persists throughout. Conversely to results from the E1 CTRs, there does not appear to be any trend with temperature. There is no dramatic change in shape indicating a dramatic change in structure such as an adsorbed layer or nucleated crystal. The sample has however clearly undergone *some* modification. Clearly this may have arisen *before* CTRs were recorded from this sample; during the first stage of E3 (3.3.2), so it is of great interest to attempt to fit this data to ascertain what it reveals about the extant interfacial structure.

The 'powder-like' peaks used to assess the undercooling in the previous section are apparent here at  $l = 4.5$  and  $l = 5.5$ . Because the majority of CTRs were recorded after the Al had re-solidified, these features dominate this region of the rod. Superimposition of powder-like peaks cannot be accounted for in the fitting process, so these data points are deleted from the dataset used for fitting. The remaining data theoretically contains the information about the structural changes in the sample, especially in the anti-Bragg positions.

The data gives a strong indication that some modification of the  $\text{Al}_2\text{O}_3$  surface has resulted from the presence of Al. Thus far, this has been based on the discrepancy between experimental data and *predicted* scattering from an *ideal*  $\text{Al}_2\text{O}_3$  {001} surface. Assessing scattering from a *real* clean  $\text{Al}_2\text{O}_3$  {001} surface would allow for a more realistic comparison and add credence to the theory that the presence of the Al modifies the CTR as observed.

#### 4.2.2 Sample W: Clean $\text{Al}_2\text{O}_3$

To better understand the shape of the CTRs from sample X displayed in Figure 4-8, a clean  $\text{Al}_2\text{O}_3$  (001) substrate, sample 'W', was mounted. This particular sample had remained untouched and would therefore be expected to give a strong, unmodified (0,1) rod to which previously collected CTRs could be compared.



**Figure 4-9 – (0,1) rods from sample W (1330 and 1351) compared with those from sample X (944 and 986), showing the effect of the presence of Al on the surface of  $\text{Al}_2\text{O}_3$**

There are clear differences between the rods from samples X and W. Some initial observations:

- A feature exists at  $l = 5$  in the sample W data; this is the same powder ring observed during the undercooling assessment on sample X (Figure 3-23), verifying this categorically did *not* arise from the Al layer on sample X, so must originate from some supporting component material not of interest here.
- Powder peaks at  $l = 4.5$  and  $l = 5.5$  are not present on the sample W scans, further verifying that these do indeed arise from the Al layer present only on sample X.
- There appears to be a slight ‘shoulder’ to the first Bragg peak on the sample W data, between  $l = 1$  and  $l = 2$ . As previously discussed, this is likely due to

misalignment effects at low  $l$  values due to the low incident angles, rather than being a real feature in the data.

The ‘hump’ between  $l = 2.5$  and  $l = 5$  from the sample X data is clearly not present in sample W. This further suggests that it is indeed the presence of the Al layer which leads to the modified surface structure in sample X. Also of note is the way in which the datasets from both samples deviate from the initial model between  $l = 5$  and the second Bragg peak at  $l = 8$ . The data from both samples exhibits a ‘dip’ in intensity between approximately  $l = 6$  and  $l = 7$  rather than following the ‘flat’ profile of the model. This perhaps illustrates the nature of real experimental samples. Despite sample W being effectively a clean  $\text{Al}_2\text{O}_3$  (001) substrate, it still exhibits some deviation from the ideal profile. This is likely due to an altered surface structure which differs from the bulk in some way. This may have arisen from exposure to air or hydration over time. However, because a similar modification exists in the sample X data, it must be something inherent to the  $\text{Al}_2\text{O}_3$  samples, rather than a modification caused by Al. Overall, with consideration for the effect of thermal drift, misalignment, etc., the sample W data is actually in reasonable agreement with the model and is an appropriate ‘control’ for sample X.

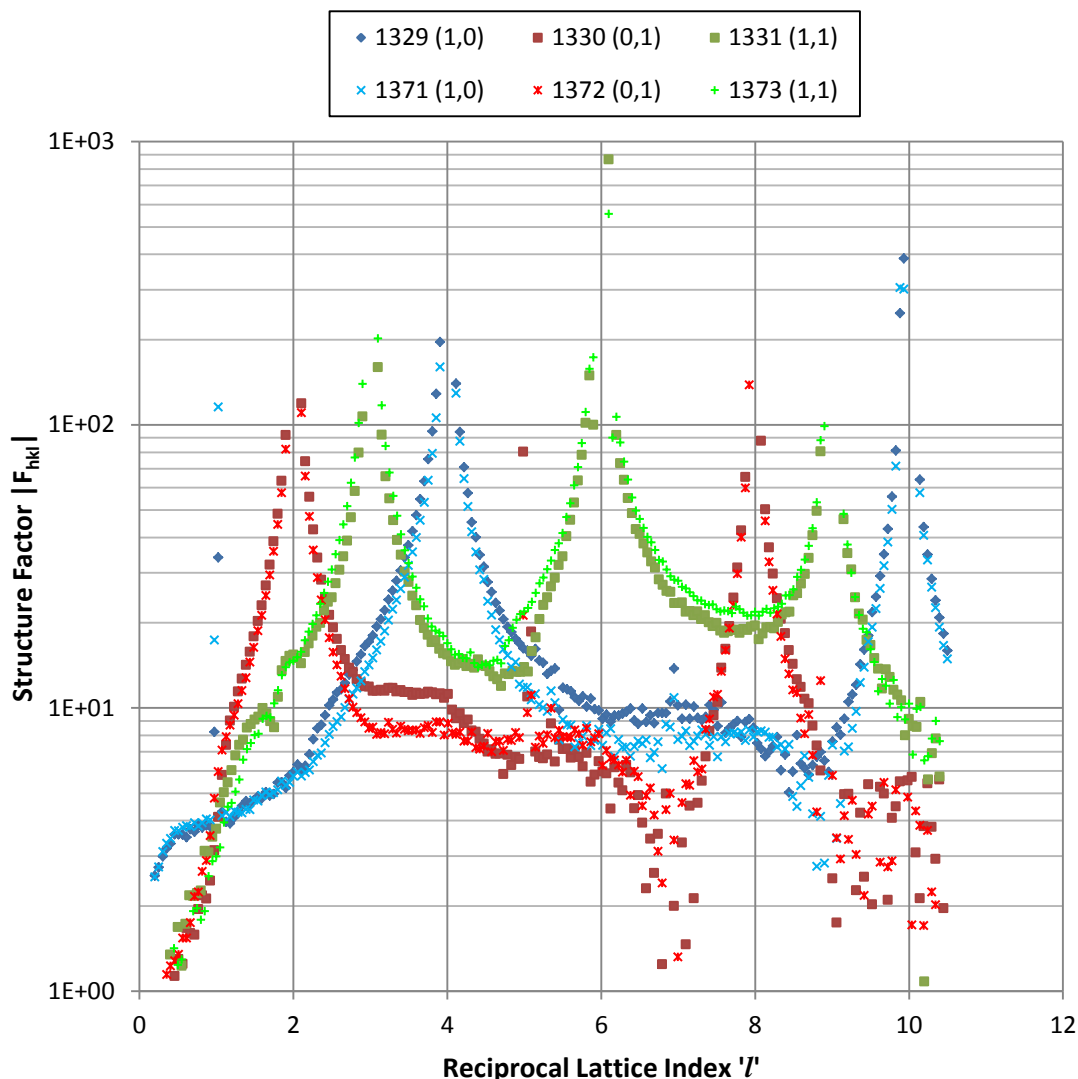
The above observations clarify that the ‘hump’ is the feature of greatest interest in the data, as it has been demonstrated that it results from Al-induced modification of the surface. The width of the ‘hump’ is approximately 3 in the reciprocal lattice vector ‘ $l$ ’, reflecting a feature in real space of approximately 1/3 of the unit cell of  $\text{Al}_2\text{O}_3$ . Using lattice vector  $\mathbf{c}$  of  $12.991\text{\AA}$ , the height of this feature is approximately  $4.3\text{\AA}$ . As the CTR is sensitive only to structures with the same periodicity as the bulk crystal, the implication is that a region of the interface with thickness  $\sim 4.3\text{\AA}$  has been modified by the presence of Al, and has adopted a structure close to that of the  $\text{Al}_2\text{O}_3$  surface. Mathematical fitting later in this chapter will explore the structure of this layer in greater detail.

#### 4.2.3 Comparing effects on surface structure of evaporation vs. crystallisation

During E3, beamline staff at ID03 posited that an evaporator would allow *in-situ* deposition of an Al layer with significantly improved cleanliness compared to the pre-sputtered approach. It would also clarify whether the changes to sample X manifest in the 'hump' (Figure 4-8 and Figure 4-9) may have arisen during *deposition* of Al, rather than during the first heating and cooling process in E3. Performing evaporation under UHV conditions would reduce oxidation of the Al, compared to deposition under the lower-quality vacuum in the Edwards sputter coater. Using sample W as a substrate, Al was deposited using the evaporator built into the UHV chamber, with an assumed deposition rate of  $\sim 0.4 \text{ \AA}/\text{min}$ . The shutter was open originally for 550s resulting in an assumed deposited thickness of  $\sim 4 \text{ \AA}$ ; however scans indicated little change had occurred. This is shown in Figure 4-9 – scan 1330 is pre-evaporation, and 1351 is post-evaporation – these rods show exactly the same profile (taking account of noise in the data)

Thus, following this initial attempt to evaporate, the shutter was simply left open while repeated scans were performed, to look for indications of deposited Al. The intention here was to deposit a layer suitably thick to infer changes to the CTRs; perhaps by generating a similar 'hump' feature as observed on sample X.

An extensive set of CTRs at different  $hkl$  indices were collected pre- and post-evaporation. The data showed that only those at relatively low values of  $h$  and  $k$  were suitably lacking in noise to give a reliable profile; i.e. the (0,1), (1,0) and (1,1) rods. Figure 4-10 displays each of these rods both before and after evaporation of Al.



**Figure 4-10 – (0,1), (1,0) and (1,1) rods collected *before* (1329-1331) and *after* (1371-1373) evaporation of Al onto sample W**

Little change is observed in the above rods; certainly no dramatic appearance of ‘hump’ like structures as observed from sample X. Minor differences between the pre- and post-evaporation rods – for example, the slight downward shift in the (0,1) between  $l = 3$  and  $l = 4$  – may arise from roughness of the sample surface. This in itself is potentially interesting; perhaps indicative of some Al atoms adopting positions in alignment with the surface termination of the  $\text{Al}_2\text{O}_3$ , resulting in (increased) roughness and lowering the intensity in anti-Bragg positions. However, this is not consistent across the entire rod, and indeed in the (1,1) rod the intensity in anti-Bragg positions appears to *increase* slightly in the post-evaporation scan.

The overall lack of modification to the rods indicates the deposited material has not adopted the crystal structure of the substrate. In turn, this demonstrates that the modification (hump) seen to sample X rods is likely a result of crystallisation of the Al against the substrate, following the heating and cooling procedure, and *not* simply the original sputter deposition during sample preparation.

The observations suggest that the evaporated Al has formed a distinct structure having no registry with the  $\text{Al}_2\text{O}_3$ <sup>14</sup>. This implies that the Al, on deposition, did not wet the surface and instead has formed microscopic droplets that have no crystallographic registry with the substrate. Post-experimental microscopy appears to suggest that this is the case; small circular patches of droplets were observed which were identified as being a distinct material rather than a substrate surface feature<sup>15</sup>. This ‘balling-up’ effect has been observed in previous experiments; in E1, the Al likely formed droplets which adopted an orientation relationship with the substrate on cooling; in E2, the ‘balling-up’ effect reduced the thermal contact area and created difficulties with further heating. As described in Chapter 3, the literature suggests Al has a high wetting angle with  $\text{Al}_2\text{O}_3$ , but this did not appear to prohibit the development of orientation relationships in E1 and the first part of E3.

The CTR’s from sample X in Figure 4-8 clearly show some modification which we now deduce *must* be due to the presence of crystalline Al. To explain this discrepancy, we must now consider the qualification in 4.2.1 that sample X had *already* been through a process of heating and cooling (in the first part of E3) *prior* to collection of CTR’s. Melting and re-solidification of the original Al layer has likely contributed to the development of some crystalline order or registry of the Al to the  $\text{Al}_2\text{O}_3$  substrate. Theoretically; in the liquid state, Al atoms would have been free to move into energetically favourable positions, adopting a structure influenced by the presence of the  $\text{Al}_2\text{O}_3$  (001) surface, retaining that

---

<sup>14</sup> Another possibility is that the rods have not changed because no evaporation actually took place; however, this is unlikely due to indications from instruments during the experiment that a flux of Al was achieved.

<sup>15</sup> Overzealous sample cleaning unfortunately removed these features so they are unable to be imaged for display here

structure on cooling and so generating the scattering profile with the characteristic ‘hump’. Subsequently, the *second* heating/cooling profile (Figure 4-7), applied during collection of the CTRs shown in Figure 4-8, did not result in any changes to the profile, suggesting the surface structure remained the same throughout the thermal cycle. This is presumably due to some local stabilisation effect; perhaps adsorption of the Al atoms onto the Al<sub>2</sub>O<sub>3</sub> structure. This theory may be tested to an extent via the model fitting procedure.

#### 4.2.4 *Fitting: Introduction*

Previous experience from E1 clarified the great difficulties in fitting poor-quality data. The level of noise and error made it extremely difficult to operate the process in a physically realistic way. With this experience, a more rigorous data collection process was implemented at E3, recording CTR’s at higher resolution and with accompanying data allowing integration to be performed and correction factors applied in the correct manner.

Reiterating from section 2.6; fitting is performed in ROD through the use of input files which describe 1) the experimental data and 2) the atomic structure of the Al<sub>2</sub>O<sub>3</sub> substrate. First, experimental data is loaded as a list of integrated and corrected structure factor values with respect to *h*, *k* and *l* coordinates. Secondly, the structure is defined. A bulk structure file defines the equilibrium Al<sub>2</sub>O<sub>3</sub> unit cell. This file remains unchanged, and within the model repeats infinitely, representing the long-range order of the Al<sub>2</sub>O<sub>3</sub> single crystal. In the model, a distinct *surface* file sits atop this. Initially this is a copy of the bulk structure, simply defining the surface layer of the substrate. To facilitate the fitting, however, the **occupancy** and **displacement** of the atoms in this surface file are parameterised. In the fitting process, ROD modifies these parameters; this alters the modelled surface structure, and thus the predicted scattering from it. The predicted structure factors are compared with the experimental values, and this process repeats many thousands of times until a reasonable fit is achieved. This is the fundamental process of data fitting.



Due to the mathematical nature of the fitting process, it is relatively straightforward for ROD to generate predicted scattering profiles which represent excellent fits to the experimental data. However – and this is the key issue – this is often achieved through modifying the occupancy and vertical displacement parameters to values which are *mathematically* valid but *physically* unrealistic. Herein lies the great challenge in fitting data. Individual parameters must be varied and monitored in order to generate a physically realistic, rather than just mathematically correct, fit to the data. As the following two sections will demonstrate, choosing to impose or not impose physical constraints can lead to quite different results.

The files used as inputs to ROD are presented in greater detail in the following figures. First, the bulk structure:

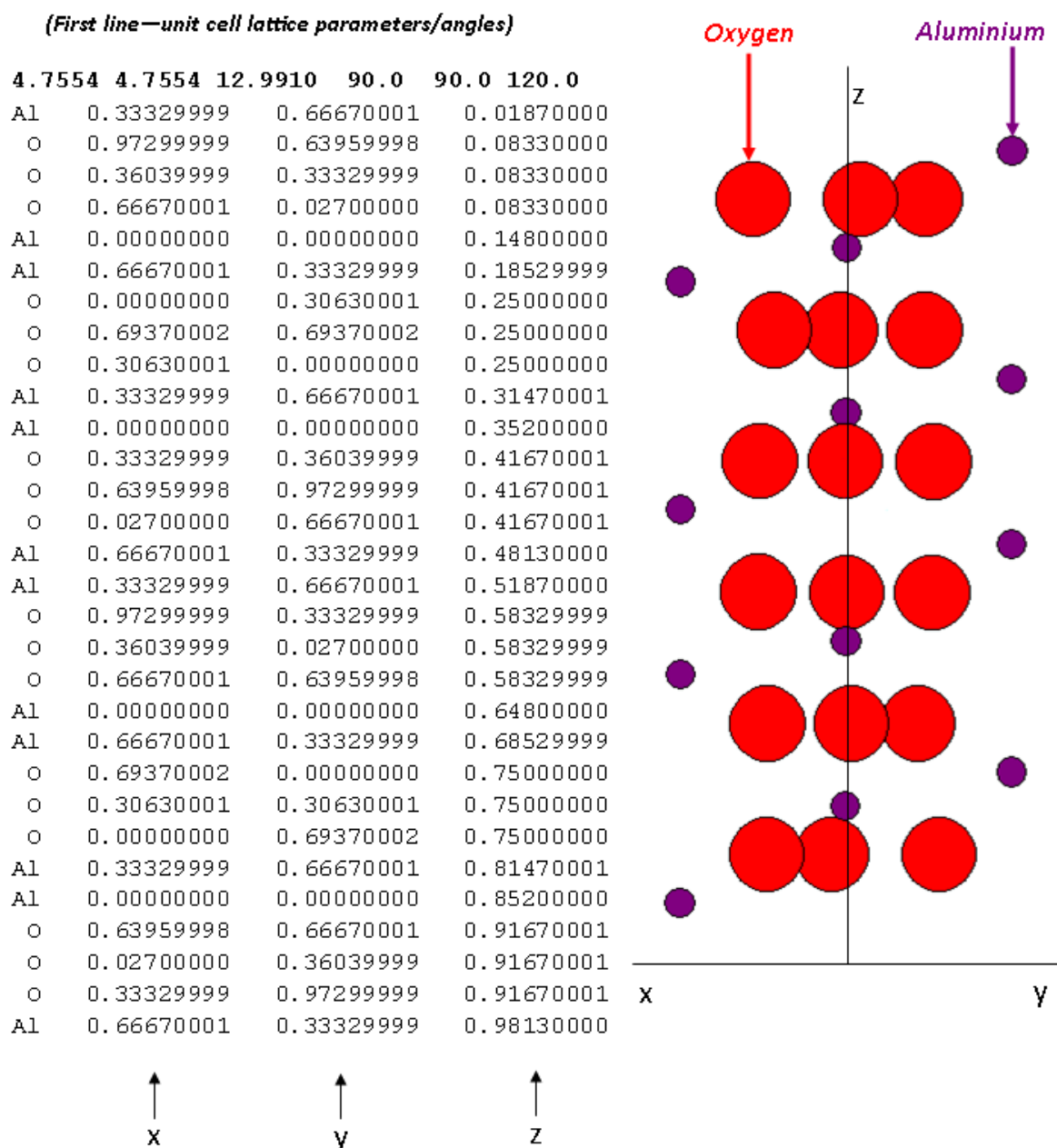
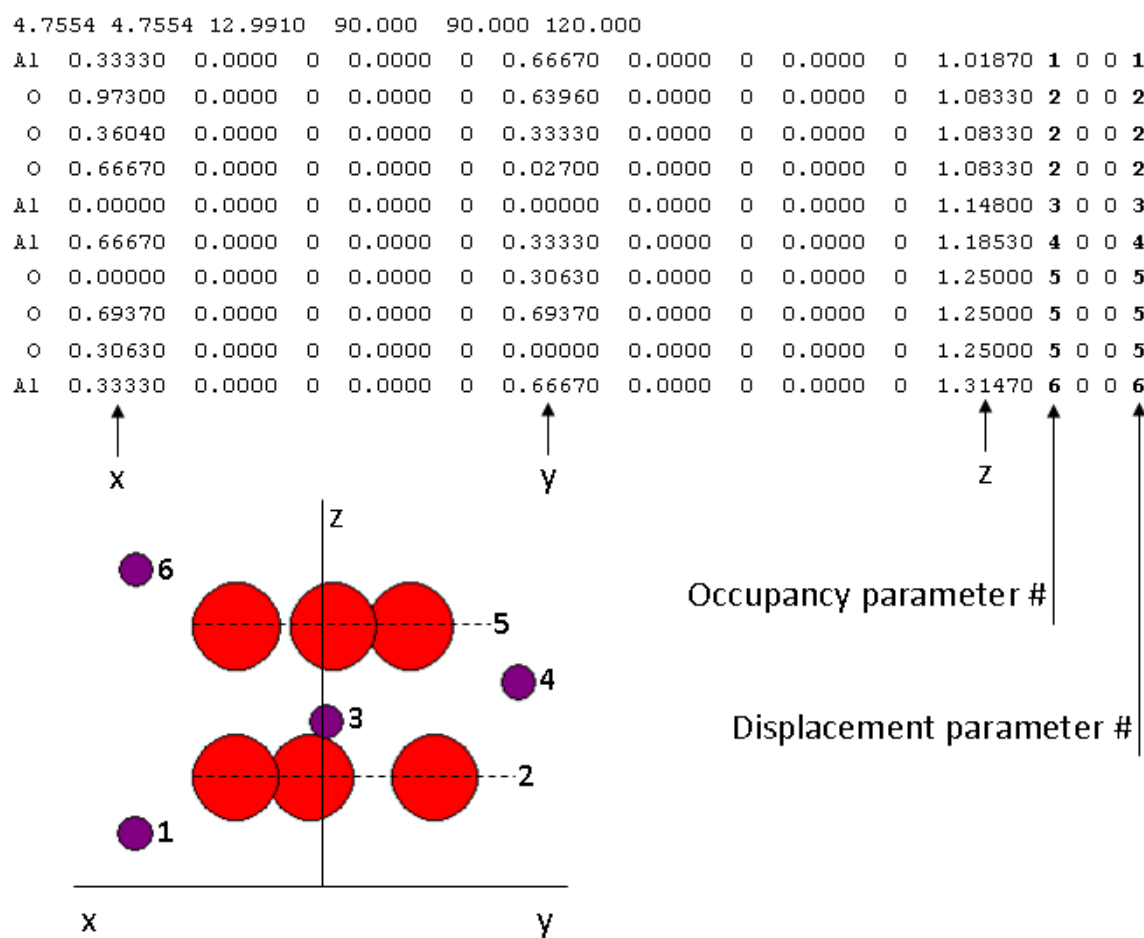


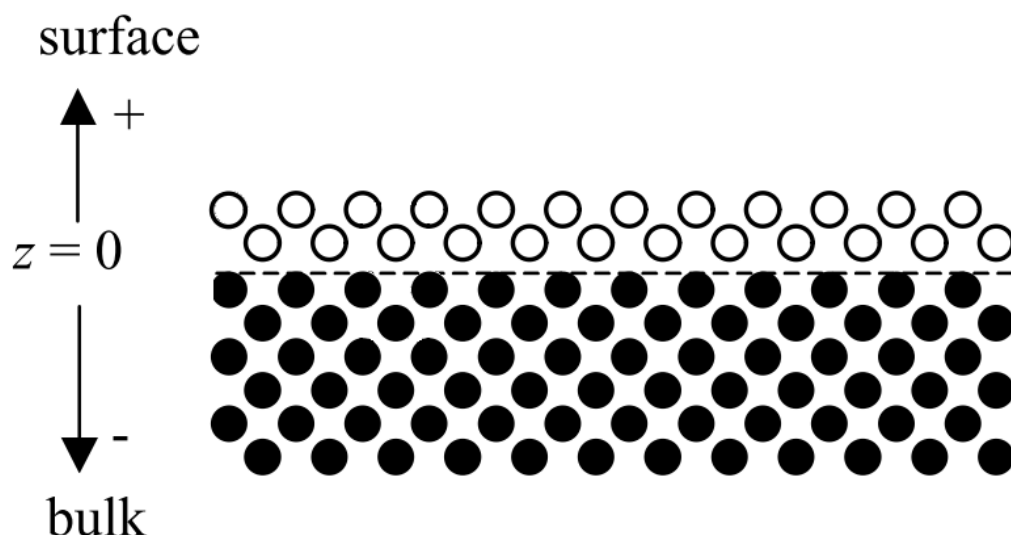
Figure 4-11 – Schematic representation of .bul file used to represent the bulk  $\text{Al}_2\text{O}_3$  structure. Atomic positions are given in the form of coordinates in x, y, z; the values are proportions of the unit cell lattice parameters (displayed in the first line of the text).

The surface file repeats the top layers of the above, with displacement and occupancy of individual atoms assigned parameter values:



**Figure 4-12 – Schematic representation of .fit file used to represent the surface of the  $\text{Al}_2\text{O}_3$  substrate. Occupancy and vertical displacement parameters refer to the individual atoms (or layers of atoms) as indicated.**

In the model the surface file sits above the bulk. The bulk structure repeats laterally in x and y, and to minus infinity in the z direction, representing the real crystal. The surface unit cell repeats only in the lateral direction. Figure 4-13 shows the model setup.



**Figure 4-13 - Model setup for ROD. The surface layer (white) sits on a bulk crystal (black) which extends to minus infinity. Adapted from Ref [86]**

Referring to the above; the atomic positions in the bulk crystal (black) are fixed. The atomic positions in the surface (white) are parameterised in the .fit file. They can be filled or vacant, via the occupancy parameter; and can move via the displacement parameter. Through variation and iteration of these parameters, ROD generates a predicted CTR profile to achieve the closest possible match to the data.

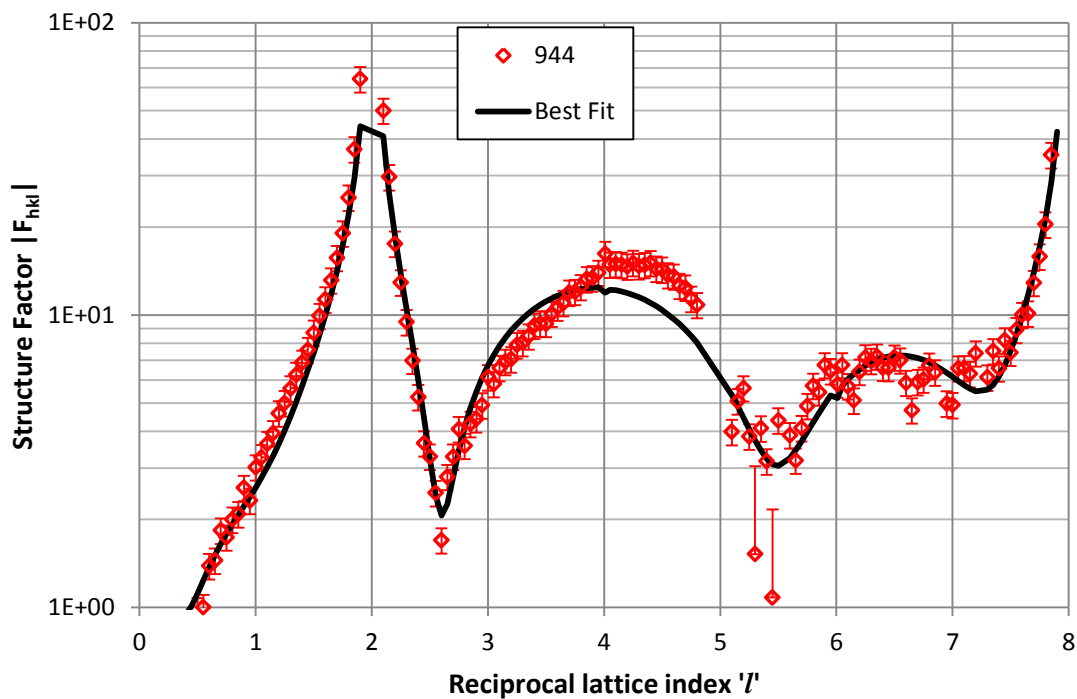
#### *4.2.5 Fitting: No Physical Constraints*

Initial fits were performed using the bulk and surface files shown in Figure 4-11 and Figure 4-12. Fitting is only permissible in ROD when the bulk and surface files have the same lattice parameters; hence it is not possible to, for example, simply have a bulk file representing  $\text{Al}_2\text{O}_3$  and a surface representing Al. Instead, the modification of the  $\text{Al}_2\text{O}_3$  surface under the *influence* of the epitaxial Al is explored.

For both samples X and W a large number of rods were collected, but for fitting purposes only a select few were chosen. Because neither sample exhibited significant change through processing, a single rod is effectively a representative sample. To streamline the fitting process, certain points were deleted from the dataset; specifically those arising from powder peaks, and those at  $l > 8$ , which were observed to be somewhat scattered and inconsistent.

#### 4.2.5.1 Sample X – Scan 944

Figure 4-14 presents the data from scan 944 and the best fit profile obtained with ROD:



**Figure 4-14 - Best fit to representative (0,1) CTR from Sample X**

The model captures the general shape of the CTR; crucially in the shape of the ‘hump’ and the oscillation immediately following it from  $l = 5.5$  to  $l = 7$ . The following shows the values of the relevant parameters used to achieve the fit above.

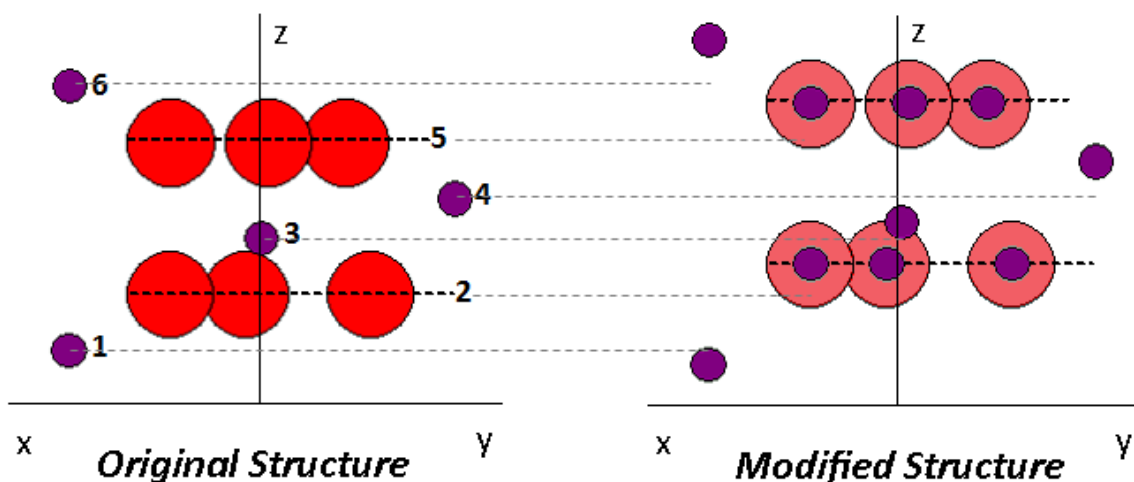
Parameter	Number	Atom type	z-displacement as proportion of unit cell	<i>Absolute displacement (Å)</i>
Scale			0.5795	-
displacement	1	Al	-0.023	-0.299
	2	O (x3)	0.1412	1.834
	3	Al	0.0199	0.259
	4	Al	0.0431	0.560
	5	O (x3)	0.1275	1.656
	6	Al	0.0878	1.141
			<b>Occupancy value</b>	
occupancy	1	Al	0.5	-
	2	O (x3)	1.75	-
	3	Al	0.5	-
	4	Al	0.5	-
	5	O (x3)	1.75	-
	6	Al	1	-

**Table 4-1 – Values of parameters used to achieve fit in Figure 4-14**

**Occupancy:** the occupancy parameter normally should only vary between 0 (vacant) and 1 (atom present); this suggests the occupancy parameters 2 and 5 would be inaccurate. However, as the model assumes a structure that repeats in the x and y directions, one can picture a scenario in which the value 1.75 represents full occupation and the other values vary in proportion to it (e.g. if there were 175 unit cells in total, all atomic positions defined by parameters 2 and 5 would be fully occupied, positions 1, 3 and 4 would be occupied in 50 of those unit cells, and position 6 in 100). It proved extremely difficult to achieve a fit where the occupancy was restricted to  $\leq 1$ , and the stated method is worth proposing due to the quality of the fit it produces.

**Displacement:** the challenge here is to only permit values which are realistic; i.e. the atoms are not moving through very large distances which would be entirely impossible. The parameters are given as values representing a proportion of the unit cell height (12.991Å in the model used) and so are also given in the table converted to an absolute distance. Here, the values for 1, 3, 4 and 6 (i.e. the Al atoms) are certainly reasonable; the values for 2 and 5 (O atoms) are perhaps *just* permissible – approx. 15% of the overall unit cell height.

The following indicates, schematically, the changes to the surface layer in terms of z-displacement:



**Figure 4-15 – Schematic indication of the change to the  $\text{Al}_2\text{O}_3$  surface structure suggested by the data fitting. The modified structure represents an expansion of the original along z. Oxygen positions are shown with O and Al atoms, to reflect the possibility that Al may in fact be present instead of O, as discussed in the text.**

Taking all the above into account, what does the fit imply about the surface structure? It is clear that there is an 'over-occupation' of oxygen (all reasonable fits were achieved with values for occupancy 2 and 5 >1). Although this is justifiable considering an infinitely repeating structure, the indication, in a more basic sense, is that the atoms in these positions are scattering very strongly. Scattering is stronger from heavier elements, and as aluminium (atomic no. 13) is heavier than oxygen (atomic no. 8), it is reasonable to suggest that the atoms in these positions are in fact aluminium rather than oxygen (see Figure 4-15), which may be possible considering the large quantity of Al present. Working with this theory, the suggestion is that Al atoms reside in the surface structure of the  $\text{Al}_2\text{O}_3$ ; adopting a structure similar to the bulk substrate (albeit somewhat expanded). This may occur via **adsorption** of Al into the surface. Occupancy values for the existing Al atom positions are all <1, indicating an imperfect crystal structure. The Al in the surface may have a tendency to disassociate from the  $\text{Al}_2\text{O}_3$  matrix if sufficiently energised; indeed this property is harnessed in the studies of Oh *et al* [4], [6]. This may have occurred during the heating and

cooling process applied in E3 S1 (3.3.2), *before* collection of CTR's, resulting in an altered surface structure prior to this part of the experiment.

In a general sense, the results indicate that the stoichiometry of the surface has been affected by the crystallisation of the Al, and that this modification remains on subsequent heating and cooling of the system. However, the preceding fit was of course achieved *without* the imposition of physical constraints, and so cannot be taken as a definitive solution. It is fair to say, for example, that the large displacement of the 'oxygen' layers, as well as the use of occupancy values  $>1$ ; remain matters for debate. Also, the model only represents modification of the existing  $\text{Al}_2\text{O}_3$  (001) surface, not *directly* taking into account any adsorption of 'extra' Al which was not part of the original  $\text{Al}_2\text{O}_3$  structure. Despite these issues, it represents a reasonable first attempt to fit the experimental data, and, taking into account the justifications described in the preceding section, is a useful exercise and a sound demonstration of the technique.

#### 4.2.6 *Fitting: Physical Constraints*

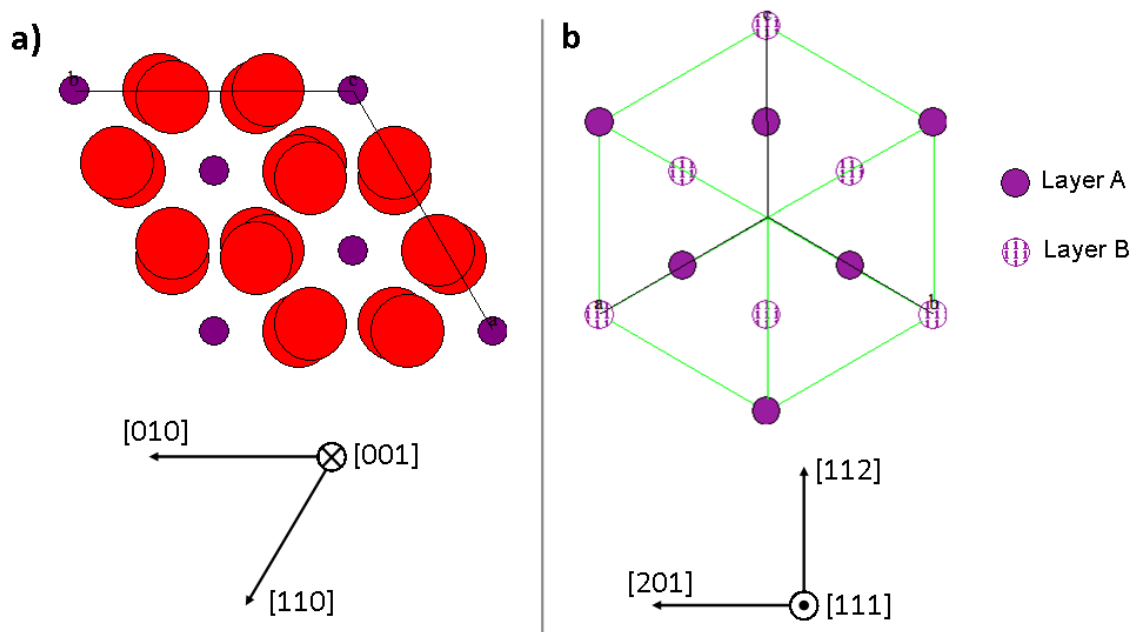
To impart some physical realism to the generated fits, observations from previous experiments can be incorporated into our understanding of the structures which form at the Al/ $\text{Al}_2\text{O}_3$  interface, providing a 'headstart' to the fitting process. E1 gave strong indications that the following **orientation relationship** develops at the interface between Al and  $\text{Al}_2\text{O}_3$ :

$$(001) \langle 110 \rangle \text{Al}_2\text{O}_3 // (111) \langle 112 \rangle \text{Al}$$

$$\text{or } (0001) \langle 11\bar{2}0 \rangle \text{Al}_2\text{O}_3 // (111) \langle 112 \rangle \text{Al}$$

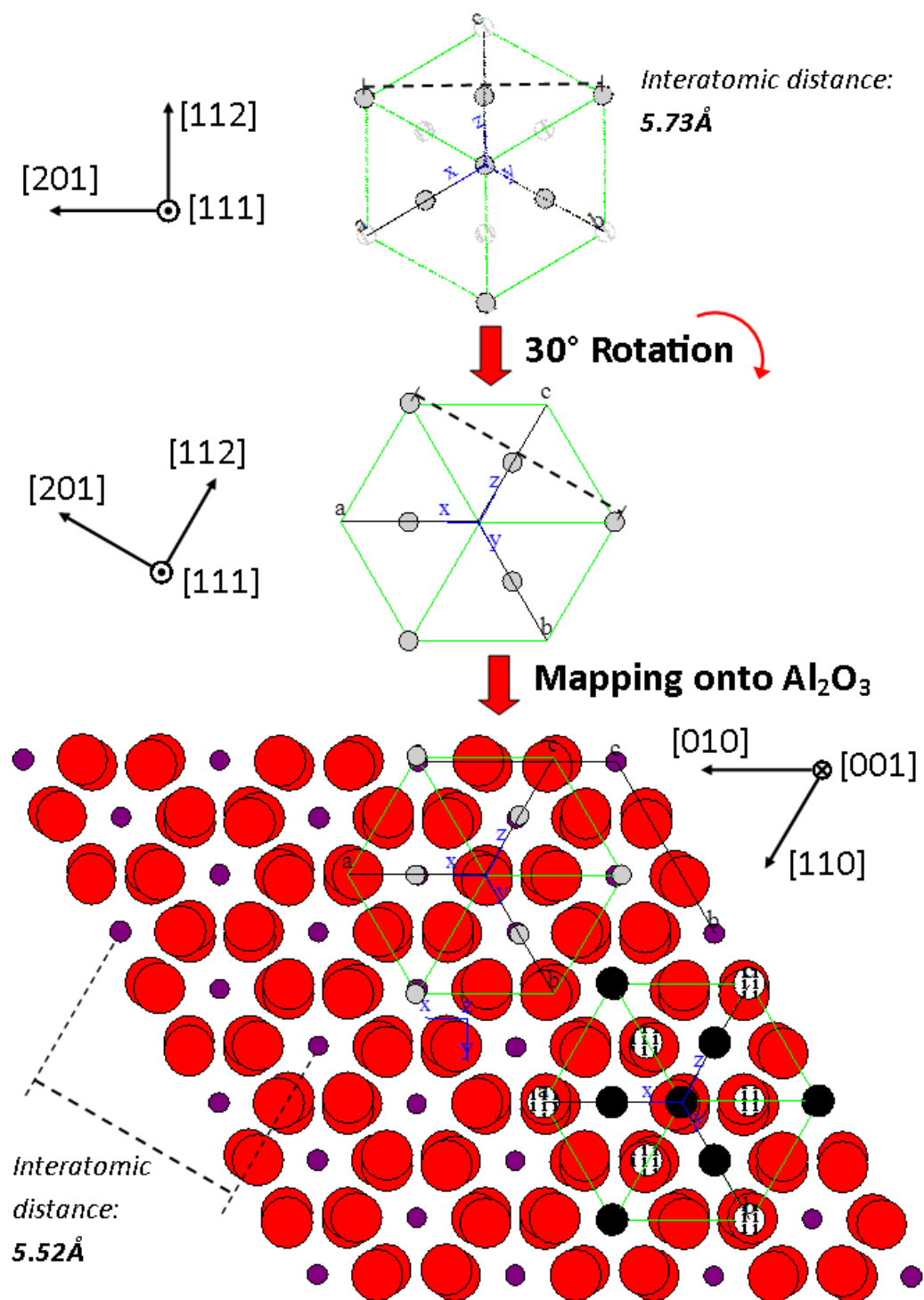
Using software package CaRIne 3.1 [126] the relevant crystal structures are generated and compared as shown in Figure 4-16.





**Figure 4-16 – Crystal structures of a)  $\text{Al}_2\text{O}_3$  (001) and b) Al(111). Images are scaled relative to each other such that the Al atoms are of equal size. Crystallographic axes are shown beneath the structures. Note that b) presents the unit cell with *two* layers of Al (111) following the ABAB stacking sequence.**

The orientation relationship indicates that Al  $\langle 112 \rangle$  lies parallel to  $\text{Al}_2\text{O}_3$   $\langle 110 \rangle$ ; this implies a  $30^\circ$  rotation of the Al unit cell such that these axes are aligned as illustrated in Figure 4-17. This rotation creates a situation whereby atoms in the Al (111) plane align close to Al sites in the  $\text{Al}_2\text{O}_3$  (001) surface. A relatively close mapping exists, accommodated by a strain of  $\sim 3.6\%$  along a chosen interatomic distance; this is not unrealistic, and perhaps indicates why this orientation relationship appears to have been favoured in experiments E1 through E3. To provide evidence for this claim, we must observe whether the use of this model results in a good fit to the data.



**Al strain to match: -3.66%**

Figure 4-17 – Schematic representation Al (111) planes, 30° rotation about  $[111]$  axis, followed by mapping onto  $\text{Al}_2\text{O}_3$  (001) surface. On the lower portion of the image, the first Al unit cell (small, grey circles) shows only the atoms within an individual (111) crystal plane (layer A). The second Al unit cell (larger, black circles) shows all remaining atoms in the unit cell (following the ABAB stacking sequence)

Based on this model, a new .fit file is created to represent the surface *plus* the first few layers of Al(111). The file is the same as the previous .fit shown in Figure 4-12, but with extra Al atoms added in positions approximately representing the (111) stacking sequence. In the model, the atoms in this region will be free to move, so exact positions are less important.

```

4.7554 4.7554 12.9910 90.000 90.000 120.000
Al 0.33330 0.0000 0 0.0000 0 0.66670 0.0000 0 0.0000 0 1.01870 1 0 0 1
O 0.97300 0.0000 0 0.0000 0 0.63960 0.0000 0 0.0000 0 1.08330 2 0 0 2
O 0.36040 0.0000 0 0.0000 0 0.33330 0.0000 0 0.0000 0 1.08330 2 0 0 2
O 0.66670 0.0000 0 0.0000 0 0.02700 0.0000 0 0.0000 0 1.08330 2 0 0 2
Al 0.00000 0.0000 0 0.0000 0 0.00000 0.0000 0 0.0000 0 1.14800 3 0 0 3
Al 0.66670 0.0000 0 0.0000 0 0.33330 0.0000 0 0.0000 0 1.18530 4 0 0 4
O 0.00000 0.0000 0 0.0000 0 0.30630 0.0000 0 0.0000 0 1.25000 5 0 0 5
O 0.69370 0.0000 0 0.0000 0 0.69370 0.0000 0 0.0000 0 1.25000 5 0 0 5
O 0.30630 0.0000 0 0.0000 0 0.00000 0.0000 0 0.0000 0 1.25000 5 0 0 5

Al 0.33330 0.0000 0 0.0000 0 0.66670 0.0000 0 0.0000 0 1.31470 6 0 0 6
Al 0.66670 0.0000 0 0.0000 0 0.33330 0.0000 0 0.0000 0 1.31470 6 0 0 6
Al 0.00000 0.0000 0 0.0000 0 0.00000 0.0000 0 0.0000 0 1.31470 7 0 0 7

Al 0.33330 0.0000 0 0.0000 0 0.33330 0.0000 0 0.0000 0 1.5000 8 0 0 8
Al 0.66670 0.0000 0 0.0000 0 0.00000 0.0000 0 0.0000 0 1.5000 8 0 0 8
Al 0.00000 0.0000 0 0.0000 0 0.66670 0.0000 0 0.0000 0 1.5000 8 0 0 8

Al 0.00000 0.0000 0 0.0000 0 0.33330 1.0000 10 0.0000 0 1.75000 9 0 0 9
Al 0.66670 -1.0000 10 0.0000 0 0.66670 -1.0000 10 0.0000 0 1.75000 9 0 0 9
Al 0.33330 1.0000 10 0.0000 0 0.00000 0.0000 0 0.0000 0 1.75000 9 0 0 9

```

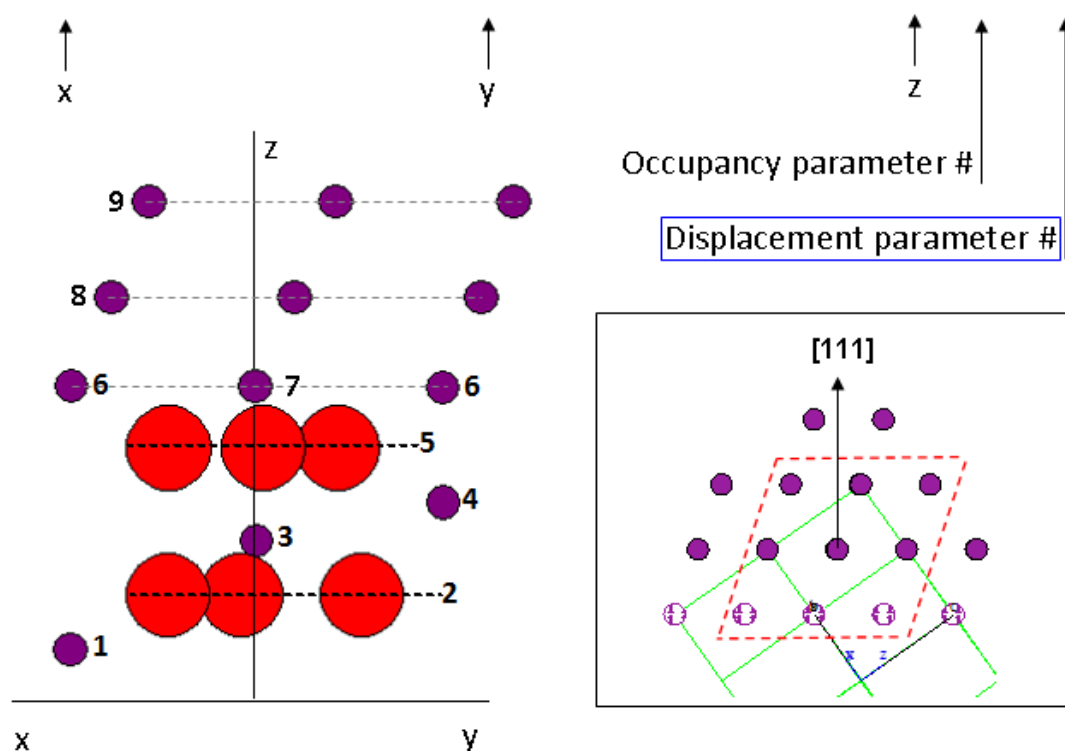


Figure 4-18 – Modified .fit file to represent  $\text{Al}_2\text{O}_3$  surface *and* the first interfacial Al (with an approximately (111) structure). Diagram is schematic; stated positions may not exactly correspond. Inset shows the equilibrium Al (111) crystal structure from a 'side view' (along [110]) for reference.

A key addition here is the implementation of parameter **10**, a further displacement parameter which permits movement of the upper level of Al atoms in the x and y directions. Previously, atom displacements have been free to alter only in the z direction.

Following an extensive process investigating the effects of individual parameters, the following shows the best fit achieved using the above. The previous fit from Figure 4-14 is included as a reference. Table 4-2 lists the parameter changes.

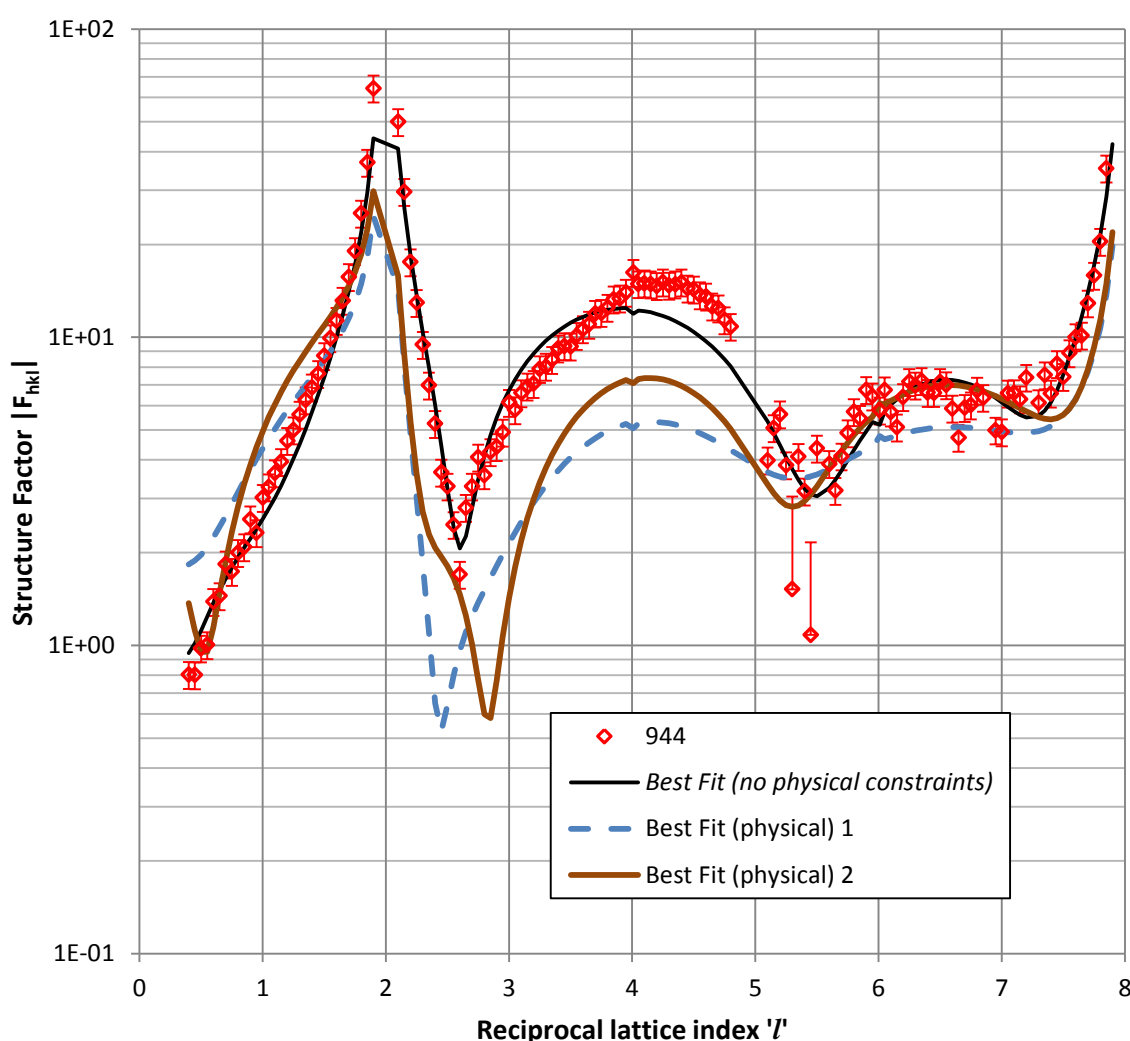
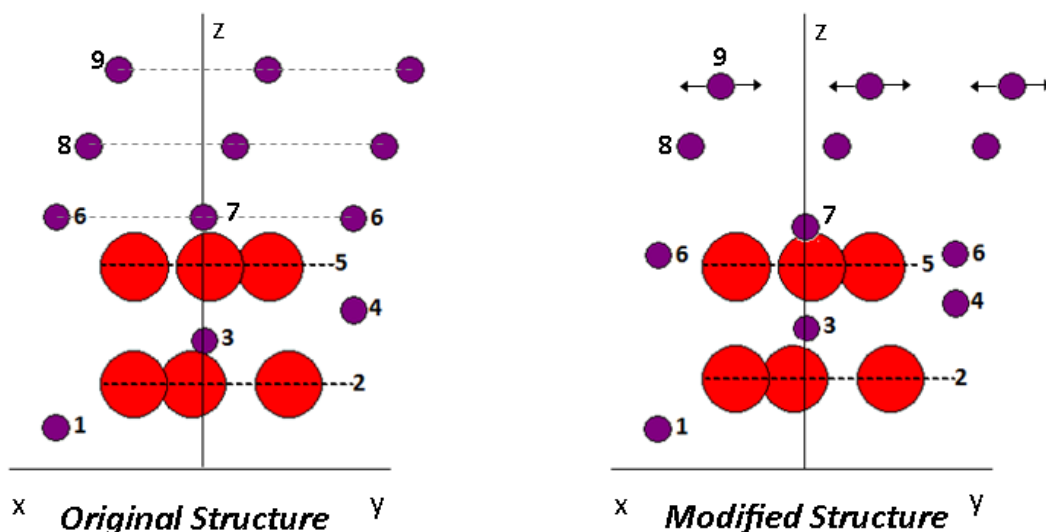


Figure 4-19 – Best fits to representative (0,1) rod from sample X. Series *Best Fit (no physical constraints)* is a repeat of the fit from Figure 4-14.

Parameter	Number	Atom type	z-displacement as proportion of unit cell	<i>Absolute displacement (Å)</i>
Scale			<i>Best fit (physical) 1: 0.2608</i> <i>Best fit 2: 0.3007</i>	-
displacement	1	Al	-0.0026	-0.0337766
	2	O (x3)	0.0098	0.1273118
	3	Al	0.0178	0.2312398
	4	Al	0.0135	0.1753785
	5	O (x3)	0	0
	6	Al	-0.117	-1.519947
	7	Al	-0.0118	-0.1532938
	8	Al	0	0
	9	Al	-0.076	-0.987316
displacement (in-plane)	10	Al	0.1	1.2991
			Occupancy value	
occupancy	1	Al	1	-
	2	O (x3)	1	-
	3	Al	1	-
	4	Al	1	-
	5	O (x3)	1	-
	6	Al	1	-
	7	Al	1	-
	8	Al	1	-
	9	Al	<i>Best fit (physical) 1: 0.5</i> <i>Best fit (physical) 2: 1.053</i>	-

**Table 4-2 - Values of parameters used for 'Best Fit (physical)' in Figure 4-19. Fits '1' and '2' result in the same values apart from differences in *Scale* and *occupancy 9*. These are indicated in the table.**

Best fits (physical) 1 and 2 as displayed in Figure 4-19 do not initially appear to describe the 'hump' as closely as the previous fit; however, this is mostly due to the scale factor (i.e. the *intensity* along the modelled profile), not the structure itself. The *shape* of the 'hump' is more important, and this certainly is captured in both fits. Corresponding parameters in the table are more physically realistic than those in Table 4-1; atomic displacements are smaller overall (excluding position 6). The modified structure implied by these values is shown schematically in Figure 4-20.



**Figure 4-20 – Schematic indication of the change to the  $\text{Al}_2\text{O}_3$  surface structure suggested by physical best fits. Arrows on atoms at position #9 indicate the displacement in x/y indicated by the parameter displacement 10.**

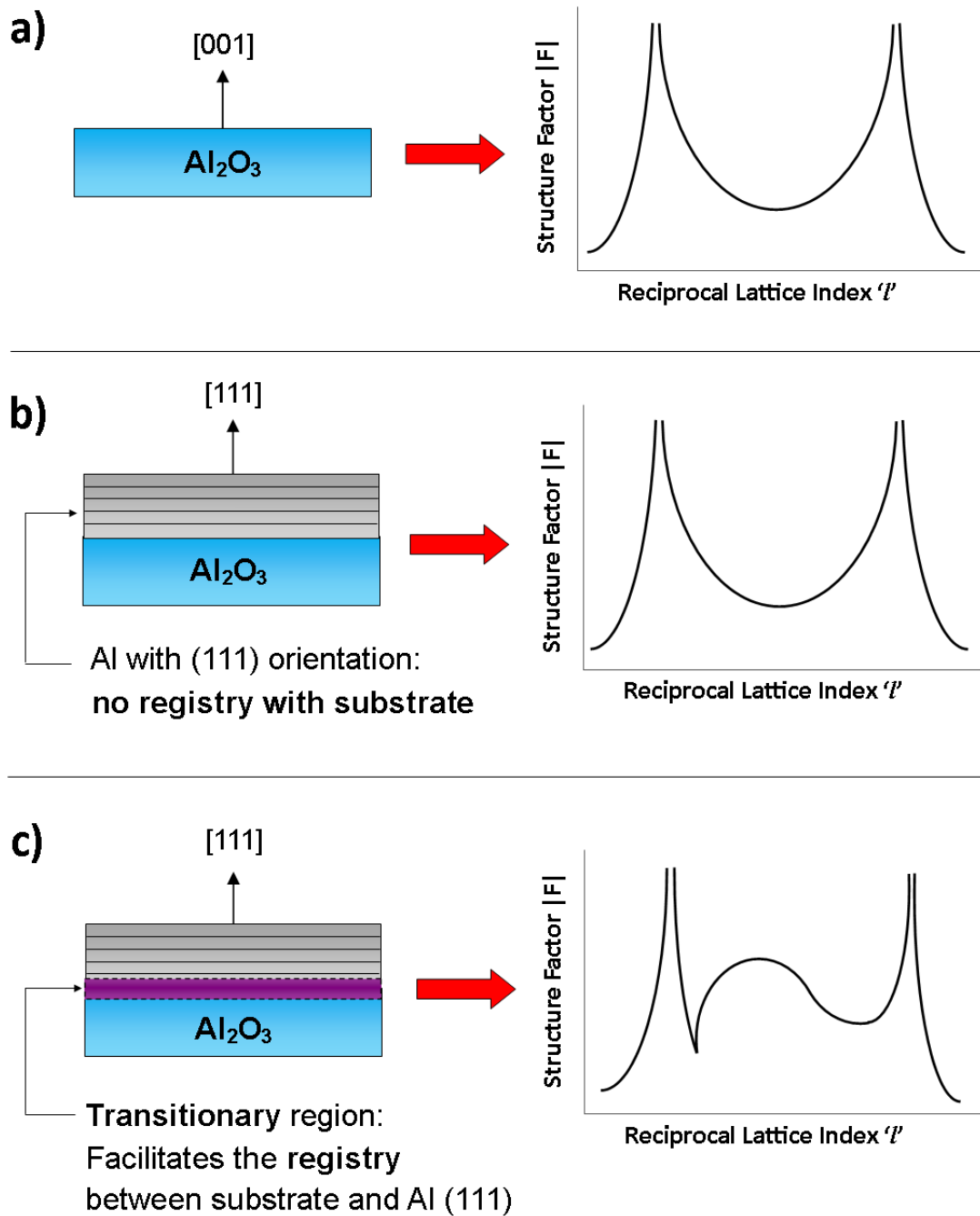
The altered atomic positions in the model suggest the existence of **strain** in the region between  $\text{Al}_2\text{O}_3$  and Al; especially in the upper part of the model which represents the first layers of Al (111). The strain appears to be **non-uniform**; there is both expansion and contraction along z. This accords with observations from E1 and E3, in which solidified Al was observed to exhibit strain along the [111] direction.

The highlighted section in Table 4-2 demonstrates the sensitivity of the CTR profile to changes to the surface atomic structure. Physical best fits ‘1’ and ‘2’ are distinguished *only* by a different value for occupancy at the top layer (layer 9 in Figure 4-20): 0.5 in best fit ‘1’ (half occupancy) and 1.053 in best fit ‘2’ (full/slight over-occupancy) yet are readily discernable in Figure 4-19 . This highlights the great challenge in achieving good fits; apparently small changes to atomic structure can result in significantly different scattering profiles. Despite this, both fits correctly capture the shape and size of the ‘hump’ feature. This indicates the validity of the original structure proposal; i.e. a semi-ordered Al (111) above the  $\text{Al}_2\text{O}_3$  (001) surface.

### 4.3 Conclusion of CTR work

It is clear from the shape of the CTR profiles in Figure 4-8 and Figure 4-19 that there has been a significant modification of the atomic structure at the interface of Al and  $\text{Al}_2\text{O}_3$ . The 'hump' feature represents a modified region approximately 4Å in thickness. This is suggested to be Al-rich due to indications from the fit in section 4.2.5 and the knowledge that Al is present on the substrate surface. Physical fits indicate the structure within this region is likely a semi-ordered epitaxial arrangement of Al atoms against a modified  $\text{Al}_2\text{O}_3$  surface, which quickly decays to equilibrium Al (111) crystallography with increasing distance from the  $\text{Al}_2\text{O}_3$  surface. This appears permissible due to reasonably close mapping between the  $\text{Al}_2\text{O}_3$  (001) surface and in-plane Al (111) structure. A model based on this assumption gives a reasonable fit to the data with, crucially, a predicted structure which appears to be physically realistic. The transitional region is suggested to accommodate strain at the interface between the substrate and crystal, allowing *above* this region to adopt the equilibrium (111) structure (thus giving no contribution to the CTR). This proposal overlaps well with years of speculation in the literature that nucleation is preceded by the formation of some kind of transitional layer between substrate and solidifying crystal; e.g. the model proposed by Fan [32] in which nucleation is preceded by the generation of a "*pseudomorphic*" solid layer. The evidence for this claim suggested by the results presented in this chapter is summarised in Figure 4-21.





**Figure 4-21 - Summary of findings in Chapter 4.** a) indicates, schematically, the ideal CTR profile obtained from a clean  $\text{Al}_2\text{O}_3$  (001) surface. b) indicates the addition of Al, with (111) planes parallel to the substrate surface, would not result in any modification to this profile due to the lack of registry with the substrate. c) indicates the existence of a semi-ordered region between the substrate and crystal and the modification to the CTR that results. The transitional region is suggested to accommodate strain between the substrate and the crystal.

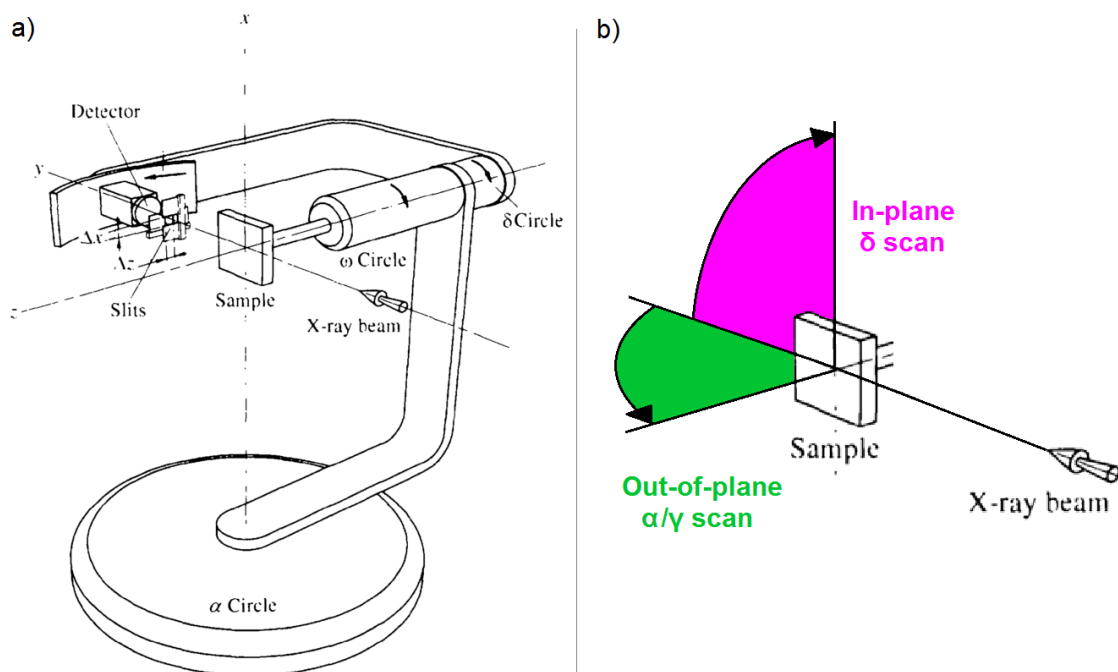
The author believes that the mechanism suggested should not be considered an absolute conclusion, but represents a strong possibility. Compared to bulk diffraction, the CTR signal arises from a relatively small number of atoms and as such can be more difficult to distinguish from background scattering. The fitting process is also challenging, as evidenced by the fact that apparently small changes in model parameters can produce large changes in the profile, and investigating these systematically is very time consuming as a result. Despite these issues, the author feels that this work represents a good demonstration of the *potential* of the techniques. Typically, structure determination using CTR's requires a set of rods at a range of different  $(h,k)$  indices, as the contribution from the surface is stronger in certain rods. Therefore, in future, a combination of better sample preparation, repeat measurements and a rigorous fitting process would be expected to produce significantly improved results and provide strong supporting evidence for the claims in this chapter.

## **5 Results: Understanding the mechanism at the interface between $\text{TiB}_2$ and Al melt**

This chapter aims to provide a better understanding of the mechanism of nucleation at the  $\text{Al/TiB}_2$  interface, which has relevance to grain refinement. Initial investigations took place during E3. Following an interesting and revealing investigation, E4 was devoted entirely to the investigation of  $\text{Al/TiB}_2$ . In this chapter, section 5.1 will detail relevant results from E3, followed by results from E4 in 5.2. Section 5.3 presents analysis pertaining to the formation of  $\text{Al}_3\text{Ti}$  at the  $\text{Al/TiB}_2$  interface, followed by conclusions in section 5.4.

The  $\text{TiB}_2$  samples at both E3 and E4 were probed using X-ray energy of 19.9keV. At the 20keV energy used in the first part of E3, strong fluorescence arose from the Mo which overloaded the detector and obscured the rest of the data. A change to 19.9keV eliminated this problem.

It is worth reiterating the relationship between scattering angles and the structural information which can be drawn from scans through them. Figure 5-1 and Table 5-1 describe the relationship between diffractometer circles and the directionality of the scattering. The angles are common to E3 (at ESRF ID03) and E4 (at Diamond I07).



**Figure 5-1 – Diffractometer angles used for characterisation. a) shows the z-axis diffractometer of the type used at ID03 (I07 is fundamentally the same, with  $\gamma$  rotating the whole diffractometer rather than just the detector). b) indicates the physical directions of the characterisation scans and how they relate to sample geometry. Adapted from [106]**

Diffractometer angles	Relation to $2\theta$	Comments
<b>Delta (<math>\delta</math>)</b>	$\delta$ : rotation about sample normal  $\delta = 2\theta$ in-plane	Gives information about the in-plane structure of the sample, i.e. across the surface/interface
<b>Alpha (<math>\alpha</math>)</b>	$\alpha$ : angle at <b>sample</b> position $\gamma$ : angle at <b>detector</b> position	Gives information about the out-of-plane structure of the sample, i.e. above the surface/interface in the direction of the sample normal
<b>Gamma (<math>\gamma</math>)</b>	$2*\alpha = 2\theta$ out-of-plane or $\gamma = 2\theta$ out-of-plane	

**Table 5-1 – Diffractometer angles**

## 5.1 Experiment Three: Sample A

The Al/TiB<sub>2</sub> sample for E3 was denoted 'sample A'. The following work represents the first time that interfacial behaviour in the Al/TiB<sub>2</sub> system has been directly investigated using these techniques. Previous studies, most prominently those of Iqbal *et al* [73]–[78] have provided useful insight into the behaviour, providing evidence for the presence of metastable Al<sub>3</sub>Ti in the *bulk melt*. Iqbal's studies illuminate a small cylindrical melt containing a large number of TiB<sub>2</sub> particles in an Al-Ti matrix, transmission through which gives rise to 2D XRD patterns from which phase transformations may be observed. The work detailed here approaches the system from a surface scattering perspective, specifically targeting the *interface* between the two materials. The experiments are thus intended to provide greater insight into the *interfacial* behaviour compared with previous work.

Sample A comprised what was essentially a 'stack' of materials; an Mo substrate, onto which a TiB<sub>2</sub> layer was sputter deposited, followed by an Al layer, also sputter deposited. In contrast to all previous samples, sample A was therefore polycrystalline throughout. As TiB<sub>2</sub> is not in single-crystal form, techniques requiring crystallographic alignment, such as CTR analysis, are not possible. Experiments are performed in a manner similar to a powder diffraction approach.

### 5.1.1 Characterisation

The initial challenge was to characterise the in- and out-of-plane scattering from the sample, to identify materials present and the relative orientation of the crystallites within. At the chosen energy of 19.9keV, corresponding to an X-ray wavelength  $\lambda = 0.623$ , Table 5-2 describes a selection of the materials and corresponding  $2\theta$  peak positions which were of greatest importance. Material data is taken from the ICSD crystallography database [127]. The ICSD holds structural data drawn from 50+ years of crystallography research and allows predicted scattering profiles to be generated from the vast range of elements and compounds studied using X-ray diffraction and similar techniques. Data

was obtained for all materials under investigation, including those expected to be present in surrounding equipment. This data could then be overlaid on the profiles from the characterisation scans to verify the presence of particular materials and phases, as shown in Figure 5-2, Figure 5-3 and Figure 5-4.

	<b>Peak Position in <math>2\theta</math> (°)</b>	<b><math>\theta</math> (°)</b>	<b><math>d</math> (Å)</b>	<b>Planar Family</b>
<b>Aluminium</b> [149]	15.32	7.66	2.338	<b>Al {111}</b>
	17.71	8.85	2.024	<b>Al {200}</b>
	25.15	12.57	1.431	<b>Al {220}</b>
	29.57	14.78	1.221	<b>Al {311}</b>
<b>TiB<sub>2</sub></b> [99]	11.06	5.53	3.232	<b>TiB<sub>2</sub> {001}</b>
	13.61	6.81	2.629	<b>TiB<sub>2</sub> {100}</b>
	17.57	8.78	2.040	<b>TiB<sub>2</sub> {101}</b>
<b>Molybdenum</b> [148]	16.08	8.04	2.227	<b>Mo {110}</b>
	22.82	11.41	1.575	<b>Mo {200}</b>
	28.06	14.03	1.285	<b>Mo {211}</b>

**Table 5-2 – Peak positions and corresponding  $d$  values (atomic spacing) for materials of interest in investigation of the Al/TiB<sub>2</sub> system. X-ray energy 19.9 keV ( $\lambda=0.623\text{\AA}$ ). Specific references to the individual studies from which structural data is taken are given in the first column.**

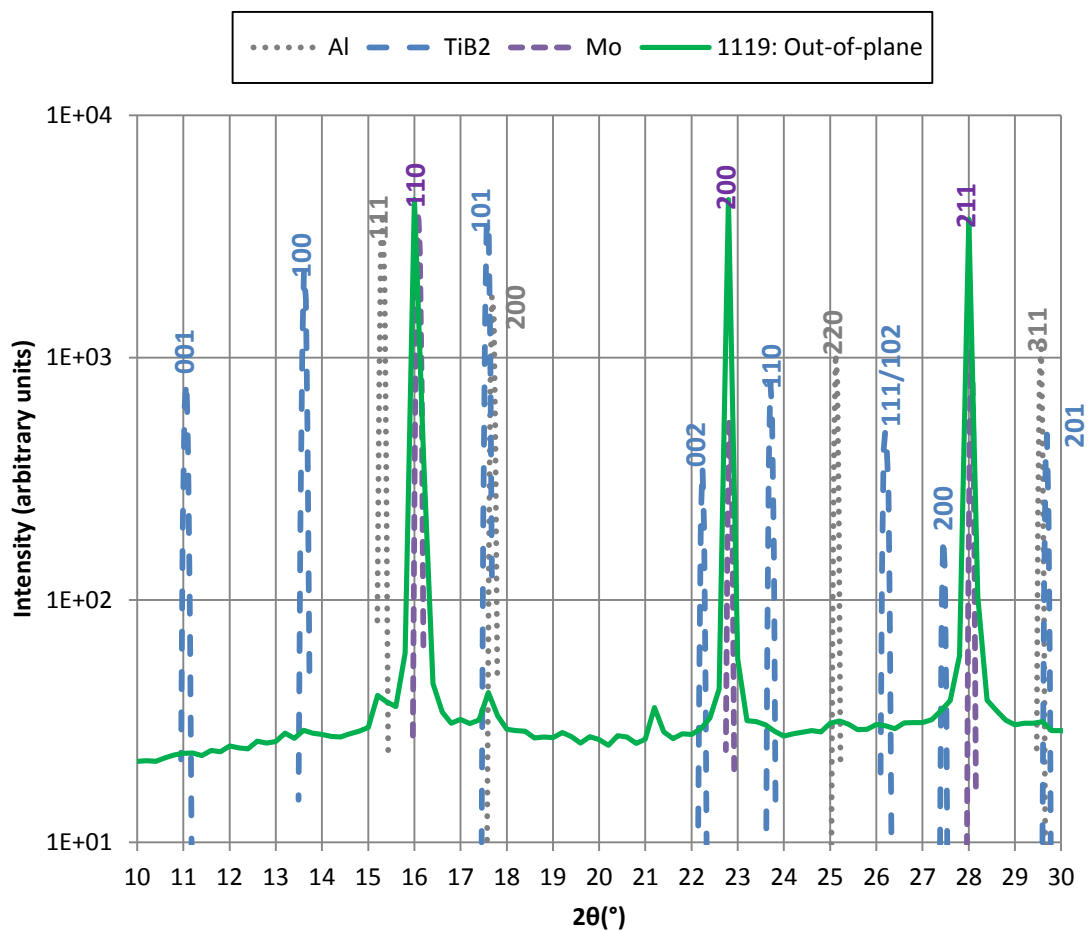


Figure 5-2 – Out-of-plane characterisation from E3 sample A. Angle of incidence varies from  $5^{\circ}$  -  $15^{\circ}$ .

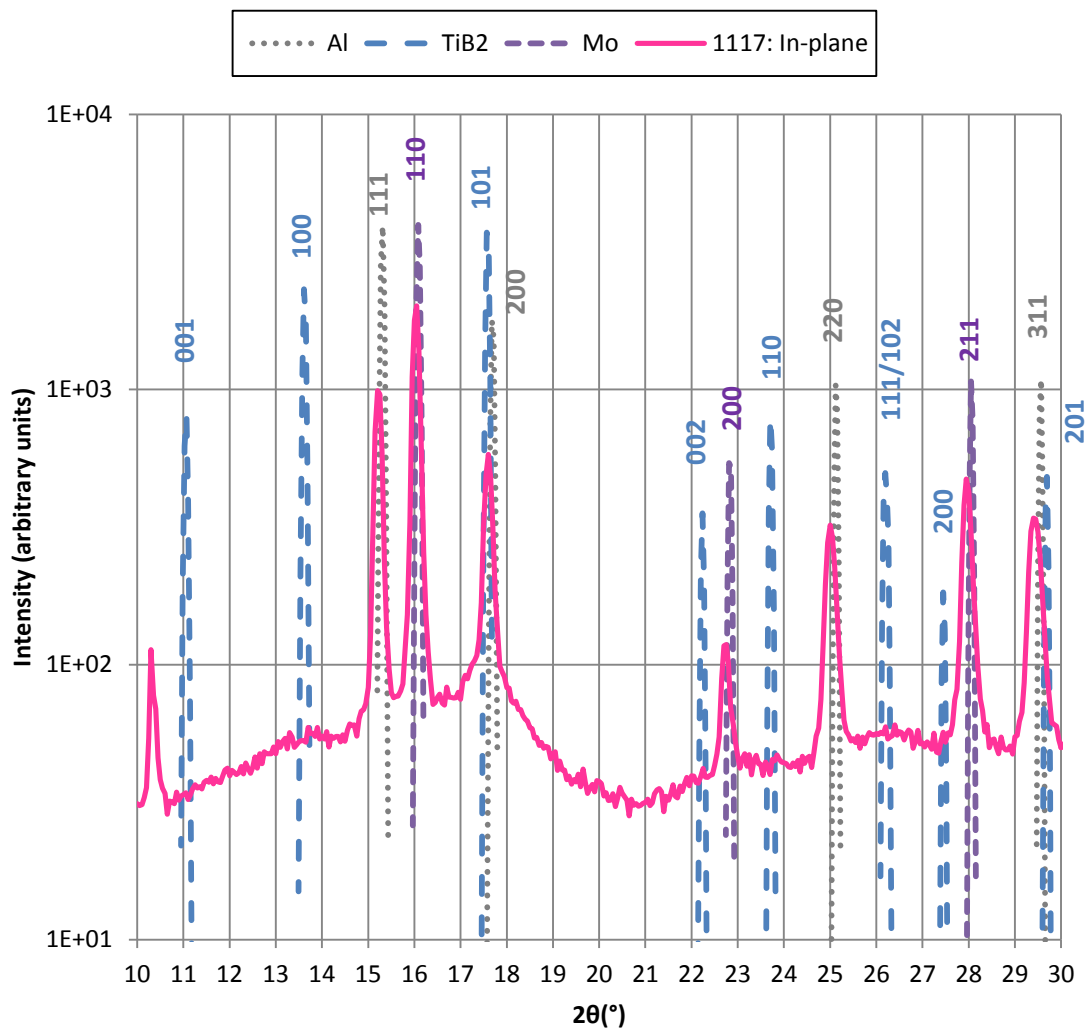
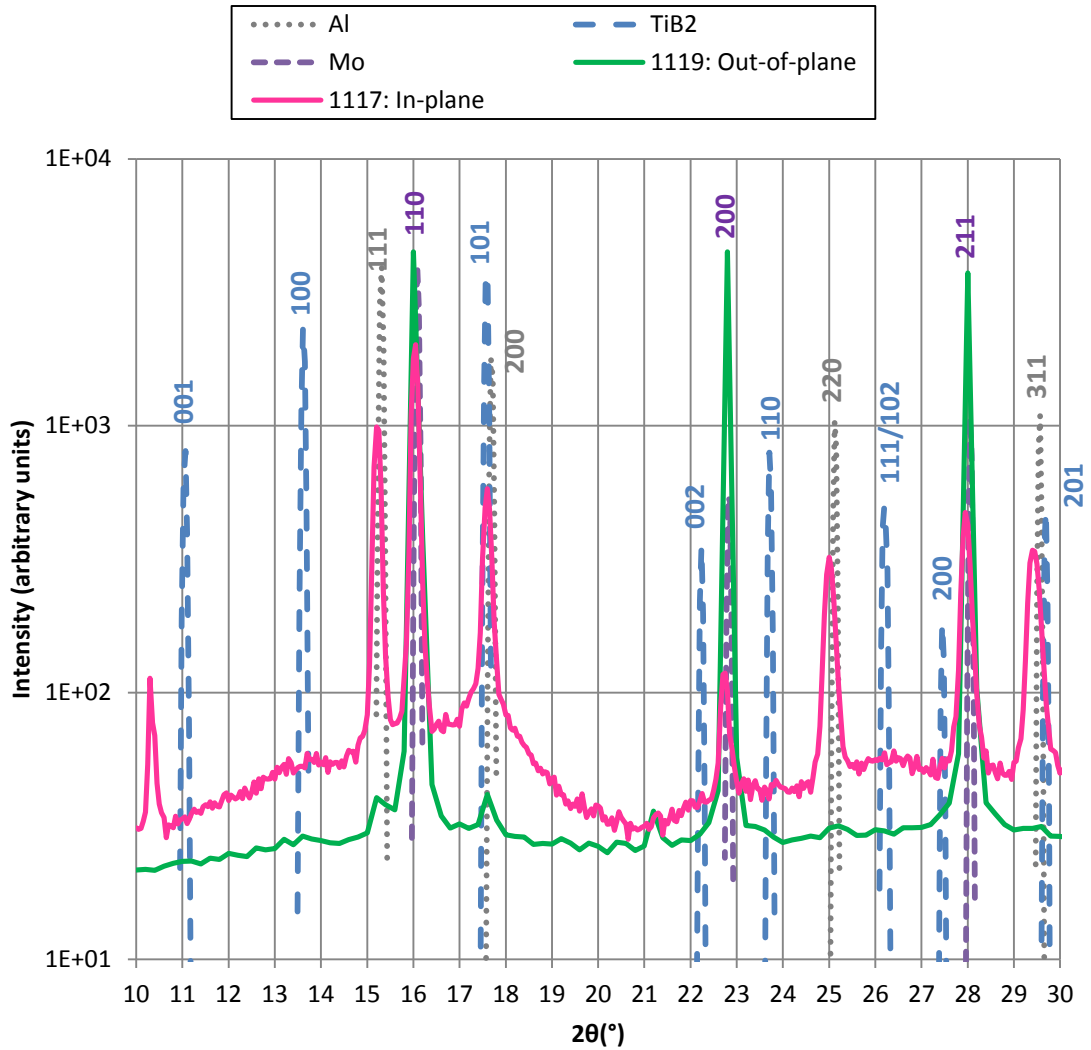


Figure 5-3 – In-plane characterisation from E3 sample A. Angle of incidence 0.2° (grazing-incidence)





**Figure 5-4 – Combined in-plane and out-of-plane scans from E3 sample A**

There are a number of conclusions to draw from the above plots. Initially, it is important to understand the differences between scans 1117 and 1119. The out of plane 1119 scan is dominated almost entirely by Mo peaks from (110) (200) and (211) planes. This is expected, as the relatively high angles of incidence cause the beam to penetrate deep into the sample. As the bulk of the sample is comprised of Mo (approximately 2mm thick) this contributes heavily to the scattering. Either side of the Mo (110) reflection there are small peaks from the (111) and (200) planes of Al, verifying the presence of the layer. However, the strength of the Mo reflections in the out-of-plane scans render this a relatively poor tool for characterisation, as the intensity tends to ‘swamp’ the other peaks. There is no apparent reflection from the TiB<sub>2</sub> layer.

The in-plane scan 1117 appears significantly more promising. Due to the very shallow angle of incidence (for  $\delta$ -scans remaining constant at  $0.3^\circ$ ) the beam penetrates less into the bulk Mo and so is more sensitive to the interfacial region between the  $\text{TiB}_2$  and Al. The consequence of this is immediately clear from Figure 5-3, where the Al  $\{111\}$ ,  $\{200\}$ ,  $\{220\}$  and  $\{311\}$  reflections are strong and readily indexed to the material data. Mo peaks are still very apparent but this is expected due to the relative thickness of the substrate. The other striking aspect of this profile is the lack of peaks which correspond to the  $\text{TiB}_2$  layer. The material data exhibits a great number of peaks within this  $2\theta$  range but there is no alignment with scan 1117; particularly, none which correspond to the (001)  $\text{TiB}_2$  orientation, showing that the desired (001) texture had not been produced in the  $\text{TiB}_2$  layer (the peak at  $2\theta = 10.3$ , on inspection, does not appear to be significant and in any case is too remote from the expected  $\text{TiB}_2$  (001) position to be considered an indicator of that orientation). Nevertheless,  $\text{TiB}_2$  was unquestionably present on the Mo surface having been observed visually prior to coating with Al. Further scans gave indications as to how the  $\text{TiB}_2$  layer is manifested in the data, and this will be discussed shortly.

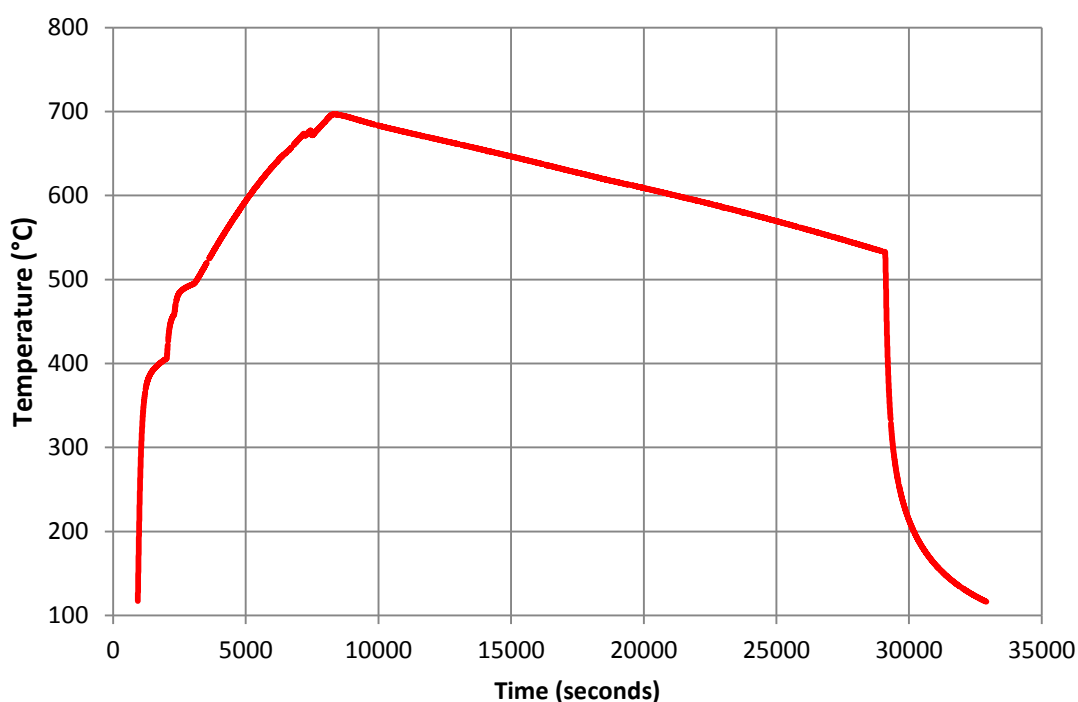
### 5.1.2 Heating and Cooling

After characterisation heating was applied to the sample to generate and observe the corresponding morphological changes. This was performed through a combination of manual heating followed by automated temperature ramping. The temperature was first raised to  $500^\circ\text{C}$  via manual control of the sample heater. Following this, a ramp was applied such that the temperature rose to  $700^\circ\text{C}$  over the course of 5000 seconds (corresponding to a slow ramp of approx.  $2.4^\circ\text{C}/\text{min}$ ) then, after scanning to confirm the phase transformation in the Al, a ramp back down to  $500^\circ\text{C}$  over 20000s (a ramp of  $0.6^\circ\text{C}/\text{min}$ ).

Via a script, both in-plane ( $\delta$ ) and out-of-plane ( $\alpha/\gamma$ ) scans were performed continuously throughout the heating and cooling process described above. This allowed a continual monitoring of the peaks of interest and the surrounding  $2\theta$  region. Based on the characterisation shown in Figure 5-2 the scans operated between  $2\theta = 14^\circ - 24^\circ$ , sufficient to capture the  $\{111\}$  and  $\{200\}$  Al peaks and

thus adopting the approach which had proved successful for the Al/Al<sub>2</sub>O<sub>3</sub> system in previous experiments. Every 5 scans, the script implemented a realignment scan to compensate for any sample movement arising from thermal expansion. Because of these, the average intensity varies from scan-to-scan, and this manifests in the data as plots slightly displaced from each other. While not ideal, this is of little consequence in the analysis which focuses on the presence (or otherwise) of particular peaks, and their relative intensities compared to other peaks within the same scan.

The following figures reveal a range of interesting aspects of the sample behaviour during the heating and cooling process. They will be analysed in the subsequent text.



**Figure 5-5 – Temperature profile applied to sample A. The slow cooling ramp was terminated slightly early due to limited remaining beamtime. The heater was switched off at that point generating the rapid cooling seen from ~29,000 seconds.**

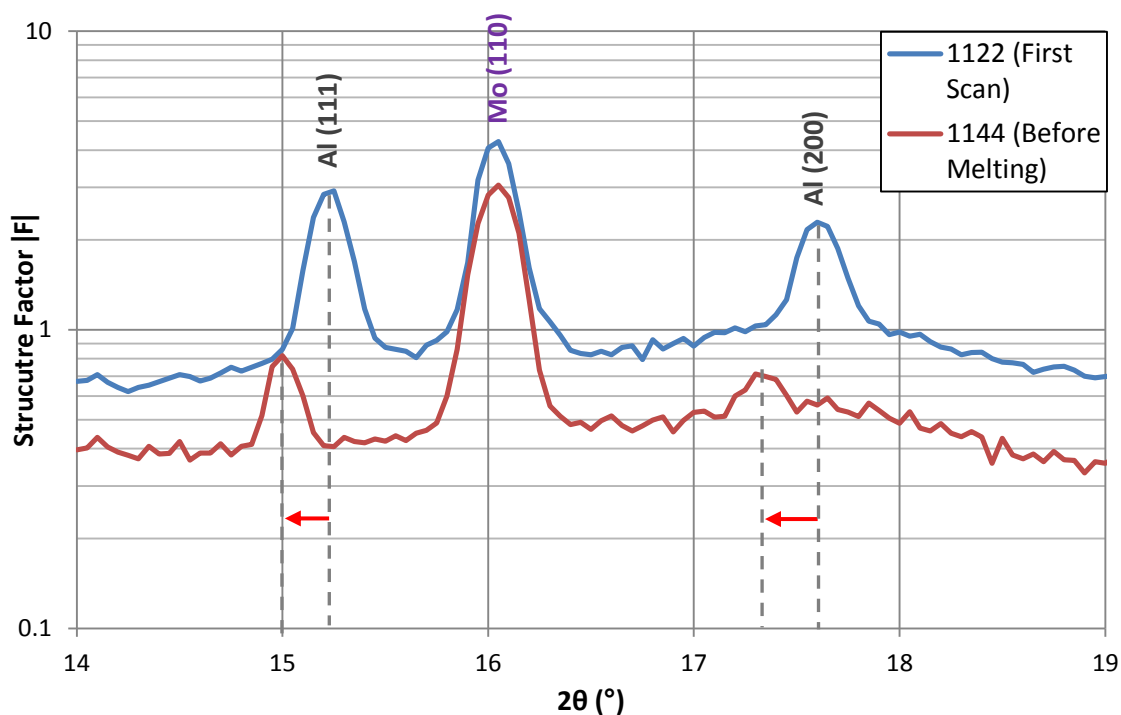


Figure 5-6 – Selected in-plane scans indicating thermal expansion in the Al layer during heating. Arrows indicate movement of Al peaks due to thermal expansion

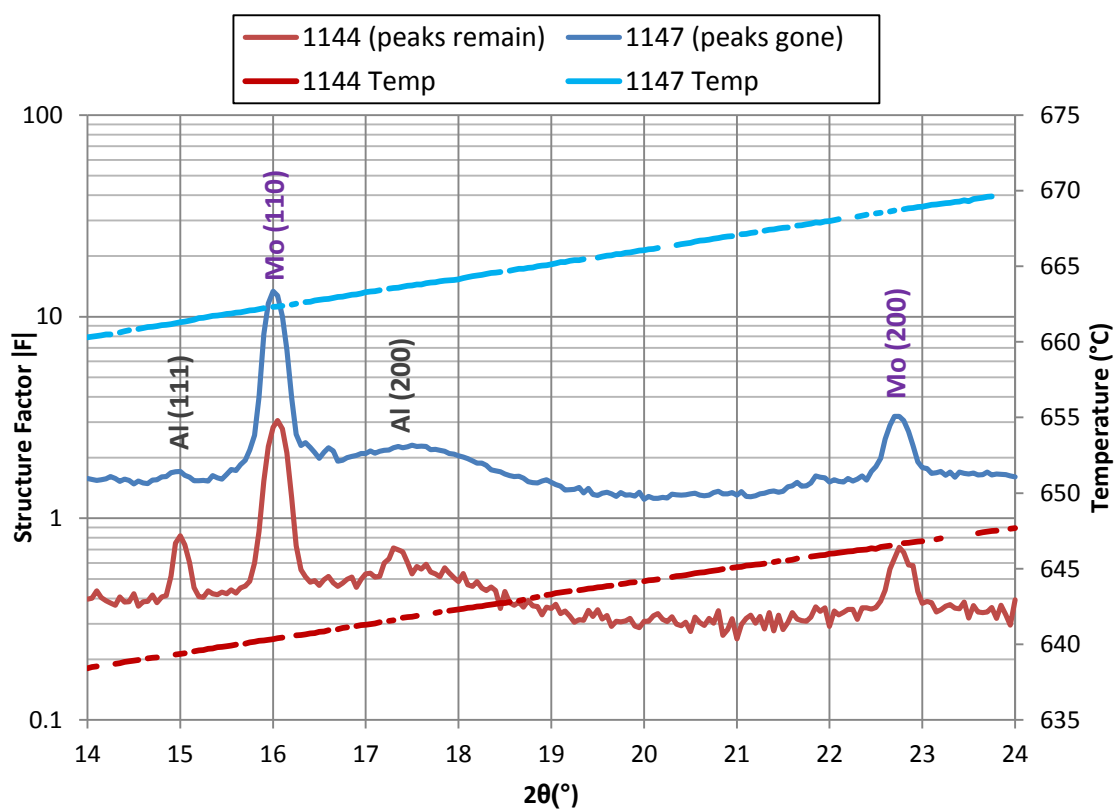
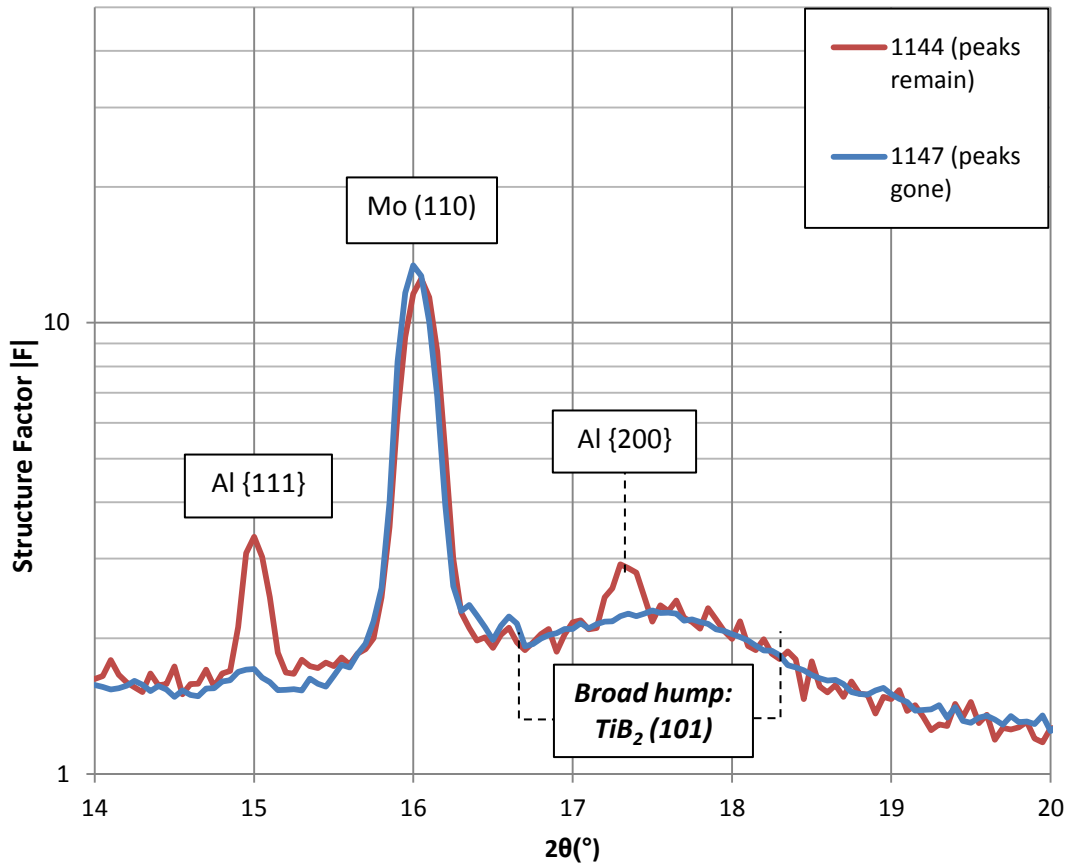


Figure 5-7 – Selected in-plane scans showing phase transition in Al, with accompanying temperature profile applied over each scan.

As expected, the Al peaks first shift (Figure 5-6) and then disappear (Figure 5-7), showing, respectively, **thermal expansion** and phase transition. This behaviour was also observed in the out-of-plane scans, but the Mo peaks are so dominant in these that it is not prudent to draw definitive conclusions from them.

Figure 5-7 clearly shows the disappearance of peaks associated with Al as the temperature increases. The temperature range displayed again corresponds to the expected Al melting temperature. The Mo substrate remains unaffected at this temperature range; note the consistency of the peaks relating to this material. The prevailing shape of the profile after the Al {111} and {200} features have disappeared reveals the character of the TiB<sub>2</sub> layer which, as was apparent from Figure 5-2, did not adopt the desired (001) texture. The region around the {200} feature appears to show a broad 'hump' beneath the location of the actual {200} peak. Referring to Figure 5-2, it is apparent that the location of the TiB<sub>2</sub> (101) reflection ( $2\theta = 17.57$ ) is almost coincident with the Al {200} position ( $2\theta = 17.71$ ). As such, the feature identified as an indicator of Al {200} is in fact likely a superposition of both Al and TiB<sub>2</sub> features. Note in the following Figure 5-8 that, while the sharper Al peaks disappear, the broad hump remains:



**Figure 5-8 – In-plane scans showing phase transition in Al; data scaled to highlight the suggested broad  $\text{TiB}_2$  (101) feature located between  $2\theta = 17^\circ$  and  $2\theta = 19^\circ$**

The suggestion is that the  $\text{TiB}_2$  has in fact adopted a general (101) texture; the breadth of the ‘hump’ suggesting that the structure is not well defined, and that there may be a considerable amount of strain within the material. Considering the polycrystalline nature of the Mo surface, this is perhaps understandable – there is no consistent, long-range crystal structure against which the  $\text{TiB}_2$  can arrange. Building on this suggestion, the indication is that the  $\text{TiB}_2$  layer was not grown to a sufficient thickness to allow this strain to relax and for the structure to adopt a stronger texture.

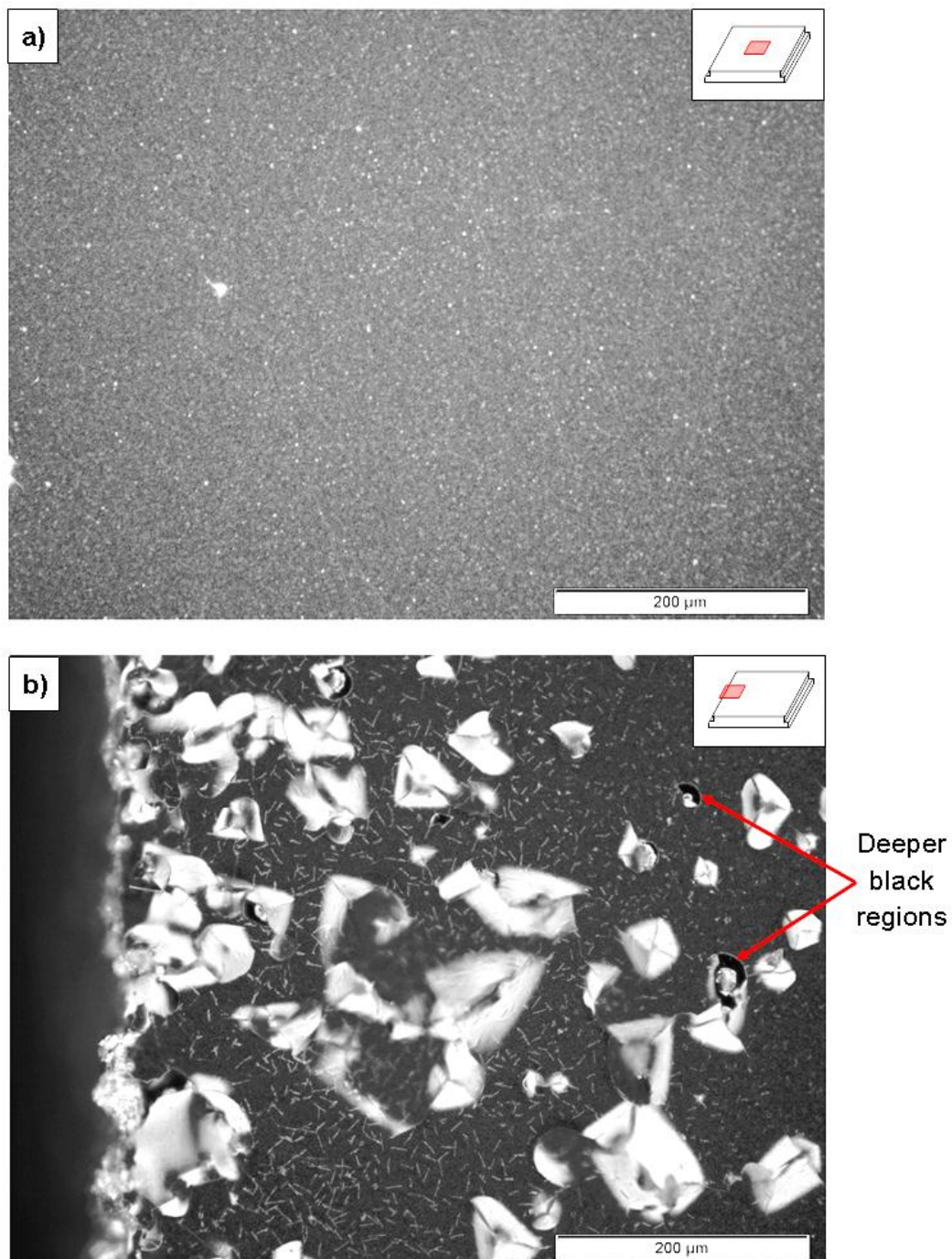
A renewed literature search to assist sample preparation for E4 found evidence to support the claims in the preceding paragraph. Sricharoenchai *et al* [123] investigated the deposition of  $\text{TiB}_2$  via sputtering under a range of conditions (variation of substrate temperature, bias voltage and cleaning procedures) finding that, contrary to the conclusions of a number of previous studies [117]–[120], [122], development of a (001) texture was in fact *not* completely

independent of sputtering parameters. In their studies,  $\text{TiB}_2$  showed an inclination for a (101) texture where conditions were similar to those used in E3 sample preparation. It is also notable that the deposited thicknesses were all at a sub-micron level, whereas the other batch of studies investigated coatings in the region of 2-3 $\mu\text{m}$  thickness. The existence of a mixed texture with (101) bias in the E3 sample suggests that in sample preparation the  $\text{TiB}_2$  layer was not grown to a sufficient thickness to a) facilitate the development of (001) texture (as indicated in [117]) or b) allow residual strain (indicated by the 'hump' shape of the feature) in the deposited layer to relax. This information, along with guidance from the aforementioned study by Sricharoenchai *et al*, would greatly assist in sample preparation for E4.

Returning to the heating and cooling of E3 sample A; on cooling, Al peaks were not observed to return as expected. As shown in Figure 5-5, the sample heater was switched off at approx. 29,000s to attempt to encourage solidification had it not already occurred; however, Al features still failed to appear.

Post-experiment observation of the sample revealed a possible reason for the lack of Al peaks in the scattering profiles. It was clear even with the naked eye that Al was indeed present on the sample surface. It appeared that this was concentrated around the edges of the sample, with little solid material in the centre, at the point where the beam was focused. The experimental team theorised that, on cooling, liquid Al migrated to the edges of the sample and solidified there. This may be a consequence of the geometry of the E3 heater. The actual heater plate is circular, while the sample itself has an approximately square footprint. The 4 corner extremities of the sample are therefore not heated directly but maintained at temperature by conduction from surrounding substrate areas. On cooling, these regions will naturally be slightly cooler than surrounding areas. Heat will also be lost more readily from the edges of the sample; this combined with the large thermal mass of the Mo means that the central region will remain marginally hotter than the edges for the duration of the cooling process. Practically, this means there is a greater driving force for solidification on the edges and corners of the sample during cooling. This

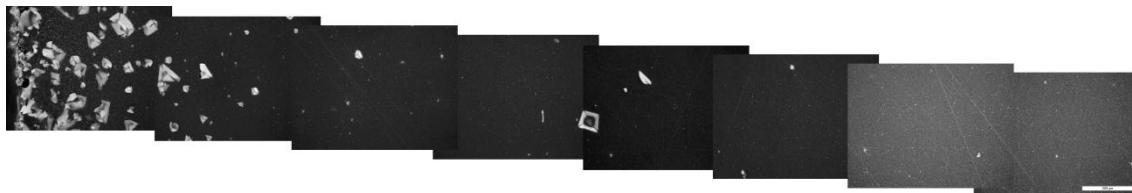
analysis was ascribed greater weight on observation of the sample under SEM, as shown in the following.



**Figure 5-9 - SEM images of sample A. Insets in top right indicate approximate position of image on sample surface. a) Centre of the sample (beam focus position). b) Edge of the sample showing a number of crystallites, assumed to be Al, though this has yet to be reliably established. Smaller, needle-shaped structures visible in b) may be either crystallites or features of the  $\text{TiB}_2$  surface. The small, deeper black regions are likely areas where the  $\text{TiB}_2$  coating has broken away.**



Further to this, the following image mosaic shows the increasing number of Al crystallites observed as one moves from the centre to the edge of the sample surface.



**Figure 5-10 – Mosaic of SEM images from sample A from edge (far left) to centre (far right) of surface. Scale bar in bottom right of image is 200 $\mu$ m (total distance covered by the above is approx. 4.2mm)**

It is clear from the data that no peaks were recorded from these Al crystallites. The low angle of incidence ( $0.3^\circ$ ) used in the in-plane scans should have guaranteed that the beam footprint would extend over the length of the sample; clearly either a) no Al resolidified in the area of this beam footprint or b) the scattering from the Al was too weak (relative to the dominant Mo) to be recorded in the scans.

Despite this issue, the experiment revealed some interesting observations. From Figure 5-9, the Al crystallites are observed to have a characteristic pyramidal shape; indeed the majority appear to have solidified with a 3-side pyramidal geometry. This is interesting as it strongly suggests that the  $\{111\}$  planes in the solidified Al are aligned parallel to the substrate surface. Looking ‘down’ the normal to the  $\{111\}$  planes, which cut through the diagonal of the FCC unit cell, one would expect to see the ‘corner’ of the unit cell or larger crystallite. This observation supports the suggestion that the aluminium is inclined to solidify with this orientation, as was the case for the Al/Al<sub>2</sub>O<sub>3</sub> system [147], and as has been observed throughout the literature [14], [27], [60], [61].

Despite the non-reappearance of the Al, interesting effects were noted on the characterisation scans during cooling, which may be relevant to the appearance of  $\text{Al}_3\text{Ti}$  in the system. This analysis will be explored separately in 5.3, in order to combine with information from experiment four.

## 5.2 Experiment Four

Experiment Four returned to beamline I07 at Diamond, and focused exclusively on the Al/TiB<sub>2</sub> system. Improved sample preparation lent the team confidence that the desired (001) texture had indeed been generated in the samples. The preparation is described in greater detail in section 2.3.4. A number of differently shaped samples were prepared; two of these were eventually used in the experiment, detailed as follows:

1. Sample V: Comprised a polished Mo plate, onto which a Ti interlayer (~0.1µm) was sputtered, followed by the TiB<sub>2</sub> (~0.5µm). This sample was designed to be used as a base onto which pure Al would be evaporated *in-situ*.
2. Sample VIII: Prepared in exactly the same way as sample V, with a further sputtering operation to deposit ~10µm of pure Al onto the TiB<sub>2</sub> surface.

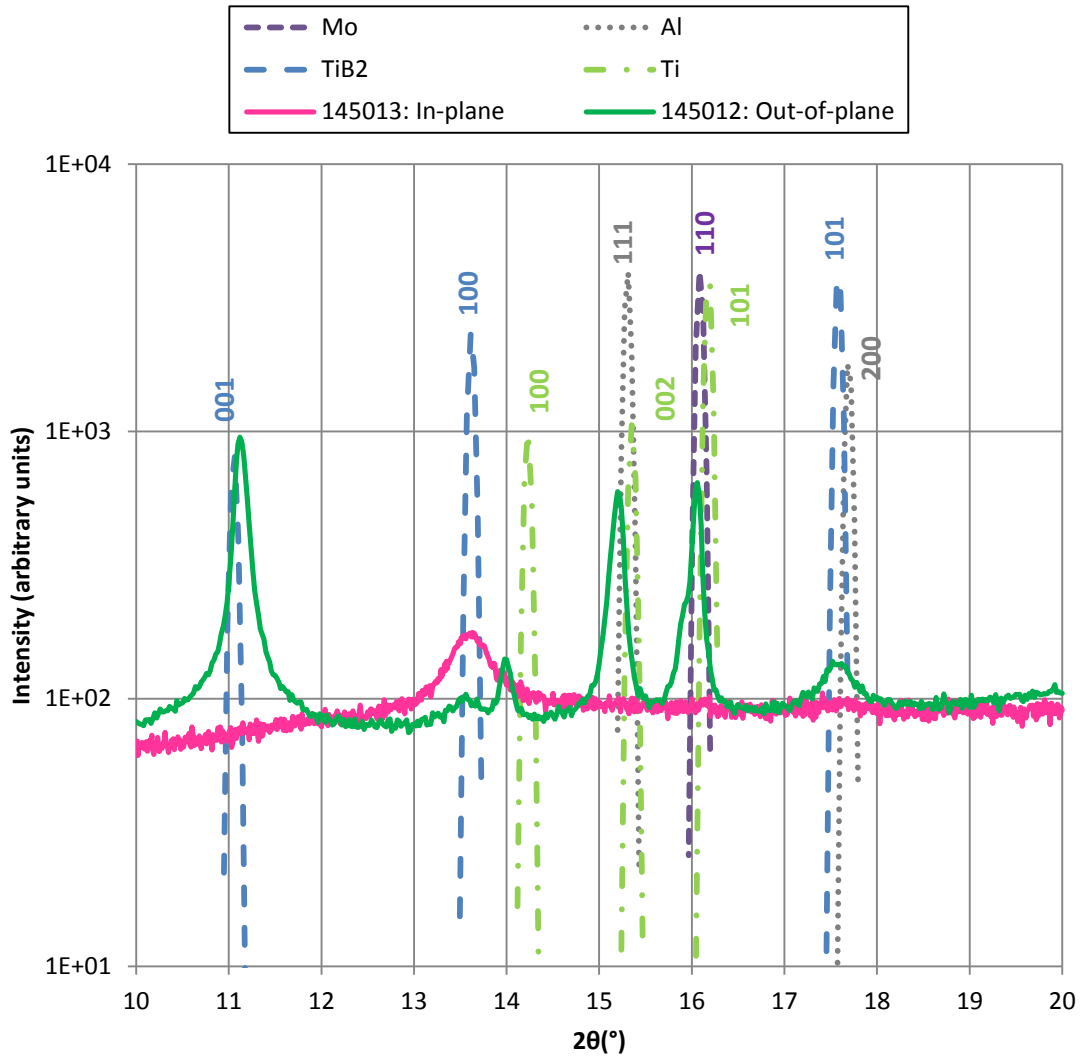
### 5.2.1 Sample V

The first sample investigated was a Mo plate with a sputter-deposited TiB<sub>2</sub> layer. As per the successful procedure of Sricharoenchai *et al*, a Ti interlayer was deposited between the Mo and TiB<sub>2</sub> [123]. This was intended to a) improve adherence and b) alleviate the build-up of strain in the TiB<sub>2</sub>; both issues that may have contributed to the undesirable morphology identified in E3 sample A. While beneficial to the sample preparation, the presence of Ti would also complicate the scattering pattern so would need careful consideration in analysis. To assist with this, the following gives the locations of Ti peaks expected to be observed in the data. The other materials are included for reference.

	Peak Position in $2\theta$ (°)	$\theta$ (°)	d (Å)	Planar Family
<b>Aluminium</b> [149]	15.32	7.66	2.338	<b>Al {111}</b>
	17.71	8.85	2.024	<b>Al {200}</b>
	25.15	12.57	1.431	<b>Al {220}</b>
	29.57	14.78	1.221	<b>Al {311}</b>
<b>TiB<sub>2</sub></b> [99]	11.06	5.53	3.232	<b>TiB<sub>2</sub> {001}</b>
	13.61	6.81	2.629	<b>TiB<sub>2</sub> {100}</b>
	17.57	8.78	2.040	<b>TiB<sub>2</sub> {101}</b>
<b>Titanium</b> [150]	14.23	7.12	2.515	<b>Ti {100}</b>
	15.36	7.68	2.332	<b>Ti {002}</b>
	16.16	8.08	2.217	<b>Ti {101}</b>
<b>Molybdenum</b> [148]	16.08	8.04	2.227	<b>Mo {110}</b>
	22.82	11.41	1.575	<b>Mo {200}</b>
	28.06	14.03	1.285	<b>Mo {211}</b>

**Table 5-3 - Peak positions and corresponding d-spacings for materials of interest in investigation of the Al/TiB<sub>2</sub> system. X-ray energy 19.9 keV ( $\lambda=0.623\text{\AA}$ )**

The intention for sample V was to use it as a base onto which pure Al could be evaporated *in-situ*. The hope was that this would lead to the cleanest possible interface between TiB<sub>2</sub> and Al. Preliminary trials had indicated that the Al would wet the TiB<sub>2</sub> surface more readily, hopefully avoiding the issues experienced with Al evaporation onto Al<sub>2</sub>O<sub>3</sub> described in section 4.2.3. Initially, the sample surface required characterisation to a) index the materials present and b) clarify whether the desired (001) texture in the TiB<sub>2</sub> layer had indeed been achieved. Figure 5-11 shows the characterisation of sample V.



**Figure 5-11 – Initial characterisation scans from E4 sample V. Plot shows in-plane  $\delta$  scan (145013) with angle of incidence  $0.3^\circ$  and out-of-plane  $\alpha/\gamma$  scan (145012) with angle of incidence varying from  $5\text{-}10^\circ$**

It is sensible to analyse Figure 5-11 in terms of each material, as follows:

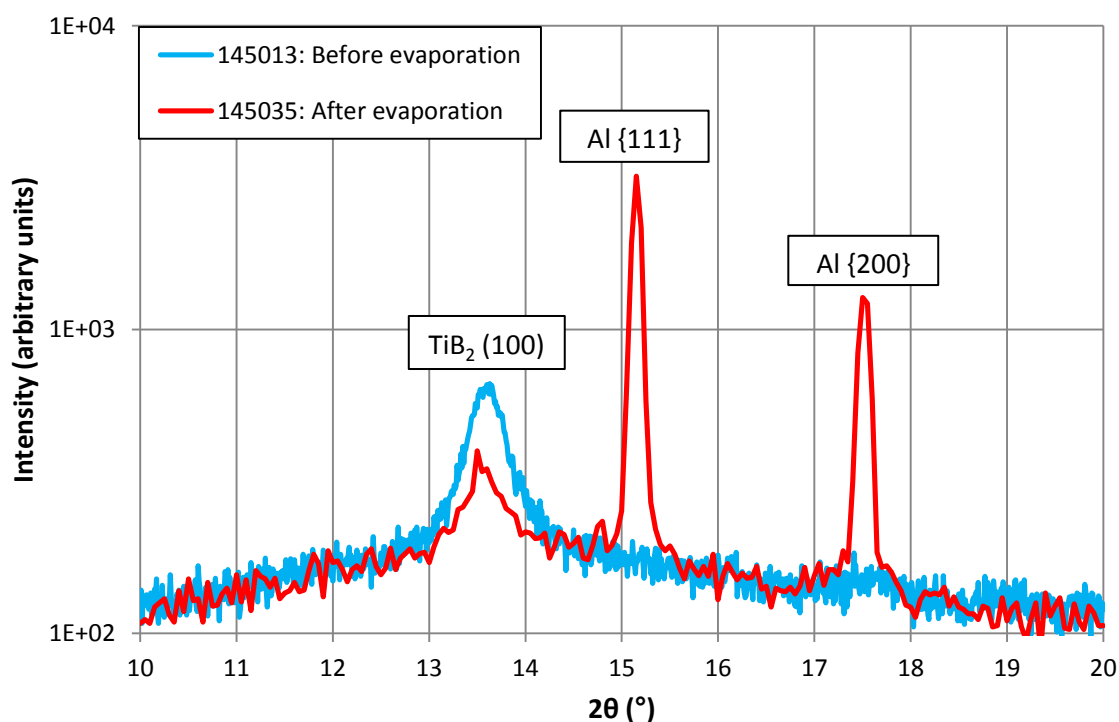
1.  $\text{TiB}_2$  – Firstly, the strength of the (001) peak in the out-of-plane scan indicates very clearly that the desired (001) texture has indeed been achieved and that (001) planes are aligned with the sample surface. There are significantly smaller peaks at the (100) and (101) locations, suggesting the existence of some of these planes in alignment with the substrate surface. However, the very low relative intensity (compared to the (001) peak) indicates this is likely scatter arising from the thin zone of mixed texture at the interface with the Ti layer. The presence of a  $\text{TiB}_2$  (100) peak in the in-plane scan further confirms the achieved texture; suggesting (100)

planes aligned perpendicular to the sample surface. Overall, the characterisation suggests that the sample has been prepared as desired; and that the surface has a texture strongly biased to the  $\text{TiB}_2$  (001) orientation.

2. Ti – Three peaks are seen in the data which correspond approximately to the (100), (002) and (101) orientations – the three closest-packed planar families – in the titanium. The thin (~100nm) layer would be expected to have a mixed texture, which is reflected here. The peaks do not perfectly align with those predicted – although the discrepancy between data and prediction is relatively consistent. The misalignment may be a result of strain in the Ti, and/or the crystal structure not being well-defined in the layer due to the small thickness. Another option is that the formation of a thin oxide layer on the Ti prior to deposition of the  $\text{TiB}_2$  has slightly altered the scattering profile. The expected peak positions for  $\text{TiO}_2$  in this  $2\theta$  range are in such close proximity to Ti that it is difficult to precisely ascertain from the data whether this has occurred.
  - a. It is notable that the data suggests a sample far ‘richer’ in Ti than would be reasonably expected, considering the relatively small quantity of elemental Ti deposited in the interlayer. This raises questions as to the exact stoichiometry of the sample as-deposited. This issue warrants separate consideration and will be discussed further at the end of section 5.2.1.
3. Mo – the sole Mo peak in this  $2\theta$  range is the (110), and is roughly coincident with the location of the Ti (101) peak. This makes the two difficult to discern, however the peak at  $\sim 2\theta = 16^\circ$  appears to have a slight ‘shoulder’ which may suggest that it is in fact a superposition of the reflections from Mo (110) and Ti (101). Also of note is the fact that the Mo reflection is significantly less dominant than that observed in the E3 sample A out-of-plane scan. This helps to confirm that a far greater thickness of  $\text{TiB}_2$  was deposited in preparation of sample V; less of the incident beam illuminates the Mo, and the material contributes noticeably less to the overall scattering as a result.

After characterisation confirmed that sample V had the appropriate  $\text{TiB}_2$  (001) surface orientation, it was used as a substrate for *in-situ* deposition of pure Al. Based on data supplied with the Al evaporator a deposition rate of between  $3.4\text{\AA}/\text{min}$  and  $11.5\text{\AA}/\text{min}$  was assumed; the resulting thickness of the deposited layer was not critical.

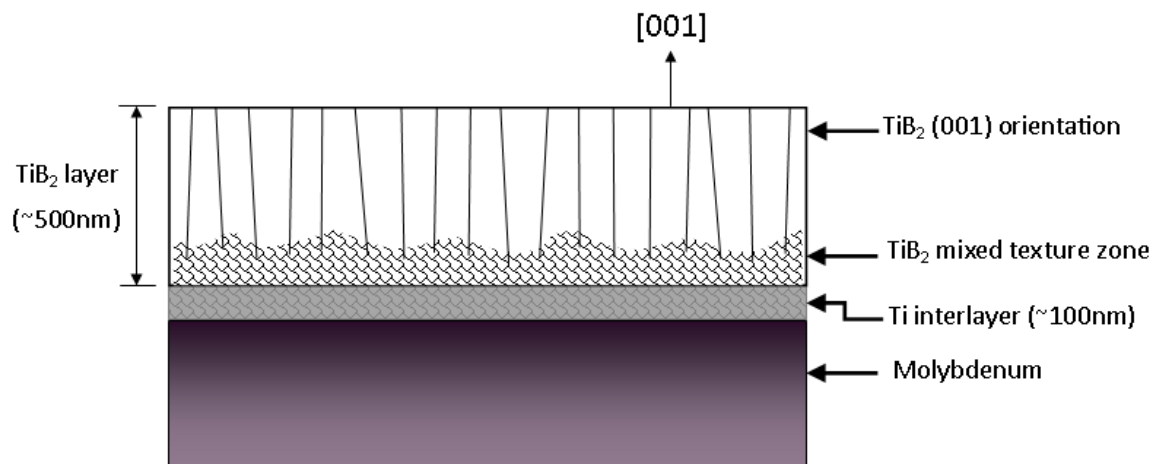
To monitor the progress of Al evaporation, a script was written to continuously repeat an out-of-plane scan between  $2\theta = 15^\circ - 18^\circ$ . The appearance of features at  $2\theta = 15.32^\circ$  and/or  $2\theta = 17.71^\circ$  would then be indicators of Al {111} and Al {200} respectively. However after a considerable time ( $\sim 2$  hours) had elapsed with no apparent change to the out-of-plane scan profile, the decision was made to perform an in-plane scan instead. Scanning in this geometry very clearly indicated the presence of Al features, as the following before and after plot shows:



**Figure 5-12 – In-plane scans of sample surface before and after evaporation of Al**

Note again that in this geometry only the (100) reflection is observed from the  $\text{TiB}_2$  – i.e. the set of planes that, in the unit cell construction, are perpendicular to the (001) observed in the out-of-plane scans. This information confirms the

following morphology which has been generated in the sample, shown in Figure 5-13:



**Figure 5-13 – Schematic of morphology generated in E4 samples**

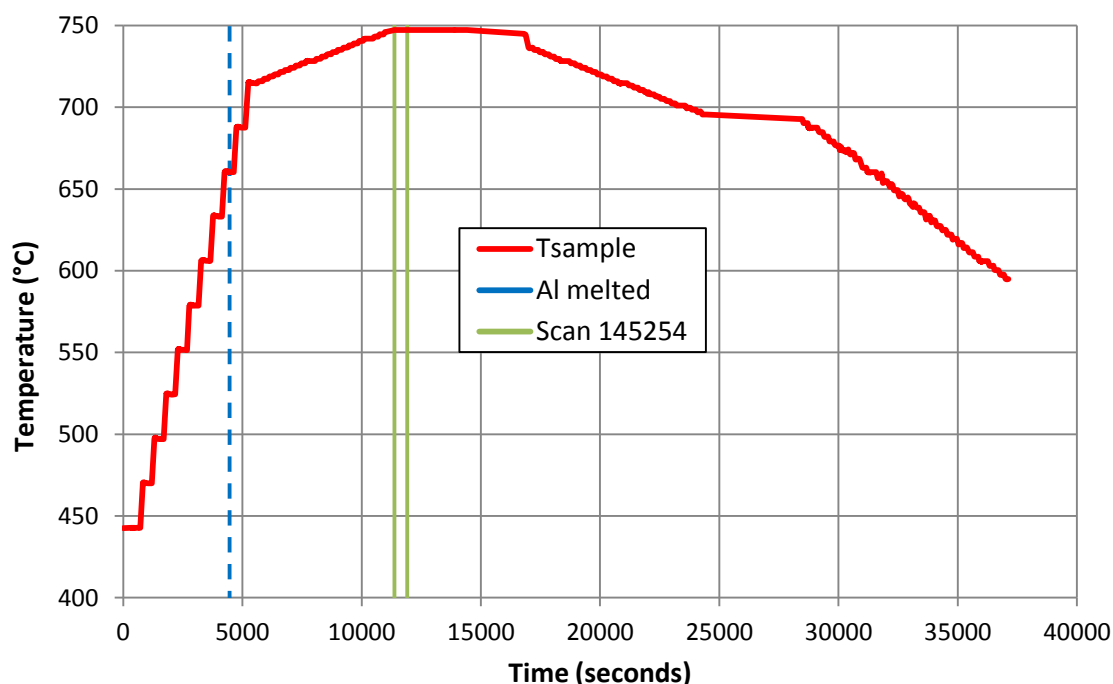
Figure 5-12 clearly shows the appearance of Al, which was observed only in this in-plane geometry. It is likely that in the out-of-plane orientation the thickness of the deposited material does not build to a sufficient extent to contribute strongly to the scattering; the relative intensity arising from other sample materials is too large by comparison. The in-plane scattering geometry is clearly appropriate for monitoring transformation of the Al, though it is sensible to continue to also collect out-of-plane data in the interests of completeness, and in the event that anything unexpected arises in this geometry.

Having verified the presence of an (albeit thin) Al layer, the next step was to heat and cool the sample to observe the changing morphology. To perform this, the diffractometer was set to cycle between the 3 Al peak positions in both an in-plane and out-of-plane geometry, taking a 10s exposure at each. Each set of 6 images were taken at the same temperature. The heating (and subsequent cooling) ramped up or down in between each image set. As with previous experiments, this process was implemented within a script which also incorporated regular re-alignment scans.

The heater control in this case was not directly incorporated into the beamline control software, but implemented through a separate Eurotherm controller.

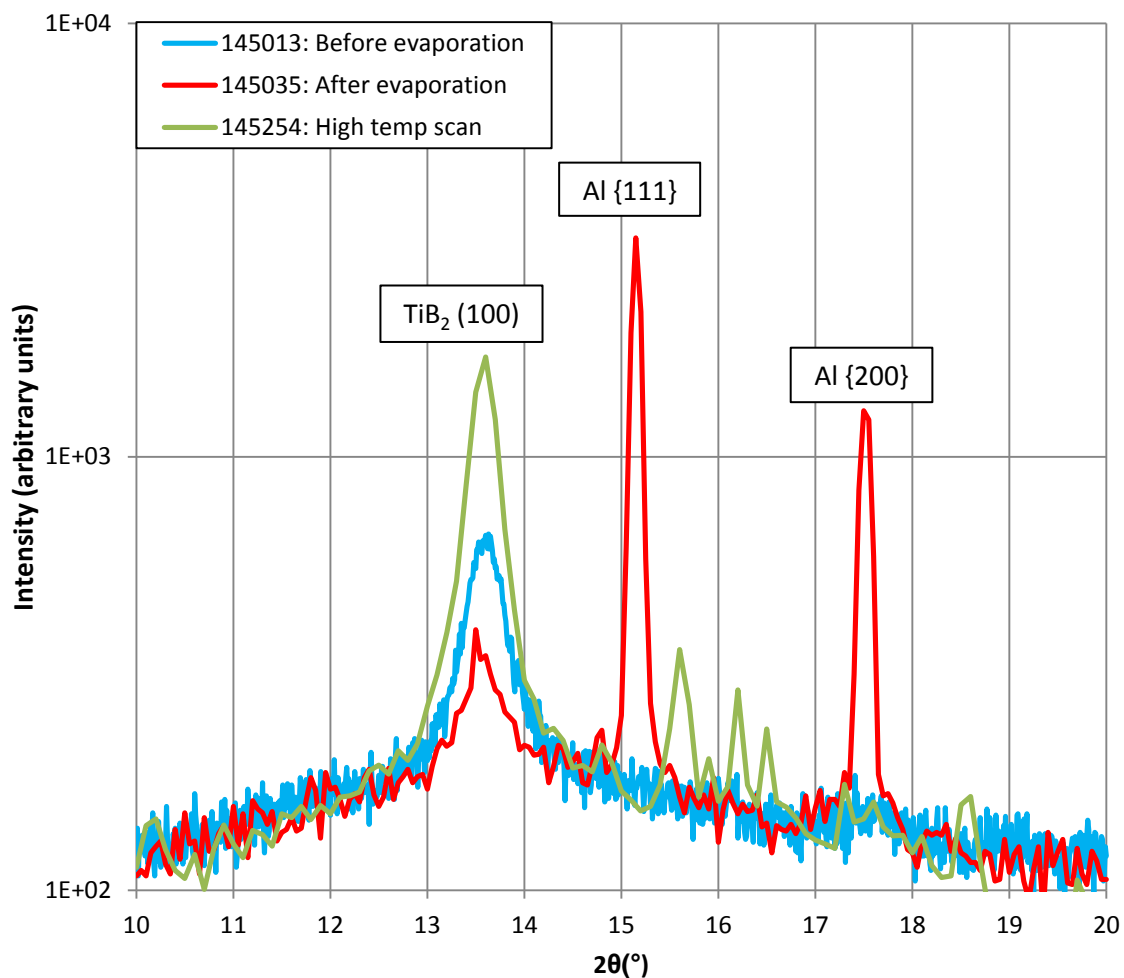


While this makes analysis somewhat more difficult, it afforded greater flexibility in the experiment itself, as temperature setpoint and ramping could be varied ‘on-the-fly’ based on observations from the detector. It is for this reason that the following temperature profile in Figure 5-14 appears somewhat inconsistent:



**Figure 5-14 – Temperature profile applied to sample V. Scan 145254 takes place at maximum temperature and is shown in Figure 5-15.**

Continual monitoring of the images at the 3 Al peak positions showed, as in previous experiments, Al features shifting to smaller  $2\theta$  positions (**thermal expansion**) followed by disappearance (melting) at the expected temperature level of  $\sim 660^{\circ}\text{C}$ . The melting point is indicated in the temperature profile above. After heating, the morphology was characterised by another in-plane scan, 145254, performed at high temperature ( $\sim 750^{\circ}\text{C}$ ), shown in Figure 5-15:



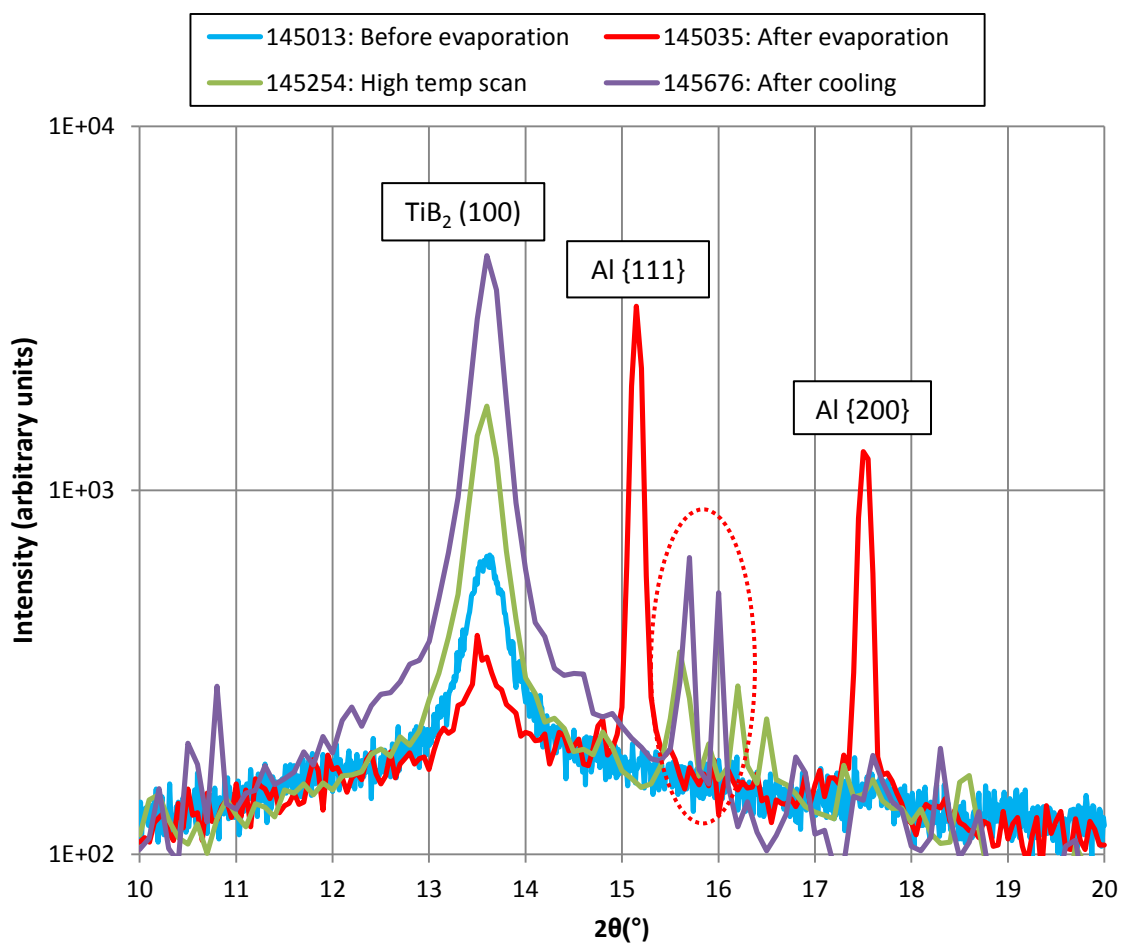
**Figure 5-15 – In plane scans of sample surface. Plots from Figure 5-12 (145013 and 145035) are repeated; 145254 is a scan performed during the high temperature hold at ~750°C**

Here the disappearance of the Al {111} and Al {200} features clearly indicates that the Al has melted and is now in the liquid state. The relative intensity of the TiB<sub>2</sub> (100) peak has increased as a result. New features, which were not present in the original structure have appeared in the region  $2\theta = 15^\circ - 17^\circ$ . This is intriguing as it indicates the development of new phases during the heating process. The re-alignment scans performed throughout the heating process should ensure that only the sample is illuminated by the incident beam, so we assume that these new features do not arise from the mounting or other surrounding equipment.

After scan 145254 the sample soaked at ~750°C for ~5000s. This was intended to ensure all the Al material was in the liquid state and wet the TiB<sub>2</sub> surface.

After this period cooling was applied and the scanning process reverted to monitoring of the 3 primary Al peak positions. This was intended to capture re-appearance of the features and thus record solidification of the Al, but this again proved elusive. No features were observed to reappear in any of the Al peak positions.

After the cooling stage of the thermal profile (Figure 5-14) concluded, the sample was re-scanned to characterise the resulting morphology:

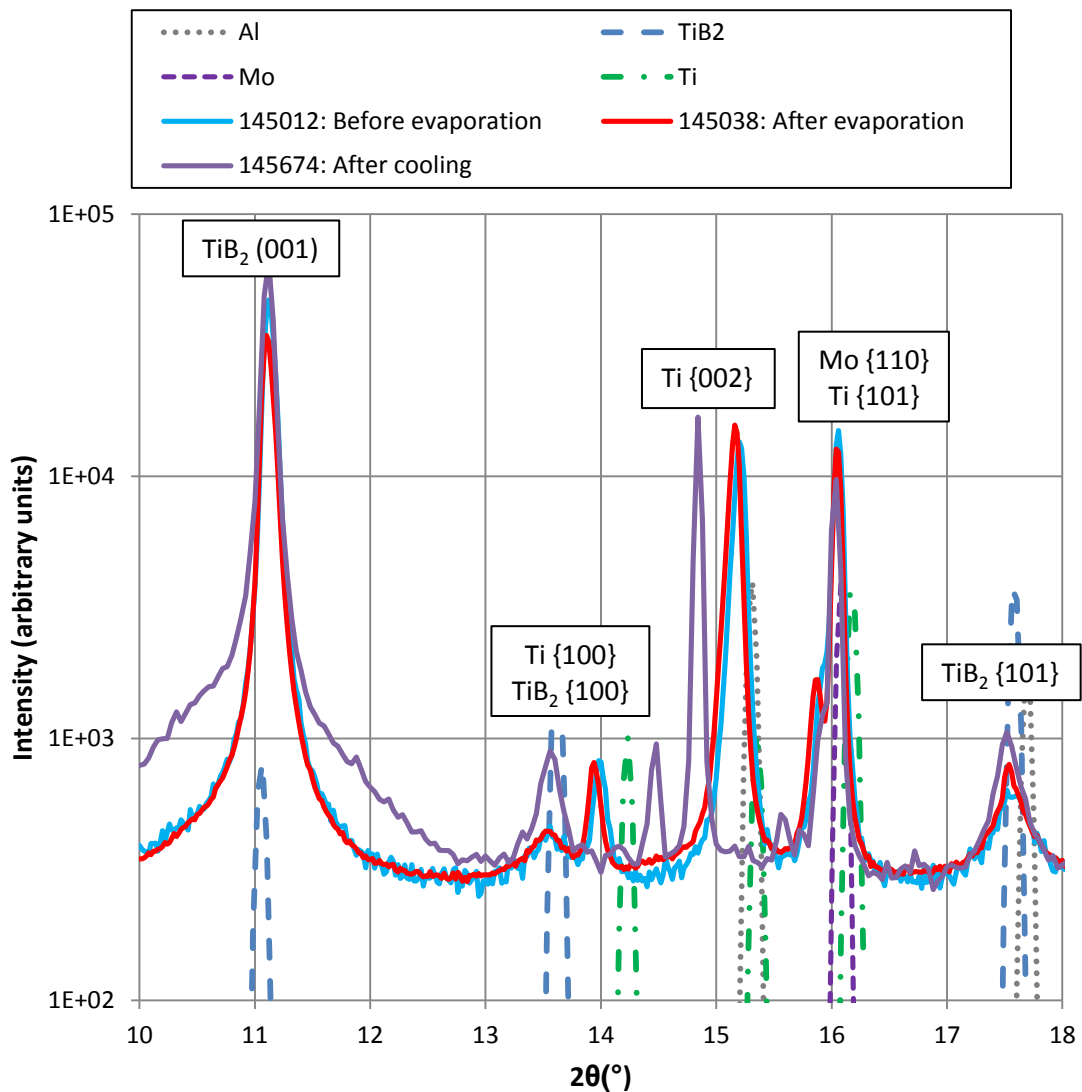


**Figure 5-16 – In plane scans of sample V surface. Features of interest in scan 145676 have been highlighted**

The most apparent conclusion from Figure 5-16 is that no Al features are observed to reappear in the cooled sample. The more intriguing observation is the appearance and apparent persistence of the two peaks highlighted by the dotted oval in the figure. Notably, the location of the peaks at values around  $2\theta$

= 15.7° and 16° may in fact indicate the presence of  $\text{Al}_3\text{Ti}$ ; suggested to form in this material system at the interface between Al and  $\text{TiB}_2$ . This mechanism remains a matter of great debate in the literature [14], [52], [53], [62], [63]; section 5.3 is devoted entirely to further analysis of this observation.

The following figures show the out-of-plane characterisation of sample V on cooling:



**Figure 5-17 - Out of plane scans of sample V surface. Key features are annotated.**

In the above, the feature in 145674 at approximately  $2\theta = 14.9^\circ$  is somewhat confusing. The strong feature at  $\sim 15.2^\circ$  in 145038 was present *prior* to evaporation (see 145012) and so cannot arise from deposited Al, but was

attributed to Ti {002} in the interlayer (the Al signal was only observed *in-plane*). During the process of evaporation, heating, and cooling, this feature has shifted to a smaller  $2\theta$ , suggesting, if the feature is assumed to be an indicator of Ti, a uniform strain in the interlayer. This is supported by a similar shift in the feature at  $14^\circ$  (in 145012 and 145038) attributed to Ti {100}. The dominant TiB<sub>2</sub> (001) peak at  $2\theta = 11.1^\circ$  appears to have broadened significantly on cooling; as such the TiB<sub>2</sub> is suggested to have strained in a non-uniform manner in the textured region. Other TiB<sub>2</sub> features, arising from the 'mixed zone' adjacent to the Ti interlayer, remain unchanged.

The capture of re-solidifying Al remained elusive; no Al features were observed on cooling in either the in-plane or out-of-plane scans. Despite this, they exhibit a range of interesting features which give indications towards various possibilities for the sample behaviour.

The use of evaporation to deposit Al *in-situ* was intended to ensure maximum cleanliness at the interface. It is however a particularly slow method of deposition. Using the most conservative (3.4Å/min) and most optimistic (11.5Å/min) deposition rates respectively, an Al layer of thickness between 40.8nm and 138nm would have been present at the commencement of the heating process. The actual quantity of pure Al material is therefore quite low, and clearly the thickness was not sufficient to generate a signal in the out-of-plane scans; this is compounded by the fact that the Ti interlayer does scatter out-of-plane despite an assumed thickness of only ~100nm itself (thus suggesting the actual Al layer thickness is likely towards the lower end of the stated range). This observation leads to the following possibilities for the behaviour of the Al during heating and cooling:

1. Al migrated away from the beam path on cooling, as was the case with E3 sample A
2. All the Al has reacted with residual oxygen in the environment to form Al<sub>2</sub>O<sub>3</sub>
3. All the Al has reacted with residual Ti on the surface of the TiB<sub>2</sub> layer to form Al<sub>3</sub>Ti

4. Some combination of 2) and 3) has occurred

To investigate, Figure 5-18 displays data from: *before* evaporation (145012), at the apex of the heating process (145255), and *after* cooling (145674); superimposing the data onto predicted peak positions (from the ICSD [127]) for a range of the materials in question:

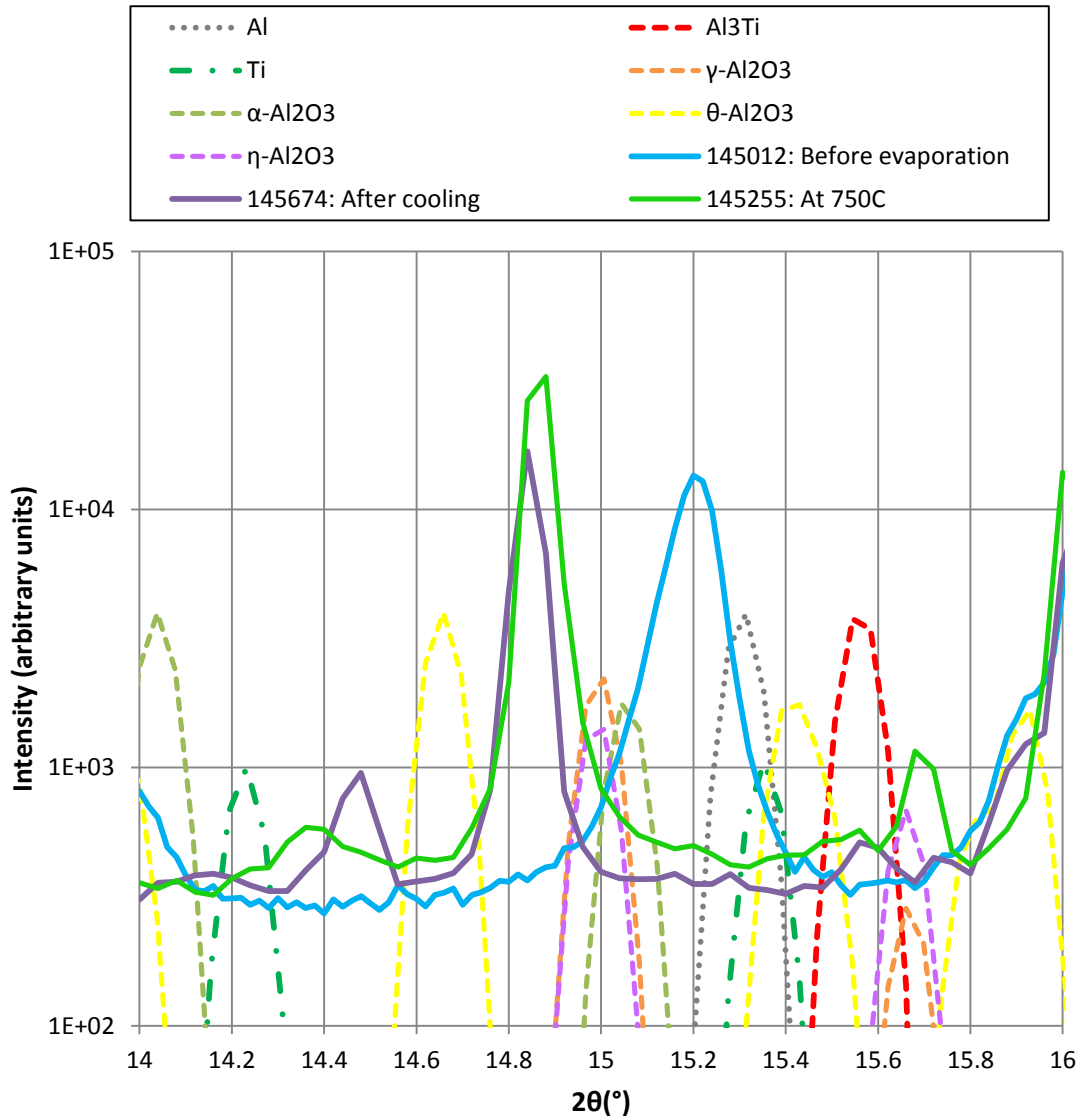


Figure 5-18 – Enlarged view ( $2\theta = 14^{\circ}$ - $16^{\circ}$ ) of the out-of-plane scans of sample V surface superimposed on material data

Here two observations can be made which provide some support for proposal 4 above:

- There is a small but noticeable peak in the post-cooled scan (145674) at the  $\text{Al}_3\text{Ti}$  {112} position of  $2\theta = 15.6^\circ$ .
- The dominant peak in the data appears initially at  $2\theta = 15.2^\circ$  and is attributed to  $\text{Ti}$  {002} despite a large shift from the expected position. On heating this peak shifts into a region associated with a number of transition aluminas, and remains in this position on cooling. The scan at the apex of the heating process (145255) was at  $\sim 750^\circ\text{C}$ ;  $\gamma\text{-Al}_2\text{O}_3$  is expected to dominate at this temperature and indeed a  $\gamma\text{-Al}_2\text{O}_3$  peak is observed in the vicinity.

It is suggested that for sample V the Al layer has, on melting, reacted with residual Ti to form  $\text{Al}_3\text{Ti}$ . This is potentially of great interest and will be explored further in section 5.3.

The mechanisms behind the large shift of the dominant peak, and the appearance of a peak at  $2\theta = 14.5^\circ$ , are somewhat unclear, especially once *known* sample materials are eliminated. The high number of peaks from different alumina phases in the region, combined with the high reactivity of Al, leads to the suggestion that these features may arise or be influenced by a mixed or ill-defined alumina phase forming in the system. Indeed, the breadth of the peaks from the ICSD data suggests that these phases are quite ill-defined in any case. These aspects merit further study, but are outside the scope of the present study.

In discussion of Figure 5-11 it was noted that the sample appears to be 'Ti-rich' despite the assumed presence of a relatively small amount of elemental Ti. It is worth considering what this may indicate about the sample preparation process itself, specifically the deposition of  $\text{TiB}_2$ . When depositing such a compound, various factors may lead to a situation whereby the deposited film has a non-stoichiometric composition [151]. These include: differing sputtering efficiencies of the constituent elements; lighter atoms (in this case, boron) being more

susceptible to collisions with the atoms of the sputtering gas; and 're-sputtering' whereby the arrival of heavier (Ti) atoms onto the substrate knocks lighter atoms out of the deposited film. The strength of the Ti features in the data suggests that there is an enriched content of this element, and this may indeed be attributable to the mechanisms described. It is difficult to characterise the sample in a way which would precisely determine whether this has taken place; however, there would clearly be implications for the behaviour of the Al immediately adjacent to the 'Ti-rich' layer. The issue will be revisited following analysis of the sample VIII data in the following section.



### 5.2.2 Sample VIII

Sample VIII represented a kind of 'bookend' to the whole project; prepared and intended to be used similarly to the first sample in E1. Sample geometry was exactly the same as sample V, but with a reasonably thick ( $\sim 10\mu\text{m}$ ) layer of Al sputter-deposited onto the  $\text{TiB}_2$  surface.

A primary motivation for this sample was to attempt to capture the resolidification of Al. This had proved challenging in both E3 and E4. E3 results indicated that slow cooling, implemented due to the low undercooling ( $<1\text{K}$ ) expected for Al on  $\text{TiB}_2$  [53], allowed liquid Al to migrate to the edges of sample A away from the beam. However, this sample did not have the ideal (001) texture, which may have influenced the proclivity of the liquid Al to solidify in a particular location. For E4 sample V, the desired texture was achieved, so slow cooling was again attempted despite the aforementioned issues in E3. Again reappearance of Al features was not observed. For E4 VIII, it was instead decided to adopt a fast quench, to *ensure* that solidified material would be present on cooling. The intention for sample VIII was thus as follows:

1. Characterise the sample morphology in-plane and out-of-plane
2. Centre detector at Al {111} peak position ( $2\theta = 15.3$ ) in the in-plane geometry
3. Apply heating while monitoring Al {111} feature
4. On Al {111} feature disappearance, immediately quench by switching off heater
5. Re-characterise sample morphology on cooling

A full out-of-plane characterisation is shown Figure 5-19, Figure 5-20 and Figure 5-21:

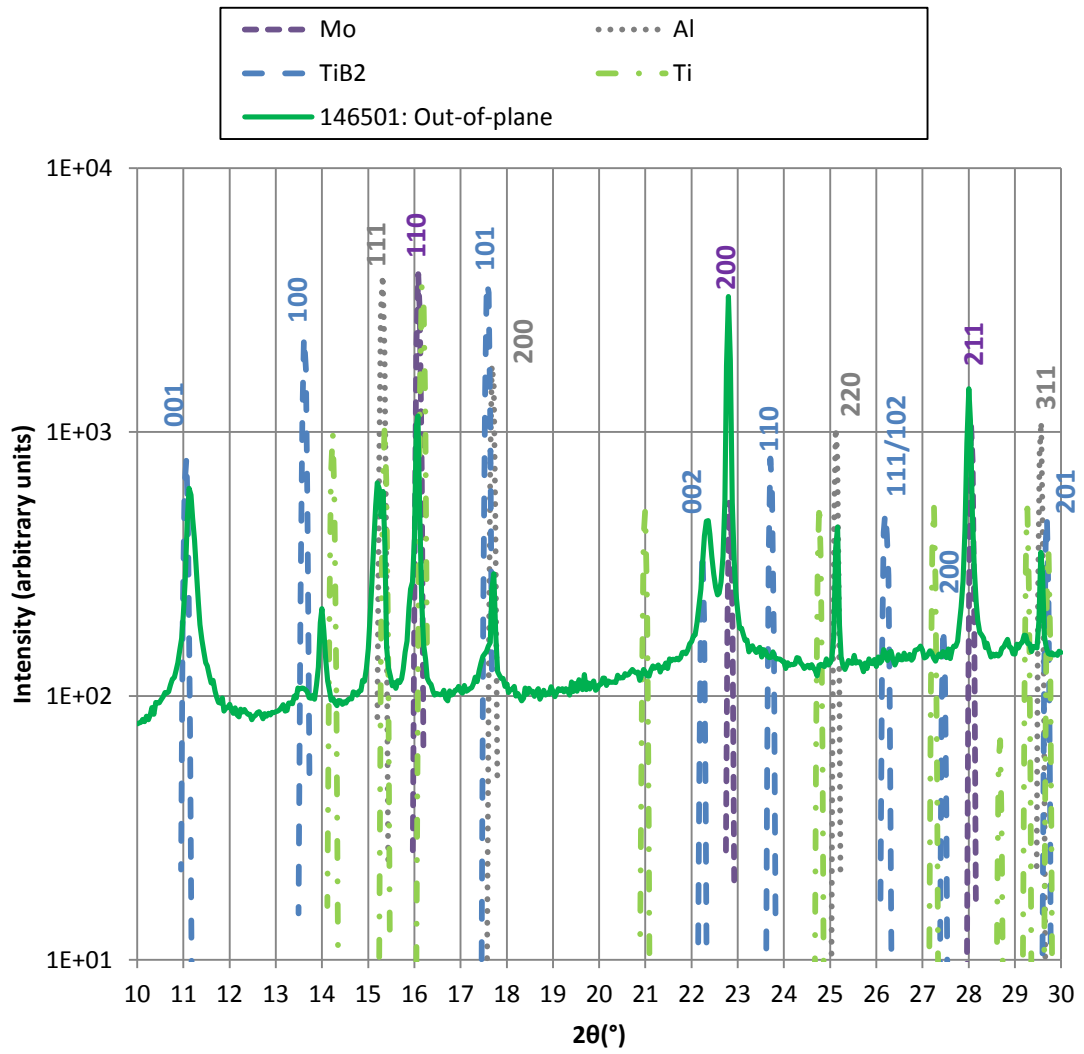


Figure 5-19 – Out-of-plane characterisation scan from E4 sample VIII with angle of incidence varying from 5° - 15°

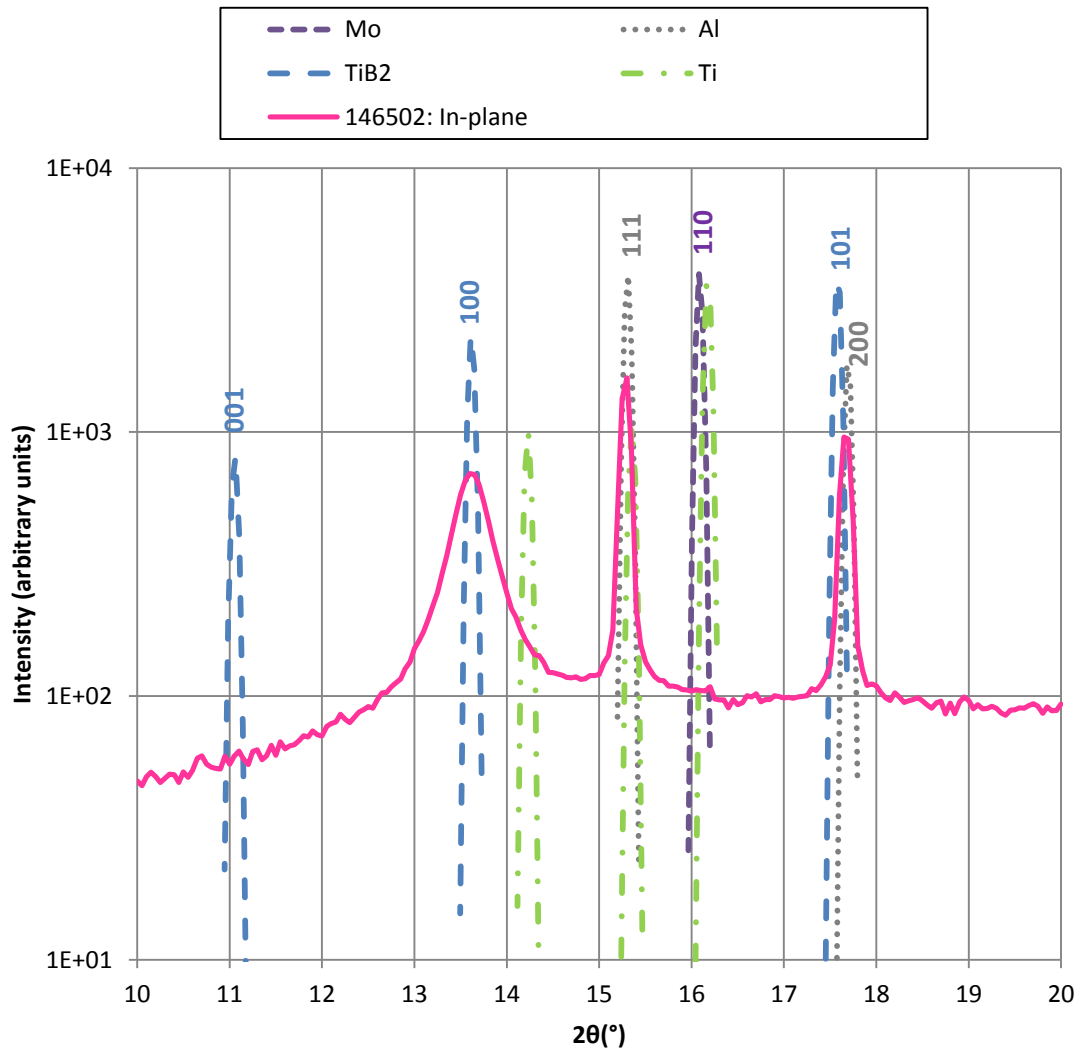
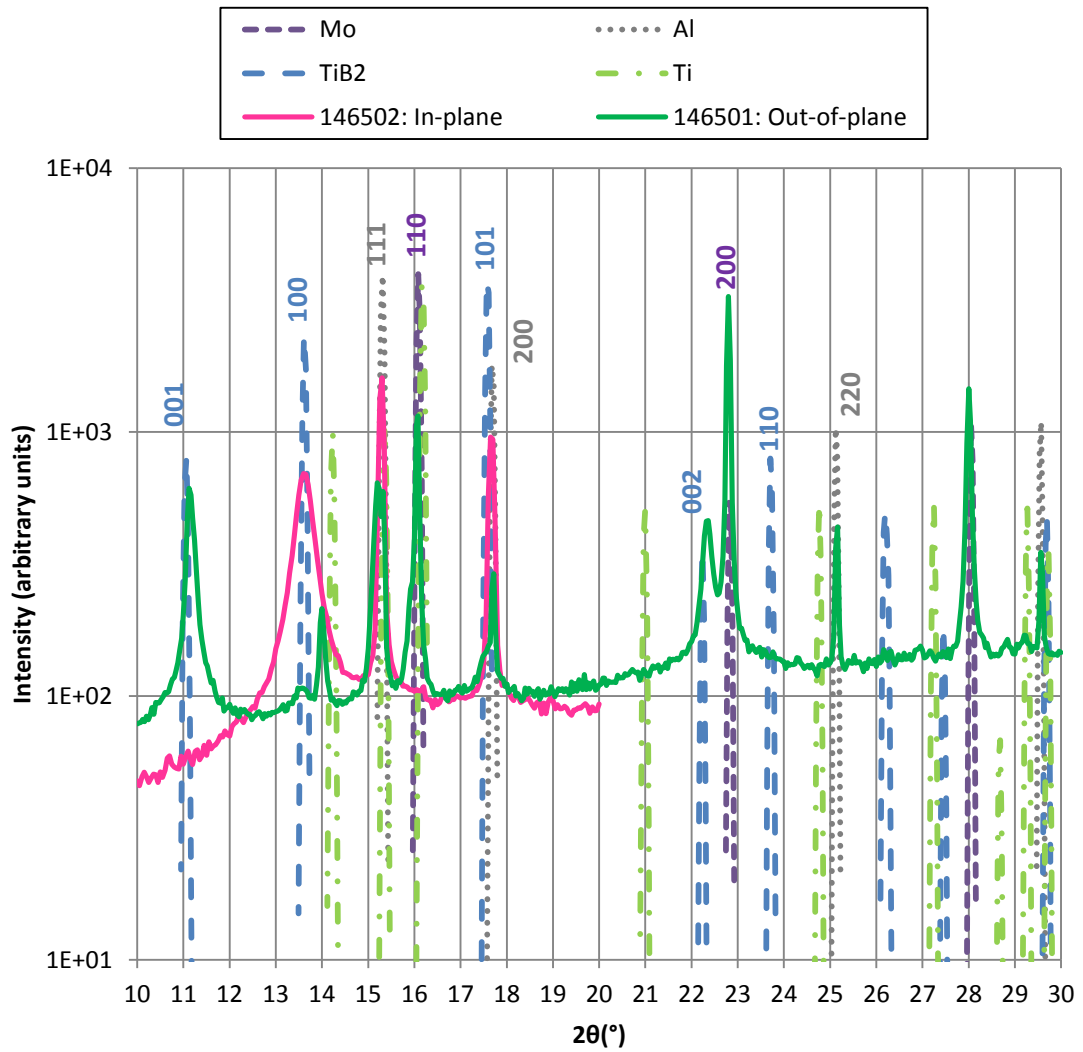
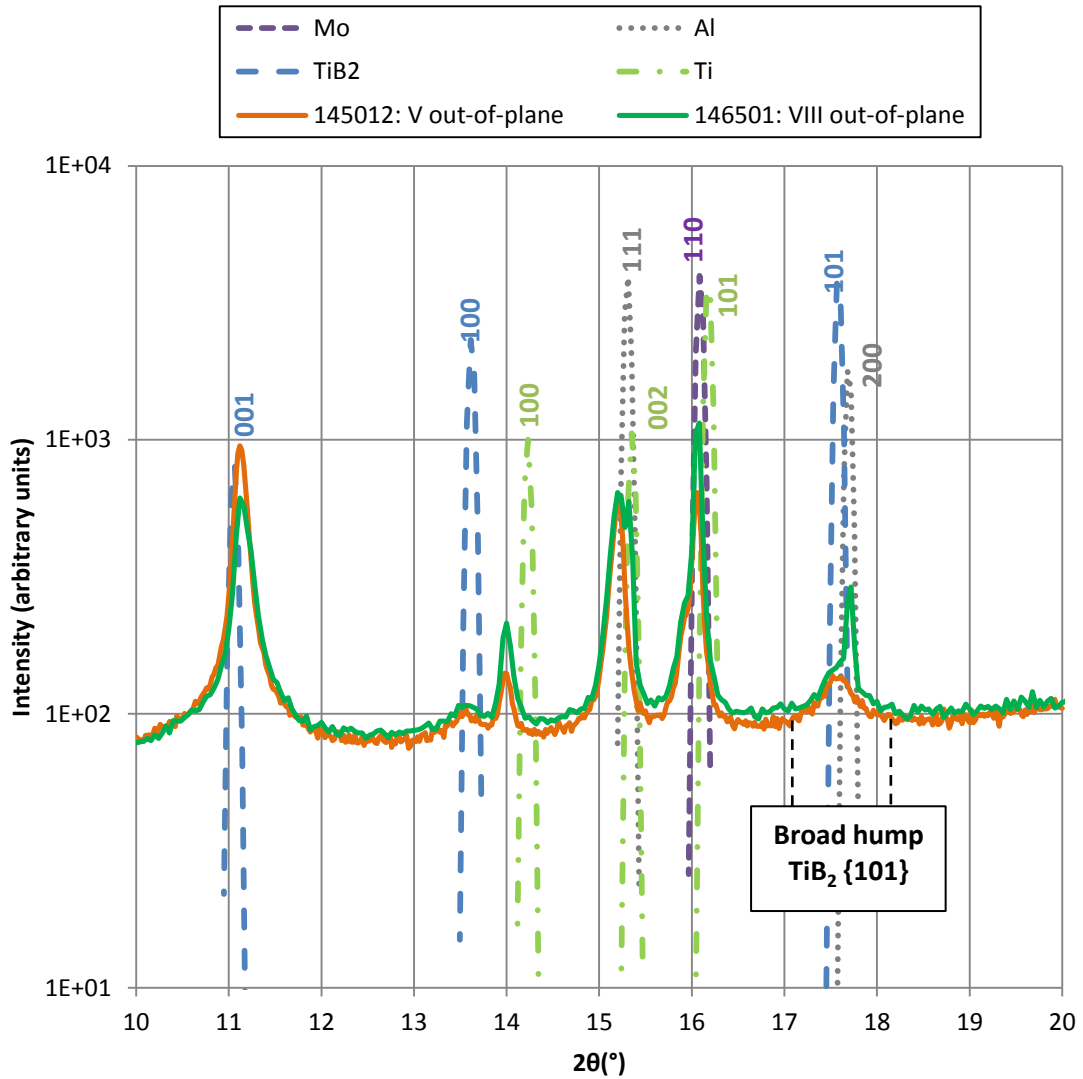


Figure 5-20 – In-plane characterisation scan from E4 sample VIII with angle of incidence 0.3°



**Figure 5-21 - Combined in-plane and out-of-plane scans from E4 sample VIII**

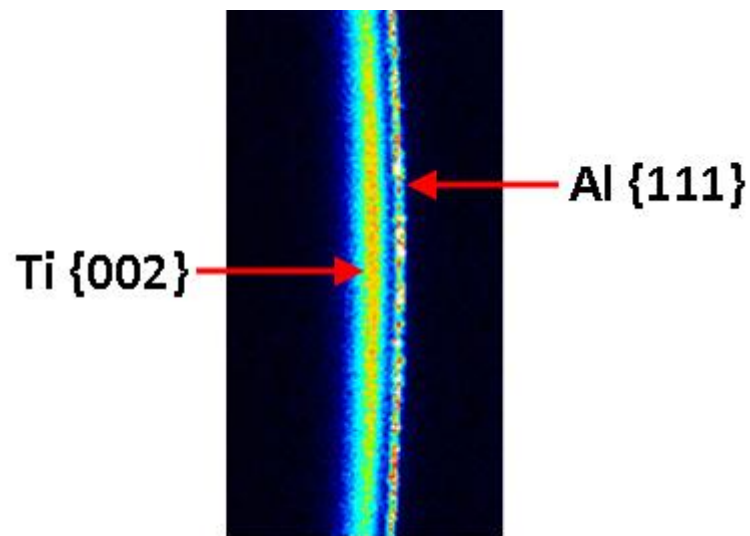
The region of greatest interest lies between  $2\theta = 10^\circ - 20^\circ$ , shown in Figure 5-22 (for clarity, just out-of-plane is shown):



**Figure 5-22 – Highlighted region of out-of-plane characterisation scan, comparing sample V (145012) with sample VIII (146501)**

Overall the morphology of sample VIII (146501) is reassuringly similar to sample V (145012), with the strong  $\text{TiB}_2$  (001) peak (Figure 5-19 also shows a strong peak for  $\text{TiB}_2$  (002) at  $\sim 2\theta = 22.3^\circ$ , further clarifying the overall (001) texture). Figure 5-22 compares the two samples. The main difference of course relates to the presence of Al on sample VIII, most clearly seen at  $2\theta = 17.5^\circ$ . Here a broad hump feature indicates the presence of the  $\text{TiB}_2$  {101} orientation that likely arises from the mixed texture zone of the  $\text{TiB}_2$  layer (Figure 5-13). In sample V, this is the only feature at this location, but for sample VIII a sharper peak is superimposed on the hump; a clear indicator of Al {200}.

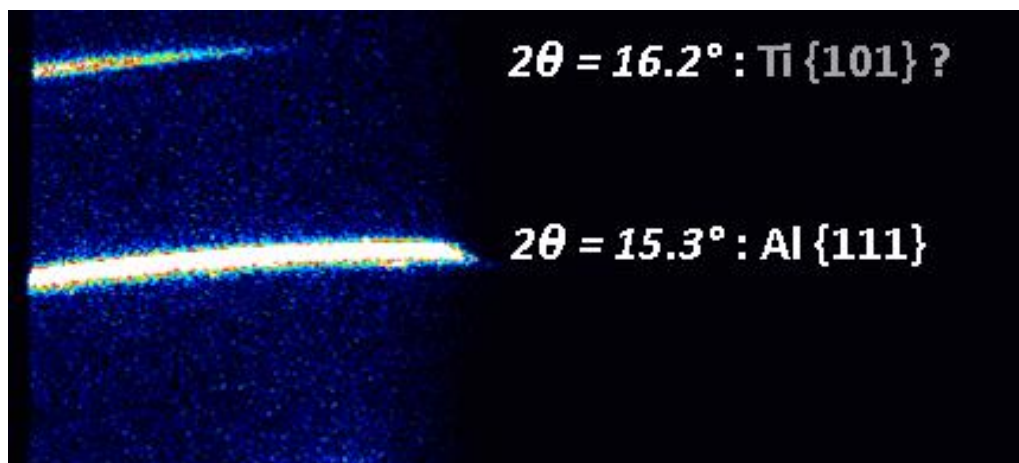
It is striking that the Al {111} peak position does not show such a clear difference between the samples. The sample VIII feature at  $\sim 2\theta = 15.3^\circ$  appears to be a double peak; observation of detector images confirms that there are indeed two distinct powder rings at this location; one arising from the Al and one from the Ti interlayer:



**Figure 5-23 – Detector at  $2\theta = 15.3^\circ$  showing two distinct rings**

This observation suggests that the Al {111} signal is slightly obscured by the Ti peak and is therefore weaker out-of-plane than expected. This is unfortunate as the {111} orientation particularly is of interest in this experiment, but as Figure 5-23 shows, the materials can be discerned with some extra investigation.

After characterisation, the detector was positioned at  $2\theta = 15.3^\circ$  in the in-plane orientation. In this geometry, no Ti {002} feature was present, minimising the potential for confusion with the Al {111}. This was therefore chosen as the 'monitoring position' to observe the phase transition in the Al. This initial condition is shown in Figure 5-24:



**Figure 5-24 - Initial condition in sample VIII as shown at ‘monitoring position’; i.e. centred at the Al {111} peak position. It is debatable whether the feature at 16.2° is indeed Ti as the beam is not expected to penetrate to the depth of the Ti layer in this geometry. The feature therefore likely arises either from Ti on the edge of the sample, or from other materials in supporting structures around the sample.**

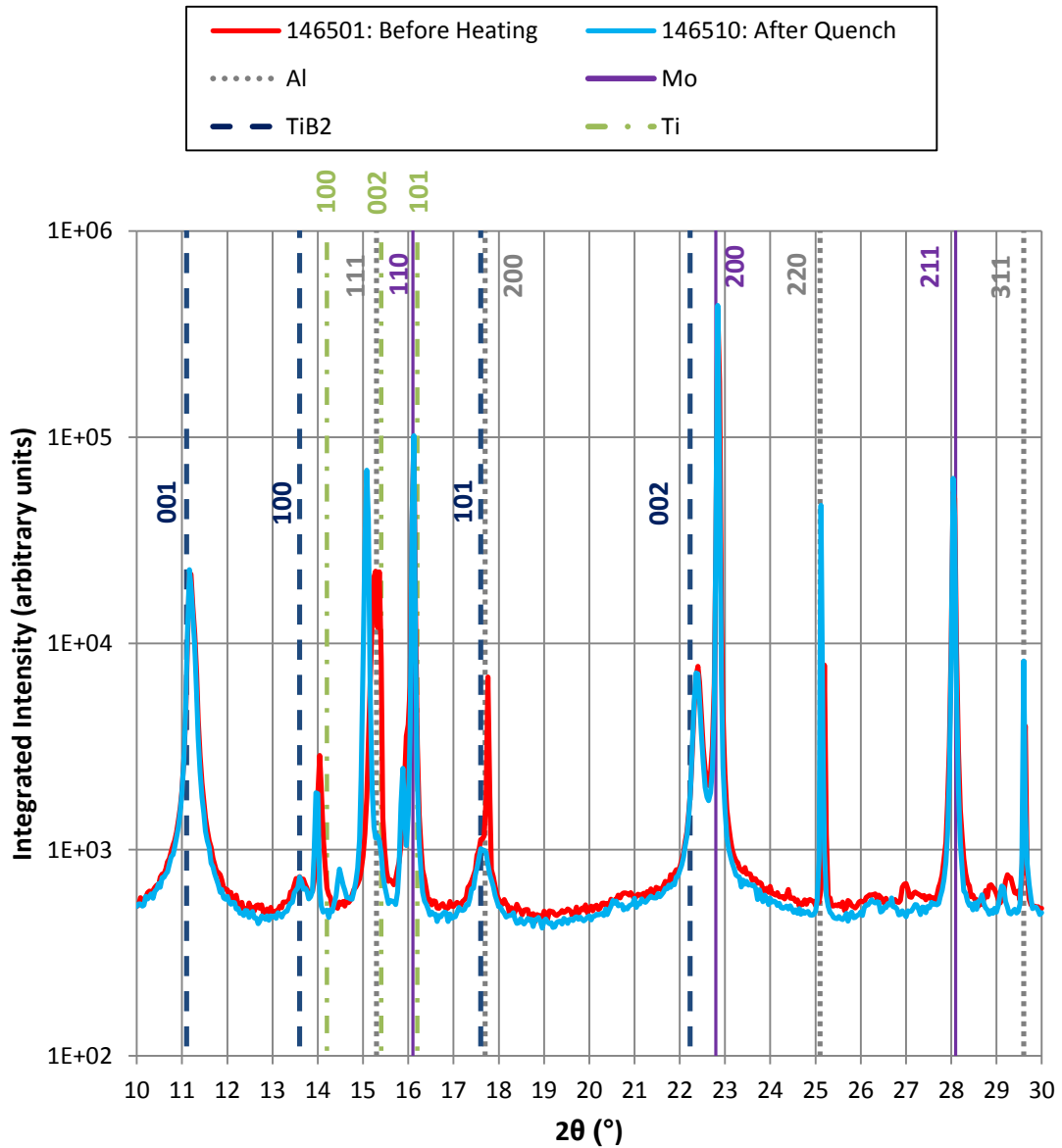
The detector orientation for Figure 5-24 was maintained throughout the heating process, allowing constant observation of the Al {111} feature. Due to time constraints heating was applied manually via the Eurotherm controller. Temperature was not correctly recorded in the scan files during this process, but the Al {111} feature behaved as expected; shifting to smaller  $2\theta$  before disappearing around the expected melting temperature of 660°C. As soon as the feature was absent, the heater was turned off; this rapidly decreased the sample temperature effectively applying a quench to the Al.

Upon quenching the Al {111} feature did not reappear in the detector window. However, direct observation of the sample via a video link<sup>16</sup> clearly showed the Al freezing almost instantly upon quenching. The fact that no Al {111} feature arose in the in-plane geometry implies that these planes may instead be aligned with the sample surface.

Due to the sporadic nature of the heating and cooling in this particular experiment, the data is presented in the following series of figures (Figure 5-25, Figure 5-26 and Figure 5-27) as ‘before’ and ‘after’ plots, allowing the transitions in morphology to be analysed. The data has been directly integrated from the

<sup>16</sup> Video is available on request

detector images; this was necessary because the pre-set ROI's used to record intensity at the beamline were not sufficiently large to capture all features.



**Figure 5-25 – Full out-of-plane characterisation of sample VIII before and after heating followed by immediate quenching. Vertical bars indicate expected peak positions for some materials of interest. Figure highlights the disappearance of the Al {200} feature and strengthening of Al {111}.**



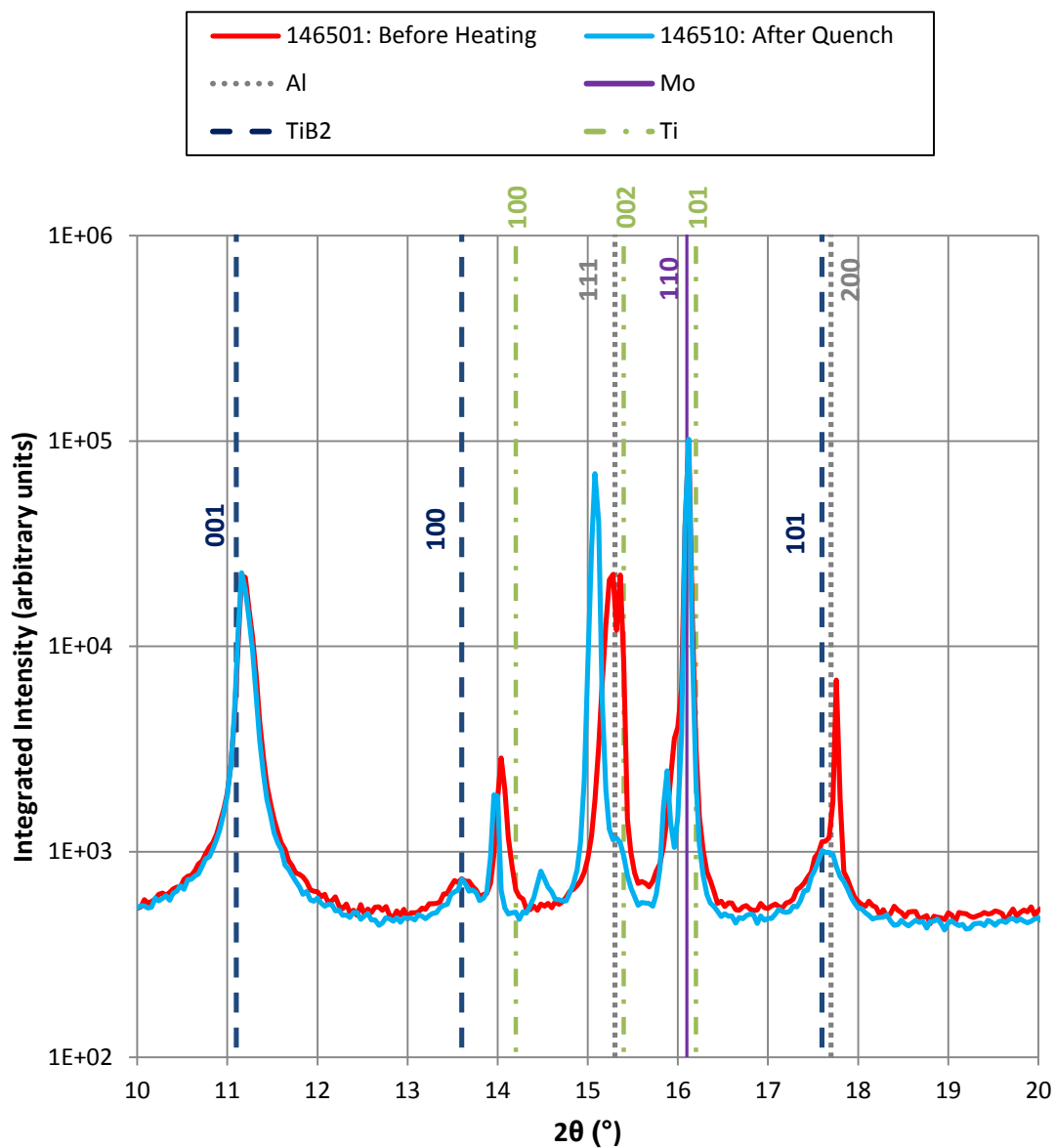
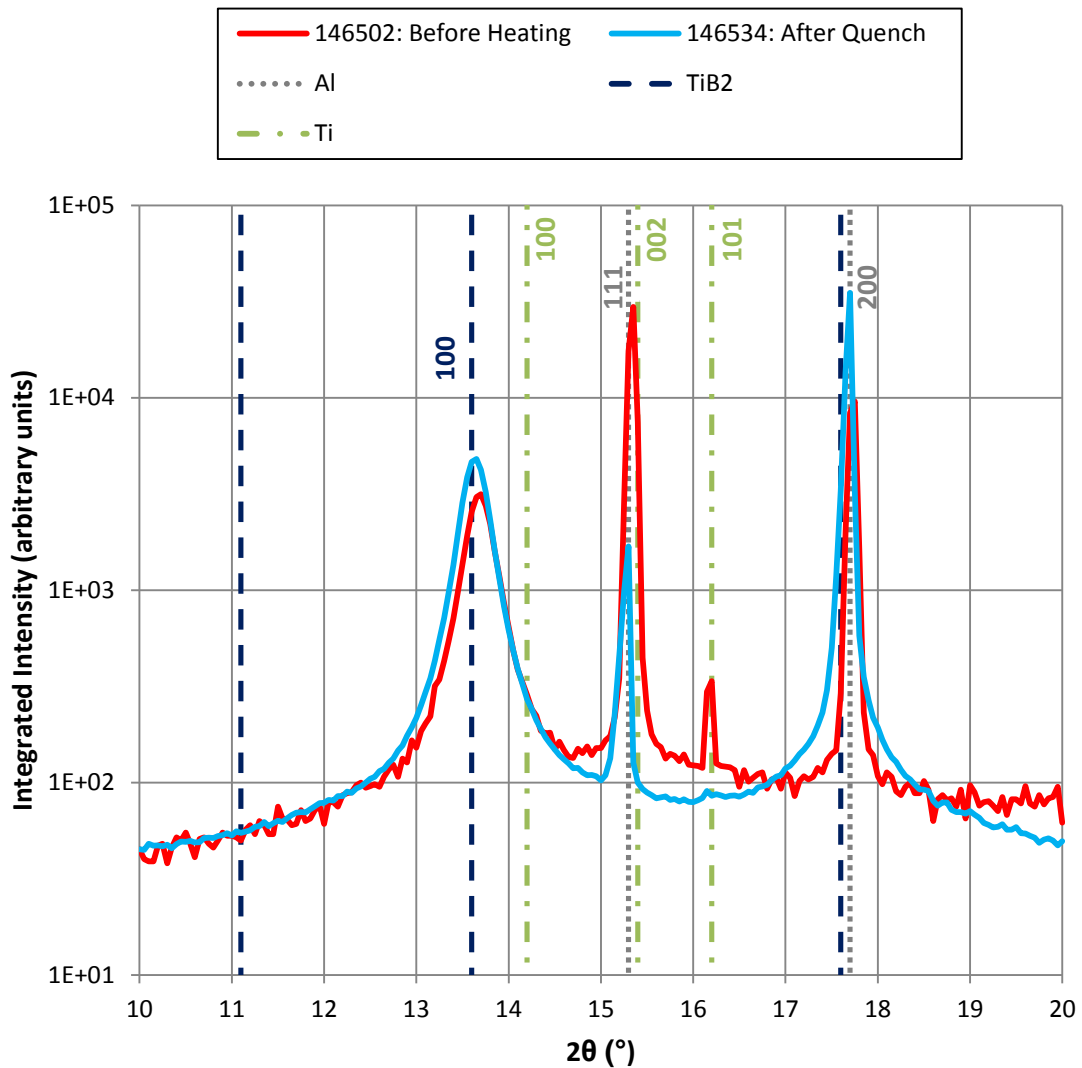


Figure 5-26 – Out of plane characterisation before and after heating: enlarged region  $2\theta = 10^\circ - 20^\circ$ .



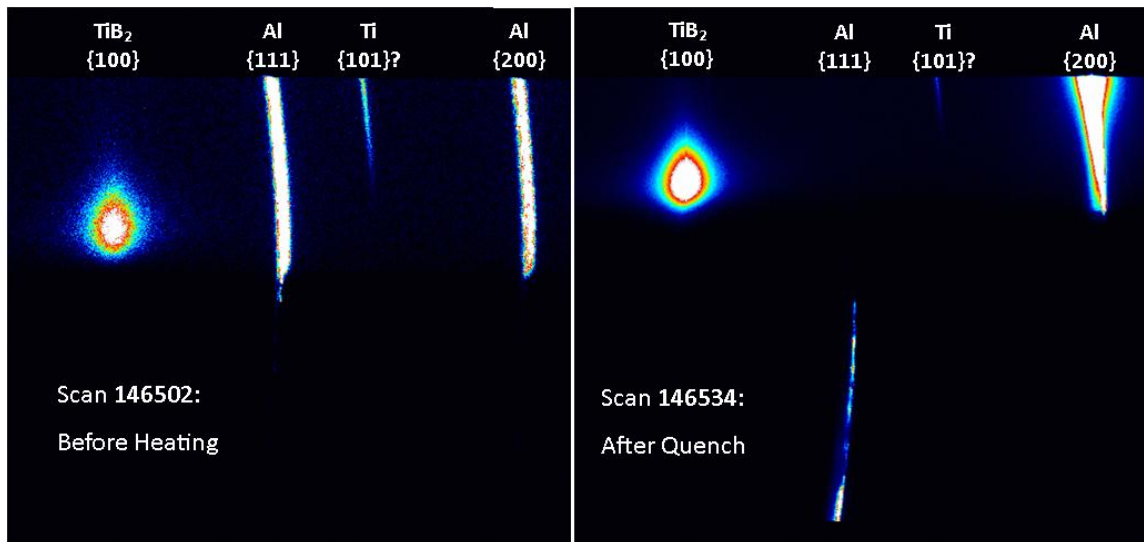
**Figure 5-27 – In-plane characterisation of sample VIII before and after heating followed by immediate quenching. Vertical bars indicate expected peak positions for some materials of interest (a selection are annotated). Figure highlights the disappearance of the Al {111} feature and strengthening of the Al {200}**

The above figures should be discussed in combination in order to fully reveal the morphological transitions in the sample. The best approach is to discuss the materials individually as follows:

1.  $\text{TiB}_2$ : The in-plane and out-of-plane data indicates a stable, strongly textured  $\text{TiB}_2$  layer which retains the desired orientation throughout the heating process. The  $\text{TiB}_2$  morphology is the same as the previous sample V; a strong (001) peak in the out-of-plane orientation indicating alignment of (001) planes with the sample surface, and a strong {100} reflection in-plane indicating that these planes are orientated perpendicular to the surface. The

expected zone of mixed texture is reflected in the presence of {100} and {101} features in the out-of-plane scan; these are likely not present in the in-plane as the beam only penetrates the uppermost part of the TiB<sub>2</sub> layer in this orientation.

2. Ti: as with sample V, there are peaks in the out-of-plane scan which can be ascribed to the three closest-packed planes of elemental Ti. The powder-like character of the features themselves (e.g. in Figure 5-23) supports the claim that they arise from the Ti layer. The Ti appears to be unaffected by the heating and cooling process, however the peak positions are in very close proximity to those from other materials. Investigation of the detector images can help to ascertain whether any changes occur in the Ti features or in the (potentially more interesting) surrounding features. This should also assist with the somewhat confusing appearance of a feature in the in-plane scan at  $2\theta = 16.2^\circ$  (see also Figure 5-24) ascribed to Ti {101}; the beam was not expected to penetrate sufficiently deep into the sample to illuminate the Ti layer in the in-plane geometry.
  - a. As with sample V there is a notable 'richness' in Ti that may be attributable to some aspect of sample preparation. This is discussed at the end of section 5.2.2.
3. Mo: present in only the out-of-plane scan due to beam penetration in this orientation. As before, however, Mo remains completely unaffected by the heating and cooling process; peak intensities remain the same at {110}, {200} and {211} positions.
4. Al: the key material under investigation and the morphology exhibits some revealing changes as a result of the heating and cooling process. To further understand these, it is helpful to present the direct detector images from the in-plane scan – i.e. those which correspond to the scans in Figure 5-27:

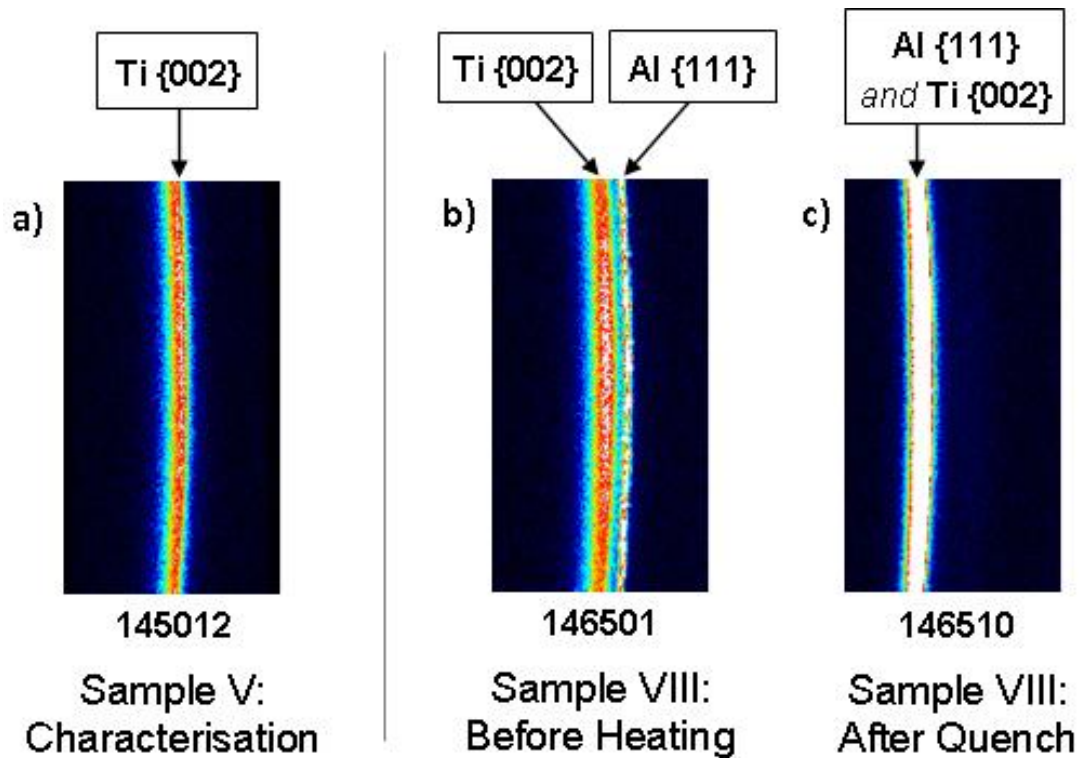


**Figure 5-28 – Montages of detector images from in-plane scans before and after thermal cycling. Refer to Figure 5-27 for comparison. Figure highlights the orientation relationship between  $\text{TiB}_2$  and Al which arises on cooling.**

Comparing the preceding set of figures, conclusions can begin to be drawn about the changing morphology of the Al, starting with the  $\{111\}$  planes. In the in-plane orientation, the  $\{111\}$  feature weakens significantly on quenching. Observation of the detector images in Figure 5-28 appears to show that the  $\{111\}$  feature, though appearing in the expected  $2\theta$  location, has moved 'beneath' the actual measurement region. It is suggested that this in fact arises from Al on the *edge* of the sample; when in the liquid state it is likely that some Al has flowed over the sides of the sample surface and when quenched has remained in that position. The lack of intensity in the location of the original  $\{111\}$  feature suggests that this orientation no longer exists in-plane. Conversely, the  $\{200\}$  feature not only stays in the expected position, but increases *significantly* in intensity (by a factor of around 10x). It also retains the characteristic ring-like profile. Overall, this suggests a strong alignment of  $\{200\}$  planes *perpendicular* to the sample surface, but randomly orientated in-plane (i.e. their angular rotation with respect to the incoming beam).

In the out-of-plane orientation, it was noted that the feature at the  $\{111\}$  position was complicated by the presence of the Ti  $\{002\}$  reflection in close proximity. It is clear from the scans however that the scattering in this approximate  $2\theta$  region has significantly increased in intensity after quenching (by a factor of approx. 3x at the peak). This observation can be lent clarity by observing the detector

images, and comparing with the previous sample V which had no Al layer during characterisation:



**Figure 5-29 - Detector images from out-of-plane scans at Al {111} peak position ( $2\theta = 15.3^\circ$ ). Brightness and contrast settings are the same in all images. a) shows the Ti {002} ring from sample V. b) shows the same Ti {002} ring, with the Al {111} ring also present, from sample VIII prior to heating. c) shows the resulting feature at the same position after heating and subsequent quenching.**

The increased intensity is particularly apparent in Figure 5-29c. It is unlikely that there is any mechanism for the Ti signal to strengthen; indeed all other Ti peaks in the out-of-plane scans remain unaffected. Therefore it is reasonable to conclude that the feature represents a strengthening {111} orientation out-of-plane. This can be understood along with the observation that there is no {111} reflection in the in-plane scans (apart from on the sample edges as previously mentioned). Overall then it is suggested that there is a strengthening of the {111} orientation out-of-plane, suggesting a degree of alignment of these planes with the sample – and thus, with the  $\text{TiB}_2$  {001} – surface. Some further qualification of this is however necessary.

The proposed Al {111} feature appears at a smaller  $2\theta$  value ( $15.1^\circ$ ) compared to the expected  $15.3^\circ$ , implying a slightly larger d-spacing of  $2.371\text{\AA}$ , compared to the equilibrium  $2.338\text{\AA}$ . This could be ascribed to a number of things, but as with previous experiments, **strain** may be the most interesting option. In this case uniform strain would be suggested as the feature exhibits a peak *shift*; rather than a *spread* as seen in E1 S1. The shift suggests an expansion of the spacing of Al {111} planes; perhaps towards a match with the  $3.232\text{\AA}$  periodicity of  $\text{TiB}_2$  (001) planes, though this would not be expected to persist through the entire thickness of the Al layer as the data suggests. Another suggestion is that the quench has retarded the normal thermal contraction of the material at an early stage, resulting in an expanded structure retained in the solidified Al. Residual strain in the structure has implications for the lattice relationship within the Al/ $\text{Al}_3\text{Ti}$ / $\text{TiB}_2$  mechanism proposed by Schumacher *et al* [14], Schumacher and Greer [27], and McKay and Schumacher [51].

Out-of-plane scans show the presence of two further Al features, representative of the {220} and {311} planar families. Both of these features appear to increase in intensity on cooling – though this alone does not reveal the full story. Once more, further information can be drawn from observation of the detector images at relevant positions as shown in Figure 5-30:

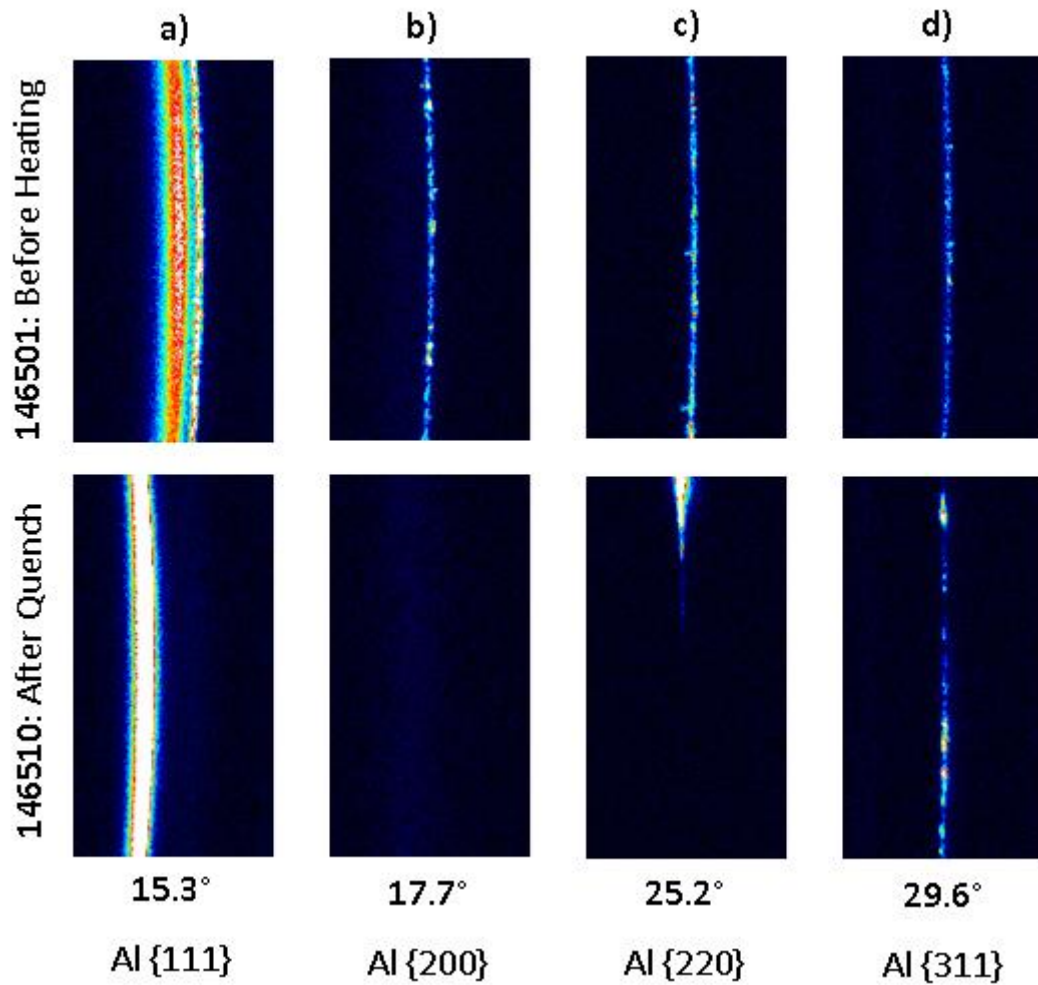


Figure 5-30 - Detector images from out-of-plane scans at a range of Al positions – a), b), c), d). Shows the transition of features before and after heating/quenching. Brightness and contrast settings are the same in all images.

The overall morphology changes in the Al layer can thus be characterised as followed:

Al Planar Family	Out-of-plane	In-plane
{111}	<b>Strengthens</b> & possibly strained	<b>Disappears</b>
{200}	<b>Disappears</b>	<b>Strengthens</b>
{220}	<b>Strengthens</b> – also appears to coarsen (feature is more spot-like)	N/A
{311}	<b>Strengthens</b> – also coarsens (spotty ring)	N/A

Table 5-4 – Morphological transitions in Al layer

The overall implication is that Al {111}, {220} and {311} planes are aligned parallel with the surface of the sample, while {200} planes lie perpendicular to it. Geometrically this is somewhat confusing; the {111}, {220} and {311} clearly have slightly different orientation with respect to each other and therefore they cannot *all* be exactly aligned with the surface. The character of the features themselves in Figure 5-30 gives some further information. The intensity and consistency of the {111} feature implies a fine-grained structure overall with a strong bias towards {111} alignment; the 'spotty' appearance of the {220} and {311} features likely indicates that a small population of Al grains exists within the layer which have the corresponding alignment. This is illustrated in Figure 5-32.

In Al grain refinement,  $\text{TiB}_2$  particles are sub-micron sized single crystals, against the (001) faces of which crystalline Al is observed to nucleate, with an initial {111} orientation. Single crystal  $\text{TiB}_2$  is difficult to obtain, especially at larger sizes, so the current work attempts to *model* the grain refinement process by using a sample with a (001) textured surface. It is unlikely that the entire sample surface has this orientation; the sample surface is certainly polycrystalline and likely comprises individual grains at a variety of orientations. The characterisation indicates that for the E4 samples a strongly biased (001) texture was obtained – and the results indicate that the Al solidified with a bias to a {111} texture. However, the relatively large size of the  $\text{TiB}_2$  surface, its random polycrystalline nature, and the relative thickness of the Al layer, means it is unsurprising that other orientations are observed in the out-of-plane direction.

Within this context the in-plane alignment can also be discussed. At the small angle of incidence used for the in-plane scan (approx.  $0.3^\circ$ ) the X-ray beam is expected to penetrate only 2-3 $\mu\text{m}$  into the Al layer. Figure 5-28 shows the {111} feature in the lower portion of the image. This indicates that the in-plane scattering has been collected from around the edge of the sample, rather than the centre. The strength of the {200} feature indicates a strong preference for this orientation in this region of the sample. It is therefore suggested that there are grains around the *edge* of the sample which have a strong {200} orientation



in plane, with the centre of the sample characterised by a bias towards a {111} texture out-of-plane.

It is also important to note that the rapid solidification method adopted in this case (quenching) provides a large thermodynamic driving force for solidification. This likely dominates over the effect of energetically favourable orientation relationships. This is reflected in the resulting morphology in the sample; the texture, though clearly adopting a {111} bias, is relatively mixed. Live observation of the sample *in-situ*<sup>17</sup> showed that the Al solidified from the 'outside-in'; i.e. the material on the edges of the sample solidified first. The strong {111} texture likely arises from the centre of the sample, because during the quench, the centre of the sample remains marginally hotter than the edge, allowing a degree of texture development over a fractionally longer solidification time.

Putting all this information together, a picture of the quenched morphology in sample VIII is constructed in Figure 5-32. The accompanying Figure 5-31 shows Al unit cells with planes of interest highlighted.

---

<sup>17</sup> Video available on request

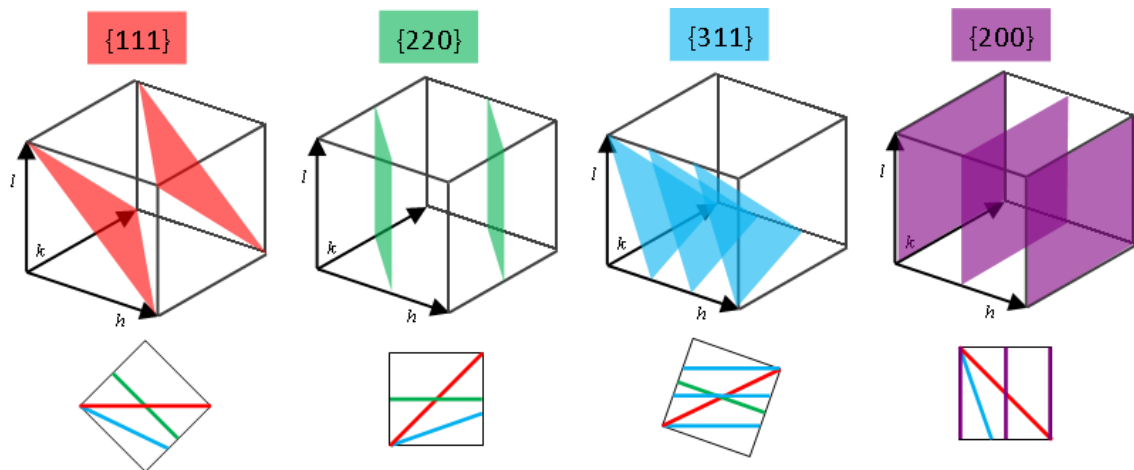


Figure 5-31 – Unit cell constructions for Al

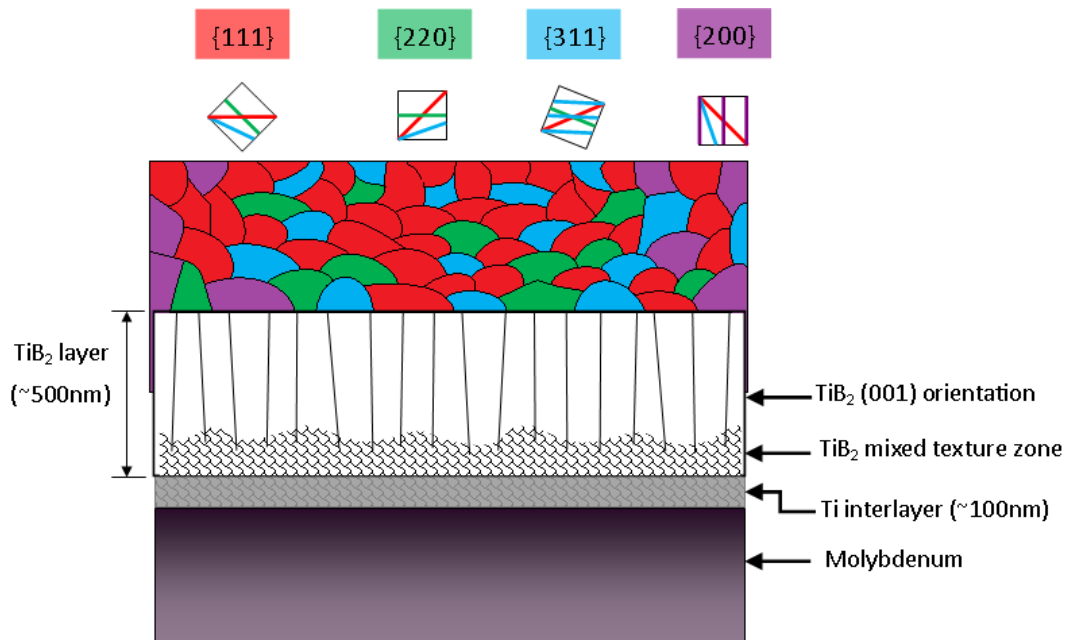
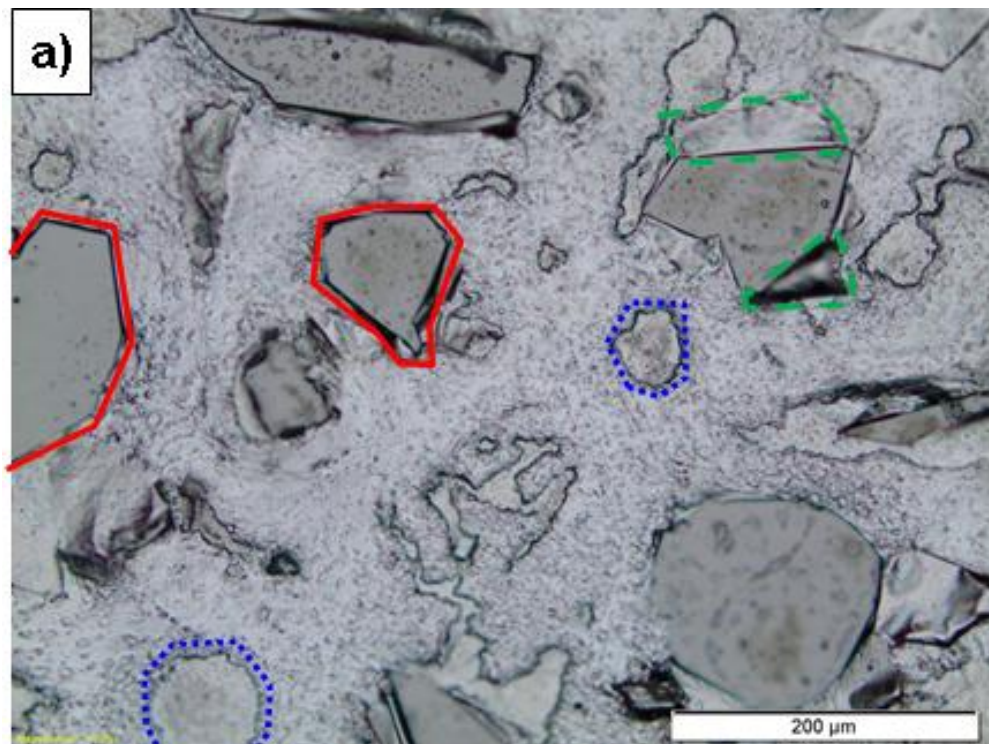


Figure 5-32 –Suggested morphology for solidified Al layer in sample VIII.

Another perspective can be gained through microscopy of the surface, shown in Figure 5-33:



**Patches**   **Blisters**   **Peeled-up 'flaps'**

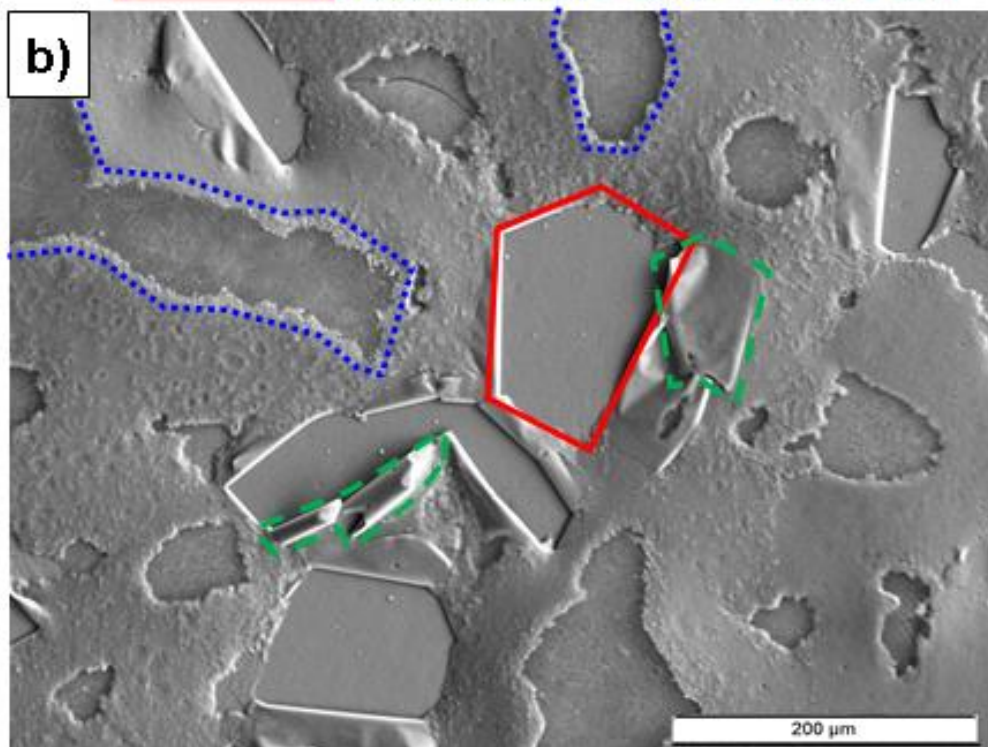
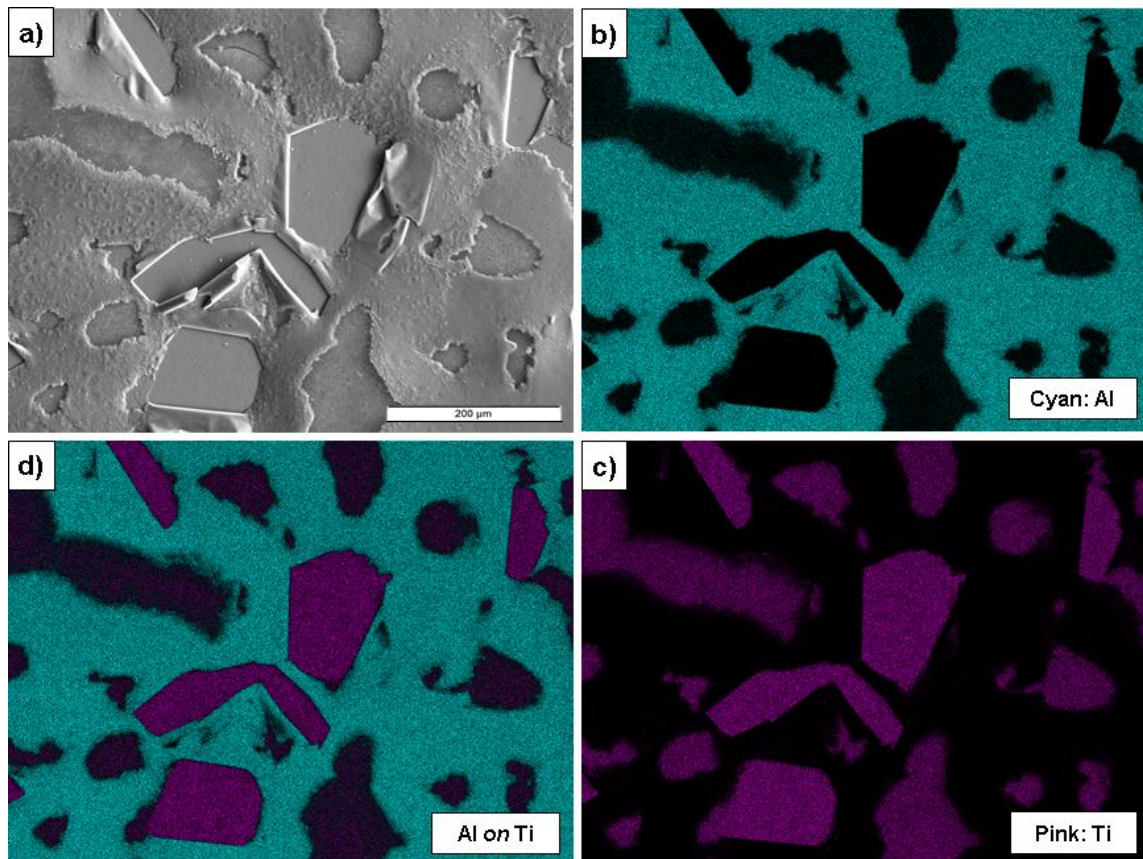


Figure 5-33 – Micrographs of sample VIII surface after quenching, from a) optical microscopy and b) SEM. Solidified Al covers the majority of the surface; coverage is broken up by 3 distinct feature types, examples of which have been identified and marked.

The figure shows that the Al covers most of the surface, broken up by occurrences of three distinct surface features, identified as **patches**, **blisters** and **peeled-up ‘flaps’**. Using EDX the elemental content of the surface can be mapped, which provides more insight into the character of the identified features.



**Figure 5-34 – EDX mapping of sample VIII surface. a) SEM micrograph showing mapped area. b) indicates areas with high Al content. c) indicates areas with high Ti content. d) clarifies the different character of the “patch” and “blister” regions by overlaying the Al onto the Ti map. Black areas in b), i.e. regions with no Al counts, are made transparent; this is then overlaid on the Ti map. Therefore in d), patch regions appear the same as c) as they comprise solely Ti; blisters appear darker due to the mixed Al-Ti content in these regions. Note that the brightness and contrast of the EDX images has been artificially increased for clarity.**

Collating the observations from Figure 5-33 and Figure 5-34, conclusions can be made about the identified surface features.

The surface **patches** are areas where the Al layer appears to have completely ‘peeled’ away exposing a flat substrate surface underneath. There is a strong Ti



signal and no Al in these, suggesting these show either the  $\text{TiB}_2$  layer or the Ti interlayer beneath. Around the edges of the patches, the Al appears to have **peeled** up, forming **flaps** and exposing the substrate beneath. These flaps have no Ti content and appear to solely comprise Al, indicating that the patches expose the  $\text{TiB}_2$  surface.

The **blisters** are more complex. They have a mixed content, although it is clearly far stronger in Ti; Al is present in these regions but is quite faint in the images. The overlay in Figure 5-34d clarifies the mixed nature as the blisters appear differently to the surface patches. The strong Ti content indicates that these are also areas of exposed  $\text{TiB}_2$  substrate, but clearly there is some residual Al remaining on the surface. It is possible that the mixed nature of the blister regions indicates the presence of some  $\text{Al}_3\text{Ti}$ , though the weakness of the Al signal appears to suggest that this has not formed in large quantities. Figure 5-35 shows a 'close-up' of Figure 5-34d to clarify the mixed content within:

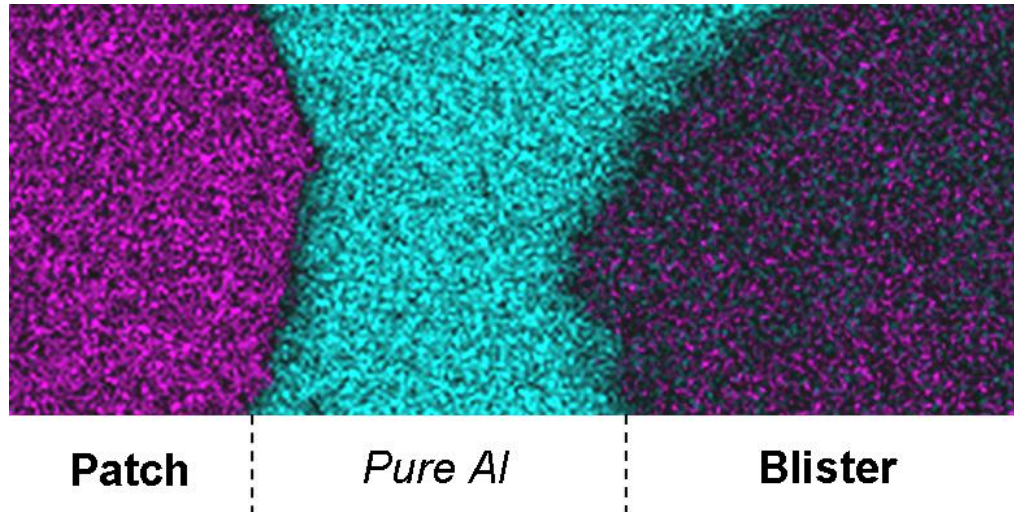


Figure 5-35 – Indicating the mixed Al-Ti content of the blister regions; patch and pure Al areas also shown for comparison.

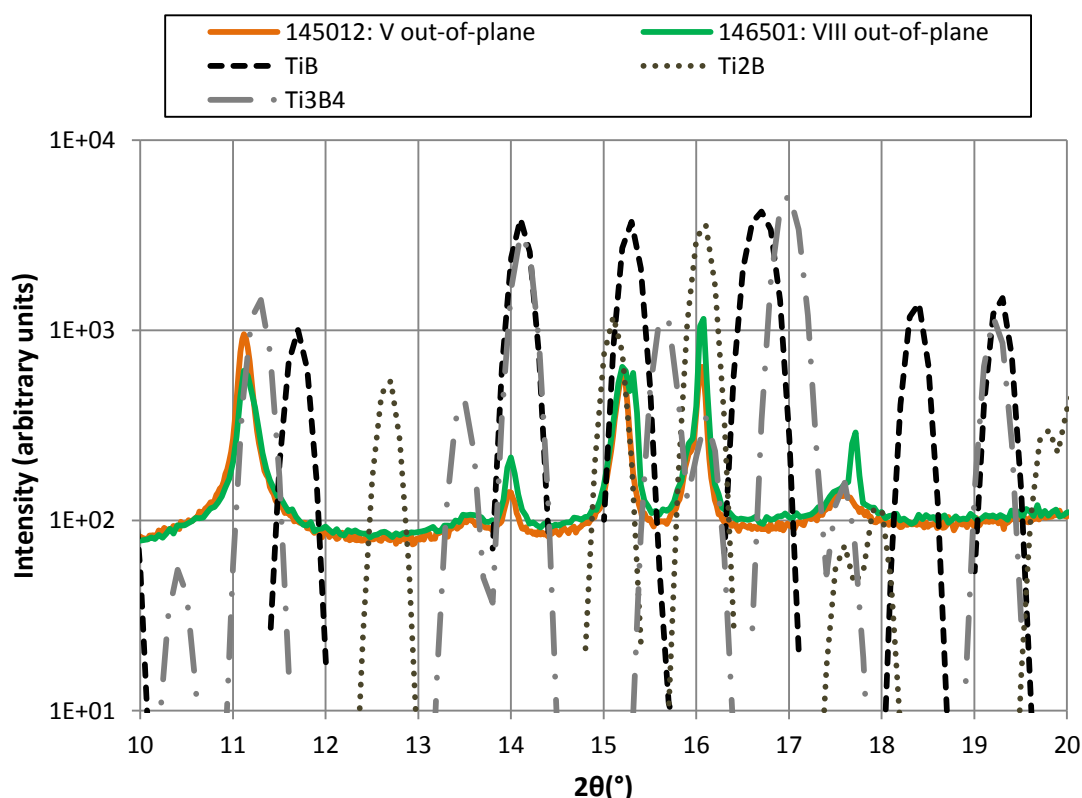
It is not possible to discern individual Al grains in the sample. The fast quenching process has likely resulted in a grain size which is too small to resolve using the microscopy techniques in Figure 5-34.

The primary challenge with the experiments using  $\text{TiB}_2$  samples has been to 'capture' solidified Al on cooling. E3 results showed that Al liquid has a tendency to migrate towards the (cooler) edges of the sample during the heating and cooling process, thus removing it from the beam path. The *in-situ* evaporation of Al used for E4 sample V did not allow a sufficient quantity of material to be deposited, and results suggest that the material which was present on the sample surface reacted to form new phases on heating leaving no pure crystalline Al. E4 sample VIII has been successful in capturing the solidified Al, but the rapid quenching method required to achieve this has likely played a dominant role in the resulting morphology, limiting the applicability of the results to an investigation of orientation relationships at the Al/ $\text{TiB}_2$  interface.

The E4  $\text{TiB}_2$  substrates represent an experimental model of the application of Greer's athermal nucleation mechanism to Al grain refinement (see section 1.4). Athermal (rather than thermally activated) nucleation is suggested to be the dominant mechanism even down to inoculant particle sizes of 1nm [15], [19]. The  $\text{TiB}_2$  substrates prepared for this work are polycrystalline in nature with a strong (001) texture; the grain size at the surface, and thus the nucleant 'patch' size, is expected to be in the region of 5-50nm. Therefore, athermal nucleation is still expected to be the dominant mechanism in these samples. Had it been possible to measure a clear  $\Delta T$  in the same manner to that in the Al/ $\text{Al}_2\text{O}_3$  experiments, this value would have represented a direct measurement of  $\Delta T_{fg}$  i.e. the undercooling required to instigate free growth; although, this does require some qualification. Athermal nucleation assumes an isothermal melt. While this is a fair assumption for individual events in an industrial case (small  $\text{TiB}_2$  particles in a comparatively very large melt); in this work, the sample/heater geometry may result in small temperature gradients which may affect the mechanism. Improvements are required to increase temperature uniformity and permit measurement of the <1K undercooling expected for Al/ $\text{TiB}_2$ . It is hoped that continued advances in temperature control, possibly via implementation of the micro-heater used in E2, will permit this in future experiments.

Further work is clearly required to tailor the Al/TiB<sub>2</sub> system for study via X-ray scattering methods, to allow the use of techniques such as CTR analysis. The current work has nonetheless produced some intriguing results, and provided indications as to appropriate methods to use in future studies. Perhaps the most enlightening aspect of the work has been the potential appearance of Al<sub>3</sub>Ti, and this aspect merits a distinct section for presentation and discussion of the evidence thereof.

Before considering this, it is sensible to comment on the rich Ti content observed in both E4 samples; V and VIII. The question is whether the composition of the deposited TiB<sub>2</sub> layer is in fact non-stoichiometric. The following figure superimposes the comparison of the two samples from Figure 5-22 on expected peak positions for a range of alternative compounds of Ti and B, specifically TiB, Ti<sub>2</sub>B, [152] and Ti<sub>3</sub>B<sub>4</sub> [153]:



**Figure 5-36 – Comparison of out-of-plane scans for samples V and VIII with expected peak positions for alternative Ti-B compounds**

While the above indicates a *degree* of peak matching, the comparison is certainly not conclusive. For example, there appears to be a reasonable match for TiB and Ti<sub>3</sub>B<sub>4</sub> phases and a peak in the data at 14°, but numerous other peaks from the Ti-B compounds have no discernable correspondence. It is therefore not appropriate to conclude that the stoichiometry of the TiB<sub>2</sub> deposition was altered such that an alternative, discrete Ti-B compound arose. Further to this, the presence of features directly attributable to TiB<sub>2</sub>, including, most importantly, a strong (001) peak, definitively indicates the presence of this specific compound. However, an enriched Ti content clearly exists in the TiB<sub>2</sub> layer in both samples, and it is sensible to suggest that this has arisen during sputter deposition of TiB<sub>2</sub>.



### 5.3 Evidence for formation of $\text{Al}_3\text{Ti}$ at the $\text{Al}/\text{TiB}_2$ interface

Experiments E3 and E4 were not able to capture melting and re-solidification of Al in a manner similar to that achieved during E1 (using  $\text{Al}/\text{Al}_2\text{O}_3$ ). However, both experiments offered interesting information pertaining to the formation of  $\text{Al}_3\text{Ti}$  at the  $\text{Al}/\text{TiB}_2$  interface during solidification.

It is well understood that  $\text{TiB}_2$  alone is not an effective inoculant, either theoretically due to the large mismatch [51], or experimentally [56]. The presence of excess Ti in the melt renders the process more effective [7]. In the present work, the layer of pure Ti in the sample is ‘sealed’ by the thicker  $\text{TiB}_2$  layer which sits upon it. However, the  $\text{TiB}_2$  surface itself likely comprises some disassociated or ‘loose’ Ti which can react with liquid Al, and as previously suggested, may in any case have a composition enriched in Ti due to a non-stoichiometric deposition.

This information is worth repeating, as both experiment three and four appear to show strong indications of the appearance of  $\text{Al}_3\text{Ti}$ . The results are readily comparable as the same energy (19.9keV) was used in both experiments. Based on further data from the ICSD, the expected peak positions for  $\text{Al}_3\text{Ti}$  are shown in Table 5-5. Other materials are included for reference. Figure 5-37 repeats the Al-Ti phase diagram for reference.

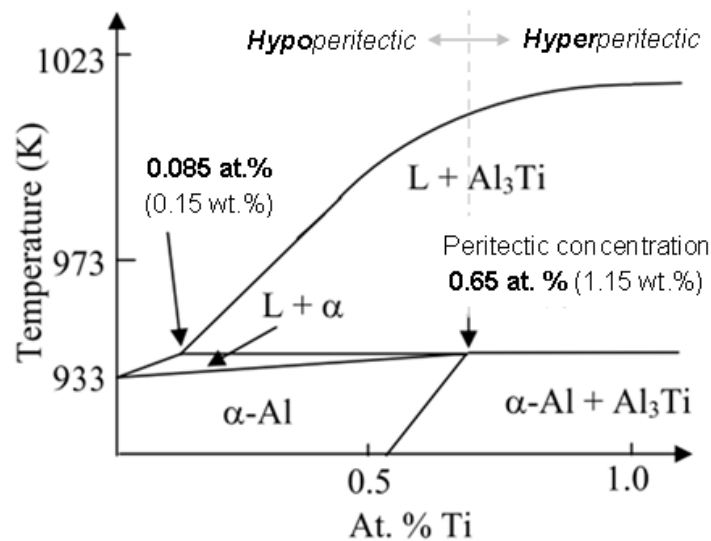


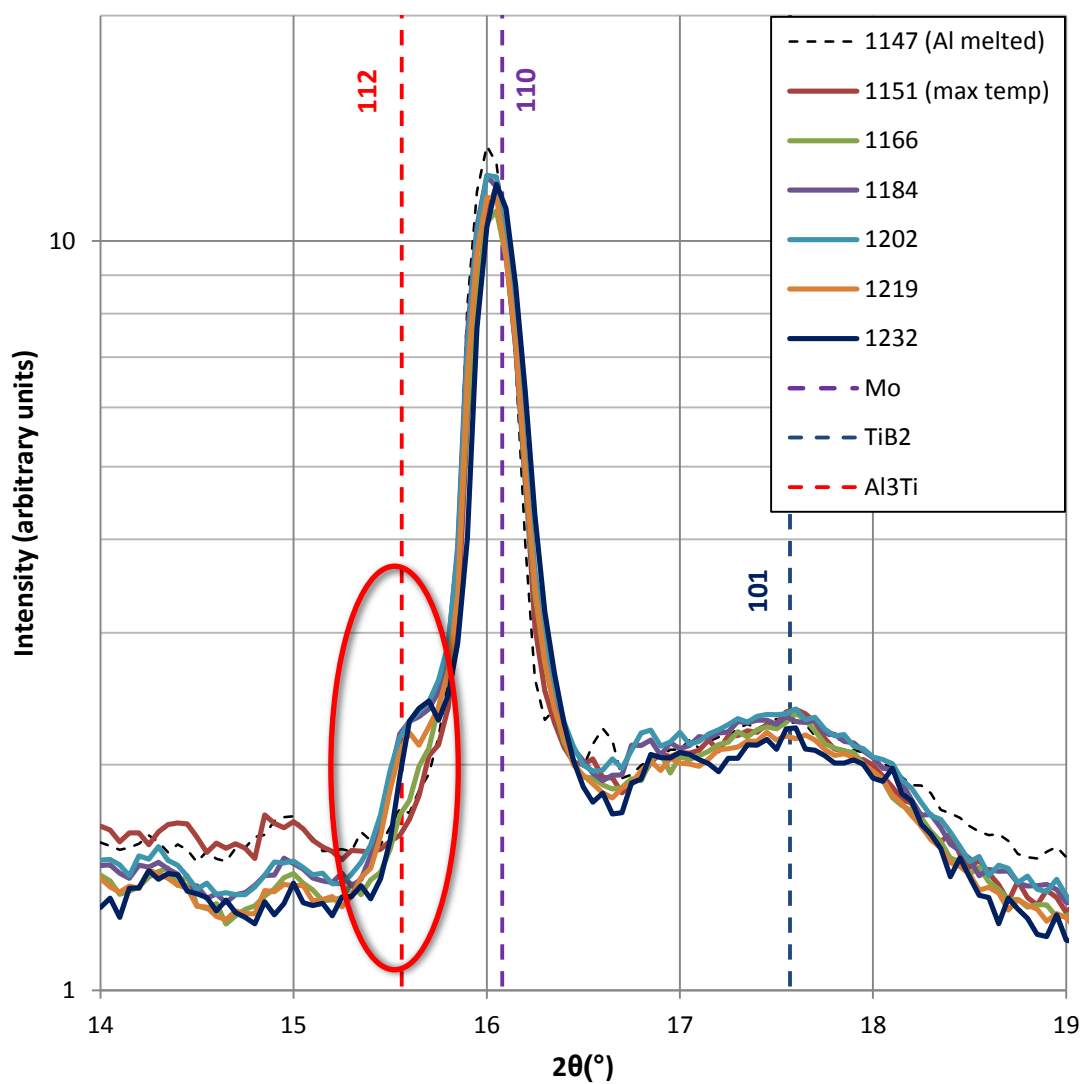
Figure 5-37 – Schematic of binary Al-Ti phase diagram. Modified from [51]

	Peak Position in $2\theta$ (°)	$\theta$ (°)	d (Å)	Planar Family
<b>Aluminium</b> [149]	15.32	7.66	2.338	<b>Al {111}</b>
	17.71	8.85	2.024	<b>Al {200}</b>
	25.15	12.57	1.431	<b>Al {220}</b>
	29.57	14.78	1.221	<b>Al {311}</b>
<b>Al<sub>3</sub>Ti</b> [154]	15.56	7.78	2.301	<b>Al<sub>3</sub>Ti {112}</b>
	16.70	8.35	2.146	<b>Al<sub>3</sub>Ti {004}</b>
	18.59	9.29	1.929	<b>Al<sub>3</sub>Ti {200}</b>
<b>TiB<sub>2</sub></b> [99]	11.06	5.53	3.232	<b>TiB<sub>2</sub> {001}</b>
	13.61	6.81	2.629	<b>TiB<sub>2</sub> {100}</b>
	17.57	8.78	2.040	<b>TiB<sub>2</sub> {101}</b>
<b>Titanium</b> [150]	14.23	7.12	2.515	<b>Ti {100}</b>
	15.36	7.68	2.332	<b>Ti {002}</b>
	16.16	8.08	2.217	<b>Ti {101}</b>
<b>Molybdenum</b> [148]	16.08	8.04	2.227	<b>Mo {110}</b>
	22.82	11.41	1.575	<b>Mo {200}</b>
	28.06	14.03	1.285	<b>Mo {211}</b>

**Table 5-5 - Peak positions and corresponding d-spacings for materials of interest in investigation of the Al/TiB<sub>2</sub> system. X-ray energy 19.9 keV ( $\lambda=0.623\text{\AA}$ )**

### 5.3.1 Experiment Three

The previous Figure 5-8 shows the in-plane character of sample A as the Al transitions from solid to liquid on heating. As described in the subsequent text, Al peaks did not reappear on cooling; only the broad TiB<sub>2</sub> {101} and strong Mo {110} feature remained in the scans. However, as the following set of figures (Figure 5-38, Figure 5-39 and Figure 5-40) clearly indicates, a ‘shoulder’ forms against the Mo peak as the system cools:



**Figure 5-38 – Selected in-plane scans from sample A during cooling stages. Region of ‘shoulder formation’ highlighted. Strong Mo {110} peak at  $2\theta = 16.08$  and broad TiB<sub>2</sub> {101} feature centred at  $2\theta = 17.57$ . Temperatures at which scans were recorded are indicated in Figure 5-39.**

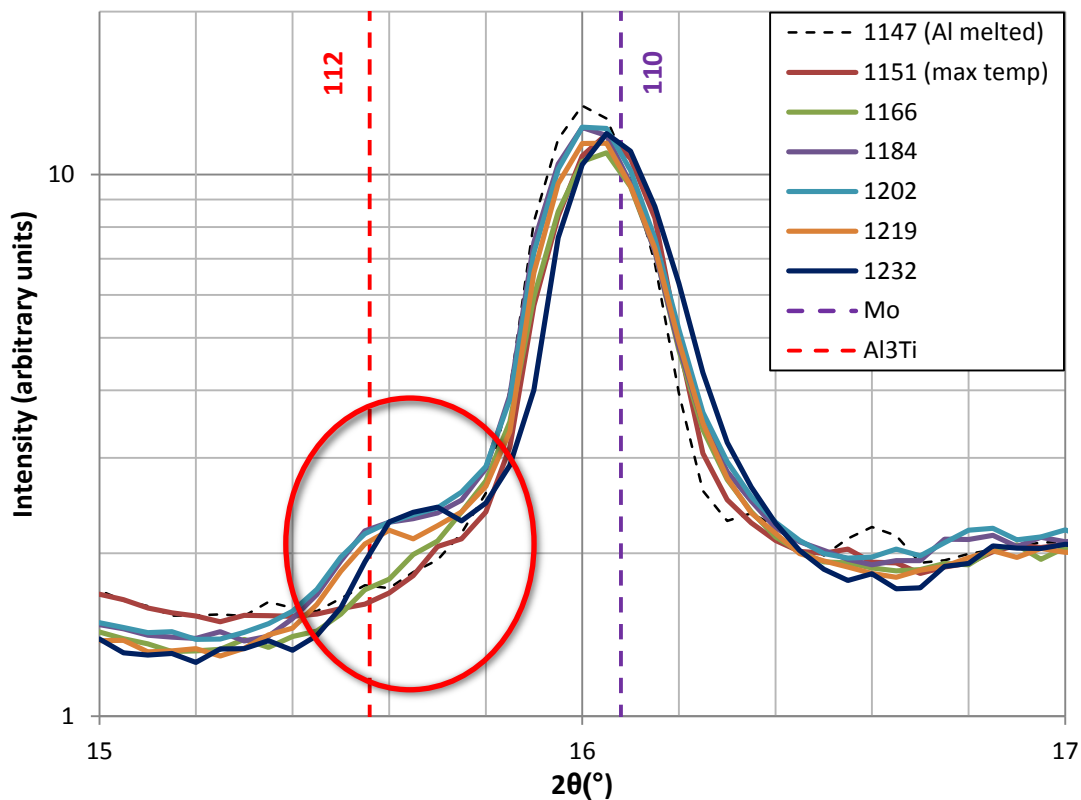


Figure 5-39 – ‘Zoom in’ on previous figure to highlight shoulder formation, suggesting the existence of Al<sub>3</sub>Ti {112}. Temperatures at which scans were recorded are indicated in

Figure 5-39.

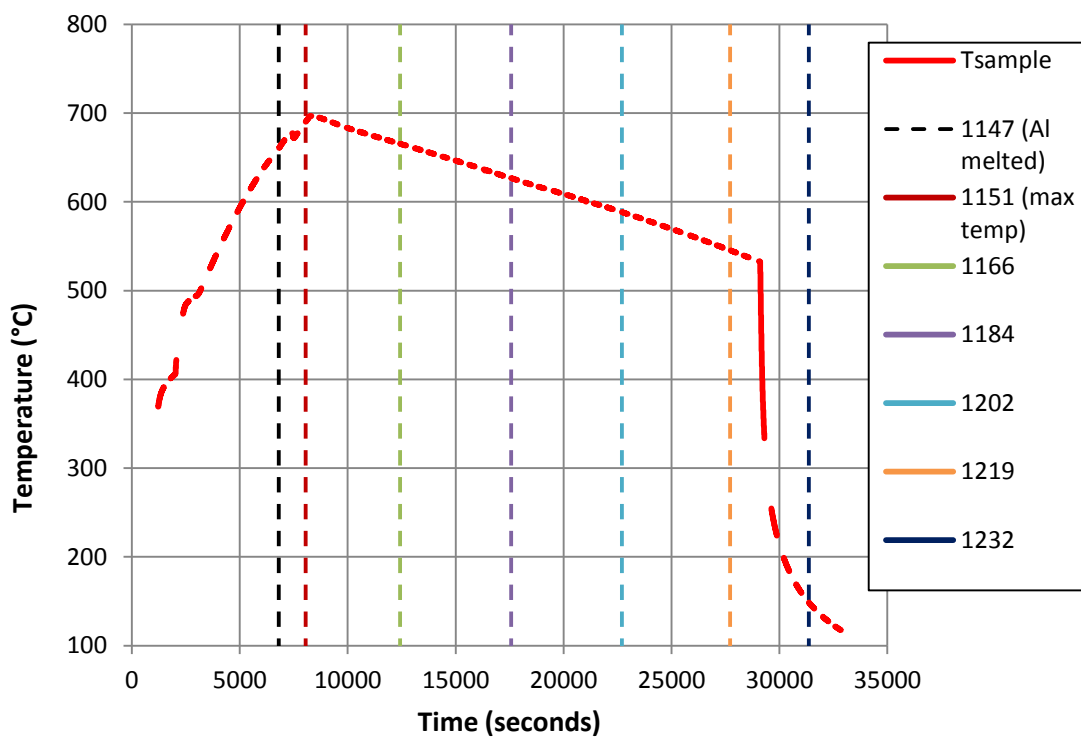
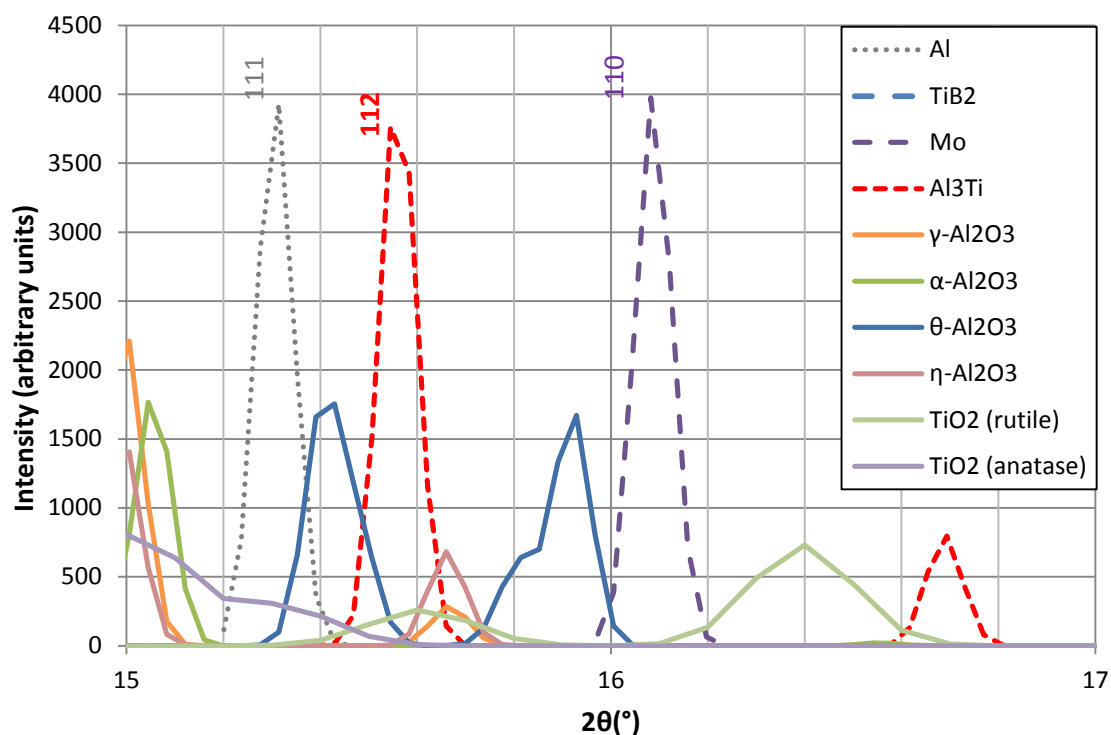


Figure 5-40 - Temperature profile indicating time and temperature of selected scans

The preceding figures show the formation of a feature centred close to  $2\theta = 15.56^\circ$ , i.e. the expected position for  $\text{Al}_3\text{Ti}$  {112}, on cooling. There are no indications of either  $\text{Al}_3\text{Ti}$  {004} or  $\text{Al}_3\text{Ti}$  {200}, however the ICSD data [154] suggests these features would be significantly weaker; if they are present, they would likely be swamped either by scattering from  $\text{TiB}_2$  {101} or the background noise. In any case, the {112} family is of greatest interest as it is exhibited in the orientation relationship between Al and  $\text{TiB}_2$  in the mechanism proposed in the literature [14], [27], [51].

These results provide a degree of supporting evidence for the formation of  $\text{Al}_3\text{Ti}$ . They must be considered with caution, however, for the following reasons:

1. The desired  $\text{TiB}_2$  (001) orientation was not achieved in sample A, therefore there is no evidence for the  $\text{Al}_3\text{Ti}$  exhibiting registry with the substrate.
2. No Al features re-appeared in the scan on cooling, therefore there is no evidence for  $\text{Al}_3\text{Ti}$  registry with crystalline Al {111}.
3. The data displayed are from in-plane scans, whereas the mechanism defines  $\text{Al}_3\text{Ti}$  {112} planes being aligned parallel to the nucleating surface (so would not be illuminated in-plane). However, because there is neither a  $\text{TiB}_2$  (001) or Al {111} signal observed parallel to the surface in this sample, it is clear that the expected orientation relationship has not developed in any case; so there is no reason to expect that  $\text{Al}_3\text{Ti}$  {112} would necessarily be aligned parallel to the surface. The presence of the peak nonetheless suggests the formation of  $\text{Al}_3\text{Ti}$ , which is in itself a relevant observation.
4. In the immediate  $2\theta$  region, scattering from a range of aluminium and titanium oxide phases are predicted, which may also account for the appearance of the shoulder. Compared to the  $\text{Al}_3\text{Ti}$ , however, predicted peak positions do not match up as precisely, and/or are expected to be very weakly scattering. It is notable, for example, that there is no match for the  $\text{Al}_2\text{O}_3$  phases which may have been observed to form on cooling in previous experiments. This information is summarised in Figure 5-41:



**Figure 5-41 – Expected peak positions from a range of oxide phases in the  $2\theta$  region 15°-17°. Note the strength of the Al<sub>3</sub>Ti feature in comparison to the oxide phases**

Recording the presence of Al<sub>3</sub>Ti is potentially of great interest due to the considerable debate in the field surrounding the mechanisms of Al nucleation and grain refinement. E4 was intended to shed further light on this issue.

### 5.3.2 Experiment Four

Revisiting the heating/cooling scans performed on the E4 samples, we now review for evidence of the appearance of  $\text{Al}_3\text{Ti}$ . As previously stated it is the  $\text{Al}_3\text{Ti}$  {112} orientation which is of interest in the context of Al nucleation; corresponding to a  $2\theta$  position of  $15.56^\circ$ .

The post-cooling scans from sample V are shown in the following. The plot shows the in-plane and out-of-plane scans post-cooling, which are the same as those previously displayed in Figure 5-16 and Figure 5-17 respectively.

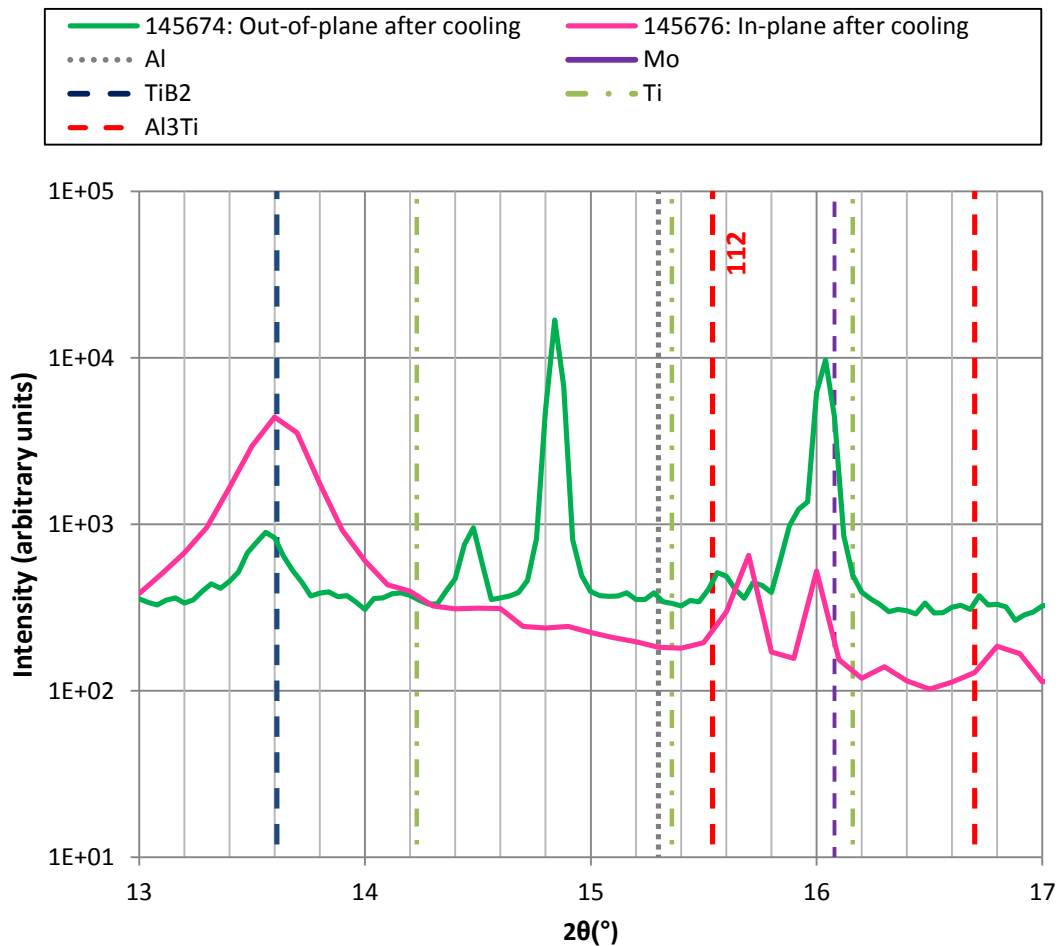
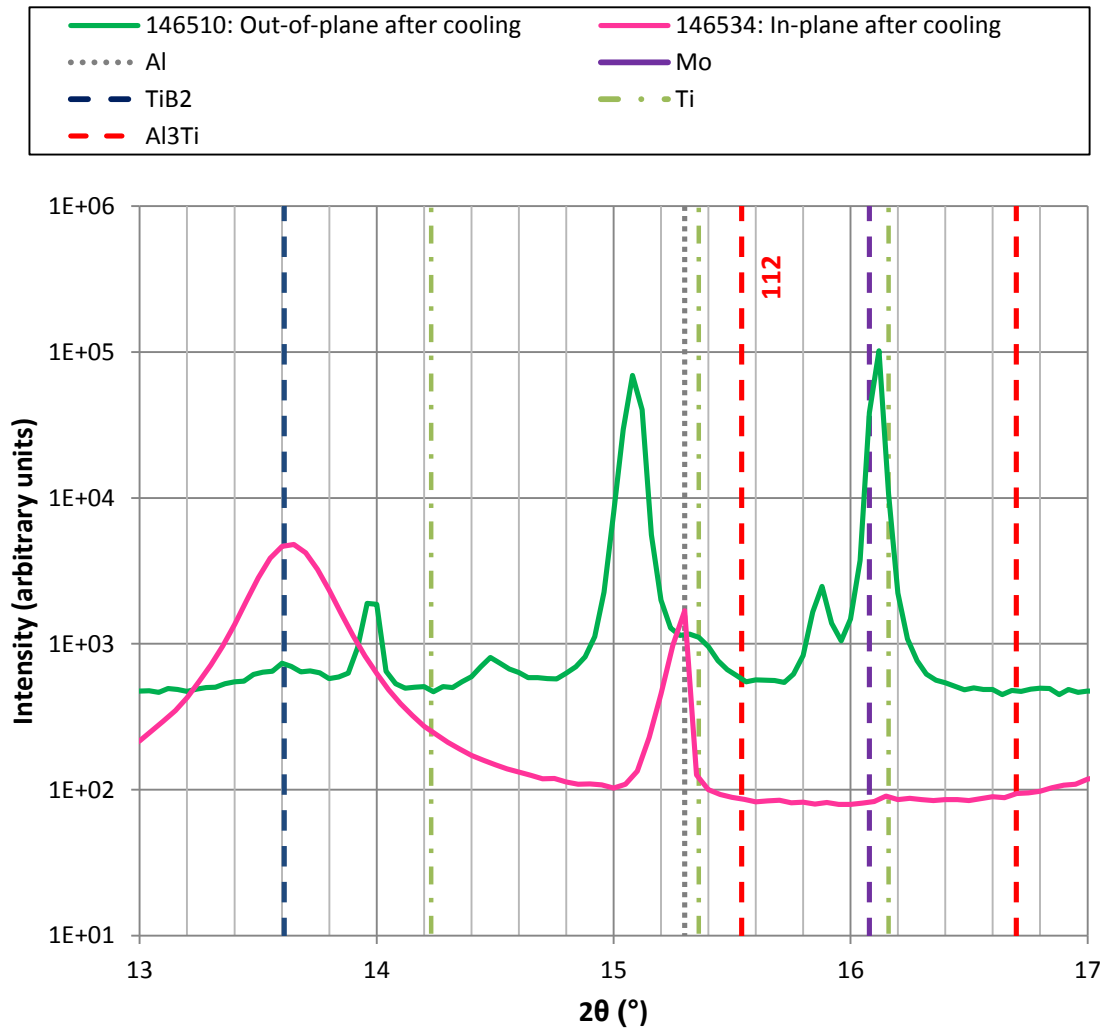


Figure 5-42 – Post-cooling scans (at room temperature) from sample V

As discussed in 5.2.1, there is a small but noticeable peak in the out-of-plane scan (145674) at  $2\theta = 15.56^\circ$  which corresponds to the  $\text{Al}_3\text{Ti}$  {112} peak position. There are also features in the in-plane scan (145676) in the region  $15.5^\circ - 16^\circ$ .

Corresponding scans from sample VIII are shown in Figure 5-43:



**Figure 5-43 – Post-cooling scans (at room temperature) from sample VIII. Note that the peak in the in-plane scan at  $2\theta = 15.3^\circ$  arises from the edge of the sample rather than the interfacial region (see Figure 5-28 for comparison)**

There is no small peak analogous to that observed in Figure 5-42; however, a feature is apparent at  $2\theta = 15.9^\circ$  against the strong Mo {110} peak at  $16.1^\circ$ .

Detector images in Figure 5-44 give another perspective on the appearance of the peaks in all 3 cases; E3 sample A and E4 samples V and VIII:



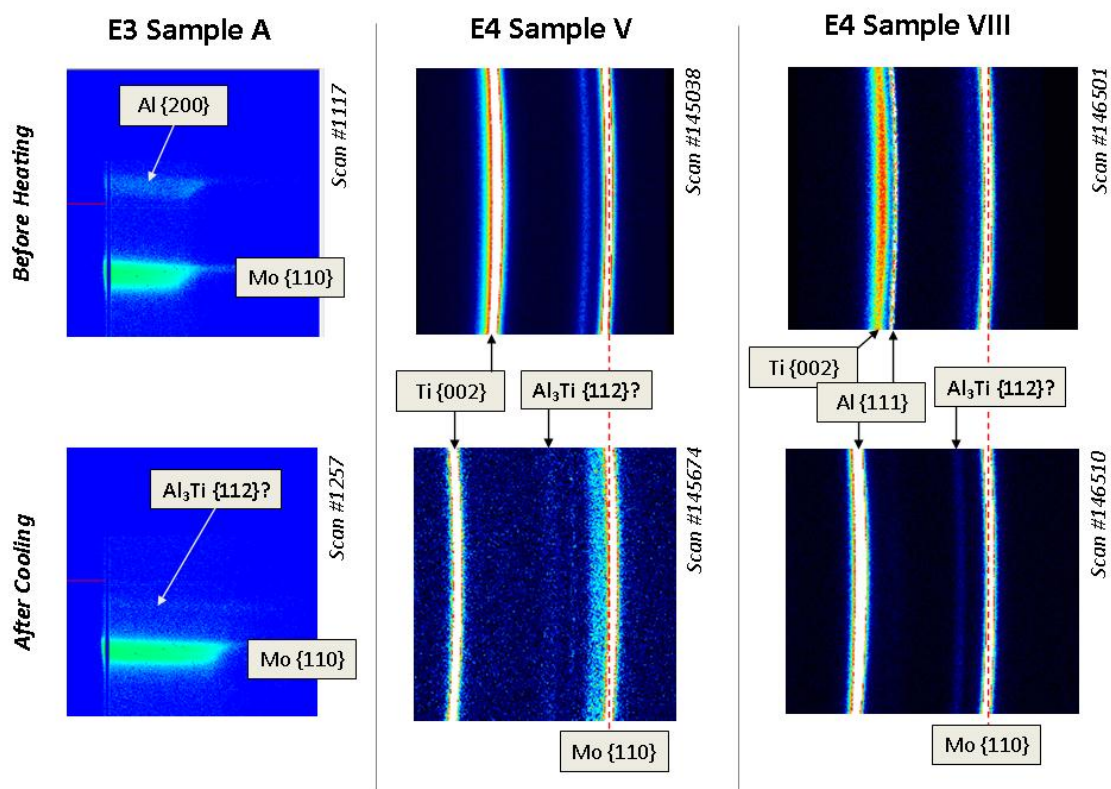


Figure 5-44 – Detector images indicating possible formation of  $\text{Al}_3\text{Ti}$ .  $\text{Ti } \{002\}$  peak shift in E4 sample V is suggested to arise from strain in the Ti interlayer as discussed following Figure 5-17. Behaviour of  $\text{Ti } \{002\}$  and  $\text{Al } \{111\}$  features from sample VIII are discussed in Figure 5-29.

The author believes that evidence for  $\text{Al}_3\text{Ti}$  is observed in the data from E3 sample A and E4 sample V. For E4 VIII there is more debate due to the proposed  $\text{Al}_3\text{Ti}$  feature arising at a slightly different  $2\theta$  location of  $15.9^\circ$ . Before discussing further, it is important to note that the expected peak position of exactly  $15.56^\circ$  is based on crystal structure data accessed through the ICSD, which is drawn from one particular study [154]. It is however fair to say that  $\text{Al}_3\text{Ti}$  is a less widely studied material than Al,  $\text{TiB}_2$  or indeed any of the other materials of relevance to this study, consequently the lattice parameters are less well-defined. Values of the fundamental lattice parameters, to our best knowledge of the literature, vary significantly:

This work [154]:  $a=3.852\text{\AA}$ ,  $c=8.584\text{\AA}$

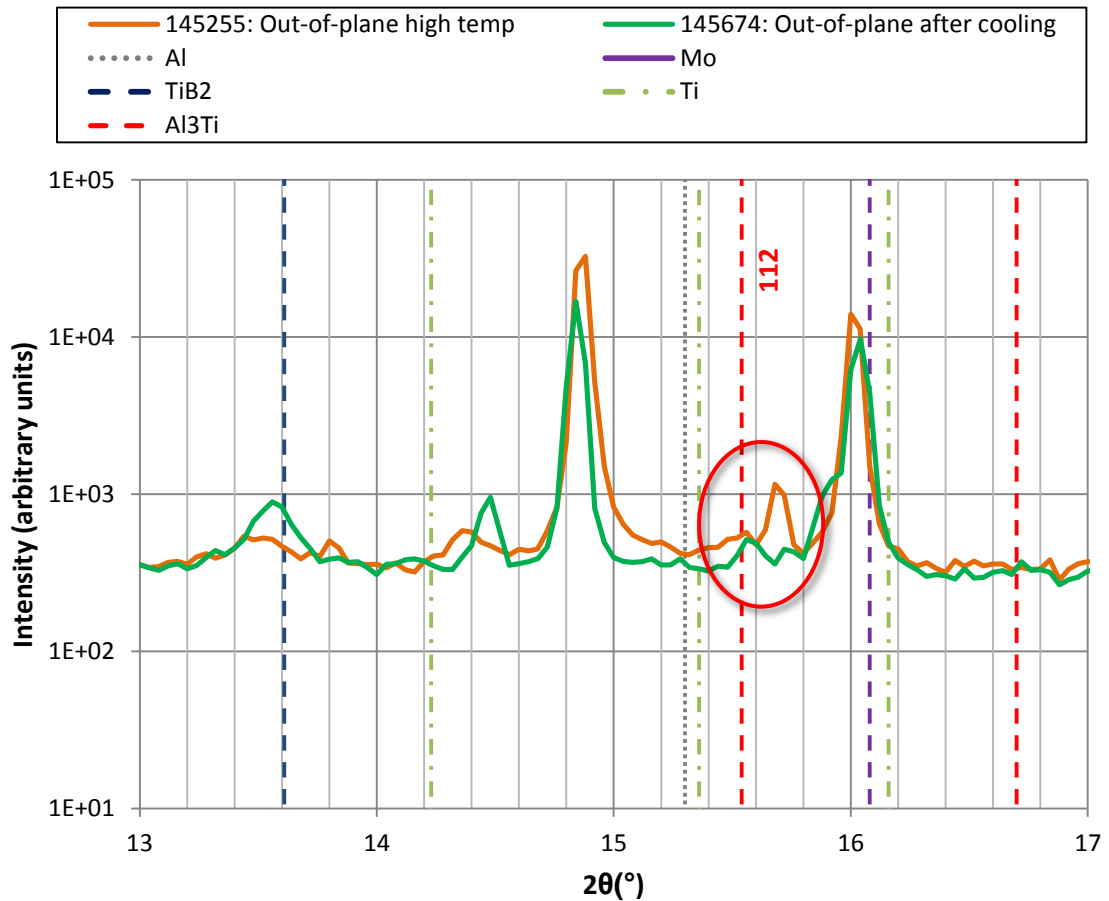
Smaller unit cell [155]:  $a=3.836\text{\AA}$ ,  $c=8.579\text{\AA}$

Larger unit cell [156]:  $a=3.863\text{\AA}$ ,  $c=8.587\text{\AA}$

The variance between upper and lower bounds (a spread of approximately  $0.03\text{\AA}$ ) would result in a shift in  $2\theta$  of approximately  $0.7^\circ$  (at  $19.9\text{keV}$ ). Applying this to the current work, it is apparent that any feature between  $2\theta = 15.3^\circ$  and  $15.9^\circ$  *could* be attributable to  $\text{Al}_3\text{Ti}$   $\{112\}$ . Separately from this, modelling studies have suggested that significant **strain** may be present in the transitional  $\text{Al}_3\text{Ti}$  structure between  $\text{TiB}_2$  and Al [157], [158] which may *also* result in a peak shift; indeed one which may *further* increase the spread in  $2\theta$ . Thus, if the feature in question from E4 sample VIII does indeed arise from  $\text{Al}_3\text{Ti}$ , it indicates that it has formed with an altered crystal structure, possibly influenced by strain. The  $15.9^\circ$  position suggests a *contraction* of the  $\{112\}$  spacing; this may be balanced by an *expansion* along the crystallographic directions parallel to the  $\{112\}$ , i.e. along the interface with  $\text{TiB}_2$  and Al. This may be an indication of the behaviour of the  $\text{Al}_3\text{Ti}$  as ‘adhesive’, straining so as to facilitate the orientation relationship between  $\text{Al}/\text{Al}_3\text{Ti}/\text{TiB}_2$ . This accords with observations from the literature (discussed in 1.7.2) that the  $\text{Al}_3\text{Ti}$  layer is under tensile strain. It is necessary to note that the proposed  $\text{Al}_3\text{Ti}$  in E3 is not *necessarily* interfacial. While it is reasonable to suggest that available Ti would likely be concentrated close to the  $\text{TiB}_2$  surface, there remains the possibility that  $\text{Al}_3\text{Ti}$  may have formed as discrete particles within the body of the Al layer, rather than adjacent to this surface. The fact that the  $\text{TiB}_2$  substrate is not (001) orientated means there is perhaps less propensity for  $\text{Al}_3\text{Ti}$  to be associated with this surface.

Contrastingly, in E4, it is highly likely that the  $\text{Al}_3\text{Ti}$  resides at the interface, owing to the scattering geometry in which the features appear. This also means it would likely have more propensity to exhibit strain. As noted in the introduction,  $\text{Al}_3\text{Ti}$   $\{112\}$  is a *non-equilibrium* face of the aluminide which is suggested to be stabilised by the boride [55]; this renders it even more likely that the formation occurs at the  $\text{Al}/\text{TiB}_2$  interface. Of course, the rapid solidification employed for sample VIII is likely to have had a dominant effect on the microstructure generation on cooling, and would also influence the final structure of  $\text{Al}_3\text{Ti}$  in the sample. Further work is necessary to discern the extent of the influence of the suggested nucleation mechanism versus the external parameters, such as cooling rate.

It is also interesting to note that  $\text{Al}_3\text{Ti}$  peak formation occurs *before* the maximum temperature in the scans is reached. This was observed during experiments on sample V, and is shown in Figure 5-45, presenting a scan (145255) which was performed while the sample was at high temperature ( $\sim 750^\circ\text{C}$ ). A peak is clearly visible at a  $2\theta$  location in close proximity to that of the identified  $\text{Al}_3\text{Ti}$  feature in the cooled structure (scan 145674).



**Figure 5-45 – Scans from sample V comparing post-cooled structure with morphology at high temperature ( $\sim 750^\circ\text{C}$ ). Highlights area around the  $\text{Al}_3\text{Ti}$  {112} peak. Scan (145255) shows features present in this region at high temperature.**

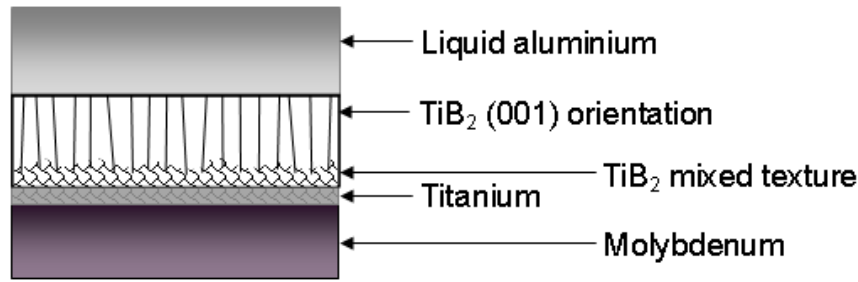
#### 5.4 Conclusions on the formation of $\text{Al}_3\text{Ti}$ in the system

Taking all observations from this chapter into account, it is reasonable to suggest that the features observed in Figure 5-44 indeed arise from  $\text{Al}_3\text{Ti}$ . Figure 5-45 indicates that the material appears which has formed in the sample while Al is in the liquid state, an effect which was also observed by Iqbal [73]. Referring back to the microscopy in Figure 5-33 and Figure 5-34, the 'blisters' show both Al and Ti content. The Al signal in the blisters is relatively weak, suggesting that if  $\text{Al}_3\text{Ti}$  is present, it is only in small quantities. This is supported by the observation that the  $\text{Al}_3\text{Ti}$  diffraction features in all experiments are quite weakly scattering, indicating a small quantity of material.

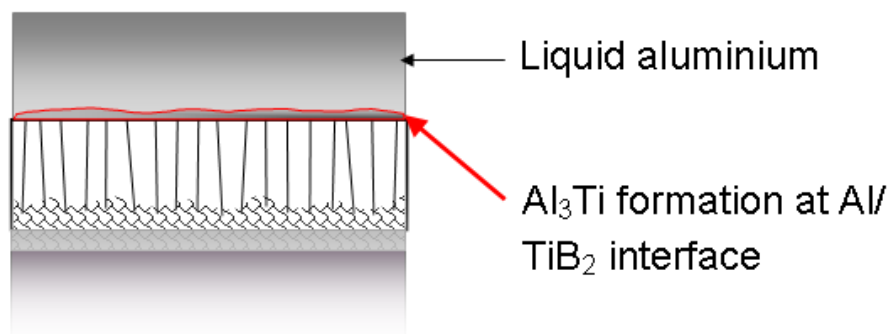
It is fair to qualify that the indications of  $\text{Al}_3\text{Ti}$  are not totally conclusive, but certainly add to the weight of evidence supporting the proposed mechanism for Al nucleation. By way of conclusion, the following graphic in Figure 5-46 summarises the mechanism leading to the formation of  $\text{Al}_3\text{Ti}$  in the samples. In Figure 5-46a, the complete sample is shown (note that the schematic representation of sample VIII is used throughout the graphic) in the scenario that the Al layer has fully transitioned to the liquid state.  $\text{Al}_3\text{Ti}$  forms at the Al/ $\text{TiB}_2$  interface while the Al remains liquid, as shown in Figure 5-46b. On cooling of the system, this interfacial  $\text{Al}_3\text{Ti}$ , with a  $\{112\}$  orientation parallel to the  $\text{TiB}_2$  (001) surface, allows Al to crystallise with  $\{111\}$  planes parallel to the interface. In the specific case of sample VIII, this results in a final morphology with a strong  $\{111\}$  texture; however, due to the combination of a) an imperfect  $\text{TiB}_2$  substrate texture and b) the quench cooling, crystallites also exist at a variety of orientations; the strong texture is likely concentrated towards the centre of the sample. Figure 5-46c indicates this. The data from sample VIII also suggests a significant residual **strain** exists in the  $\text{Al}_3\text{Ti}$  layer. Comparing this to the indications of  $\text{Al}_3\text{Ti}$  from samples A and V suggests that the strain in sample VIII may arise primarily due to the quench cooling; however, it is notable that a degree of strain is expected in the structure to facilitate the transition between the crystal lattices of Al and  $\text{TiB}_2$ .

Enriched Ti content in the E4 samples, indicated by the strength of peaks attributed to this material, clearly has implications for the suggested formation of  $\text{Al}_3\text{Ti}$ . Assuming a higher Ti content implies that the composition of the 'melt', i.e. the liquid aluminium on the sample surface, likely lies in a region of the phase diagram where the formation of  $\text{Al}_3\text{Ti}$  is thermodynamically favourable. This would support the assertion that the features detailed in the preceding section do indeed arise from  $\text{Al}_3\text{Ti}$ . Thus, while the data cannot be used to support the assertion that  $\text{Al}_3\text{Ti}$  will form even at hypoperitectic concentrations, it does indicate that there is a proclivity for this compound to form in this material system. Indeed, the actual peritectic concentration is so low in Al-Ti (0.65%at) that it is fair to suggest that, for a given 'melt', a Ti content in excess of this may exist almost inevitably, resulting in the appearance of  $\text{Al}_3\text{Ti}$  even at supposedly hypoperitectic compositions.

a) *Aluminium in liquid state*



b) *At high temperature (~750°C)*



c) *Solidified structure and orientation relationship*

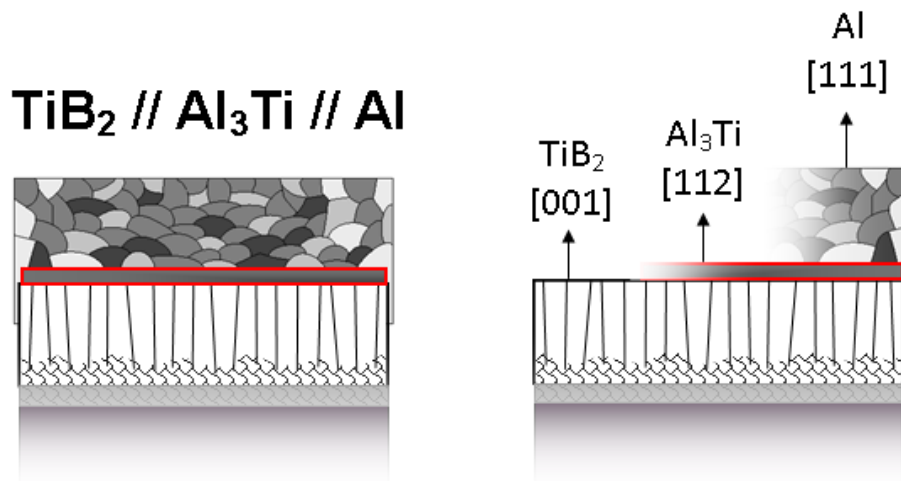


Figure 5-46 – Proposal for the formation of  $\text{Al}_3\text{Ti}$  in the experimental samples, using sample VIII as a schematic case. a) shows the original, sputter-deposited Al layer transitioning to the liquid state on heating. b)  $\text{Al}_3\text{Ti}$  forms while at the interface between liquid Al and  $\text{TiB}_2$  substrate. c) shows the suggested structure on cooling; i.e.  $\text{Al}_3\text{Ti}$  as an interfacial layer between  $\text{TiB}_2$  substrate and solidified Al crystal, with orientation relationship  $\text{TiB}_2 (001) // \text{Al}_3\text{Ti} \{112\} // \text{Al} \{111\}$ , as suggested by out-of-plane scattering data.

## 6 Conclusions

This section briefly summarises the preceding work. Section 6.1 will assess the project in terms of its feasibility for investigating Al/substrate interfaces. Section 6.2 presents a breakdown of the important outcomes. Finally, section 6.3 will discuss the potential for future work based on the results achieved and the challenges identified during experiments and analysis.

### 6.1 Feasibility study

The primary objective for this project was to assess the feasibility of using novel X-ray scattering techniques to probe the interaction at solid ( $\text{Al}_2\text{O}_3$  or  $\text{TiB}_2$ ) / liquid (Al) interfaces, with regard to heterogeneous nucleation. The results presented are an excellent demonstration that the methods are viable and produce useful data. The work has however proved challenging, and these achievements have only been possible through significant preparatory work and the development of novel sample preparation techniques.

The surface scattering techniques used in this project are usually applied to meticulously prepared, exceptionally clean samples.. Surfaces exhibit very little roughness, and in many cases are atomically flat. This however is not a good representation of *real* scenarios; thus, the great challenge for this work was to apply the techniques to engineering systems (where atomic flatness is unrealistic). Aluminium was chosen due to its great importance in engineering and industry. It is however highly reactive (leading to oxidation effects which complicated the results) and has a reasonably high melting point compared to, for example, tin or gallium; these aspects presented difficulties both in running experiments and analysing the resulting data.

Significant work was undertaken to minimise surface roughness and maximise surface cleanliness in sample preparation, as these were deemed essential aspects for successful scattering experiments. The methodology led to the collection of a range of interesting, practical data, resulting in both quantitative

values and qualitative descriptions of mechanisms pertaining to nucleation and growth.

Using a single crystal  $\text{Al}_2\text{O}_3$  substrate was an important first step. The large 'window' of undercooling in the  $\text{Al}/\text{Al}_2\text{O}_3$  system was critical for an initial study. Using a single crystal permits the use of techniques such as CTR analysis; this was crucial in the attempt to marry more typical surface diffraction experiments to the study of aluminium nucleation. For the  $\text{Al}/\text{TiB}_2$  system, feasibility was dependent on the preparation of appropriate  $\text{TiB}_2$  samples. Achieving the desired (001) orientation in the samples proved challenging. Due to the importance of the  $\text{TiB}_2$  (001) face to Al nucleation, this was a critical aspect of the experiment. The in-situ heating plus sputter-deposition method proved successful in generating strongly texture  $\text{TiB}_2$  substrates, and this is a most encouraging outcome of the project.

Temperature control was another major challenge in the project. The sample heaters used at I07 and ID03 were adequate for the most part, but did not offer the required degree of temperature stability necessary to study the undercooling in  $\text{Al}/\text{TiB}_2$ , which is expected to be less than 1K. The heater developed in-house *did* exhibit the desired stability, but could not be modified in time for use in later experiments. The results certainly demonstrate that the study was *feasible* using existing beamline equipment; however, temperature control would be perhaps the most pressing element to improve for further investigation; the perceived 'next step' would be to use the heater device in combination with  $\text{Al}/\text{TiB}_2$  samples.

## 6.2 Key outcomes

Here the outcomes of the project are reviewed against the aims defined in 1.10 and reiterated at the beginning of chapter 3.

Measurement of the **undercooling** required for nucleation of Al crystal on a specific crystal plane of a substrate has been one of the major achievements of



the project. This was achieved through the observation of characteristic Al diffraction features.  $\Delta T$  values of 88°C and 66°C were recorded for Al on  $\text{Al}_2\text{O}_3$  (001). These compare favourably with values from the literature; however, in this work, undercooling is recorded against a specific crystal plane; this represents a great benefit of the methods used in this project compared with alternative techniques such as thermal analysis. Temperature resolution improved progressively over the course of the project, from  $\pm 11^\circ\text{C}$  initially to  $\pm 0.05^\circ\text{C}$  in later work.

The collection of in-plane and out-of-plane scattering data has allowed identification of the **orientation relationships** that develop on cooling with a high degree of confidence. Al on  $\text{Al}_2\text{O}_3$  exhibited a strong  $\text{Al}_2\text{O}_3$  (001) // Al (111) relationship. For Al on  $\text{TiB}_2$ , a detailed study of the behaviour of individual Al features revealed information about the resulting morphology in the Al layer. Evidence for  $\text{Al}_3\text{Ti}$  was observed; consequently this led to the identification of the  $\text{TiB}_2$  (001) //  $\text{Al}_3\text{Ti}$  {112} // Al {111} orientation relationship predicted by theoretical and experimental studies of the system.

X-ray diffraction is highly sensitive in terms of spatial resolution allowing **thermal expansion** to be identified to a fine degree. The movement of scattering features in reciprocal space is very apparent, easily identified and measured using detector images and/or scattering data, yet these correspond to minute translations and movements in real space. This permits a kind of ‘amplified’ view on the behaviour of the atomic-scale structures within the sample materials. The measured thermal expansion in Al compares favourably with theoretical values.

The spatial resolution of the techniques also allows **strain** to be identified. Solidified Al on  $\text{Al}_2\text{O}_3$  showed strong indications of **non-uniform strain** along the  $\langle 111 \rangle$  direction near the interface. Subsequent CTR analysis gave indications as to how the crystal lattice accommodates this strain, suggesting the existence of a **transitional layer** between  $\text{Al}_2\text{O}_3$  (001) and Al (111).

CTR analysis proved challenging but ultimately has provided some of the most interesting results. The **transitional layer** is intriguing for two reasons. Firstly, it accords with indications from literature that nucleation may be preceded by the growth of a “*psuedomorphic*” layer. Secondly; ordering in the liquid state is heavily suggested to be confined to material just adjacent to the crystal surface, and, in terms of the layered structures, exhibit a transition from ‘crystal-like’ to ‘liquid-like’. The proposed **transitional layer** exhibits a similar transition from ‘Al<sub>2</sub>O<sub>3</sub>-like’ to ‘Al-like’.

The work on the Al/TiB<sub>2</sub> system is unique in that it directly inspects the interface between the two materials. This is first time that such targeted investigation has been attempted. The formation of **Al<sub>3</sub>Ti** is evidenced and suggested to be present as a strained layer between the TiB<sub>2</sub> substrate and solidifying Al.

### 6.3 Future Work

Perhaps the most important aspect in considering any future work is the multi-disciplinary nature of this project. The study has combined expertise from engineering, physics, and chemistry; requiring a working knowledge of many complex principles and specialised techniques. Further work must continue to respect this.

There is great potential for the extension of this project into a more generic study of nucleation. As suggested, a good first step would be to attempt to use the heater device with Al/TiB<sub>2</sub> samples. The same methods could be also applied to other inoculant/melt systems and materials. It would perhaps be sensible to initially investigate non-oxidising systems such as gold, to reduce the complexity of the scattering patterns and allow more straightforward peak indexing; however, this would arguably be less relevant to industrial systems.

CTR analysis would certainly merit further investigation. The surface sensitivity of the technique means it is highly appropriate for investigating adsorption or similar processes which modify the interface between a nucleant and a

solidifying material. In identifying **transitional layers**, the results indicate the potential of the technique. Suggestions for future work include: collecting more rods, including those at symmetry-equivalent positions; increasing the resolution of data points; and maintaining isothermal conditions during collection. These factors would result in a high quality, consistent data set and thus permit greater confidence in the resulting structure determinations.

The use of a single crystal  $\text{TiB}_2$  substrate would represent a significant step in the development of this technique and would further increase the relevance of the studies to the industrial case. Sample preparation has been a major aspect of this project, to achieve a specific  $\text{TiB}_2$  (001) orientation, due to the importance of this plane in nucleation of Al. The preparation method used in this work successfully created samples with the appropriate orientation; however, these were of course polycrystalline samples exhibiting a strong (001) *texture*. With the available technology and facilities, this was the optimum approach to represent the interface between a  $\text{TiB}_2$  particle and the surrounding Al melt. A single crystal  $\text{TiB}_2$  substrate would permit greater control over the orientation, and allow the use of crystallographic techniques such as CTR analysis. This would offer the opportunity to probe the atomic structure and strain at the Al/ $\text{TiB}_2$  interface in unprecedented detail, and help in assessing how this relates to the nucleation of crystalline Al from substrates.

Continued, cumulative development of the methods used in this project will permit increasingly more detailed investigations of the nucleation behaviour of metals against inoculants or other substrates of industrial importance. In the long term, it is hoped that this kind of study can lead to benefits for industry; in terms of understanding grain refinement behaviour and allowing study and selection of new refiner materials and alloy systems; and benefits to the scientific community, in increasing understanding of nucleation mechanisms and leading to enrichment of current nucleation theory.

## 7 References

- [1] AMC, “46th census of world casting production,” *Modern Casting*, no. December, pp. 25–29, 2012.
- [2] I. of C. M. Engineers, “The Global Castings Industry.” [Online]. Available: [http://www.icme.org.uk/about\\_castings.asp](http://www.icme.org.uk/about_castings.asp). [Accessed: 13-Oct-2013].
- [3] S. H. Oh, M. F. Chisholm, Y. Kauffmann, W. D. Kaplan, W. Luo, M. Rühle, and C. Scheu, “Oscillatory mass transport in vapor-liquid-solid growth of sapphire nanowires,” *Science*, vol. 330, no. 6003, pp. 489–93, Oct. 2010.
- [4] S. H. Oh and C. Scheu, “In-situ HRTEM Studies of Alumina-Aluminum Solid-Liquid Interfaces,” *Korean J. Electron Microsc. Spec.*, vol. 24, no. 1, pp. 19–24, 2006.
- [5] S. Lee and Y.-M. Kim, “Direct observation of in-plane ordering in the liquid at a liquid Al/ $\alpha$ -Al<sub>2</sub>O<sub>3</sub>( $\bar{1}10\bar{2}$ ) interface,” *Acta Mater.*, vol. 59, no. 4, pp. 1383–1388, Nov. 2010.
- [6] S. H. Oh, Y. Kauffmann, C. Scheu, W. D. Kaplan, and M. Rühle, “Ordered liquid aluminum at the interface with sapphire,” *Science*, vol. 310, no. 5748, pp. 661–3, Oct. 2005.
- [7] P. S. Mohanty and J. E. Gruzleski, “Mechanism of grain refinement in aluminium,” *Acta Metall. Mater.*, vol. 43, no. 5, pp. 2001–2012, 1995.
- [8] W. D. Callister and D. G. Rethwisch, *Materials Science and Engineering*, 8th ed. Wiley, 2011.
- [9] K. F. Kelton and A. L. Greer, *Nucleation in Condensed Matter*. Pergamon Materials Series, 2010.
- [10] J. Dantzig and M. Rappaz, *Solidification*. Lausanne: CRC Press, 2009.
- [11] D. Turnbull, “Formation of Crystal Nuclei in Liquid Metals,” *J. Appl. Phys.*, vol. 21, pp. 1022–1028, 1950.
- [12] W. Barchet, “The Validity of the Spherical Cap Approximation in Heterogeneous Nucleation,” *J. Atmos. Sci.*, vol. 26, pp. 112–114, 1969.
- [13] D. Turnbull, “Theory of catalysis of nucleation by surface patches,” *Acta Metall.*, vol. 1, pp. 8–14, 1953.
- [14] P. Schumacher, A. L. Greer, J. Worth, P. V Evans, M. A. Kearns, P. Fisher, and A. H. Green, “New studies of nucleation mechanisms in aluminium alloys: implications for grain refinement practice,” *Mater. Sci. Technol.*, vol. 14, no. May, pp. 394–404, 1998.

- [15] T. E. Quested and A. L. Greer, "Athermal heterogeneous nucleation of solidification," *Acta Mater.*, vol. 53, no. 9, pp. 2683–2692, May 2005.
- [16] A. L. Greer, A. M. Bunn, A. Tronche, P. Evans, and D. Bristow, "Modelling of inoculation of metallic melts: application to grain refinement of aluminium by Al-Ti-B," *Acta Mater.*, vol. 48, no. 11, pp. 2823–2835, 2000.
- [17] A. L. Greer, "Grain refinement of alloys by inoculation of melts," *Philos. Trans. R. Soc. A Math. Phys. Eng. Sci.*, vol. 361, no. 1804, pp. 479–495, Mar. 2003.
- [18] J. C. Fisher, D. Turnbull, and J. H. Hollomon, "Nucleation," *J. Appl. Phys.*, vol. 19, no. 8, pp. 775–784, 1948.
- [19] A. L. Greer and T. E. Quested, "Heterogeneous grain initiation in solidification," *Philos. Mag.*, vol. 86, no. 24, pp. 3665–3680, Aug. 2006.
- [20] T. E. Quested and A. L. Greer, "The effect of the size distribution of inoculant particles on as-cast grain size in aluminium alloys," *Acta Mater.*, vol. 52, no. 13, pp. 3859–3868, Aug. 2004.
- [21] D. Walton, "Nucleation of vapour deposits," *J. Chem. Phys.*, vol. 37, no. 10, p. 2182, 1962.
- [22] B. E. Sundquist, "On 'Nucleation catalysis in supercooled liquid tin,'" *Acta Metall.*, vol. 11, pp. 630–632, 1963.
- [23] B. Chalmers, *Principles of Solidification*. New York: John Wiley, 1964, pp. 77–83.
- [24] W. Kim and B. Cantor, "An adsorption model of the heterogeneous nucleation of solidification," *Acta Metall. Mater.*, vol. 42, no. 9, pp. 3115–3127, 1994.
- [25] B. Cantor, "Heterogeneous nucleation and adsorption," *Philos. Trans. R. Soc. A Math. Phys. Eng. Sci.*, vol. 361, no. 1804, pp. 409–417, Mar. 2003.
- [26] C. Ho and B. Cantor, "Heterogeneous nucleation of solidification of Si in Al-Si and Al-Si-P alloys," *Acta Metall. Mater.*, vol. 43, no. 8, 1995.
- [27] P. Schumacher and A. L. Greer, "High-resolution transmission electron microscopy of grain-refining particles in amorphous aluminum alloys," *Light Met.*, pp. 745–754, 1996.
- [28] B. Vonnegut and D. Turnbull, "Nucleation Catalysis," *Ind. Eng. Chem.*, vol. 44, no. 6, pp. 1292–1298, Jun. 1952.
- [29] G. Tóth, G. Tegze, T. Pusztai, and L. Gránásy, "Heterogeneous Crystal Nucleation: The Effect of Lattice Mismatch," *Phys. Rev. Lett.*, vol. 108, no. 2, pp. 1–4, Jan. 2012.

- [30] B. Cantor, "Impurity effects on heterogeneous nucleation," *Mater. Sci. Eng. A*, 1997.
- [31] D. Zhang and B. Cantor, "Effect of Ge on the heterogeneous nucleation of Pb solidification by Al," *J. Cryst. Growth*, vol. 104, 1990.
- [32] Z. Fan, "An Epitaxial Model for Heterogeneous Nucleation on Potent Substrates," *Metall. Mater. Trans. A*, vol. 44, no. March, pp. 1409–1418, 2013.
- [33] W. J. Huisman, J. F. Peters, M. J. Zwanenburg, S. A. de Vries, T. E. Derry, D. Abernathy, and J. F. van der Veen, "Layering of a liquid metal in contact with a hard wall," *Nature*, vol. 111, no. November, pp. 109–129, 1996.
- [34] W. D. Kaplan and Y. Kauffmann, "Structural Order in Liquids Induced By Interfaces With Crystals," *Annu. Rev. Mater. Res.*, vol. 36, no. 1, pp. 1–48, Aug. 2006.
- [35] T. U. Schüllli, R. Daudin, G. Renaud, A. Vaysset, O. Geaymond, and A. Pasturel, "Substrate-enhanced supercooling in AuSi eutectic droplets.," *Nature*, vol. 464, no. 7292, pp. 1174–7, Apr. 2010.
- [36] Y. Kauffmann, S. H. Oh, C. T. Koch, A. Hashibon, C. Scheu, M. Rühle, and W. D. Kaplan, "Quantitative analysis of layering and in-plane structural ordering at an alumina–aluminum solid–liquid interface," *Acta Mater.*, vol. 59, pp. 4378–4386, Apr. 2011.
- [37] A. L. Greer, "Supercool order," *Nat. Mater.*, vol. 5, no. January, pp. 13–14, 2006.
- [38] A. L. Greer, "Materials science: A cloak of liquidity.," *Nature*, vol. 464, no. 7292, pp. 1137–8, Apr. 2010.
- [39] S. E. Donnelly, R. C. Birtcher, C. W. Allen, I. Morrison, K. Furuya, M. Song, K. Mitsuishi, and U. Dahmen, "Ordering in a fluid inert gas confined by flat surfaces.," *Science*, vol. 296, no. 5567, pp. 507–10, Apr. 2002.
- [40] M. F. Reedijk, J. Arsic, F. Hollander, S. de Vries, and E. Vlieg, "Liquid Order at the Interface of KDP Crystals with Water: Evidence for Icelike Layers," *Phys. Rev. Lett.*, vol. 90, no. 6, pp. 1–4, Feb. 2003.
- [41] E. Vlieg and M. F. Reedijk, "Liquid Order at a Solid-liquid Interface," *ESRF website*, 2006. [Online]. Available: <http://www.esrf.eu/UsersAndScience/Publications/Highlights/2002/Surfaces/SIS1>.
- [42] J. Kang, J. Zhu, C. Curtis, D. Blake, G. Glatzmaier, Y.-H. Kim, and S.-H. Wei, "Atomically Abrupt Liquid-Oxide Interface Stabilized by Self-

- Regulated Interfacial Defects: The Case of Al/Al<sub>2</sub>O<sub>3</sub> Interfaces,” *Phys. Rev. Lett.*, vol. 108, no. 22, pp. 1–5, May 2012.
- [43] M. F. Reedijk, J. Arsic, F. de Theije, M. McBride, K. Peters, and E. Vlieg, “Structure of liquid Sn on Ge(111),” *Phys. Rev. B*, vol. 64, no. 3, pp. 5–8, Jun. 2001.
  - [44] W. J. Huisman, “Modelling the atomic density across a solid–liquid interface,” *Surf. Sci.*, vol. 402–404, no. 1, pp. 866–870, May 1998.
  - [45] A. Hashibon, “Atomistic study of structural correlations at a model solid/liquid-metal interface,” Ph.D Thesis, Technion - Israel Institute of Technology, Haifa, Israel, 2002.
  - [46] A. Hashibon, J. Adler, M. Finnis, and W. D. Kaplan, “Atomistic study of structural correlations at a liquid–solid interface,” *Comput. Mater. Sci.*, vol. 24, no. 4, pp. 443–452, Jul. 2002.
  - [47] A. Hashibon, J. Adler, M. Finnis, and W. D. Kaplan, “Ordering at Solid-Liquid Interfaces Between Dissimilar Materials,” *Interface Sci.*, vol. 9, no. 3–4, pp. 175–181, 2001.
  - [48] H. Men and Z. Fan, “Effects of lattice mismatch on interfacial structures of liquid and solidified Al in contact with hetero-phase substrates: MD simulations,” *IOP Conf. Ser. Mater. Sci. Eng.*, vol. 27, p. 012007, Jan. 2012.
  - [49] H. Reichert, O. Klein, H. Dosch, M. Denk, V. Honkimäki, T. Lippmann, and G. Reiter, “Observation of five-fold local symmetry in liquid lead,” *Nature*, vol. 408, no. 6814, pp. 839–41, Dec. 2000.
  - [50] E. O. Hall, “The Deformation and Ageing of Mild Steel: III Discussion of Results,” *Proc. Phys. Soc. Sect. B*, vol. 64, no. 9, pp. 747–753, Sep. 1951.
  - [51] B. J. McKay and P. Schumacher, “Heterogeneous Nucleation Mechanisms of TiB<sub>2</sub> Particles in Al Alloys,” *Shape Cast. John Campbell Symp. TMS*, pp. 155–164, 2005.
  - [52] D. McCartney, “Grain refining of aluminium and its alloys using inoculants,” *Int. Mater. Rev.*, vol. 34, no. 5, 1989.
  - [53] B. S. Murty, S. A. Kori, and M. Chakraborty, “Grain refinement of aluminium and its alloys by heterogeneous nucleation and alloying,” *Int. Mater. Rev.*, vol. 47, no. 1, pp. 3–29, Feb. 2002.
  - [54] A. L. Greer, P. S. Cooper, M. W. Meredith, W. Schneider, P. Schumacher, J. A. Spittle, and A. Tronche, “Grain Refinement of Aluminium Alloys by Inoculation,” *Adv. Eng. Mater.*, vol. 5, no. 12, pp. 81–91, Feb. 2003.

- [55] T. E. Quested, "Understanding mechanisms of grain refinement of aluminium alloys by inoculation," *Mater. Sci. Technol.*, vol. 20, no. 11, pp. 1357–1369, Nov. 2004.
- [56] M. Guzowski and G. Sigworth, "The role of boron in the grain refinement of aluminum with titanium," *Met. Trans., A;(United States)*, vol. 18, no. April, pp. 603–619, 1987.
- [57] L. F. Mondolfo, "Grain Refinement in Castings and Welds," in *Grain Refinement in Castings and Welds*, G.J. Abbaschian and S.A. David (Eds.); Warrendale, PA: The Minerals, Metals & Materials Society (TMS), 1993.
- [58] J. Pearson and M. A. Kearns, "Optimisation of Grain Refiners in the Cast House Based on Recent Development Programmes," in *5th Australasian-Asian Pacific Conference on Aluminium Cast House Technology*, Warrendale, PA: The Minerals, Metals & Materials Society (TMS) pp. 87–101, 1997.
- [59] M. Johnsson, L. Backerud, and G. Sigworth, "Study of the mechanism of grain refinement of aluminum after additions of Ti- and B-containing master alloys," *Met. Trans., A*, vol. 24, no. 2, pp. 481–491, 1993.
- [60] P. Schumacher and A. L. Greer, "Heterogeneously nucleated  $\alpha$ -Al in amorphous aluminium alloys," *Mater. Sci. Eng. A*, vol. 178, no. 1–2, pp. 309–313, Apr. 1994.
- [61] P. Schumacher and A. L. Greer, "Enhanced heterogeneous nucleation of  $\alpha$ -Al in amorphous aluminium alloys," *Mater. Sci. Eng. A*, vol. 181–182, pp. 1335–1339, May 1994.
- [62] M. Easton and D. H. St John, "Grain Refinement of Aluminum Alloys : Part I. The Nucleant and Solute Paradigms — A Review of the Literature," *Metall. Mater. Trans. A*, vol. 30A, no. June, pp. 1613–1623, 1999.
- [63] M. Easton and D. H. St John, "Grain Refinement of Aluminum Alloys : Part II. Confirmation of, and a Mechanism for, the Solute Paradigm," *Metall. Mater. Trans. A*, vol. 30, no. June, pp. 1625–1633, 1999.
- [64] A. Cibula, "The Grain Refinement of Aluminum Alloy Castings by Additions of Titanium and Boron," *J. Inst. Met.*, vol. 80, pp. 1–16, 1951.
- [65] P. Schumacher and B. J. McKay, "TEM investigation of heterogeneous nucleation mechanisms in Al–Si alloys," *J. Non. Cryst. Solids*, vol. 317, no. 1–2, pp. 123–128, Mar. 2003.
- [66] F. A. Crossley and L. F. Mondolfo, "Mechanism of grain refinement in aluminum alloys," *Trans. AIME*, vol. 191, pp. 1143–1148, 1951.



- [67] J. A. Marcantonio and L. F. Mondolfo, "Grain refinement in aluminum alloyed with Ti and some other elements," *Met. Trans., A*, vol. 2, pp. 465–471, 1971.
- [68] L. Backerud and S. Yidong, "Grain-refining mechanisms in aluminium as a result of additions of titanium and boron, Part 1," *Aluminium*, vol. 67, pp. 780–785, 1991.
- [69] L. Backerud and S. Yidong, "Grain-refining mechanisms in aluminium as a result of additions of titanium and boron, Part 2," *Aluminium*, vol. 67, pp. 910–915, 1991.
- [70] G. P. Jones, "New Ideas on the Mechanism of Heterogeneous Nucleation in Liquid Aluminium," *NPL Report, DMA (A)*, vol. 19. National Physical Laboratory, Teddington, 1983.
- [71] D. H. St John, M. Qian, and P. Cao, "The Interdependence Theory: The relationship between grain formation and nucleant selection," *Acta Mater.*, vol. 59, no. 12, pp. 4907–4921, Jul. 2011.
- [72] B. L. Bramfitt, "The effect of carbide and nitride additions on the heterogeneous nucleation behaviour of liquid iron," *Metall. Trans.*, vol. 1, no. 7, pp. 1987–1995, 1970.
- [73] N. Iqbal, N. H. van Dijk, S. Offerman, M. Moret, L. Katgerman, and G. Kearley, "Real-time observation of grain nucleation and growth during solidification of aluminium alloys," *Acta Mater.*, vol. 53, no. 10, pp. 2875–2880, Jun. 2005.
- [74] N. Iqbal, N. H. van Dijk, S. Offerman, N. Geerlofs, M. Moret, L. Katgerman, and G. Kearley, "In situ investigation of the crystallization kinetics and the mechanism of grain refinement in aluminum alloys," *Mater. Sci. Eng. A*, vol. 416, no. 1–2, pp. 18–32, Jan. 2006.
- [75] N. Iqbal, N. H. van Dijk, S. Offerman, M. Moret, L. Katgerman, and G. Kearley, "Nucleation kinetics during the solidification of aluminum alloys," *J. Non. Cryst. Solids*, vol. 353, no. 32–40, pp. 3640–3643, Oct. 2007.
- [76] N. Iqbal, "Experimental study of ordering kinetics in aluminum alloys during solidification," *Acta Mater.*, vol. 51, no. 15, pp. 4497–4504, Sep. 2003.
- [77] N. Iqbal, N. H. van Dijk, T. Hansen, L. Katgerman, and G. J. Kearley, "The role of solute titanium and TiB<sub>2</sub> particles in the liquid–solid phase transformation of aluminum alloys," *Mater. Sci. Eng. A*, vol. 386, no. 1–2, pp. 20–26, Nov. 2004.
- [78] N. Iqbal, "Solidification: real-time investigation of grain nucleation and growth during liquid to solid phase transformation of aluminum alloys," Ph.D Thesis, TU Delft, Delft, Netherlands, 2005.

- [79] A. M. Bunn, P. Schumacher, M. A. Kearns, C. B. Boothroyd, and A. L. Greer, "Grain refinement by Al–Ti–B alloys in aluminium melts: a study of the mechanisms of poisoning by zirconium," *Mater. Sci. Technol.*, vol. 15, no. October, pp. 1115–1123, 1999.
- [80] B. D. Cullity and S. R. Stock, *Elements of X-Ray Diffraction*. Prentice Hall, 2001.
- [81] J. Als-Nielsen and D. McMorrow, *Elements of Modern X-Ray Physics*. John Wiley & Sons, 2001.
- [82] "Matter: Geometry of Diffraction." [Online]. Available: <http://www.matter.org.uk/diffraction/geometry/default.htm>.
- [83] E. Vlieg, "Integrated Intensities Using a Six-Circle Surface X-ray Diffractometer," *J. Appl. Crystallogr.*, vol. 30, no. 5, pp. 532–543, Oct. 1997.
- [84] I. Robinson, "Crystal truncation rods and surface roughness," *Phys. Rev. B*, vol. 33, no. 6, pp. 3830–3836, Mar. 1986.
- [85] T. P. Trainor, "Surface and Interface X-Ray Scattering," *1st Annual SSRL Workshop on Synchrotron X-ray Scattering Techniques in Materials and Environmental Sciences*, 2006. [Online]. Available: [http://www-ssrl.slac.stanford.edu/conferences/workshops/scatter2006/talks/trainor\\_in terface\\_scattering\\_ssrl\\_wkshop.pdf](http://www-ssrl.slac.stanford.edu/conferences/workshops/scatter2006/talks/trainor_in terface_scattering_ssrl_wkshop.pdf).
- [86] E. Vlieg, "ROD: a program for surface X-ray crystallography," *J. Appl. Crystallogr.*, vol. 33, no. 2, pp. 401–405, Apr. 2000.
- [87] O. Shpyrko, R. Streitel, V. S. K. Balagurusamy, A. Grigoriev, M. Deutsch, B. Ocko, M. Meron, B. Lin, and P. S. Pershan, "Surface crystallization in a liquid AuSi alloy," *Science*, vol. 313, no. 5783, pp. 77–80, Jul. 2006.
- [88] P. Srirangam, M. J. Kramer, and S. Shankar, "Effect of strontium on liquid structure of Al–Si hypoeutectic alloys using high-energy X-ray diffraction," *Acta Mater.*, vol. 59, no. 2, pp. 503–513, Jan. 2011.
- [89] O. Magnussen, B. Ocko, M. Regan, K. Penanen, P. S. Pershan, and M. Deutsch, "X-ray reflectivity measurements of surface layering in liquid mercury," *Phys. Rev. Lett.*, vol. 74, no. 22, pp. 4444–4447, 1995.
- [90] F. Grey, R. Feidenhans'l, J. Pedersen, M. Nielsen, and R. Johnson, "Pb/Ge (111) 1 x 1: An anisotropic two-dimensional liquid.," *Phys. Rev. B. Condens. Matter*, vol. 41, no. 13, p. 9519, 1990.
- [91] S. Sinha, "Surface structure reflectometry with X-rays," *Curr. Opin. Solid State Mater. Sci.*, vol. 1, no. 5, pp. 645–652, Oct. 1996.

- [92] H. Mo, G. Evmenenko, S. Kewalramani, K. Kim, S. N. Ehrlich, and P. Dutta, "Observation of surface layering in a nonmetallic liquid.," *Phys. Rev. Lett.*, vol. 96, no. 9, p. 096107, Mar. 2006.
- [93] P. S. Pershan, "X-Rays as probe of liquid interfaces," *Physica A*, vol. 172, no. 1–2, pp. 17–19, 1991.
- [94] O. Magnussen, M. Regan, E. Kawamoto, B. Ocko, P. S. Pershan, N. Maskil, M. Deutsch, S. Lee, K. Penanen, and L. Berman, "X-ray reflectivity studies of the surface structure of liquid metals," *Phys. B Condens. Matter*, vol. 221, no. 1–4, pp. 257–260, 1996.
- [95] H. Chen, "Surface/interface X-ray diffraction," in *Materials Science Forum*, 1995, vol. 189, no. 2, pp. 95–106.
- [96] C.-J. Yu, A. Richter, A. Datta, M. Durbin, and P. Dutta, "Observation of molecular layering in thin liquid films using X-ray reflectivity," *Phys. Rev. Lett.*, vol. 82, no. 11, pp. 2326–2329, Mar. 1999.
- [97] W. J. Huisman, J. F. Peters, J. W. Derks, H. G. Ficke, D. L. Abernathy, and J. F. van der Veen, "A new X-ray diffraction method for structural investigations of solid-liquid interfaces," *Rev. Sci. Instrum.*, vol. 68, no. 11, p. 4169, 1997.
- [98] P. Fenter and N. C. Sturchio, "Mineral–water interfacial structures revealed by synchrotron X-ray scattering," *Prog. Surf. Sci.*, vol. 77, no. 5–8, pp. 171–258, Jan. 2004.
- [99] S. Otani and Y. Ishizawa, "Preparation of TiB<sub>2</sub> single crystals by the floating zone method," *J. Cryst. Growth*, vol. 140, no. 3–4, pp. 451–453, 1994.
- [100] M. J. Uttormark, J. W. Zanter, and J. H. Perepezko, "Repeated nucleation in an undercooled aluminum droplet," *J. Cryst. Growth*, vol. 177, no. 3–4, pp. 258–264, Jun. 1997.
- [101] B. A. Mueller and J. H. Perepezko, "The undercooling of aluminium," *Met. Trans., A*, vol. 18, no. 13, pp. 1143–1150, 1987.
- [102] H.-T. Li, Y. Wang, M. Xia, Y. Zuo, and Z. Fan, "Harnessing Oxides in Liquid Metals and Alloys," in *John Hunt International Symposium*, Z. Fan and I. Stone (Eds.); Brunel University Press, pp. 93–110, 2011.
- [103] Y. Wang, H.-T. Li, and Z. Fan, "Oxidation of Aluminium Alloy Melts and Inoculation by Oxide Particles," *Trans. Indian Inst. Met.*, vol. 65, no. 6, pp. 653–661, Oct. 2012.
- [104] Diamond Light Source, "I07 - Surface and Interface Diffraction." [Online]. Available: <http://www.diamond.ac.uk/Home/Beamlines/I07.html>.

- [105] ESRF, "ID03 - Surface Diffraction Beamline." [Online]. Available: <http://www.esrf.eu/UsersAndScience/Experiments/StructMaterials/ID03>.
- [106] E. Vlieg, "A (2+3)-Type Surface Diffractometer: Mergence of the z-Axis and (2+2)-Type Geometries," *J. Appl. Crystallogr.*, vol. 31, no. 2, pp. 198–203, Apr. 1998.
- [107] M. Gautier, J. Duraud, and L. Pham Van, "Influence of the Al<sub>2</sub>O<sub>3</sub> (0001) surface reconstruction on the Cu/Al<sub>2</sub>O<sub>3</sub> interface," *Surf. Sci. Lett.*, vol. 249, no. 1–3, pp. L327–L332, 1991.
- [108] B. Qi, B. Agnarsson, K. Jonsson, S. Olafsson, and H. P. Gislason, "Characterisation of high-temperature annealing effects on  $\alpha$ -Al<sub>2</sub>O<sub>3</sub> (0001) substrates," *J. Phys. Conf. Ser.*, vol. 100, no. 4, p. 042020, Mar. 2008.
- [109] P. R. Ribič and G. Bratina, "Behavior of the (0001) surface of sapphire upon high-temperature annealing," *Surf. Sci.*, vol. 601, no. 1, pp. 44–49, Jan. 2007.
- [110] F. Cuccureddu, S. Murphy, I. V. Shvets, M. Porcu, H. W. Zandbergen, N. S. Sidorov, and S. I. Bozhko, "Surface morphology of c-plane sapphire ( $\alpha$ -alumina) produced by high temperature anneal," *Surf. Sci.*, vol. 604, no. 15–16, pp. 1294–1299, Aug. 2010.
- [111] W. Ip, M. Kucharski, and J. M. Toguri, "Wetting Behaviour of Aluminium and Aluminium Alloys on Al<sub>2</sub>O<sub>3</sub> and CaO," *J. Mater. Sci. Lett.*, vol. 12, pp. 1699–1702, 1993.
- [112] P. Shen, H. Fujii, T. Matsumoto, and K. Nogi, "Wetting of (0001)  $\alpha$ -Al<sub>2</sub>O<sub>3</sub> single crystals by molten Al," *J. Phys. Chem. B*, vol. 48, pp. 779–784, 2003.
- [113] A. Klintner, G. Mendozasuarez, and R. Drew, "Wetting of pure aluminum and selected alloys on polycrystalline alumina and sapphire," *Mater. Sci. Eng. A*, vol. 495, no. 1–2, pp. 147–152, Nov. 2008.
- [114] E. Rocha-Rangel, P. F. Becher, and E. Lara-Curzio, "Reactive-Wetting of Alumina by Molten Aluminum Alloys," *Mater. Sci. Forum*, vol. 442, pp. 97–102, 2003.
- [115] P. Patnaik, *Handbook of Inorganic Chemicals*. New York: McGraw-Hill, 2003.
- [116] J.R. Calvert and R.A. Farrar, *An Engineering Data Book*. Palgrave, 1999.
- [117] M. Berger, E. Coronel, and E. Olsson, "Microstructure of d.c. magnetron sputtered TiB<sub>2</sub> coatings," *Surf. Coatings Technol.*, vol. 185, no. 2–3, pp. 240–244, Jul. 2004.

- [118] M. Berger, M. Larsson, and S. Hogmark, "Evaluation of magnetron-sputtered TiB<sub>2</sub> intended for tribological applications," *Surf. Coatings Technol.*, vol. 124, pp. 253–261, 2000.
- [119] M. Berger, L. Karlsson, M. Larsson, and S. Hogmark, "Low stress TiB<sub>2</sub> coatings with improved tribological properties," *Methods*, vol. 401, pp. 179–186, 2001.
- [120] T. Shikama, Y. Sakai, M. Fukutomi, and M. Okada, "Deposition of TiB<sub>2</sub> films by a co-sputtering method," *Thin Solid Films*, vol. 156, pp. 287–293, 1988.
- [121] P. Losbichler and C. Mitterer, "Non-reactively sputtered TiN and TiB<sub>2</sub> films: influence of activation energy on film growth," *Surf. Coatings Technol.*, vol. 97, pp. 567–573, 1997.
- [122] M. Berger, "Development and Tribological Characterisation of Magnetron Sputtered TiB<sub>2</sub> and Cr/CrN Coatings," Ph.D Thesis, University of Uppsala, Uppsala, Finland, 2001.
- [123] P. Sricharoenchai, N. Panich, P. Visuttiptikul, and P. Wangyao, "Effect of Substrate Temperature, Biasing and Sputter Cleaning on the Structure and Properties of Nanostructured TiB<sub>2</sub> Coatings on High Speed Steel," *Mater. Trans.*, vol. 51, no. 2, pp. 246–252, 2010.
- [124] Aremco, "High Temperature Ceramic & Graphite Adhesives," *Aremco*, 2013. [Online]. Available: [http://www.aremco.com/wp-content/uploads/2010/11/A02\\_13.pdf](http://www.aremco.com/wp-content/uploads/2010/11/A02_13.pdf).
- [125] C. Neumann, E. Sondermann, F. Kargl, and A. Meyer, "Compact high-temperature shear-cell furnace for in-situ diffusion measurements," *J. Phys. Conf. Ser.*, vol. 327, p. 012052, Dec. 2011.
- [126] C. Boudias and D. Monceau, "CaRIne Crystallography 3.1." <http://pro.wanadoo.fr/carine.crystallography/>, <http://pro.wanadoo.fr/carine.crystallography/>, p. available at <http://pro.wanadoo.fr/carine.crystall>, 2011.
- [127] FIZ Karlsruhe, "Inorganic Crystal Structure Database," 2014. [Online]. Available: <http://icsd.cds.rsc.org/>.
- [128] D.-J. Wang and S.-T. Wu, "The influence of oxidation on the wettability of aluminum on sapphire," *Acta Metall. Mater.*, vol. 42, no. 12, pp. 4029–4034, Dec. 1994.
- [129] P. Shen, H. Fujii, T. Matsumoto, and K. Nogi, "The influence of surface structure on wetting of  $\alpha$ -Al<sub>2</sub>O<sub>3</sub> by aluminum in a reduced atmosphere," *Acta Mater.*, vol. 51, no. 16, pp. 4897–4906, Sep. 2003.

- [130] G. Levi and W. D. Kaplan, "Oxygen induced interfacial phenomena during wetting of alumina by liquid aluminium," *Acta Mater.*, vol. 50, no. 1, pp. 75–88, Jan. 2002.
- [131] Diamond Light Source Software Group and European Synchrotron Radiation Facility Software Group, "Data Analysis Workbench (DAWN)." [Online]. Available: <http://www.dawnsi.org/>. [Accessed: 19-Nov-2012].
- [132] V. A. Sole, E. Papillon, M. Cotte, P. Walter, and J. Susini, "A multiplatform code for the analysis of energy-dispersive X-ray fluorescence spectra," *Spectrochim. Acta B*, vol. 62, pp. 63–68, 2007.
- [133] J. Schindelin, I. Arganda-Carreras, E. Frise, V. Kaynig, M. Longair, T. Pietzsch, S. Preibisch, C. Rueden, S. Saalfeld, B. Schmid, J.-Y. Tinevez, D. J. White, V. Hartenstein, K. Eliceiri, P. Tomancak, and A. Cardona, "Fiji: an open-source platform for biological-image analysis.," *Nat. Methods*, vol. 9, no. 7, pp. 676–82, Jul. 2012.
- [134] E. Vlieg, "A concise ROD manual," pp. 1–23.
- [135] P. G. Debenedetti, *Metastable Liquids: Concepts and Principles*. Princeton: Princeton University Press, 1996.
- [136] D. Siegel, L. H. Jr, and J. Adams, "Adhesion, atomic structure, and bonding at the  $\alpha$ -Al<sub>2</sub>O<sub>3</sub>(0001)/Al(111) interface: A first principles study," *Phys. Rev. B*, vol. 3, no. 0001, pp. 1–23, 2002.
- [137] A. E. Lita and J. E. Sanchez, "Characterization of surface structure in sputtered Al films: Correlation to microstructure evolution," *J. Appl. Phys.*, vol. 85, no. 2, pp. 876–882, 1999.
- [138] T. Onishi, E. Iwamura, and K. Takagi, "Morphology of sputter deposited Al alloy films," *Thin Solid Films*, vol. 340, no. February 1998, pp. 306–316, 1999.
- [139] H. J. Stone, M. J. Peet, H. K. D. H. Bhadeshia, P. J. Withers, S. S. Babu, and E. D. Specht, "Synchrotron X-ray studies of austenite and bainitic ferrite," *Proc. R. Soc. A Math. Phys. Eng. Sci.*, vol. 464, no. 2092, pp. 1009–1027, Apr. 2008.
- [140] J. W. Elmer and E. D. Specht, "Measurement of Sn and In Solidification Undercooling and Lattice Expansion Using In Situ X-Ray Diffraction," *J. Electron. Mater.*, vol. 40, no. 2, pp. 201–212, Dec. 2010.
- [141] A. Korsunsky and K. Wells, "Mapping two-dimensional state of strain using synchrotron X-ray diffraction," *Scr. Mater.*, vol. 39, no. 12, pp. 1705–1712, 1998.
- [142] A. Guagliardi, "Powder Diffraction Pattern: Origin of Line Broadening & Peak Shape Functions," *Summer School on Structure Determination from*

*Powder Diffraction Data*, 2008. [Online]. Available:  
<http://www.scribd.com/doc/101569110/Antonella-Guagliardi#scribd>.

- [143] P. Lamparter and R. Kniep, "Structure of amorphous  $\text{Al}_2\text{O}_3$ ," *Phys. B*, vol. 236, pp. 405–406, 1997.
- [144] H. Sawada, "Residual electron density study of  $\alpha$ -aluminum oxide through refinement of experimental atomic scattering factors," *Mater. Res. Bull.*, vol. 29, no. 2, pp. 127–133, Feb. 1994.
- [145] M. R. Rowles, "On the calculation of the gauge volume size for energy-dispersive X-ray diffraction.," *J. Synchrotron Radiat.*, vol. 18, no. 6, pp. 938–41, Nov. 2011.
- [146] A. J. Brown, H. B. Dong, P. B. Howes, and C. L. Nicklin, "Exploring the Use of a Synchrotron X-Ray Scattering Method to Investigate Nucleation," *Mater. Sci. Forum*, vol. 765, pp. 102–106, Jul. 2013.
- [147] A. J. Brown, H. B. Dong, P. B. Howes, and C. L. Nicklin, "In situ observation of the orientation relationship at the interface plane between substrate and nucleus using X-ray scattering techniques," *Scr. Mater.*, vol. 77, pp. 60–63, Apr. 2014.
- [148] H. . Swanson and E. Tatge, "Standard X-ray diffraction powder patterns I." pp. 1–95, 1953.
- [149] A. S. Cooper, "Precise lattice constants of germanium, aluminum, gallium arsenide, uranium, sulphur, quartz and sapphire," *Acta Crystallogr.*, no. 15, pp. 578–582, 1962.
- [150] T. Novoselova, S. Malinov, W. Sha, and A. Zhecheva, "High-temperature synchrotron X-ray diffraction study of phases in a gamma Ti Al alloy," *Mater. Sci. Eng. A*, no. 371, pp. 103–112, 2004.
- [151] C. Jeynes, N. P. Barradas, J. R. Wilde, and A. L. Greer, "Composition of Ni–Ta–C thick films using simulated annealing analysis of elastic backscattering spectrometry data," *Nucl. Instruments Methods Phys. Res. B*, vol. 163, pp. 287–292, 2000.
- [152] H. Yan, Q. Wei, S. Chang, and P. Guo, "A first-principle calculation of structural, mechanical and electronic properties of titanium borides," *Trans. Nonferrous Met. Soc. China*, vol. 21, no. 7, pp. 1627–1633, Jul. 2011.
- [153] R. G. Fenish, "A new intermediate compound in the titanium-boron system,  $\text{Ti}_3\text{B}_4$ ," *Trans. Metall. Soc. AIME*, vol. 236, p. 804, 1966.
- [154] P. Norby, "Preparation and Structure of  $\text{Al}_3\text{Ti}$ ," *actachemscand.dk*.

- [155] CrystalMaker, "Al<sub>3</sub>Ti Structure." [Online]. Available: [http://som.web.cmu.edu/structures/S028-Al<sub>3</sub>Ti.html](http://som.web.cmu.edu/structures/S028-Al3Ti.html). [Accessed: 10-Apr-2014].
- [156] Y. V. Milman, D. B. Miracle, and S. I. Chugunova, "Mechanical behaviour of Al<sub>3</sub>Ti intermetallic and L12 phases on its basis," *Intermetallics*, vol. 9, pp. 839–845, 2001.
- [157] J. Wang, A. Horsfield, P. Lee, and P. Brommer, "Heterogeneous nucleation of solid Al from the melt by Al<sub>3</sub>Ti: Molecular dynamics simulations," *Phys. Rev. B*, vol. 82, no. 14, pp. 1–10, Oct. 2010.
- [158] J. Wang, A. Horsfield, U. Schwingenschlögl, and P. D. Lee, "Heterogeneous nucleation of solid Al from the melt by TiB<sub>2</sub> and Al<sub>3</sub>Ti: an ab initio molecular dynamics study," *Phys. Rev. B*, vol. 82, no. 18, pp. 1–10, 2010.
- [159] "Standard test procedure for aluminium alloy grain refiners (TP-1)." The Aluminium Association, Washington DC, 1990.